Simulation and Prediction of Machining Conditions Influences on Part Surface Integrity and Metallic Particle Emission using Multi-Physics Modeling

by

Irfan ULLAH

MANUSCRIPT-BASED THESIS PRESENTED TO ÉCOLE DE TECHNOLOGIE SUPÉRIEURE IN PARTIAL FULFILLMENT FOR THE DEGREE OF DOCTOR OF PHILOSOPHY
Ph.D.

MONTREAL, JUNE 26, 2025

ÉCOLE DE TECHNOLOGIE SUPÉRIEURE
UNIVERSITÉ DU QUÉBEC

BOARD OF EXAMINERS

THIS THESIS HAS BEEN EVALUATED

BY THE FOLLOWING BOARD OF EXAMINERS

Mr. Victor Songmene, Thesis supervisor
Département de génie mécanique, École de technologie supérieure

Ms. Esther T. Akinlabi, Thesis Co-Supervisor
Department of Mechanical Engineering, Colorado State University

Mr. Tony Wong, Chair, Board of Examiners
Département de génie des systèmes, École de technologie supérieure

Mr. Mohammad Jahazi, Member of the Jury
Département de génie mécanique, École de technologie supérieure

Mr. Walid Jomaa, Member of the Jury
Department of Mathematics and Industrial Engineering, Polytechnique Montréal

Mr. Serafettin Engin, External Examiner
Senior Fellow, Metal Cutting Manufacturing Technology Pratt & Whitney Canada Corp

THIS THESIS WAS PRESENTED AND DEFENDED

IN THE PRESENCE OF A BOARD OF EXAMINERS AND THE PUBLIC

ON JUNE 13, 2025

AT ÉCOLE DE TECHNOLOGIE SUPÉRIEURE

ACKNOWLEDGEMENTS

I would like to express my heartfelt gratitude to all those who have supported me, directly or indirectly, in successfully accomplishing this research work.

First and foremost, my deepest appreciation goes to my supervisor, Prof. Victor Songmene, and my co-supervisor, Prof. Esther T. Akinlabi, for their invaluable mentorship, guidance, and continuous academic and personal support. Their unwavering encouragement and insightful supervision have been instrumental in shaping this dissertation. I am truly grateful for their inspiration and guidance throughout my time at École de technologie supérieure (ÉTS).

I would also like to extend my sincere appreciation to my thesis committee members, Prof. Tony Wong, Prof. Mohammad Jahazi, Prof. Walid Jomaa, and Mr. Serafettin Engin for their time and effort in evaluating my thesis. Their valuable suggestions and constructive feedback have significantly contributed to improving the quality of this work.

A special thank you to Dr. Li Binxun, my former colleague, for his guidance, support, and assistance in finite element modeling. His help has been greatly appreciated.

I am also deeply grateful to all my past and present research fellows. Their camaraderie and support have made my time in the lab truly enjoyable. I feel fortunate to have been a part of LIPPS and will always cherish the friendships and collaborations I have built there. I wish them all great success in their future endeavors.

Finally, no words can fully express my deepest gratitude to my mother, brothers, sisters, and friends. Their unconditional love, encouragement, and unwavering support have been my greatest strength. Without them, I would not be where I am today.

Simulation et prédiction de l'influence des conditions d'usinage sur l'intégrité de surface des pièces et l'émission de particules métalliques à l'aide d'une modélisation multiphysique

Irfan ULLAH

RÉSUMÉ

Les progrès dans le développement des machines-outils à haute performance et des outils de coupe ultra-durs ont fait que le fraisage à sec à grande vitesse (HSDM) est devenu une technique de finition prometteuse pour l'usinage de matériaux difficiles à usiner, tels que le titane et ses alliages. Cependant, ce procédé crée des charges thermomécaniques intenses aux interfaces outil-copeau et outil-pièce qui induisent des altérations métallurgiques significatives dans sous la couche de surface usinée. Ces altérations comprennent la recristallisation dynamique (DRX), la transformation de phase et les changements d'orientation de la texture qui modifient les propriétés mécaniques de la sous-surface et influencent par conséquence la résistance à la fatigue et la durée de vie des composants fabriqués.

Malgré des recherches approfondies sur l'intégrité des surfaces usinées des pièces en titane et ses alliages, la plupart des études se sont concentrées sur le processus de tournage, avec une analyse théorique limitée des mécanismes physiques qui régissent la modification des propriétés mécaniques et métallurgiques près de la surface lors de l'usinage à haute vitesse. De plus, l'émission de particules métalliques fines et ultrafines pendant l'usinage représente un risque critique pour la sécurité et la santé des opérateurs, ce qui a conduit à l'adoption de réglementations de plus en plus rigoureuses pour limiter l'exposition. Ces émissions influencent aussi les performances de coupe et la durée de vie des outils. Alors que des études antérieures ont porté sur l'émission de particules de divers matériaux, les recherches sur l'alliage Ti-6Al-4V restent rares. Les mécanismes distincts de formation des copeaux et de libération des particules dans l'alliage Ti-6Al-4V nécessitent une étude approfondie du comportement de ce matériau lors de l'usinage, afin d'exploiter son potentiel tout en garantissant l'efficacité du processus, la durabilité environnementale et la sécurité opérationnelle.

Dans cette étude, les mécanismes d'évolution microstructurale, ainsi que d'autres caractéristiques de l'intégrité de surface (déformation plastique, formation de bavures, rugosité de surface, dureté, etc.) et les émissions de particules induites par les charges thermomécaniques lors du HSDM du Ti-6Al-4V, sont étudiés à l'aide d'approches de modélisation multi-échelles et d'expérimentations. Cette recherche basée sur des manuscrits est structurée comme suit

Tout d'abord, un modèle couplé d'éléments finis (température-déplacement) reproduisant le processus de fraisage a été établi pour l'usinage à haute vitesse de l'alliage Ti-6Al-4V. Dans le modèle proposé, le solveur Abaqus/Explicit a été utilisé pour coupler le dommage matériel et son énergie de rupture. La géométrie du copeau, variable dans le temps, a été numérisée en petits éléments avec des angles de rotation de la fraise distincts et des intervalles de temps discrets.

Le modèle a été validé par rapport aux efforts de coupe, à la morphologie du copeau et à la température. De bonnes corrélations ont été obtenues entre les résultats numériques et expérimentaux. Ce modèle d'éléments finis a fourni des variables de base de l'état critique, y compris la température, la contrainte et la déformation, essentielles pour les prévisions ultérieures de l'évolution de la microstructure. Ensuite, les équations de Zenner-Holloman (Z-H) et de Hall-Petch (H-P) ont été combinées dans un sous-programme défini par l'utilisateur (FORTRAN) pour modéliser la recristallisation dynamique (DRX) et estimer la taille des grains et la microdureté des pièces. Deuxièmement, à l'aide d'une sous-routine définie par l'utilisateur, des modèles théoriques de transformation de phase thermo-métallo-mécanique ont été intégrés dans la simulation de coupe du Ti-6Al-4V à l'aide du logiciel Abaqus/Explicit. Les distributions du champ de contrainte et de déformation de la température ont été récupérées à partir d'un modèle simulé validé pendant le chauffage rapide de l'alliage. Ces états de champ ont ensuite été utilisés pour modéliser le processus de refroidissement, en déterminant la fraction de volume de la phase α'. Les résultats ont révélé que pendant le chauffage rapide, la transformation de phase (c'est-à-dire de la phase α à la phase β) commence dans la région où la température dépasse les transitions de phase initiales de l'alliage Ti-6Al-4V, et presque toute la phase α a été transformée en phase β lorsque la température de coupe a franchi la température de transformation. Lors du refroidissement, l'effet de trempe a induit une transformation inverse de la phase β en phase α', affinant davantage la structure du grain.

Troisièmement, un modèle de fraisage simplifié a été développé, où l'épaisseur du copeau non déformé est approximée comme une fonction sinusoïdale pour la prédiction des contraintes résiduelles à l'intérieur de la pièce fraisée. Les fluctuations périodiques de la déformation plastique et de la contrainte résiduelle pendant le processus de fraisage ont été dévoilées. Enfin, les profils de contraintes résiduelles simulés pour la surface et la sous-surface usinées ont été comparés aux mesures expérimentales, et l'influence des charges thermomécaniques sur la formation des contraintes résiduelles a été étudiée en profondeur. Enfin, une approche expérimentale a été utilisée pour étudier la corrélation entre les paramètres d'usinage, la formation de copeaux, l'intégrité de la surface et l'émission de particules. Les résultats ont montré qu'une augmentation de la vitesse de coupe entraînait initialement une augmentation de la dentelure des copeaux, de l'épaisseur de la couche déformée, des émissions de particules et de la rugosité de la surface, suivie d'une diminution ultérieure. En revanche, l'augmentation de la vitesse d'avance et de la profondeur de coupe intensifie systématiquement ces effets. Une relation directe a été observée entre les émissions de particules et les paramètres d'intégrité de la surface usinée, tels que la profondeur de déformation plastique, la formation de bavures, la rugosité de surface et la morphologie des copeaux. Cette recherche améliore la compréhension théorique et les applications pratiques dans le domaine de la fabrication, offrant des informations précieuses aux industries, aux chercheurs et aux institutions universitaires. Les résultats contribuent au développement de stratégies d'usinage optimisées qui améliorent l'intégrité de la surface des pièces et atténuent les impacts des émissions de particules fines sur l'environnement et la santé lors de l'usinage à grande vitesse de l'alliage Ti-6Al-4V.

Mots-clés: Recristallisation Dynamique, Fraisage à Grande Vitesse, Modélisation Multi-physique, Évolution Microstructurale, Propriétés Mécaniques, Transformation de Phase, Émissions de Particules, Intégrité de Surface, Alliage Ti-6Al-4V

Simulation and Prediction of Machining Conditions Influences on Part Surface Integrity and Metallic Particle Emission using Multi-Physics Modeling

Irfan ULLAH

ABSTRACT

With the advancement of high-performance machine tools and ultrahard cutting tool materials, High-Speed Dry Milling (HSDM) has emerged as a promising finishing technique for machining difficult-to-cut materials such as titanium and its alloys. However, this process creates intense thermomechanical loads at the tool-chip and tool-part interfaces, which induce significant metallurgical alterations in the subsurface of the machined surface layer. These alterations include Dynamic Recrystallization (DRX), phase transformation and textural orientation changes, which modify the mechanical properties of the subsurface and consequently influence the fatigue strength and service life of manufactured components.

Despite extensive research into the integrity of machined surfaces of titanium and its alloy, most studies have focused on the turning process, with limited theoretical analysis of the physical mechanisms governing the modification of near-surface mechanical and metallurgical properties during high-speed machining. Furthermore, the emission of fine and ultra-fine metal particles during machining represents a critical risk to the safety and health of operators, which has led to the adoption of increasingly stringent regulations to limit exposure. These emissions also influence cutting performance and tool life. While previous studies have investigated the emission of particles from various materials, research on the Ti-6Al-4V alloy remains limited. The distinct mechanisms of chip formation and particle release in Ti-6Al-4V alloy requires an in-depth study of this material's behavior during machining, in order to capitalize on its potential while ensuring process efficiency, environmental sustainability and operational safety.

In this study, the microstructural evolution mechanisms, along with other surface integrity features (plastic strain, burr formation, surface roughness, hardness, etc.) and particle emissions induced by thermo-mechanical loads during HSDM of Ti-6Al-4V, are investigated using multiscale modeling and experimental approaches. This manuscripts-based research is structured as follows:

First, a temperature-displacement coupled Finite Element (FE) model, replicating the actual milling process, was established for the HSM of Ti-6Al-4V alloy. In the proposed model, Abaqus/Explicit solver was utilized to couple the material damage and its fracture energy. The time-varying chip geometry was digitized into small elements with distinct cutter rotation angles and discrete time intervals. The model was validated against cutting forces, chip morphology and temperature; Strong correlations between numerical and experimental results were obtained. This FE model provided critical state field variables, including temperature, stress, and strain, essential for subsequent microstructural evolution predictions. Following that, the Zenner-Holloman (Z-H) and Hall-Petch (H-P) equations were combined in a user-defined subroutine (FORTRAN) to model dynamic recrystallization (DRX) and estimate grain size and microhardness. The results indicated that at higher cutting speeds and feed rates, grain refinement

occurred more prominently in the adiabatic shear band (ASB) than on the cutting surfaces. In contrast, microhardness exhibited an inverse correlation with grain size, increasing with cutting speed and feed rate. The influence of plastic strain and temperature on grain size during chip segmentation was also examined. Experimental validation confirmed a strong correlation between the developed model and observed results regarding grain size and parts microhardness. Secondly, using a user-defined subroutine, thermo-metallo-mechanical phase transformation theoretical models were integrated into Ti–6Al–4V cutting simulation using Abaqus/Explicit software. The temperature and stress-strain field distributions were retrieved from a validated simulated model during the rapid heating of the alloy. These field states were then used to model the cooling process, determining the volume fraction of the α'-phase. The results revealed that during the rapid heating, the phase transformation (i.e., α- to β)-phase starts within the region where the temperature exceeds the initial phase transitions of Ti-6Al-4V alloy, and almost all of the α-phase has been transformed into β-phase when the cutting temperature crossed the transus temperature. Upon cooling, the quenching effect induced a reverse transformation from the β-phase to the α'-phase, further refining the grain structure.

Thirdly, a simplified milling model was developed, where the undeformed chip thickness is approximated as a sinusoidal function for residual stress prediction within the milled part. The periodic fluctuations of plastic strain and residual stress during the milling process were unveiled. Finally, the simulated residual stress profiles for the machined surface and subsurface were compared with experimental measurements, and the influence of thermo-mechanical loads on residual stress formation was thoroughly investigated.

Finally, an experimental approach was employed to investigate the correlation between machining parameters, chip formation, surface integrity, and particle emission. The results demonstrated that increasing cutting speed initially led to greater chip serration, deformed layer thickness, particle emissions, and surface roughness, followed by a subsequent decrease. In contrast, increasing feed rate and depth of cut consistently intensified these effects. A direct relationship was observed between particle emissions and machined surface integrity parameters such as plastic deformation depth, burr formation, surface roughness, and chip morphology. This research enhances theoretical understanding and practical applications in the field of manufacturing, offering valuable insights for industries, researchers, and academic institutions. The findings contribute to the development of optimized machining strategies that improve surface integrity and mitigate the environmental and health impacts of fine particle emissions in HSDM of Ti-6Al-4V alloy.

Keywords: Dynamic Recrystallization, High Speed milling, Multi-physics modeling, Microstructure evolution, Mechanical properties, Phase Transformation, Particle Emissions, Surface Integrity, Ti-6Al-4V alloy

TABLE OF CONTENTS

Page

LIST OF TABLES

LIST OF FIGURES

LIST OF ABBREVIATIONS

ASB	Adiabatic shear band
BCC	Body centered cubic
CFs	Cutting forces
CT	Cutting Temperature
CDZs	Cutting Deformation Zones
DD	Dislocation density
DRX	Dynamic recrystallization
EBSD	Electron back scattering diffraction
ES	Equivalent strain
FE	Finite element
FEM	Finite element method
FWHM	Full width at half maximum
GS	Grain size
HRC	Rockwell hardness
HSM	High-Speed Milling
HSDM	High-speed dry milling
HV	Vickers hardness
IP	Inverse pole
J-C	Johnson Cook

JMAK	Johnson-Mehl-Avrami-Kolmogorov
MRR	Material removal rate
OM	Optical microscopy
RS	Residual stress
SEM	Scanning electron microscopy
SPD	Severe plastic deformation
SR	Strain rate
TW	Tool wear
TEM	Transmission electron microscopy
XRD	X-ray diffraction
ZH	Zener-Hollomon

LIST OF SYMBOLS AND UNITS OF MEASUREMENTS

A	Initial yield strength (MPa)
a_e	Radial depth of cut (mm)
a_p	Axial depth of cut (mm)
B	Hardening modulus (MPa)
C	Strain rate hardening coefficient (-)
C_0	Initial hardness (HV)
C_1	Material constant (-)
d	Instantaneous depth of cut (mm)
d_0	Initial grain size (μm)
$d_{\varphi\psi}$	Interplanar spacing (-)
E	Young's modulus (MPa)
f_z	Feed rate (mm/tooth)
G_f	Fracture energy (J)
G_s	Degree of segmentation (-)
H	Serrated chip peak (μm)
h	Serrated chip valley (μm)
l_c	Cutting length (mm)
p	Pressure stress (MPa)
Q	Activation energy (KJ/mol)

q	Von Mises stress (MPa)
R	Universal gas constant (J/K/mol)
R	Milling tool radius (mm)
T	Current temperature ($^{\circ}C$)
T_{room}	Room temperature ($^{\circ}C$)
T_{melt}	Melting temperature ($^{\circ}C$)
T_{MS}	Martensitic transformation temperature ($^{\circ}C$)
V_c	Cutting speed (m/min)
$V_{\alpha'}$	Volume fraction of α'-phase (%)
V_{β}	β-phase volume fraction (%)
ν	Poisson's ratio (-)
w	Damage initiation variable (-)
X	Martensitic transition rate (-)
Z	Zener-Hollomon parameter (-)
t_c	Instantaneous chip thickness (mm)
φ_1	Angular displacement (º)
θ_s	Cutter entry angle (º)
σ	Flow stress (MPa)
σ_{φ}	Surface stress (MPa)
σ_{11}	Residual stress in X-direction (MPa)

σ_{22}	Residual stress in Y-direction (MPa)
ε	Plastic strain (-)
ε_{cr}	Critical strain (-)
ε_t	Transformation strain (-)
ΔH_{tr}	Latent heat of transformation (-)
τ_f	Frictional shearing stress (MPa)
τ_{crit}	Critical shear stress (MPa)
η	Stress triaxiality (-)
μ	Coulomb's friction coefficient (-)

INTRODUCTION

This chapter discusses the motivation, research challenges, objectives, and structure of the thesis, focusing on the HSM of Ti-6Al-4V alloy. The research is motivated by the desire to improve surface integrity, which is critical for the performance of Ti-6Al-4V components in various industries. However, several challenges hinder its optimization, including complex microstructure evolution, variations in mechanical properties, and the generation of harmful particle emissions during machining. Understanding and addressing these challenges are essential for improving machining efficiency, enhancing component durability, and ensuring environmental and occupational safety. The chapter concludes by outlining the thesis organization, which systematically explores these aspects to advance the understanding and optimization of HSM for the Ti-6Al-4V.

Motivation

The evolving industrial expansions in the past few decades need increasingly productive components manufacturing technologies that can match the required pace of development. Economic growth and strict ecological constraints also require cost-effective and environmentally friendly manufacturing processes with minimum adverse effects. High-speed milling (HSM) is among the most cost-effective and efficient modern manufacturing technologies, broadly employed in aerospace, automotive, aircraft, and die- and mold-making industries to increase productivity and simultaneously improve the surface qualities of the end products (Ullah, Zhang, Zhang & Wang, 2021b). Recently, various advanced forming technologies, such as laser processing, powder metallurgy, and 3D printing, have greatly assisted the advancement and development of the machinery manufacturing industry, as science and technology have made progress. Nevertheless, machining still plays an essential role in forming. The final forming of the most critical parts is still dominated by cutting, a mechanical manufacturing method with the broadest application possibility. Despite numerous advantages, the workpiece-tool and

chip-tool interface experiences a lot of heat during HSM, dramatically influencing machined surface integrity, accelerating tool wear (TW), and reducing cutting efficiency (Ullah *et al.*, 2021b). Various lubrication techniques were introduced to minimize the TW and improve machinability. However, standard cutting fluids usually need significant energy and resource consumption, which might be incompatible with the present notion of "creating a resource-saving and environmentally friendly society." Pertaining to the effect of changing machining atmospheres upon the machinability, it is also important to note that the use of these cutting fluids will produce a massive amount of waste solution; as a result, it will not only pollute the environment but also have a significant influence on the machinist's wellbeing (Kumar & Kumar, 2021). Hence, it is urgent to develop green and sustainable advanced manufacturing technology to replace traditional cutting methods. The requirements should be environmentally friendly, harmless, and waste-free, saving resources and production costs. For machining, sustainable manufacturing technologies are mainly based on innovations in tool technology and changes in lubrication methods. With the emergence of high-performance machine tools and the continuous improvement of cutting tool materials, high-speed dry milling (HSDM) that does not use cutting fluid has been valued by academia and industry in the modern manufacturing system (Li et al. 2019). HSDM can fully meet the basic requirements of green and sustainable manufacturing technology and is known as one of the most promising advanced manufacturing technologies (Haber, Jiménez, Peres & Alique, 2004). Compared with the other traditional cutting methods, HSM has undeniable advantages, such as the realization of cutting instead of grinding, small surface roughness value, larger Material Removal Rate (MRR), high production efficiency, low cost, low energy consumption, and small environmental pollution. Although HSM has demonstrated significant application benefits and future growth potential, it still confronts several hurdles, particularly when cutting difficult-to-machine materials. Titanium and its alloys are among such materials which is used in various industrial sectors, including biomedical, automobile, aerospace, and marine (Hojati, Daneshi, Soltani, Azarhoushang & Biermann, 2020).

This popularity is due to their remarkably high strength-to-weight ratio and tremendous corrosion resistance (Ginting & Nouari, 2009). However, lower heat conductance, excessive reactivity to chemicals, and minimal modulus of elasticity contribute to inadequate machining behavior, substantially impacting the product's surface characteristics. Despite the recent advancements in machining technology and broad manipulation of such alloys, the machining of titanium continues to be a vital issue from an industrial perspective. Numerous research works have been reported on the machinability of titanium, including surface geometry, chip formation (Velásquez, Bolle, Chevrier, Geandier & Tidu, 2007), cutting forces (Sun, Brandt & Dargusch, 2009), and tool wear (Ezugwu, Bonney, Da Silva & Çakir, 2007). However, research on the quality of the cutting surface layer, especially microstructural evolution and macro-mechanical properties of cutting deformation zones under the action of multiple physical models, is rarely reported. In addition, Ti-6Al-4V with multi-scale microstructure lacks in-depth research and interpretation on the evolution mechanism of cutting subsurface and chip microstructure. Similarly, emissions of fine particles produced during machining represent a health hazard. Laws to protect against harmful particles are becoming increasingly strict. The size of dust particles, where they are deposited in the body, and how dangerous they are. Experimental research in the field of particle emissions shows that their emissions (sizes, distribution, concentrations) and behavior in the machining environment depend on the cutting tool geometry, machining parameters, strategies, and materials, as well as the response of the material to the cutting process (Khettabi, Songmene, Zaghbani & Masounave, 2010b). The presence of these particles also modifies the cutting process and the tool's performance. Previous research has investigated a variety of materials but has mostly disregarded titanium alloys. The chip formation and particle emission in titanium alloys differ dramatically from those in other materials. Hence, it would benefit research communities to include this factor while machining.

Research Challenges

During HSM, the material microstructure in the machined subsurface changes consistently, adversely affecting the mechanical properties of the cutting surface layer and significantly influencing the final products' service performance and fatigue life. Considering the existing research, numerous studies have been reported on the machinability of Ti-6Al-4V. However, the most prominent study focuses on the turning process. It is worth mentioning that during the milling process, the occlusion of cutting tools, chips, and certain other factors instantly transforms into a thermomechanical load, which has a significant impact on the quality of the machined surface layer, particularly the microstructural evolution and macroscopic mechanical properties. In addition, the influence of the onset of chip flow on machined surface integrity remains inadequately explored and requires further investigation. Furthermore, in numerous studies, the complex 3D milling process is often simplified into a 2D cutting simulation to reduce computational complexity; however, existing FE models tend to produce overly homogeneous and uniform chips. Hence, an accurate FE model is required to replicate the actual milling process. In addition, it has also been realized that little is known about particle emission during the machining of titanium and its alloys. For clean machining, dust emission is crucial for safeguarding the health and safety of workers, maintaining environmental quality, adhering to regulations, and ensuring efficient and high-quality production processes. Hence, proper research should be conducted to control the particle emissions during titanium machining.

Research Objectives

This Ph.D. dissertation focuses on simulating and predicting the influence of machining conditions on part surface integrity and metallic particle emissions in HSDM of Ti-6Al-4V. A multiscale FE model has been developed with the purpose of real-time and quantitatively capturing the microstructure evolution, including grain size, phase transformations, and mechanical properties

in the cutting deformation zones. The model accurately captures the effects of thermo-mechanical loading conditions and metallurgical alterations during milling of Ti-6Al-4V. Furthermore, an experimental approach is employed to analyze metallic particle emissions and their correlation with surface integrity. This combined approach will optimize machining processes, improve surface quality, and enhance worker safety and environmental sustainability. Building on challenges identified in previous research, the following long-term and short-term objectives are outlined, which aim to advance scientific understanding and industrial practices in high-speed machining of titanium alloys.

Long-term Objectives

Develop a multiscale FE model for the milling process, integrated with experimental validation, to simulate and predict the influence of machining conditions on part surface integrity—including microstructure evolution, phase transformation, and macroscopic mechanical properties as well as metallic particle emissions during HSM of Ti-6Al-4V. This comprehensive framework will provide useful insights for optimizing the milling process, improving surface quality, and enhancing environmental and worker safety.

Short-term Objectives

The following short-term objectives are designed to systematically address key aspects of the long-term goal. These objectives focus on advancing the understanding of microstructure evolution, mechanical properties evaluation, and particle emissions in the context of HSM.

1. A multiscale FE model for microstructure prediction during HSM of Ti-6Al-4V.

   This first objective focuses on the development and validation of a simplified multiscale FE model to predict microstructure changes in Ti-6Al-4V during HSM. The model considers both thermal and mechanical loads, specifically the effects of cyclic thermal loads (heating and cooling) on subsurface grain refinement. By addressing the gap in understanding how

intermittent cutting conditions influence microstructure compared to other traditional cutting processes, this model provides insights into the combined role of thermal and mechanical loading. Additionally, the effect of chip serration on grain size has been analyzed, confirming the model's reliability in predicting microstructure changes under HSM conditions.

2. A Phase transformation prediction model for Ti-6Al-4V during HSM.

   The second objective focuses on developing a thermo-metallo-mechanical phase transformation model for Ti-6Al-4V during high-speed milling (HSM), incorporating the effects of high stress, large strain, and rapid thermal cycles. The proposed model advances existing approaches by accounting for dynamic recrystallization and the high strain rates characteristic of the cutting process, thereby providing a more accurate representation of phase transformation behavior during milling.

3. Quantitative evaluation of macroscopic mechanical properties of the cutting surface layer.

   This objective focuses on the investigation of how machining conditions influence the macroscopic mechanical properties (such as residual stress and hardness) of the cutting surface in Ti-6Al-4V. The quantitative evaluation includes the prediction of cyclic residual stresses using both FE modeling and experimental approaches. The relationship between thermo-mechanical loads and residual stress has been systematically analyzed, providing critical data that improves the HSM efficiency and part performance, with particular emphasis on cyclic residual stress behavior and its impact on fatigue life.

4. Particle emissions investigation during HSM of Ti-6Al-4V alloy.

   This study involves experimental investigations into metallic particle emissions during the dry cutting of Ti-6Al-4V. The focus is on understanding the correlation between surface integrity, thermo-mechanical loads, and the quantity and size distribution of emitted particles. The objective is to generate insights that support the reduction of health risks and the enhancement of environmental safety, ultimately contributing to the development of safer and more sustainable machining processes.

Thesis outlines

This study focuses on the HSM of Ti-6Al-4V, with an emphasis on developing a multi-physics modeling framework to simulate and predict the influence of machining conditions on part surface integrity and metallic particle emissions. The first section presents the motivation behind the study, the challenges associated with HSM, and the significance of Ti-6Al-4V in industrial applications. It also addresses the research gaps in the field, followed by the formulation of the research aims and objectives. Finally, the overall framework of the dissertation is described. Based on the current state of research in surface integrity and particle emissions during machining, the dissertation is structured into six chapters. The workflow (Fig. 0.1) of the dissertation and the description of each chapter are described as follows.

Chapter 1: This chapter provides an overview of the research background and highlights the significance of HSM across various industries. It reviews the machinability of Ti-6Al-4V and the current research status concerning machined surface integrity and the mechanical properties of the cutting surface layer during HSM. Additionally, it discusses prediction models for metallurgical alterations and the evolution of macro-mechanical properties. The chapter also examines particle emissions generated during machining. Finally, it identifies research gaps and outlines the primary research content and approach of this study.

Chapter 2: This chapter details the research methodology employed in the study. It describes the experimental setup, including the milling setup, experimental plan, workpiece material, and cutting tool. Additionally, it covers the sample preparation process for analyzing chip morphology and metallurgical alterations in the cutting surface layer. The characterization techniques used throughout the research are presented, along with the experimental procedures for evaluating macro-mechanical properties, measuring surface roughness, and analyzing particle emissions. The computational methodology applied in this study is also described.

Chapter 3: This chapter introduces the first objective of the study by developing and validating a simplified FE milling model for Ti-6Al-4V. This model serves as the foundation for the subsequent phase of the study. A user-defined subroutine is integrated into the model to predict grain size and microhardness within the cutting deformation zones. The chapter then investigates the impact of variations in stress-strain and temperature on grain size and validates the model by comparing the predicted results with experimentally observed machined subsurface grain structures and microhardness values.

Chapter 4: This chapter introduces the second objective of the research, which is the development of a thermo-metallo-mechanical FE model for predicting phase transformations during HSM of Ti-6Al-4V. The model successfully predicts phase transitions during both the heating and cooling stages. Temperature and stress-strain field distributions during the rapid heating stage are obtained from the validated simulation model, enabling the determination of the β-phase volume fraction. The final state from the heating phase is then used as the initial condition for the cooling process model, where the α'-phase volume fraction is determined. Finally, advanced characterization techniques were employed to validate the developed model.

Chapter 5: This chapter focuses on the third main objective of the research using a combined numerical and experimental approach for an in-depth analysis of RS prediction in the milled part of Ti-6Al-4V. The study examines the cyclic variation of plastic strain and RS in both the machined surface and subsurface. The chapter establishes the correlation between thermo-mechanical loads and RS distribution, providing valuable insights into the evolution of stresses during HSM of Ti-6Al-4V.

Chapter 6: The final chapter investigates the correlation between machined surface integrity, chip formation, and particle emissions. A series of milling experiments is conducted to analyze the influence of machining parameters on chip formation, surface integrity, and particle

emissions. The study establishes and discusses a quantitative relationship between machined surface integrity and particle emissions, offering deeper insights into their interdependence.

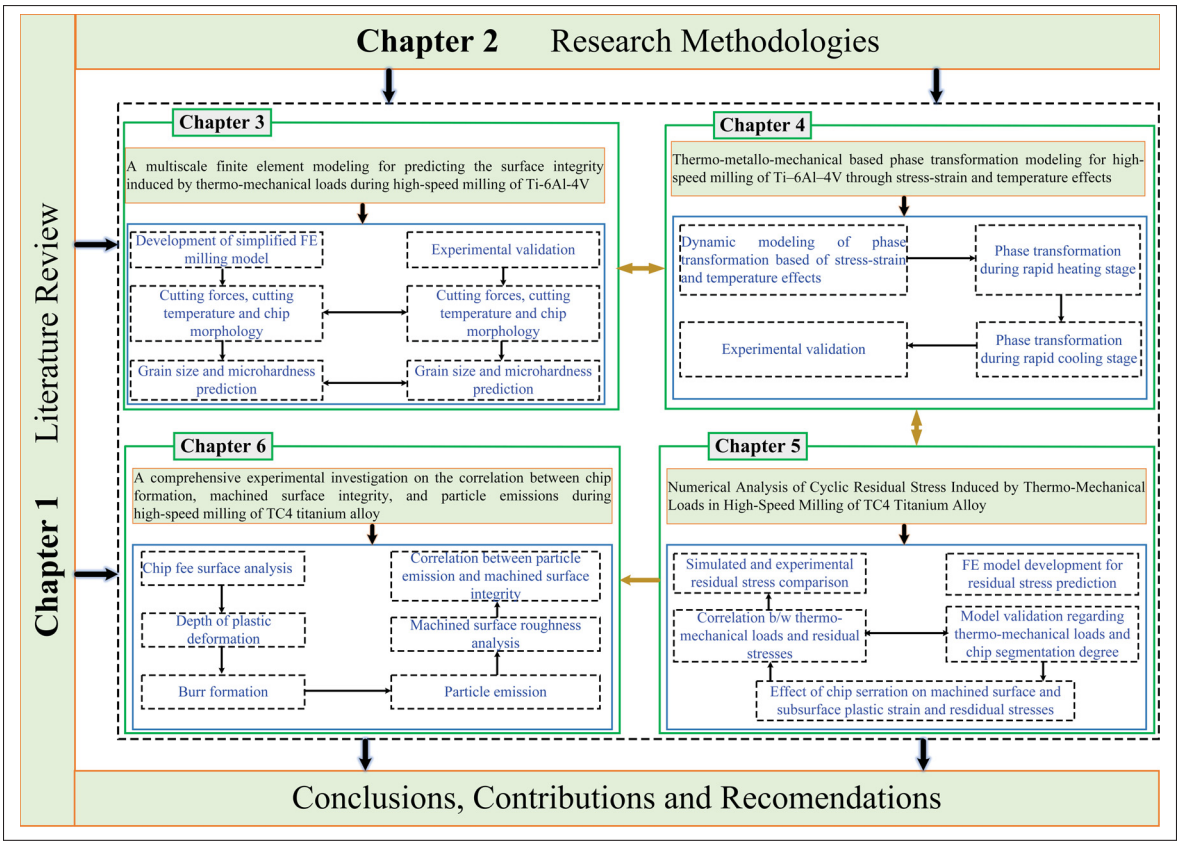

Figure 0.1 Flowchart description of the dissertation framework

CHAPTER 1

LITERATURE REVIEW

1.1 Introduction

Green manufacturing technology has long been a primary focus of the machinery manufacturing industry due to its notable advantages in environmental sustainability and resource efficiency. Among these technologies, high-speed dry milling (HSDM) has garnered significant attention as a prominent green manufacturing approach. Current research on the surface quality achieved through HSDM predominantly emphasizes surface geometric characteristics, while limited studies explore the microstructural evolution and mechanical properties of the cutting deformation zone and the machined surface layers. This chapter reviews and synthesizes the existing research on the evolution mechanisms, predictive modeling, and mechanical property evaluation of cutting surface materials in the deformation zones of HSDM. It identifies the key gaps and challenges in the field and establishes this dissertation's research objectives and scope.

1.2 Research background and significance

High-speed dry milling, a cutting-edge manufacturing method, remains one of the most extensively utilized machining processes. While emerging technologies like additive manufacturing have progressed beyond rapid prototyping to the production of structural and functional components, metal machining continues to be indispensable. This is due to its versatility, superior surface finish, high material removal efficiency, and ability to process nearly all metallic materials (Wang *et al.*, 2021). The global machining market is worth around USD 402.56 billion by 2024 and is anticipated to reach around USD 755.66 billion by 2034, growing at a compound annual growth rate of 6.5% from 2024 to 2034 (Research, 2024). Despite the recent advancements in developing high-performance machine tools and flexibility, HSM continuously faces challenges, especially during the machining of difficult-to-cut materials.

1.3 Machinability of titanium and its alloys

Titanium and its alloys are among the materials that are broadly employed in various industries, such as aerospace, biomedical, automobile, and die and mold, because of their outstanding combination of high strength-to-weight ratio, exceptional corrosion resistance, and high fracture resistance characteristics (Fang & Wu, 2009). Conversely, high chemical reactivity, low thermal conductivity and elastic modulus, and phase transformation at elevated temperatures make them difficult to machine. The high demand for titanium across various industries has motivated manufacturing experts to look for techniques to improve the material removal rate and enhance the machinability of titanium and its alloys. Ti−6Al−4V holds a substantial market share among other alloys, constituting approximately 50% of all titanium alloys (Singh *et al.*, 2020). Some prominent industries with extensive applications of Ti−6Al−4V are depicted in Fig. 1.1.

Figure 1.1 Prominent applications of titanium and its alloys across various industries

The machining of Ti−6Al−4V is quite different from that of other conventional materials. The additional complexities during the machining process of this alloy arise due to its response to the moving cutting tool (Pramanik & Littlefair, 2015). For instance, this alloy has a high yield stress to tensile strength ratio (> 0.9), and its flow stress increases significantly with the strain rate, particularly when the strain rate exceeds $10^3 s^{-1}$ which is easily achievable in any machining process. The machining of Ti−6Al−4V is an old topic of interest. Numerous experimental and theoretical investigations were conducted on the machining aspects, including cutting forces, chip morphology, and RS. However, the majority of the studies were focused on the turning process. The results obtained from the turning process cannot be applied to the milling process since, in the latter case, intermittent cutting comes into existence; as a result, the cutting tools are subjected to various aggressive circumstances. During the milling process of Ti−6Al−4V alloy, the cutting tool is subjected to numerous failure modes due to substantial loading and unloading conditions (Pramanik, 2014). This phenomenon influences the machined surface qualities, dimensional accuracy, and, most importantly, end mechanical product properties. The crucial characteristics that unfavorably affect the machinability of Ti−6Al−4V will be introduced in the following section using a combination of performance criteria, like chip formation and part quality.

1.3.1 Chip formation during high-speed machining of Ti-6Al-4V alloy

Chip formation is a typical index used to evaluate materials' machinability and the mechanical response of the working material under the influence of tool geometry, cutting parameters, and material properties. Generally, the evolution of microscopic structure in chips faithfully reflects the phenomenon of mechanical and thermal loads in the cutting process, which can provide an important reference for an in-depth understanding of the cutting process and improve the quality of a cutting surface. In addition, it can also help in understanding the mechanical behavior of materials and thus further predict changes in material properties during cutting. Various types of chips can form during metal cutting, with their characteristics influenced by factors such as cutting speed, feed rate, and tool geometry. One common type is the continuous chip,

illustrated in Fig. 1.2(a). These chips are produced under steady-state shear deformation and are characterized by their long, unbroken form and smooth surface, which indicates efficient material removal and minimal tool wear. Continuous chips are typically associated with stable machining processes and a high-quality surface finish on the workpiece. However, when the cutting speed increases or the thermal conductivity of the workpiece material is low, heat generated in the shear zone cannot dissipated effectively. This results in localized adiabatic shear, leading to an unsteady cutting process and the formation of serrated chips, as shown in Fig. 1.2(b). Another type of chip, the discontinuous chip Fig. 1.2(c), forms at higher cutting speeds and higher feed rates. These chips are shorter and fragmented, often arising from brittle material behavior or less favorable machining conditions. While discontinuous chips can indicate higher tool wear and a rougher machined surface, they are easier to handle and evacuate from the cutting zone.

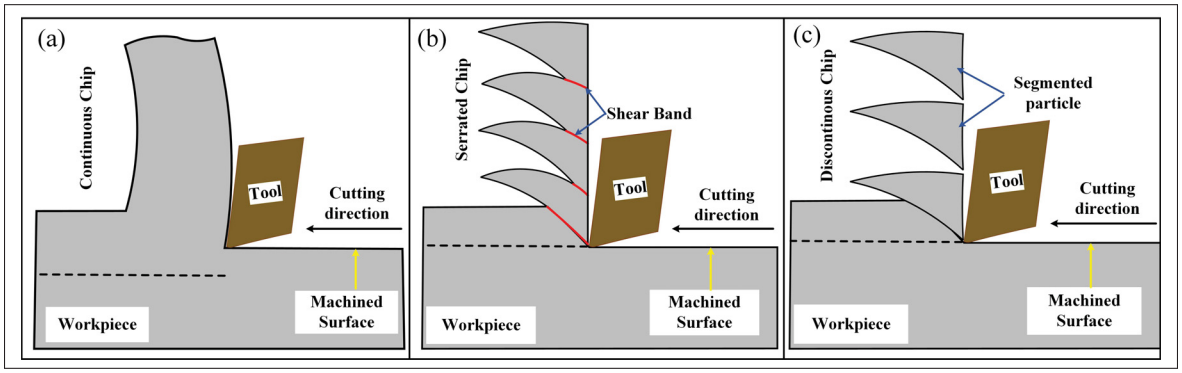

Figure 1.2 Schematic diagram of chip formation during HSM of Ti−6Al−4V alloy

A substantial experimental, theoretical, and FE-based investigation has been conducted on the chip formation process during the HSM of Ti-6Al-4V. Among them, the cyclic crack/fracture initiation and propagation mechanism and the thermo-plastic instability theory, also known as adiabatic shear theory, are two well-proposed approaches to manipulate the serrated chip's formation mechanism (Ullah *et al.*, 2021b; Neugebauer *et al.*, 2011). (Wang, Liu, Su, Song & Ai, 2015) examined the fracture characteristic features of chips during the cutting process and discovered the occurrence of ductile-to-brittle transformation. Similarly, (Liu, Zhang, Xu & Zhao, 2018) tried to uncover the pathway of serrated chip formation during HSM of Ti−6Al−4V alloy, and found that the adiabatic shear band for serrated chips is similar at cutting speeds ranging

from 250 m/min to 500 m/min, but the GS was increased and both equiaxed and columnar grains were reported at 500 m/min (Fig. 1.3).

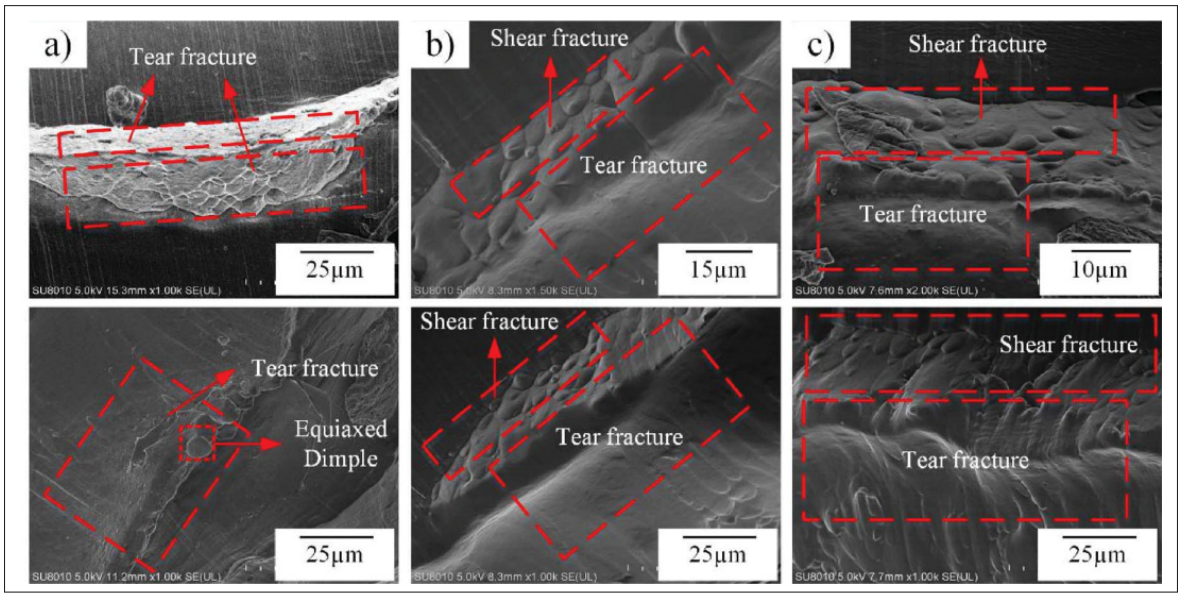

Figure 1.3 Fracture characteristics of gaps in serrated chips at (a) 250 m/min, (b) 375 m/min and (c) 500 m/min
Taken from Liu *et al.* (2018)

It is also believed that the material's microstructure strongly influences chip formation when machining Ti−6Al−4V. As indicated in Fig. 1.4 (Wang *et al.*, 2015) examined the geometrical and metallurgical alternations of the Ti−6Al−4V chips by dividing the shear into a deformation band, deformation band, and phase change band and phase change band and acknowledged that the transformations triggered are martensitic phase transformations of β-Ti with BCC structure to α'' phase with orthorhombic structure. In contrast, (Velásquez, Tidu, Bolle, Chevrier & Fundenberger, 2010) observed no phase changes inside the shear bands.

According to the literature review, most researchers focus on chip morphological features and formation mechanisms during turning. Not like milling, turning produces more homogeneous and uniform chips. Furthermore, the thermo-mechanical loads applied to the cutting tool remain generally uniform during turning, indicating a significant difference between the two machining techniques. In milling, however, the undeformed chip thickness fluctuates as the cutting tool

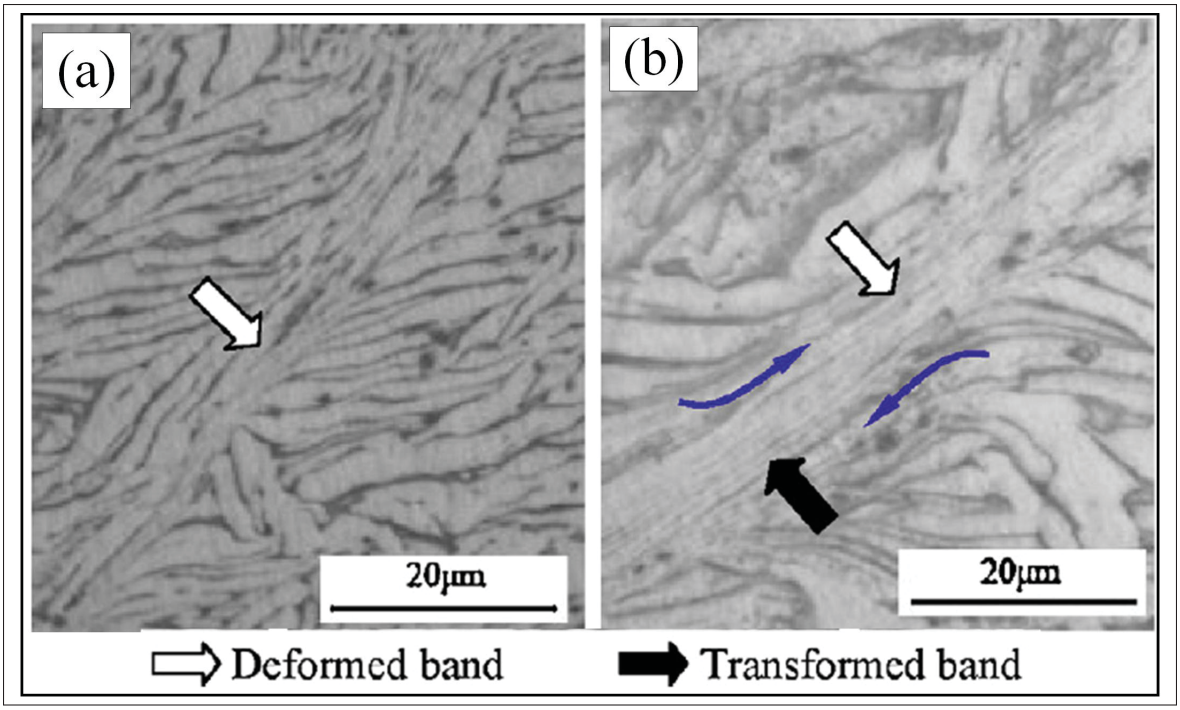

Figure 1.4 Shear bands' micro-features of saw-tooth chips obtained at different cutting speeds; (a) 30.2 m/min; (b) 126.6 m/min
Taken from Wang *et al.* (2015)

advances, resulting in variations in the thermo-mechanical. Furthermore, due to the intermittent nature of milling, cutting tools experience some vibration when interacting with the workpiece. As a result, a thorough investigation of chip formation in milling is required to lay a theoretical framework for understanding the formation mechanisms of machined surfaces and enhancing cutting quality.

1.3.2 Surface integrity during High-speed machining

The concept of surface integrity, first introduced by Field and Kahles in the early 1960s, describes the physical, mechanical, and metallurgical characteristics of a workpiece's surface and subsurface after machining. It encompasses aspects such as surface topography, metallurgical changes, and mechanical properties. A key advantage of HSM is maintaining excellent surface integrity in the final machined component. Surface topography primarily influences the contact

conditions and stress concentrations on machined components, while metallurgical alterations in the machining-affected zone govern the surface's mechanical properties (Wang *et al.*, 2021). These factors collectively impact the overall performance and service life of the component. The following sections provide a brief overview of recent studies and findings on surface integrity, including metallurgical changes, surface topography, and the mechanical characteristics of machined surfaces.

1.3.3 Microstructural alterations of the machined subsurface in High-speed machining

In recent years, microstructural modifications in the cutting surface layer have gained increasing attention and are now widely recognized as a critical surface integrity parameter influencing surface properties and overall performance. To better define this concept, the cross-sectional area of the machined sample that exhibits structural differences from the original substrate, as observed under OM or SEM, is collectively termed the subsurface, also referred to as the metamorphic layer. This subsurface layer comprises various microstructural features, including but not limited to the white layer, dark layer, and plastic deformation layer (Fig. 1.5).

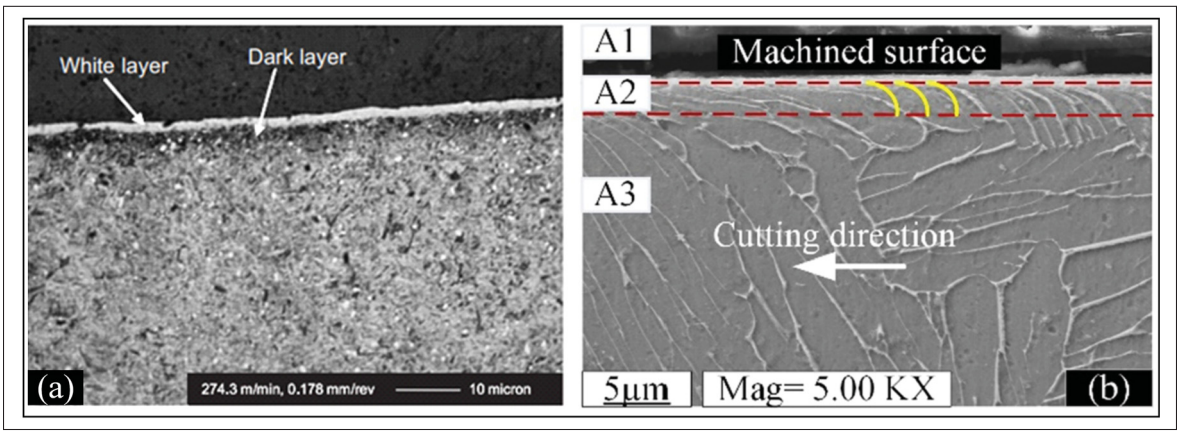

Figure 1.5 Metamorphic layer irregularities
Taken from Ramesh & Melkote (2008); Ullah, Zhang, Zhang & Li (2021a)

Microstructural evolution in the machining of titanium conceals phase transformation (PT), dynamic crystallization, GS, and twinning, with a combined effect of thermo-mechanical

interactions. HSM can induce SPD in the cutting deformation zone, adversely affecting a series of crystal defects in the internal microstructure, such as torsional deformation, dislocation plug, twin recrystallization, etc. Fig. 1.6 describes a relationship between these characteristics.

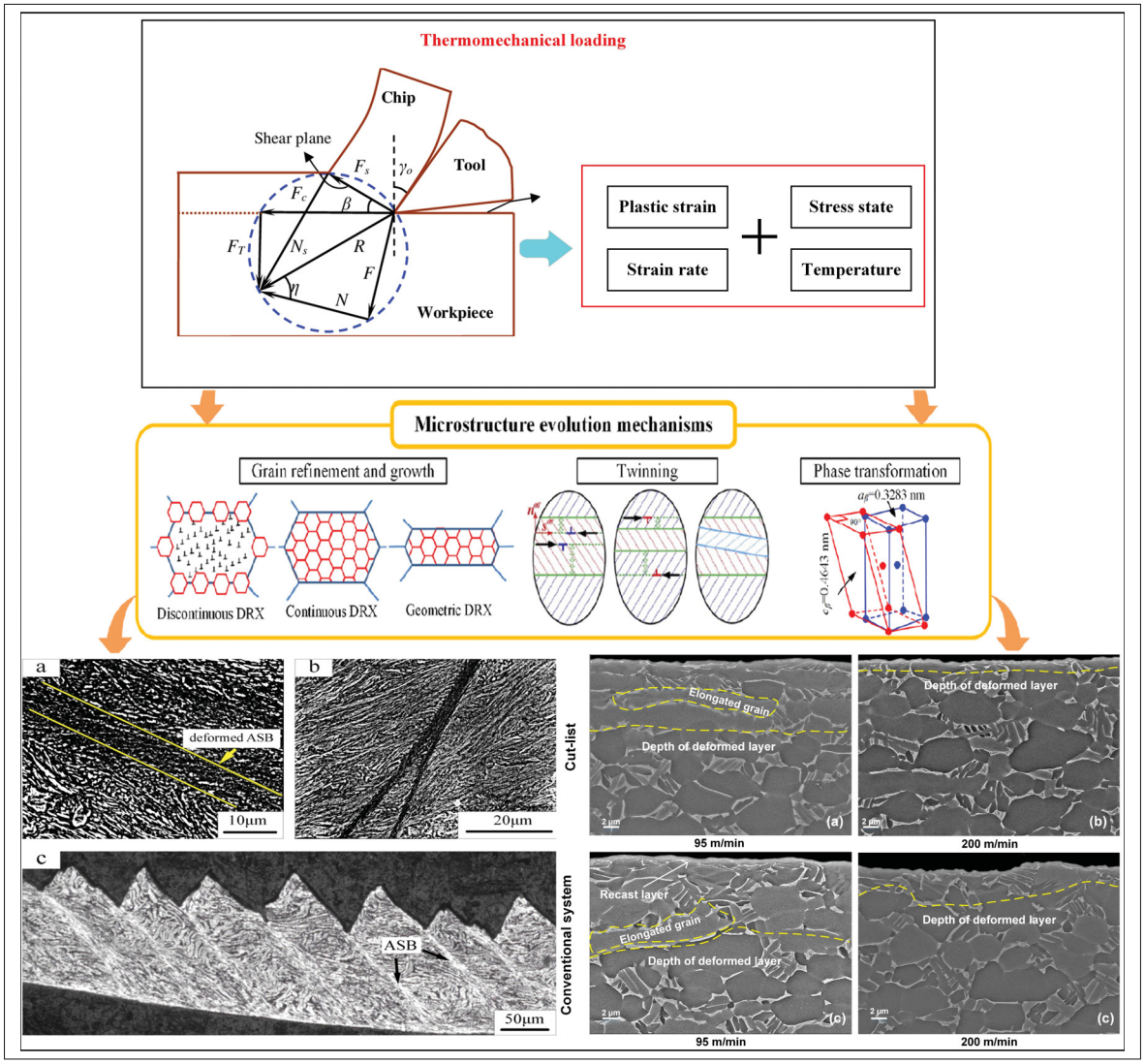

Figure 1.6 Machining induced microstructural changes within the CDZs
Taken from Liu *et al.* (2022a); Wan, Zhu, Liu & Tang (2012)

To represent different levels of material's microstructure and to better understand the machining impact on CDZs, the influence of microstructural evolution needs to be analyzed through a variety of advanced materials characterization techniques, which can provide more reference and feedback for machining information (Guo, Li & Jawahir, 2009). Besides, optimizing the quality

of cutting subsurface and controlling the workpiece's mechanical properties can supply useful insights about machining. The existing literature reports two abnormalities in titanium and its alloy machining. The first anomaly involves the formation of plastic deformation, approximately 11 μm thick when machined using the WC tool. An analogous deviation, measuring a few μm, arose in the dry machining of Ti-6242S alloy, attributed to elevated temperatures and high pressure (Ginting & Nouari, 2009). The second type is a transformed layer (white layer) reported by (Ullah *et al.*, 2021a) located on the uppermost portion of the machined surface, which emerges when tool WC is employed. (Velásquez *et al.*, 2010)) conducted a detailed examination of the cross-section of the machined surface and subsurface formed during the HSM of Ti−6Al−4V alloy at cutting speeds ranging from 20 m/min to 420 m/min. Their study revealed significant plastic deformation in the cutting subsurface, with the severity increasing as the cutting speed rose. However, they did not observe the presence of a transformed layer.

Some researchers have established a connection between worn tools and microstructural alterations. In the early stages of tool wear, no defects were observed by (Che-Haron & Jawaid, 2005); however, substantial plastic and microstructural deformation was reported with increasing tool wear. (Sun & Guo, 2009) conducted preliminary research on titanium by employing milling under a favorable lubrication environment. They discovered that β-Ti close to the cutting surface is responsible for plastic deformation, and its degree reduces as the cutting speed increases. However, they did not notice phase restoration. Apart from titanium, the creation of dark and white layers on the cutting surface is frequently observed while cutting steel. Through TEM bright and dark field analysis, (Zhang, Duan, Wang & Sun, 2018) found that the GS (GS) in both dark and transformed layers formed by hard cutting of steel are nanoscale and anticipated that the appearance of nano-grains in this layer is a result of the coupling effect of phase change and plastic deformation. In contrast, the grain refinement observed in the dark layer results from high-temperature tempering and plastic deformation. By employing the EBSD technique, (Xiong, Hu, Hu & Zeng, 2016) observed a sharp increase in grain boundary density of small angles on the cutting subsurface of Fe-Si-based steel. Taking pure iron as a research

object, (Nagashima, Yoshino & Terano, 2018) obtained dynamically recrystallized grains, which proved that cutting can be used to obtain an ultra-fine grain structure.

It can be seen that there are two problems existing in the subsurface (metamorphic layer), whose microstructure is different from that of the substrate. On the one hand, research conclusions on the evolution mechanism of microstructure in cutting various materials are different. On the other hand, there is no uniform conclusion on the mechanism of evolution of subsurface microstructure in HSM of Ti-6Al-4V, and there is a lack of systematic research results.

1.3.4 Phase transformation analysis in High-speed machining

The highly coupled interactions of mechanical and thermal loads and energy conversion in HSM present a complex nonlinear problem. During HSM, severe shear deformation occurs in the CDZs while a large amount of heat is generated and absorbed quickly, leading to an instantaneous rise in temperature. In this extreme environment, the metallurgical state of the workpiece material undergoes significant changes, including grain distortion, dynamic recovery, dynamic recrystallization, and phase transformation.

Commercial α-β titanium alloys naturally contain 10–20% β-phase at ambient temperature, while the volume fraction of the α-phase decreases from approximately 80% at room temperature to around 20% at 975 °C. The α-β transus temperature typically ranges between 950 °C and 1050 °C, depending on the alloy composition (Zhang, Shivpuri & Srivastava, 2014). Since the α-phase is roughly three times stronger than the β-phase within this temperature range, variations in phase fraction and microstructural characteristics (e.g., GS) significantly influence the flow stress behavior of titanium alloys during machining. The phase transition mechanism is significantly different from conventional heat treatment processes in machining. In the cutting process, phase transformation is primarily influenced by: (1) Mechanical load and SPD, which alter the microstructure through strain-induced transformations. (2) Surface interactions with the surrounding environment may lead to oxidation or other chemical changes. (3) Rapid heating and quenching cause localized microstructural modifications due to extreme thermal gradients.

Currently, the research on phase transformation is mainly through experimental analysis. By employing the XRD technique, (Han, Melkote, Haluska & Watkins, 2008) and (Hosseini, Ryttberg, Kaminski & Klement, 2012) measured residual austenite content in the transformed layer during the machining of AISI 1045 and AISI 52100 steel, respectively, and found that residual austenite content in the heat-induced transformed layer was higher than that of the substrate. However, (Brown *et al.*, 2019) reported no phase transition in the transformed layer during the machining of Ti−6Al−4V. Similarly, (Ullah *et al.*, 2021a) utilized the XRD technique to analyze the phase transformation in milling experiments on Ti−6Al−4V alloy. The authors reported white layer formation on the machined surface but observed no phase transformation.

Taking temperature as a primary indicator, (Kaynak, Taşcıoğlu, Sharif, Suhaimi & Benefan, 2022) predicted the phase transition responses in the machining of Ni-rich NiTiHf memory shape alloy. The authors reported that the transformation temperature increased between 5% and 10% during the machining process. (Kim & Kwon, 2002) experimentally analyzed the phase transformation induced by tool flank wear during AISI 1045, 1070, and 4340 steel turning. The author performed SEM, XRD, and TEM analyses. The results demonstrated that flank wear is diminished as the cementite phase at the newly formed surface dissociates and diffuses into the matrix of the austenitic phase.

1.4 Finite element modeling and process performance predictions

The finite element method (FEM) is one of the most widely used simulation techniques in engineering, particularly in solid mechanics (Liu *et al.*, 2022a). It exists in various forms, each suited to analyzing different aspects of material behavior and response. Many researchers have employed FEM in mechanical manufacturing to gain deeper insights into the cutting process. Commercial FE software, such as LS-DYNA, DEFORM 2D/3D, Abaqus, AdvantEdge, and others, has been extensively utilized for process analysis in industrial and academic. Additionally, FEM serves as an effective tool for real-time analysis of the cutting quality mechanism. However, machining involves a complex thermo-mechanical coupling process characterized by large strains and high strain rates, making the selection of an appropriate constitutive model a challenging task.

The reliability and accuracy of an FE model largely depend on its ability to capture the dynamic mechanical behavior of the workpiece through an appropriate constitutive model (Le *et al.*, 2024). As summarized in Table 1.1, some of the most frequently used constitutive models include

Table 1.1 Material constitutive models for simulation of machining process
Taken from Le *et al.* (2024)

Constitutive Model	Equation	Advantages
Johnson-Cook (J-C)	$\sigma = (A + B\varepsilon^n)\left[1 + C\ln\left(\frac{\dot{\varepsilon}}{\dot{\varepsilon}_0}\right)\right] \times \left[1 - \left(\frac{T - T_{\text{room}}}{T_{\text{melt}} - T_{\text{room}}}\right)^m\right]$	Parameterized; applicable to most materials
Zerilli-Armstrong (Z-A)	$\sigma = C_0 + C_1 \exp(-C_3 T + C_4 \ln\frac{\varepsilon}{\dot{\varepsilon}_0}) + C_5\varepsilon^n$ (for bcc crystal structures) $\sigma = C_0 + C_2\varepsilon^n \exp(-C_3 T + C_4 \ln\frac{\varepsilon}{\dot{\varepsilon}_0})$ (for fcc crystal structures)	Captures coupling of strain, strain rate, temperature, and crystal structure.
Oxley	$\sigma = \sigma_0(T, \dot{\varepsilon})e^{n(T,\dot{\varepsilon})}$	Suitable for low-carbon steel slip line modeling.
Usei-Maekawa-Shirakashi	$\sigma = \sigma_0(T, \dot{\varepsilon})\left(\int_{\text{path}} \frac{K_T}{e^n}\dot{\varepsilon}^m d\varepsilon\right)^n$	Provides accurate predictions of forces and strain rate effects
Power law	$\sigma = \sigma_0\left(\frac{\varepsilon}{\varepsilon_0}\right)^n\left(\frac{\dot{\varepsilon}}{\dot{\varepsilon}_0}\right)^m \times \left(\frac{T}{T_0}\right)^p$	Predicts forces, shear angle, chip thickness

Johnson-Cook (J-C), Zerilli-Armstrong (Z-A), Oxley, Usei-Maekawa-Shirakashi, Power-Law, and the Size Effect (SE) model. Among these, the J-C constitutive model is widely applied due to its versatility. It accounts for strain hardening, strain rate sensitivity, and thermal softening in flow stress calculations. The chip morphology predicted using the J-C model in FE simulations closely matches experimental measurements, validating its effectiveness in material simulation. Comparative analyses of four constitutive models demonstrate that the J-C model accurately predicts shear angles and cutting forces. Furthermore, its reliability in predicting cutting temperature and tool wear has been confirmed by experimental results. As depicted in Fig. 1.7, the J-C model effectively simulates cutting forces, cutting temperature, and chip morphology, making it a robust choice for machining simulations. Similarly, modeling friction behavior at the tool/chip interface is another challenging task during the machining simulation. In the cutting

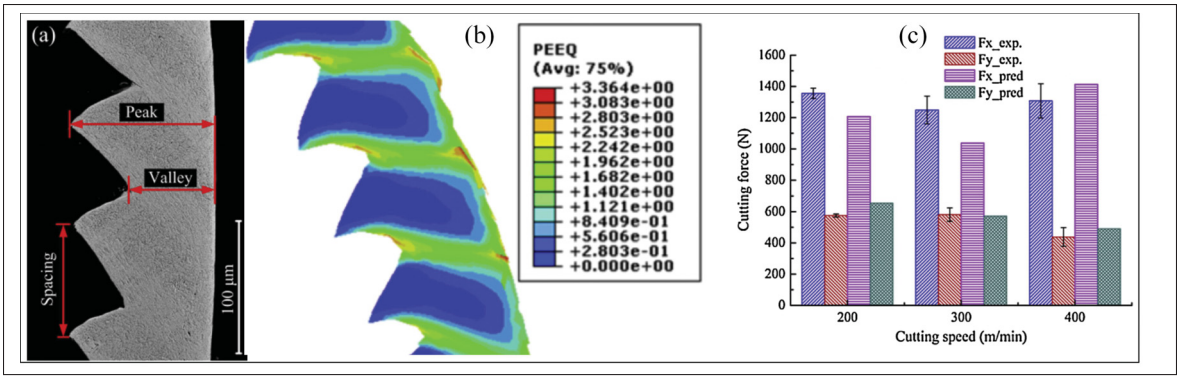

Figure 1.7 Experimental and Simulated chip morphology and cutting force by J-C model
Taken from Li, Zhang, Zhang & Li (2019c)

simulation, the tool rake face, the flowing chip contact surface, and the flank face and machined surface will generate drastic friction, which will cause the abnormal distribution of stress and strain in the tool and workpiece, leading to deformation. A reasonable friction model must be applied to control the workpiece and tool deformation. Some researchers have attempted friction coefficient measurement during machining by employing photo elastic methods, split-tool, and ball-on-disk friction tests using a high-speed tribometer (Jiang, Yan & Rong, 2013; Sartkulvanich, Altan & Göcmen, 2005; Özel, 2006). Due to the difficulty and inaccuracy of experimentally measured friction coefficients, it was often determined by calibrating finite element models based on matching the experimental results with the corresponding simulation results. Some prominent and widely accepted friction models in machining simulations are listed in Table 1.2. The Zorev model is regarded as the most efficient and reliable friction model.

Table 1.2 Friction model for machining simulations
Taken from Sadeghifar, Sedaghati, Jomaa & Songmene (2018)

Model	Formula
Coulomb friction model:	$\tau = \mu\sigma_n$
Constant Coulomb friction coefficient at the entire tool-chip interface shear friction model:	$\tau = m\tau_y$
Constant shear friction coefficient at the entire tool-chip interface Zorev model:	$\tau = \tau_y$ when $\mu\sigma_n \geq \tau_y$, $0 < x \leq I_p$
Constant shear friction coefficient in sticking region and constant Coulomb friction coefficient in sliding region:	$\tau = \mu\sigma_n$ when $\mu\sigma_n < \tau_y$, $I_p < x \leq I_p$

Numerous researchers have undertaken significant numerical investigations on cutting simulations for Ti−6Al−4V alloy to correctly describe serrated chip production. (Shuang, Chen & Ma, 2018) successfully simulated the machining process of Ti−6Al−4V, capturing serrated chip formation at very high cutting speeds. (Wang, Xiao, Astakhov & Liu, 2019) looked at the effect of stress triaxiality in the first deformation zone on serrated chip production and fracture strain distribution. They developed a fracture strain model that incorporated strain rate and stress triaxiality effects, and their finite element (FE) predictions demonstrated that accounting for the stress state significantly enhanced simulation accuracy. (Calamaz, Coupard & Girot, 2008) proposed the TANH material model, which improved predictions of serrated chip and CFs (Fig. 1.8) shape by accounting for strain softening. However, one significant drawback of the TANH model was the assumption of strain relaxation at ambient temperature. Later, (Calamaz, Coupard,

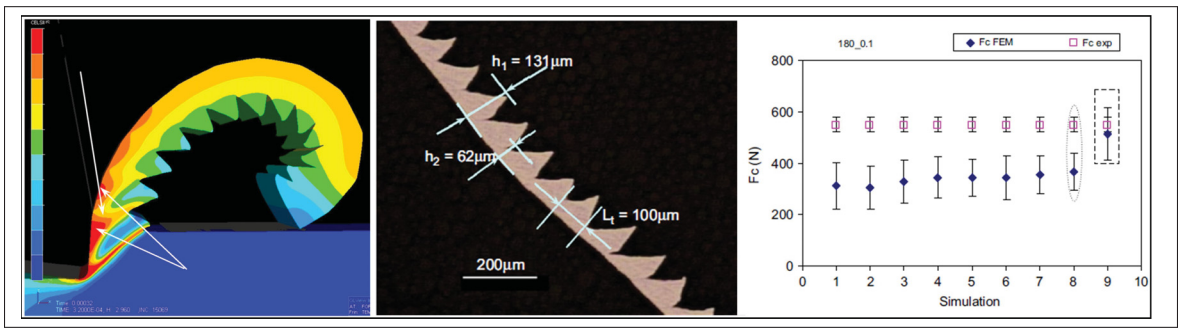

Figure 1.8 Simulated and experimental chip morphology and CFs using TANH model Taken from Calamaz *et al.* (2008)

Nouari & Girot, 2011) incorporated the strain-softening phenomenon into the Johnson-Cook (J-C) model by modifying the plastic strain term to simulate saw-tooth chip formation in the orthogonal machining of Ti−6Al−4V alloy, achieving satisfactory results. Similarly, (Ducobu, Rivière-Lorphèvre & Filippi, 2014) conducted a numerical study employing three different models: Lagrangian with the J-C model, Lagrangian with the TANH model, and ALE with the TANH model to simulate serrated chip formation in orthogonal cutting of Ti−6Al−4V. Their findings demonstrated that the combination of shear band formation and crack propagation plays a crucial role in the development of serrated chips. From the preceding explanation, it is clear that each model has a particular area of applicability and boundary conditions. In addition,

selecting an appropriate constitutive model depends on the research objective. An appropriate constitutive model is required to ensure an accurate depiction of mechanical behavior while retaining high computing efficiency and reflecting the underlying physics of the machining process. The Johnson-Cook (J-C) model is unique among constitutive models because of its simplicity and efficacy in explaining strain, strain-rate, and temperature-dependent behavior, making it ideal for high-strain-rate processes such as high-speed machining (HSM). Unlike more computationally complex models, the J-C model is experimentally calibrated and extensively used. Its capacity to forecast adiabatic shear banding, thermal softening, and strain-hardening effects makes it a viable option for both industrial and research applications, providing an ideal mix of accuracy and computational efficiency.

1.4.1 Finite element modeling for microstructure evolution during HSM

In recent years, research on metal materials with complicated crystal structures has attracted the attention of many scholars because grain refinement achieved by different processes can significantly improve yield strength, ductility, and fracture toughness of machined parts (Junior, Guedes & Balancin, 2012; Amuda & Mridha, 2012). Till now, researchers mainly obtain micron or nanometer-scale GS through plastic deformation processes, such as Equal channel angular processing (ECAP), High-pressure torsion (HPT), and Cold rolling (Ding, Shen & Shin, 2011). Although advanced characterization methods can be used to quantitatively describe the microstructural evolution of CDZs, such as GS. However, preparing a metallographic observation sample requires much time and energy and will destroy the cutting workpiece, wasting material resources. As a result, FE models are getting much attention, as they require minimal experiments for validation. As one of the most important indicators for measuring the evolution of microstructural structure, the GS of the cutting subsurface is closely related to physical quantities during the cutting process, such as temperature field, strain field, strain rate, and other factors. There are currently two main types of microstructural models used to predict the evolution of GS during metal cutting: (1) Kocks-Mecking (KM), which is a physics-based model based on the fundamental principles of mechanics, thermodynamics, and material

science, explicitly describing the physical phenomenon. (2) semi-empirical models based on the Zener-Hollomon (Z-H) equation and Johnson-Mehl-Avrami-based dynamic recrystallization Kolmogorov (JMAK) model rely on empirical data by describing and updating flow stress as a function of strain, strain rate, and thermo-mechanical loads variations without delving into the underlying physical mechanisms. (Keller & Hug, 2017) utilized the Kocks-Mecking model for reproducing size effect, GSs, and thickness of nickel polycrystals. Similarly, (Ding *et al.*, 2011) carried out an FE simulation by integrating a physics-based model for the GS evolution of Al 6061 T6 alloy and OFHC Copper in the cutting process. The results indicated that low strain, high strain rate, and thermal loads result in a coarse and elongated grain structure, and dislocations accumulate more as strain increases, as shown in Fig. 1.9. Subsequently, (Ding

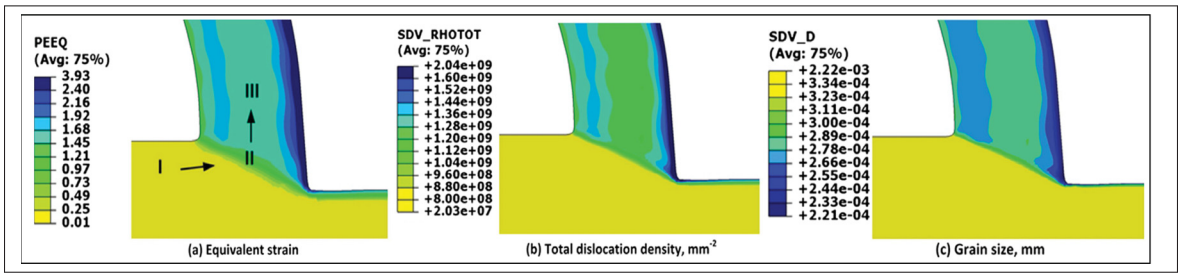

Figure 1.9 Prediction of OFHC DD and GS based on dislocation model
Taken from Ding *et al.* (2011)

& Shin, 2013, 2014) combined the previously developed dislocation density microstructure prediction model with a two-dimensional turning model of pure titanium and a three-dimensional turning simulation model of AISI 52100 steel in AdvantEdge and Abaqus/Explicit simulation software, respectively. Following parameter correction and calibration, the model's ability to predict changes in GS in the CDZs of AISI 52100 steel and pure titanium was demonstrated by comparison with the observed GS. (Liu, Salahshoor, Melkote & Marusich, 2015) developed a DD-based model by considering the dislocation drag effect at a high strain rate. The accuracy of the established model was experimentally verified against various cutting speeds. Although these models can effectively capture certain microstructural features, many physical parameters involved are difficult to identify and can significantly increase computational time, making them less practical for industrial machining applications. Consequently, phenomenological

models remain widely accepted, as they treat microstructural alterations as a homogeneous variable throughout the machining process, providing a more feasible approach for industrial use (Wang et al. 2016, 2022; Xu et al. 2020b). DRX is a key factor in GS evolution during metal cutting. As explained by (Fanfoni & Tomellini, 1998), two primary types of dynamic recrystallization (DRX) govern metal deformation: discontinuous dynamic recrystallization (dDRX) and continuous dynamic recrystallization (cDRX). As demonstrated in Fig. 1.10, JMAK and Z-H equation-based models are commonly used with phenomenological laws to model DRX-induced microstructure development. Both models require critical strain to be reached or surpassed. In terms of predicting GSs induced by DRX (Arısoy & Özel, 2015; Özel & Arisoy,

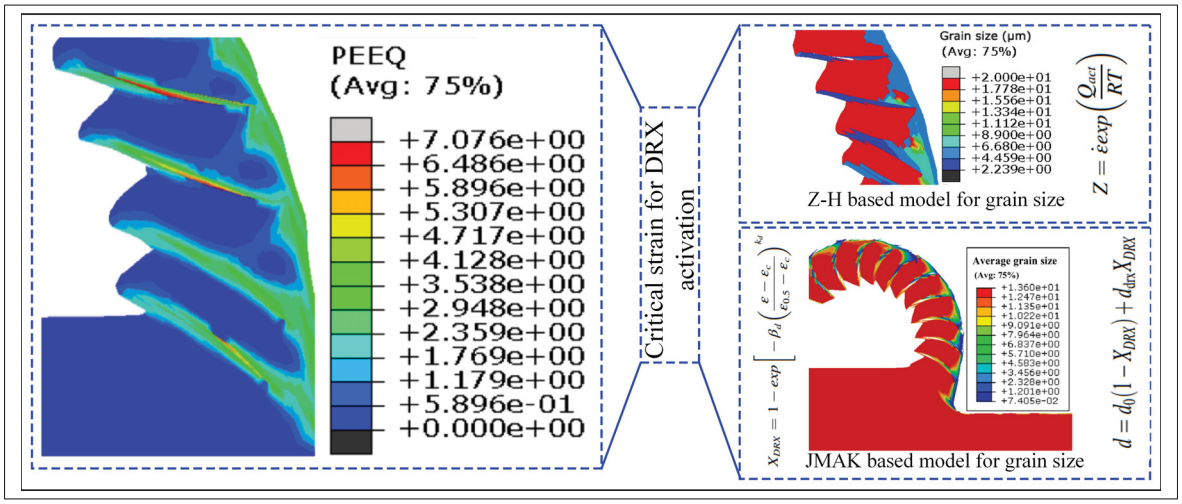

Figure 1.10 Grain size prediction in machining with JMAK and ZH models
Taken from Shu, Ren, Zhou & Wang (2024); Wang, Liu, Wang, Song & Wan (2016b)

2014), successively applied the JMAK model to simulate and predict cutting subsurface GS of Inconel 100 and Ti−6Al−4V, and the DRX kinetics and GS were predicated. (Mondelin, Valiorgue, Rech, Coret & Feulvarch, 2013) first, initial conditions for DRX of 15-5PH martensitic steel through dynamic comprewere were determined. Further evolution behavior of grain was described by JMAK dynamic model, and then combined with SEM and EBSD analysis results, DRX behavior that occurred in cutting subsurface was proved. Besides the JMAK model, the Zenner-Holloman (Z-H) equation, also based on DRX and critical strain, was successfully implemented for microstructural forecast, as it is relatively simple, with fewer parameters to be

determined, better universality, and a more comprehensive range of materials. By employing the Z-H model, (Rotella & Umbrello, 2014) predict the GS and microhardness of Ti−6Al−4V alloy under dry and cryocold cutting conditions. The experimental results also confirmed the applicability of the model. By keeping the feed rate constant and increasing the cutting speed, their finding indicates that GS decreased under both conditions with increased cutting speed (Fig. 1.11). Besides, Jafarian, Umbrello & Jabbaripour (2016) applied the microscopic model based on the Z-H empirical equation for the simulation prediction of cutting subsurface GS of nickel-based alloy Inconel and verified the model through cutting experiments. Similarly, (Wang *et al.*, 2016b) combined the Z-H equation with the Hall-Petch equation to determine the GS and microhardness of the CDZs in the machining of Ti−6Al−4V alloy. Analyzing the existing

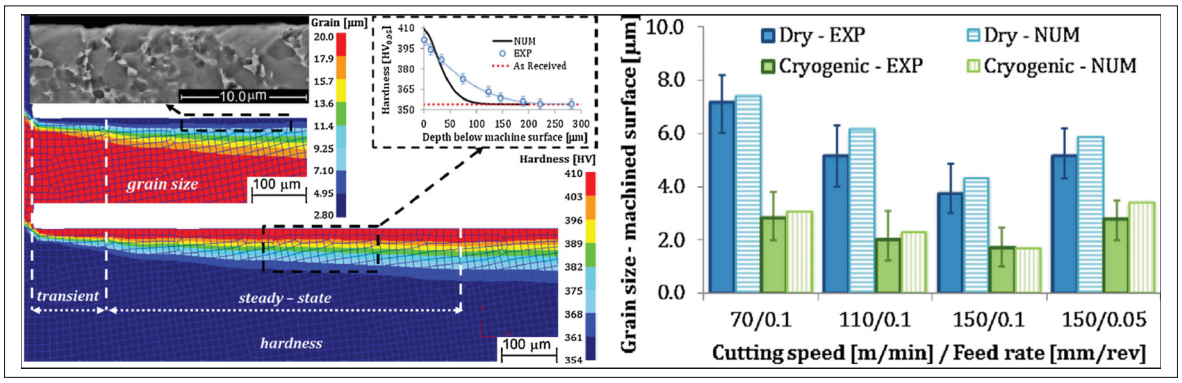

Figure 1.11 Prediction of GS and hardness of Ti−6Al−4V cutting by the empirical model Taken from Rotella & Umbrello (2014)

research, it is not difficult to see that the microstructure prediction model used to predict the GS evolution generally reflects the mathematical relationship between the physical variables of the cutting process and GS, and is calibrated or corrected. The model shows good adaptability and high prediction accuracy, and it can be used to describe the evolution behavior of microstructure during metal cutting. However, among the above-mentioned microstructure prediction models, the JMAK and the physics-based models are more complex, require many parameters to be determined, and are more difficult to obtain. In comparison, the model based on the Z-H equation is relatively simple, has fewer parameters to be determined, is more versatile, and has a relatively wider range of materials.

1.4.2 Finite element simulations on phase transformation during the machining process

High temperatures, rapid heating, and subsequent cooling are inherent to machining processes, often triggering phase transformations within the material. The specific phases involved depend on the material's crystal structure and thermal properties. For Ti-6Al-4V, the typical sequence of phase transformations during heating and cooling involves transitions from the dual-phase structure (α + β) to a fully β-phase, followed by melting, and then the reverse sequence upon cooling potentially leading to the formation of either an (α + β) structure or α' martensite (Liu & Shin, 2019). The formation of α' martensite, however, is not guaranteed and requires a precise thermal pathway. It generally occurs when the material cools rapidly from temperatures above the β-phase region to below the martensite start temperature (T_{Ms}). Besides, the cooling rate also play a crucial role in determining the extent of martensitic transformation (Fig. 1.12). Experimental studies have indicated that a cooling rate higher than 410° C/s is required to achieve a complete transformation to α' martensite. When the cooling rate falls between 410° C/s and 20° C/s, only a partial formation of the α'-phase is expected. If the cooling rate is below 20° C/s, martensitic transformation does not occur (Ahmed & Rack, 1998). Due to the extreme thermal gradients and rapid time scales involved in machining, directly

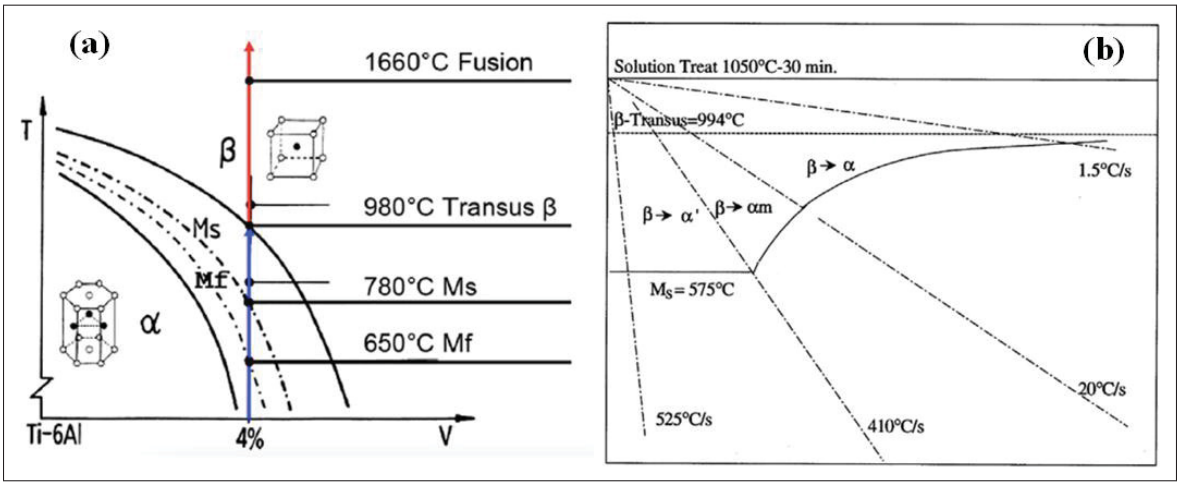

Figure 1.12 Phase diagram as function of heating and cooling rates for Ti-6Al-4V
Taken from Liu & Shin (2019)

measuring phase transformations in real-time is highly challenging. As a result, researchers have turned to finite element (FE) simulations and phase transformation prediction models to estimate and analyze the complex phase changes induced by cutting processes. During the orthogonal machining of hardened AISI 52100 steel, (Ramesh & Melkote, 2008) developed an FE model to simulate white layer formation (Fig. 1.13) under thermally dominant cutting conditions promoting martensitic phase transformations. Their model incorporated two critical criteria: (1) the temperature of material points must surpass the Austenite transition temperature, marking them as, and (2) these transformed points must subsequently cool below the martensite transition temperature to complete the phase transformation. This model has since been applied in various machining simulations, demonstrating strong predictive capability for estimating the depths of white and dark layers on machined surfaces (Mahnken, Wolff & Cheng, 2013; Pan, Liang, Garmestani & Shih, 2016). To explore the mechanism of phase transition in

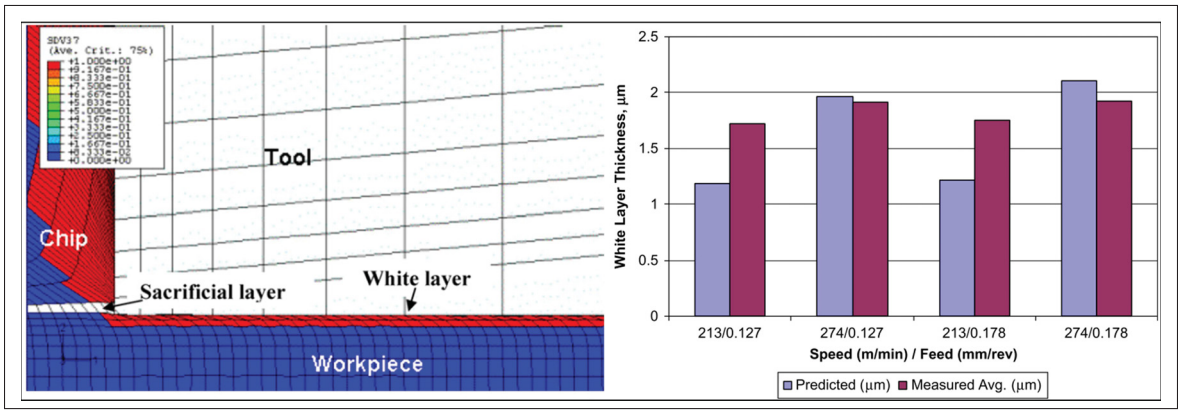

Figure 1.13 White layer thickness prediction in orthogonal cutting of hardened steel
Taken from Ramesh & Melkote (2008)

orthogonal cutting of AISI 1045 Steel, (Ding & Shin, 2012) established a theoretical model of cutting phase transition with the help of Abaqus/Explicit simulation software and realized the prediction of ferrite-pearlite transformation and austenite under high-temperature conditions, respectively. Through the analysis of simulation results (Fig. 1.14(a)), it can be seen that the phase transition occurs at the tool-chip contact area. (Duan, Kong, Hao & Zhou, 2013) modified the theoretical austenite phase transition temperature equation considering alloy composition and stress-strain effect, and then predicted austenite phase transition temperature by extracting

the strain energy and stress output values by FE simulation and comparing the results with finite element temperature field, and developed a model of white layer prediction with critical temperature as an evaluation index. (Kaynak, Manchiraju & Jawahir, 2015) set a visual theoretical model for the transformation of austenite into martensite during the cutting process of NiTi alloy, wrote a user subroutine in FORTRAN language, and embedded it into cutting simulation software 2D-DEFORM (Fig. 1.14(b)) and pointed out that Vc is inversely proportional to the amount of martensite generated. (Schulze *et al.*, 2015) divided existing cutting phase transition prediction models into three types, namely, the time-phase transition temperature model, stress-strain induced phase transition model, and temperature-stress-strain coupling effect phase transition model, and verified the effectiveness of three-phase transition prediction models by comparing FE simulation values and experimental results. Recently, (Zhang *et al.*, 2014) developed an

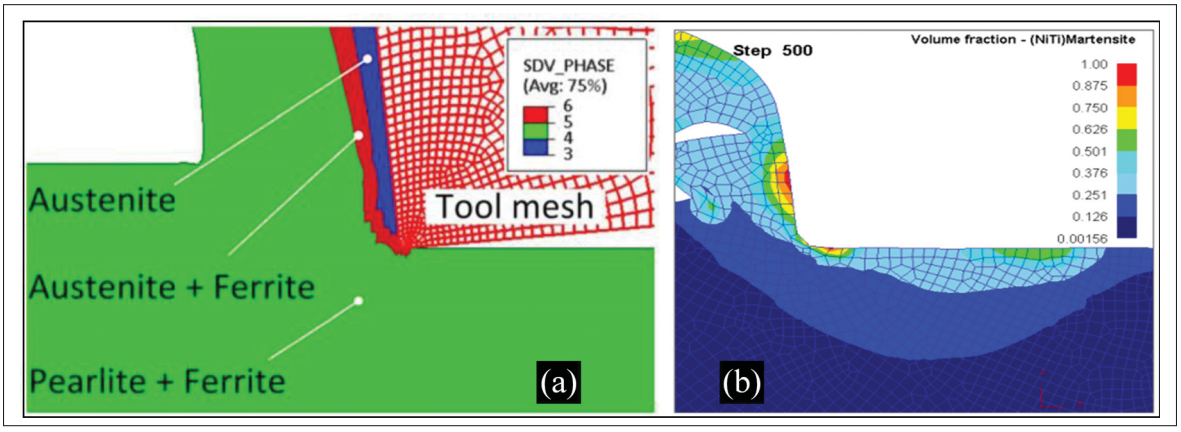

Figure 1.14 Phase transition during machining; (a) AISI 1045 Steel, and (b) NiTi alloy Taken from Ding & Shin (2012); Kaynak *et al.* (2015)

SCM-based FE model to predict the phase transition during the machining of Ti−6Al−4V alloy. In their investigation, the cutting temperature was set as a deciding factor to roughly estimate the β-phase volume fraction. By simulating cutting temperature field distribution, they explored phase transition behavior occurring in the shear zone of titanium alloy sawtooth chips (Fig. 1.15). From the literature, it is clear that the phase transition prediction mainly focuses on non-conventional processes and is limited to experimental methods. The existing phase transformation models are insufficient to fully capture the complex phase evolution

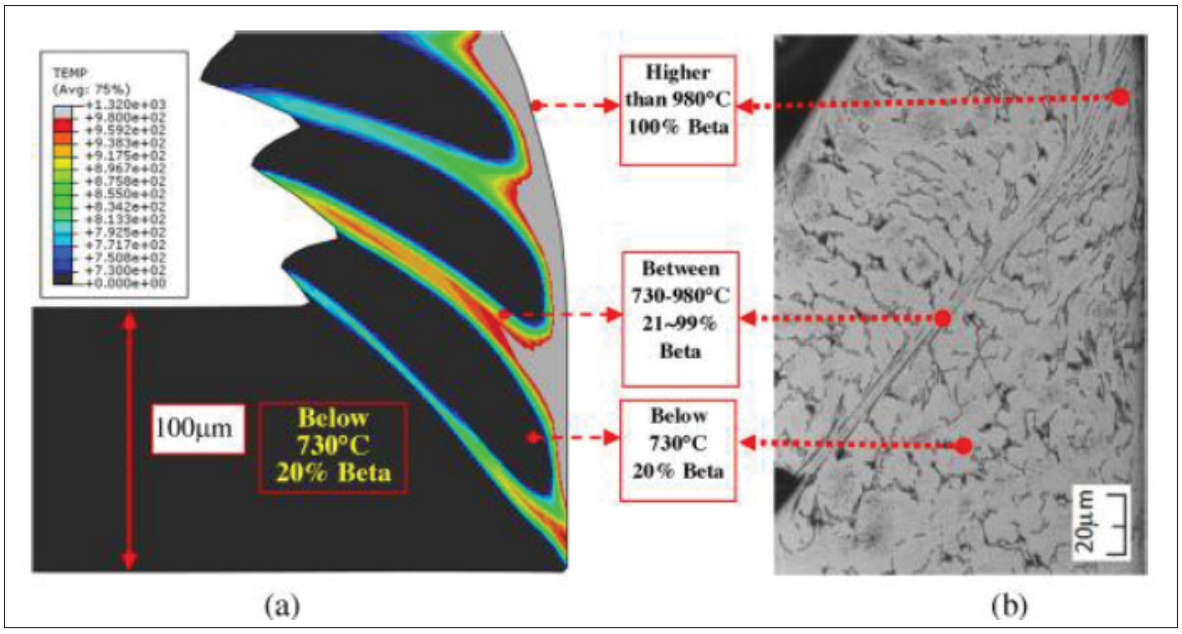

Figure 1.15 Phase transformation prediction in Ti−6Al−4V based on thermal loading
Taken from Zhang *et al.* (2014)

behavior during titanium cutting. Moreover, it remains unclear which specific phase contributes most effectively to the service performance of the machined surface. Therefore, the phase transformation during metal cutting can be improved only when factors such as large strain and high edge strain rate, etc., are taken into account during the adaptability of the phase change model, and shortcomings of the phase change model based on a single physical factor can be overcome.

1.5 Mechanical properties evolution of the cutting subsurface

The evolution of mechanical properties of the cutting subsurface is a direct consequence of the intense thermo-mechanical loads experienced during machining. The SPD occurring in the cutting deformation zone, combined with extreme friction at the tool-workpiece and tool-chip interfaces, generates a substantial rise in cutting temperature. This interplay of high strain, strain rate, and thermal effects induces significant alterations in the subsurface microstructure. As is well known, the mechanical properties of materials at the macroscopic scale are strongly

influenced by their microstructural characteristics, including GS, DD, and phase composition. Key mechanical properties such as hardness, yield strength, tensile strength, and fracture toughness evolve in response to these microstructural changes. Specifically, machining-induced residual stress and hardness variations play a crucial role in determining the mechanical performance of the finished component. Hence, the following section provides a brief literature review on the RS and hardness of the cutting surface and subsurface.

1.5.1 Machining-induced residual stress prediction in the machined parts

The prediction of residual stress in machined parts is essential for ensuring their long-term service performance and structural integrity. RS arising from the complex thermo-mechanical interactions during machining can significantly influence key material properties such as corrosion resistance, fatigue life, and deformation behavior. Depending on their nature and distribution, RS can either enhance or degrade the functional performance of machined components. In general, compressive RS has been found to enhance the service life of the product (Ullah, Zhang & Waqar, 2022). In contrast, tensile RS can be detrimental, as they promote stress corrosion cracking and reduce fatigue resistance, potentially leading to premature failure (Yang, Liu, Ren & Zhuang, 2016). Additionally, RS distribution also affects the dimensional stability of machined parts, potentially causing undesirable distortions that compromise precision and assembly tolerances. The primary methods for the prediction of RS can be categorized into three approaches: (1) experimental methods, (2) analytical methods, and (3) numerical methods (Zhou, 2024). Regarding experimental method, one of the founding works in assessing the RS due to machining was undertaken by (Henriksen, 1951), who investigated the effect of thermo-mechanical loads on RS during orthogonal cutting of low-carbon steel. Later, (Zlatin & Field, 1973) explored the influence of milling conditions on RS, reporting that gentle milling tends to induce compressive RS, whereas abusive milling leads to tensile stresses in the machined surface layer. The impact of cutting speed on RS distribution was further demonstrated by (Narutaki, Murakoshi, Motonishi & Takeyama, 1983) during dry and wet machining of Ti−6Al−4V alloy. Their findings indicated that compressive RS increased with cutting speed and were higher in

dry machining than in wet conditions. Similarly, as depicted in Fig. 1.16 (Sun & Guo, 2009) reported that the magnitude of compressive residual in the feed direction increases with cutting speed and decreases with feed rates. Their finding also unveal that the compressive RS in feed direction was approximately 30% greater than in the cutting direction during the end milling of Ti−6Al−4V alloy. Beyond machining parameters, the effect of tool wear on RS profiles during

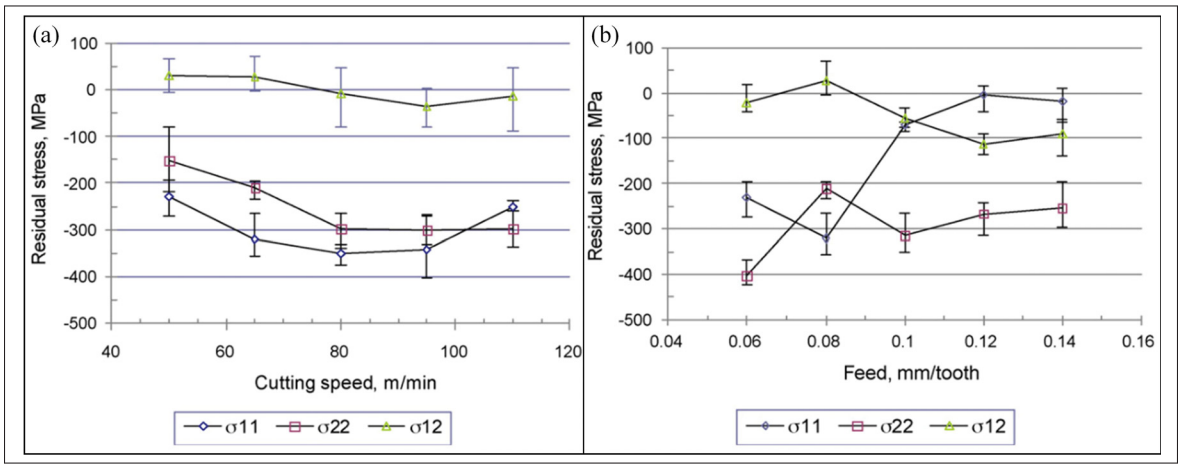

Figure 1.16 Effect of cutting speed and feed rate on RS
Taken from Sun & Guo (2009)

turning and hard milling has been well-documented (Le *et al.*, 2024). Moreover, cutting-edge radius has been identified as having a fivefold greater impact on RS compared to other process parameters. In addition to experimental studies, some researchers have developed analytical models to predict RS in machining. However, these models often rely on excessive assumptions and simplified interpretations of cutting processes, limiting their accuracy and reliability. As a result, there is a growing interest in developing high-fidelity simulation models to enhance the accuracy of RS predictions in machining. Numerous FE models have been extensively developed to predict RS when cutting hard-to-machine materials. By incorporating accurate mechanical behavior and tool and workpiece geometries, these simulations offer valuable insights into the mechanisms driving RS formation. Since the early 2000s, considerable efforts have been undertaken to advance FE techniques for estimating RS during the manufacturing process (Waqar, Guo & Sun, 2022; Wang, Liu, Guo, Zhao & Liu, 2017a). For instance, (Chen, El-Wardany & Harris, 2004) developed a 2D FE model to study the impact of tool wear on RS

distribution during the orthogonal cutting of Ti−6Al−4V alloy. (Wyen, Jaeger & Wegener, 2013) explored the role of cutting-edge radius, noting that it significantly affected compressive RS in up milling (Fig. 1.17(a)) compared to down milling (Fig. 1.17(b)) of Ti−6Al−4V (Fig. 1.17). In another study, (Rao, Dandekar & Shin, 2011) analyzed the face milling of Ti−6Al−4V and observed that increasing flank wear decreased maximum RS across various cutting conditions. Acknowledging that these studies collectively offer crucial insights into predicting RS within

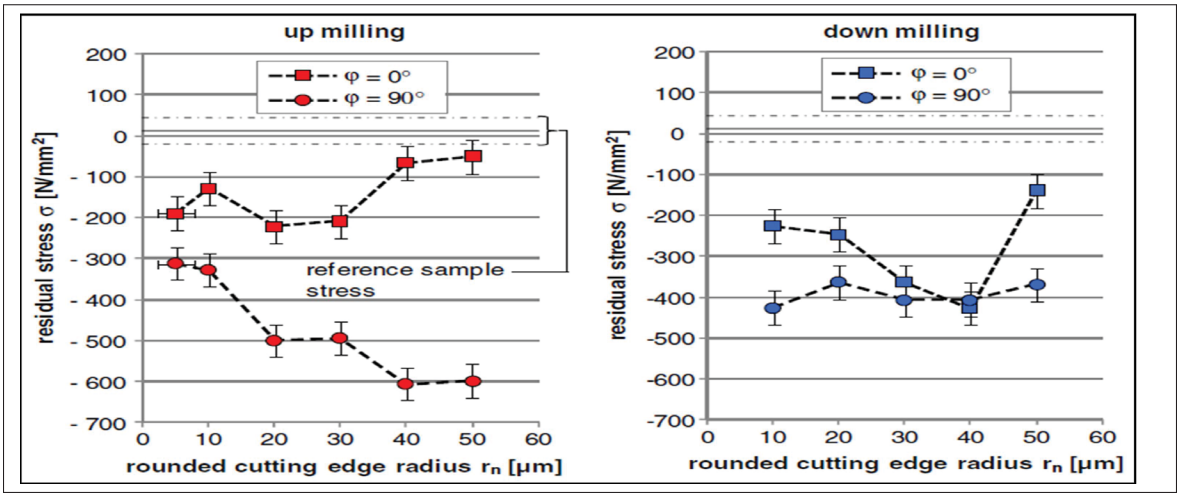

Figure 1.17 RS prediction in the cutting surface of Ti−6Al−4V alloy using various cutting edges
Taken from Wyen *et al.* (2013)

machining processes. However, there has been relatively less emphasis on considering the influence of tool wear on RS allocation. It's worth highlighting that during milling operations, the abrupt transition to a thermo-mechanical load significantly influences both SPD and the feasibility of compressive and tensile stresses. Additionally, the oversight effect of serrated chip flow initiation, which is intricately linked to RS distribution in machined components, should not go unnoticed.

1.5.2 Hardness prediction within the cutting surface layer

Besides RS prediction, the hardness of the cutting surface layer is another critical parameter to monitor due to its tight connection with metallurgical alterations. Hardness changes arise

due to strain hardening and heat impacts at the surface and subsurface levels. The intense plastic deformation at the cutting zone causes work hardening, increases DD, and refines the microstructure, especially in ductile metals. However, high heat input can cause thermal softening, which reduces hardness in certain areas. The hardened layer's depth is determined by machining factors such as cutting speed, depth of cut, tool material, and the workpiece's metallurgical alterations. In rare circumstances, phase transitions can occur, further impacting microhardness progression. Generally, two types of hardness are frequently utilized for the machined components: Rockwell hardness (HRC) and Vickers hardness (HV). HRC is suggested for some typical concerns of metallurgical substances, including microstructure constituents and phase fractions, while HV is more focused on special physical issues, especially in terms of DD and GS (Liu *et al.*, 2022a). Initially, (Umbrello, Rizzuti, Outeiro, Shivpuri & M'Saoubi, 2008) developed a model that defined HRC as a function of the initial hardness and transient temperature during machining. However, this model had a limitation as it did not differentiate between tempering and quenching, two key metallurgical processes that influence hardness variations. To address this weakness, (Umbrello & Filice, 2009) refined the model by incorporating the hardness fluctuations associated with forming white and dark layers on the machined surface. These layers arise due to extreme thermal and mechanical loads during machining. The developed model well predicted the hardness of the cutting surface layer (Fig. 1.18). Similarly, several researchers adopted HV hardness to predict the hardness of the cutting surface layer, as it is relevant to microstructure features at the microscale. The hardness of cutting surface was reported to be greater than the substrate material (Wang & Liu, 2018; Arisoy & Özel, 2015; Moussaoui, Mousseigne, Senatore, Chieragatti & Monies, 2013). It is also claimed that lower hardness is not due to thermal softening but due to the edge consequence in the measurement procedure.

1.6 Metallic particle emission during the machining process

Particle emissions during the mechanical machining process have become a growing concern due to their detrimental effects on the environment, operator health, machined components, and overall energy consumption. The generation of fine particulate matter, particularly from

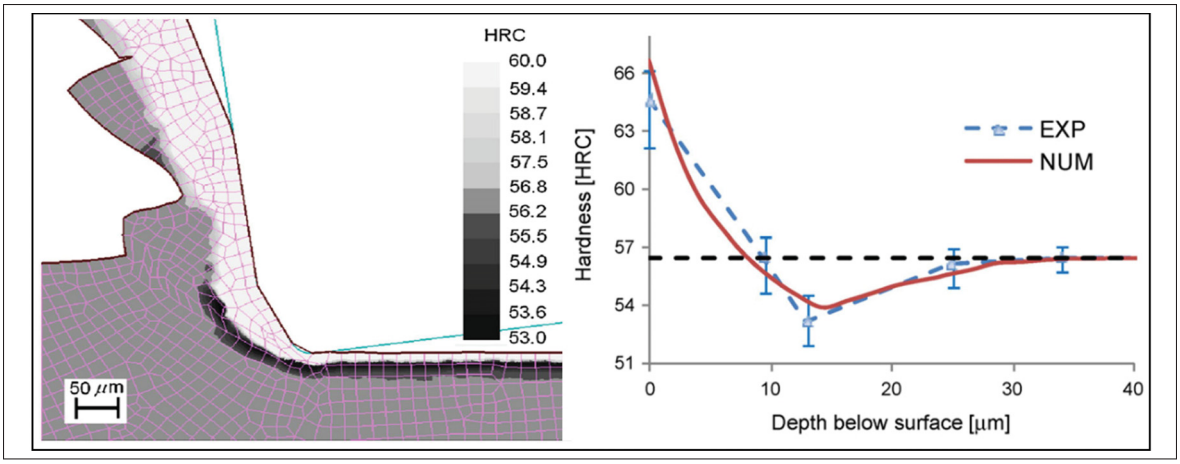

Figure 1.18 Simulated and experimental validation of cutting surface layer hardness
Taken from Umbrello & Filice (2009)

HSM, poses serious environmental hazards, contributing to air pollution and contamination of surrounding ecosystems. Additionally, prolonged exposure to airborne particles can adversely affect machine operators, including respiratory disorders, skin irritation, and even long-term conditions such as pneumoconiosis. From a manufacturing perspective, these emissions can compromise the integrity of machined parts by leading to surface contamination, reduced dimensional accuracy, and accelerated TW. Furthermore, the excessive energy consumption associated with the machining process, particularly those involving high MMR and inefficient chip evacuation, exacerbates the overall carbon footprint of manufacturing industries. Fig. 1.19 illustrates the representation of particles of varying sizes in the human respiratory system. It has been proved that breathable particles with a diameter of $leq10$ μm can harm human health more than particles exceeding 10 μm (Massin *et al.*, 1996). Particles with smaller diameters can penetrate and linger in deeper regions of the respiratory system, causing more adverse health effects. Similarly, the particles with diameters exceeding 10 μm can be prevented from entering beyond the nasal cavity. However, particles with a diameter of $\leq$ 10 μm can easily penetrate the respirational structure. Evaluated particles in this size range can potentially cause long-term harm to the health of operators (Ma, Aviv, Guo & Braham, 2021). Another widely recognized classification method for particle emissions has been recommended by the American Conference of Governmental Industrial Hygienists (ACGIH) and the International

Organization for Standardization (ISO). This classification system, adopted by most professional organizations, is primarily used for assessing particulate matter's impact on specific respiratory system regions. According to this method, particles inhaled through the nose or mouth are categorized as inhalable particulates. Those that pass through the throat and reach deeper into the respiratory tract are called thoracic particulates. Further, the finest particles that penetrate the alveolar region, where gas exchange occurs, are classified as respirable particulates. During dry and wet machining, a significant proportion of emitted dust and oil mist particles fall within the respirable particulate category. In HSDM operations, particles ranging in diameter from 1 to 4 μm are particularly hazardous, as they can quickly enter the bronchi of the operator and accumulate in the lungs, leading to potential respiratory health risks.

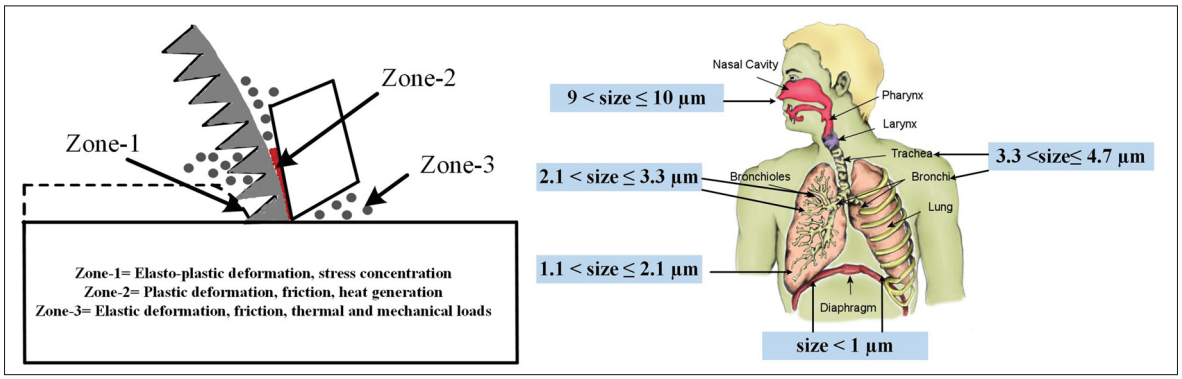

Figure 1.19 Particle emission during metal cutting and its impact on humans' health

1.6.1 Main Influencing Factors and their correlation with particle emissions

Numerous studies have investigated the factors influencing particle emissions in various machining environments, highlighting the critical role of cutting parameters, cooling conditions, workpiece material, and cutting tool characteristics. Cutting parameters and tool coatings significantly affect the generation of particulate matter, with higher speeds and aggressive cutting conditions typically leading to increased particle emissions. In the early 2000s, (Arumugam, Malshe, Batzer & Bhat, 2003) conducted cutting experiments on aluminum-silicon alloy in a dry environment and found that the combination of low cutting speed, high feed rate, and depth of

cut tends to produce more particle emission. Similarly, (Djebara, Songmene & Bahloul, 2013) also proved that cutting speed is the most influential factor affecting the ultrafine particle during dry machining of 2024-T351, 6061-T6, and 7075-T6 aluminum alloys. In addition, studies have reported that dust generation is particularly significant during dry drilling of Al-Si-Mg alloys at moderate cutting speeds, compared to both lower and higher speed ranges. This phenomenon is attributed to the complex interactions between material properties, cutting forces, and heat generation, which influence chip fragmentation and particle dispersion. Beyond machining parameters, cooling and lubrication strategies play a crucial role in mitigating particle emissions. (Sujova, 2012) highlighted that the health risks associated with oil mist particles in wet machining processes largely depend on the cooling medium's toxicity. Unlike traditional cutting fluids, cooling methods such as liquid nitrogen and dry ice/CO_2 cryogenic cooling generate N_2 and CO_2, which are not harmful to operators and do not contribute to long-term respiratory issues.

Furthermore, several analytical models have been developed to better understand and quantify particle emissions under various machining conditions. These models help predict emission levels based on key parameters such as cutting speed, lubrication type, and material properties, enabling manufacturers to optimize machining strategies for improved workplace safety and environmental sustainability. An analytical model based on Needelman-Lemond's for particle emission was proposed by (Khettabi *et al.*, 2010b), which considered tool-chip friction and the material's plastic deformation. The same author examined the impact of simulated aging on processing parameters employing an advanced threshold (dust generation) and reported that particle emissions were reduced by about 30% under the same cutting conditions. Recently, (Mohamed-Amine, Mohamed, Abdelhakim & Victor, 2021) experimentally and analytically investigated the tool/workpiece interfaces and demonstrated their impacts on dust emission. They employed response surface methodology to inspect the impact of various process parameters and the interaction between each process parameter.

1.6.2 Controlling particle emission and dispersion during machining

In terms of controlling/decreasing particle emissions in metal machining, various approaches have been implemented by different researchers. These methods include but are not limited to optimizing cutting parameters, selecting appropriate cooling conditions, improving the ductile qualities of workpiece materials, and selecting proper cutting tools (Arumugam *et al.*, 2003; Khettabi, Songmene & Masounave, 2007). On the one hand, optimizing cutting parameters can effectively reduce particle generation during machining. On the other hand, it has been recommended that for brittle materials, lower cutting speeds are preferable to reduce particle emissions, whereas, for ductile materials, higher cutting speeds result in lower emissions than low and moderate cutting speeds (Zhao *et al.*, 2023). Besides, improving workpiece materials' ductility can also help reduce particle emissions. By employing the 8520 DustTrak Aerosol Monitor, (Balout, Songmene & Masounave, 2007) examined the impact of pre-heating and pre-cooling procedures on the toughness of 70-30 brass, wrought 6061, and foundry A356 aluminum alloys during drilling. Their findings indicated that pre-cooling can modify chip formation, resulting in lower mechanical load and a considerable reduction in fine particle emissions by at least 70%, depending on the material and cutting circumstances. In contrast, pre-heating enhanced chip ductility, which resulted in more significant particle emissions. The proper selection of cutting tool shapes can significantly minimize particle production during machining. Cutting tools with a higher rake angle can be used to reduce tool-chip contact duration, thus lowering particle emissions (Shnfir, Kouam & Songmene, 2020). Additionally, tools with negative rake angles can improve particle emission control throughout the cutting process.

It is evident from the above literature that earlier research has explored various materials; however, titanium and its alloys have been largely overlooked. The formation of chips and the release of particles from titanium alloys differ significantly from other materials. Additionally, existing studies on dust generation have primarily focused on turning and grinding processes, often employing lubrication. However, the role of dry milling in promoting environmentally sustainable manufacturing remains underexplored. It is also critical to recognize that during

milling operations, the abrupt transition to complex thermo-mechanical loads significantly affects surface plastic deformation, burr formation, and the development of other surface defects. Moreover, the influence of serrated chip flow initiation, which is closely associated with potential degradation of surface integrity and directly linked to particle emissions, has often been overlooked. Hence, it becomes essential to systematically investigate these aspects, with particular attention given to correlating particle emissions, chip formation, and machined surface integrity.

1.7 Summary

This chapter provides a brief overview of the research background and significance of this study. It discusses the machinability of Ti-6Al-4V and the microstructural evolution (including GS and phase transformation) during HSM. Additionally, an introduction to machining simulations and the mechanical properties of the cutting surface was presented. The study highlights the critical role of material properties, cutting parameters, and tool characteristics in determining both the quality of the machined surface and the environmental impact associated with particle emissions during machining operations.

The main issues identified in the current research are as follows:

While several researchers have made notable advancements in developing FE models to predict chip morphology and thermo-mechanical loads, most of these models are based on turning processes. The complexities associated with milling, such as tool geometry, cutting kinematics, and the variation in the undeformed chip layer, present significant challenges for model development. Therefore, there is a need for a comprehensive, realistic, and computationally efficient FE model for milling that accurately replicates actual milling processes and addresses specific research objectives.

Moreover, while existing studies on surface integrity have predominantly focused on cutting process optimization and experimental regression analysis, there is a clear need for a more integrated computational modeling approach. This approach should predict both the material

microstructure and the mechanical attributes of the cutting surface. The role of phase transformation during machining is critical in determining flow stress behavior, machined surface hardness, and chip formation. A deeper understanding of phase transformation mechanisms will be essential for improving surface quality control during machining operations.

Additionally, the emission of fine particles during high-speed dry milling of Ti-6Al-4V, especially in the absence of lubricants, requires further investigation. Existing research has largely overlooked particle formation in titanium alloys, and more attention is needed on particle generation during milling, rather than turning or grinding. This will help in developing more sustainable and safer machining processes.

CHAPTER 2

RESEARCH METHODOLOGY

2.1 Introduction

This chapter describes the research methods adopted in this work, focusing on the HSM of Ti-6Al-4V. It provides an overview of the experimental and computational approaches used to investigate the effects of HSM on surface integrity, including microstructure evolution, mechanical properties evaluation, and particle emissions. The methods and materials employed for machining tests, surface characterization, and finite element modeling are briefly introduced. While detailed descriptions of specific methodologies are presented in Chapters 3, 4, 5, and 6, this chapter serves as a foundation by summarizing the overall research methodologies.

2.2 Experimental work

Several variables influence the machining process, directly affecting its efficiency and outcomes. Therefore, exploring ways to control these parameters to enhance productivity and cost-effectiveness is essential. Since the surface integrity of machined components is influenced by

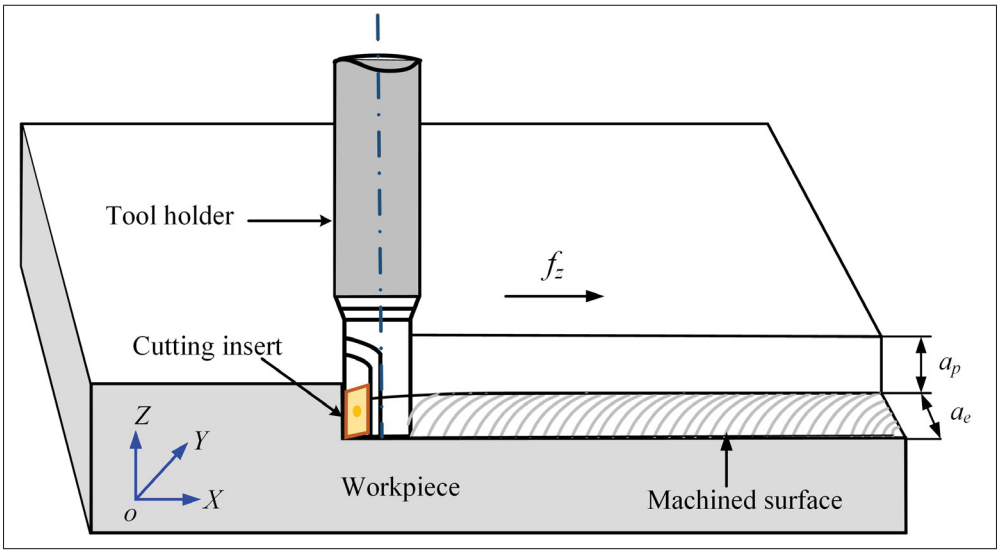

Figure 2.1 Schematic diagram of high-speed milling process

multiple input parameters, such as cutting speed (Vc), feed per tooth (fz), radial depth of cut (ae), and axial depth of cut (ap), as defined in Fig. 2.1. Considering the increasing demand for industrially manufactured components and the unique characteristics of HSM for Ti-6Al-4V alloy, the machining parameters were set within the following ranges: cutting speed (150–550 m/min), feed rate (0.10–0.30 mm/tooth), axial depth of cut (1.0–1.8 mm), and radial depth of cut (1.0–2.2 mm).

2.2.1 Experimental design

To gain deeper insights into the impact of varying cutting conditions on the machinability of Ti-6Al-4V, a single-factor experimental design was employed, allowing for the assessment of each parameter's individual effect. The details of the experimental design are provided in Table 2.1. As demonstrated in Fig. 2.2, the milling experiments were conducted on a 3-axis vertical CNC machining center (Huron K2X10), having a maximum spindle speed of 28,000 rev/min under dry cutting conditions. All sets of experiments were operated in dry conditions, and no coolants were used.

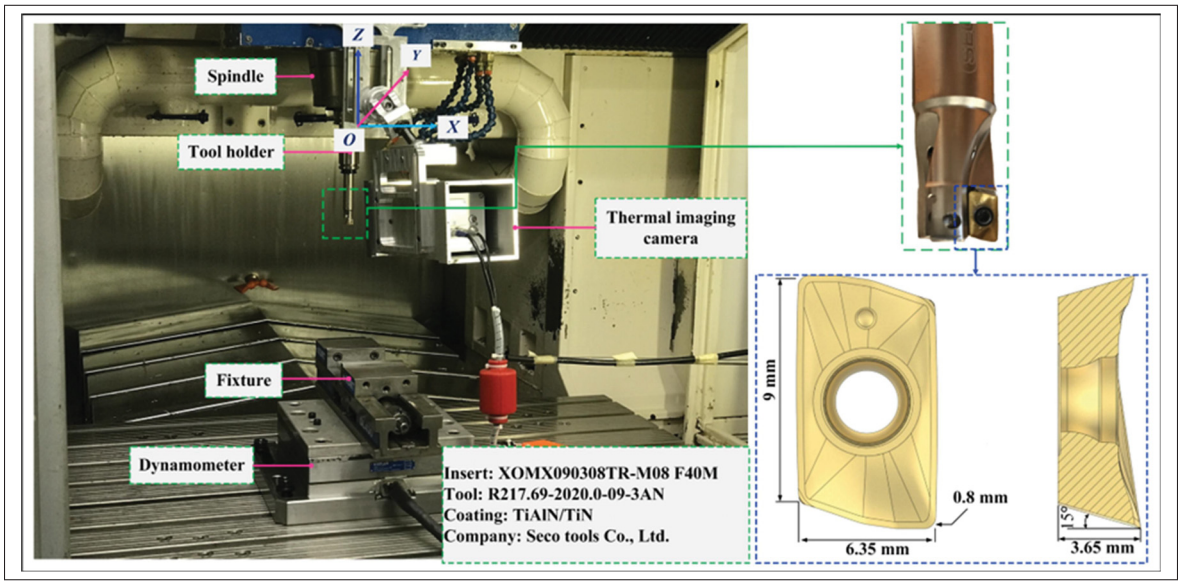

Figure 2.2 High-speed milling experimental setup

Table 2.1 Cutting Conditions for Milling Process of Ti-6Al-4V Alloy

Calibration	Test No.	Cutting Speed V_c (m/min)	Axial Depth of Cut a_p (mm)	Radial Depth of Cut a_e (mm)	Feed Rate f_z (mm/tooth)
Group A	A1	150	1.4	1.6	0.20
	A2	250	1.4	1.6	0.20
	A3	350	1.4	1.6	0.20
	A4	450	1.4	1.6	0.20
	A5	550	1.4	1.6	0.20
Group B	B1	150	1.4	1.6	0.10
	B2	150	1.4	1.6	0.15
	B3	150	1.4	1.6	0.20
	B4	150	1.4	1.6	0.25
	B5	150	1.4	1.6	0.30
Group C	C1	150	1.4	1.0	0.20
	C2	150	1.4	1.3	0.20
	C3	150	1.4	1.6	0.20
	C4	150	1.4	1.9	0.20
	C5	150	1.4	2.2	0.20
Group D	D1	150	1.0	1.6	0.20
	D2	150	1.2	1.6	0.20
	D3	150	1.4	1.6	0.20
	D4	150	1.6	1.6	0.20
	D5	150	1.8	1.6	0.20

2.2.2 Workpiece and cutting tool material

In the current study, a Ti-6Al-4V alloy with 92.25% α-phase and 7.5% β-phase was implemented as a material test during HSM. The alloy chemical composition is labeled in Table 2.2. The average hardness (HV) of the received alloy was 324 MPa. The workpiece material was cut into blocks using an electric wire discharge machine. PVD-coated cemented carbide inserts provided by the SECO Tools Company (Sweden) were employed. This is particularly suitable for HSM applications due to the excellent wear resistance and toughness, which can withstand the dynamic loading conditions. Table 2.3 defines the cutting insert's detailed geometry.

Table 2.2 Chemical Composition of Ti-6Al-4V Alloy

Element	Wt. %	Element	Wt. %	Element	Wt. %
Al	6.11–6.14	V	3.89–4.01	Sn	1.4–2.6
Fe	0.31–1.1	Cu	0.34–90	C	≤0.04
O	≤0.22	N	≤0.05	Ti	Balance

Table 2.3 Detail geometry of cutting insert

Item	Description
Cutting insert designation	XOMX090308TR-M08, MP3000
Tool diameter	20
Tool material	PVD-coated cemented carbide
Corner radius	0.8
Clearance angle	15
Rake angle	10
Cutting edge count	2
Lead angle	90

2.2.3 Cutting forces and temperature measurement

As indicated in Fig. 2.3, a piezoelectric dynamometer (Kistler type 9255B) was used to record the cutting forces (Fx, Fy, and Fz) at a sampling frequency of 10 kHz. The workpiece was

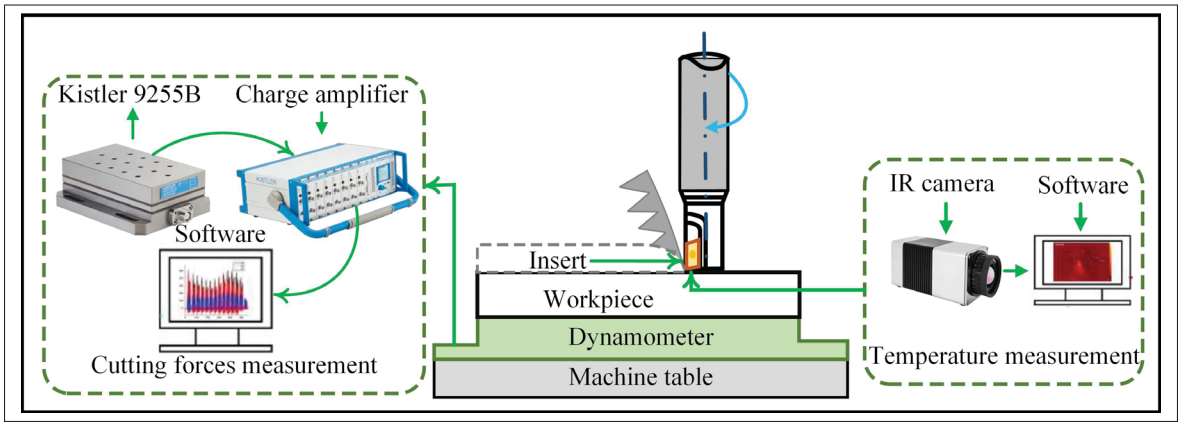

Figure 2.3 Schematic diagram of cutting forces and cutting temperature measurement

fastened tightly to the dynamometer by bolts, and then the dynamometer is fixed to the machine tool with the help of a fixture. During the machining of Ti-6Al-4V alloy, a large amount of heat is generated at the tool-workpiece and chip-tool interface, dramatically influencing the machined surface integrity. The current research work determined the cutting temperature by employing an Infrared (IR) thermal imaging camera, details of which (i.e., specifications, emissivity, etc.) have been provided in Chapter 3.

2.2.4 Geometrical and Metallurgical Characterization of Chips and Cutting Surface Layer

To analyze the microstructural evolution of the cutting surface layer, samples were extracted from the machined part, as illustrated in Fig. 2.4, and ground using a series of abrasive papers. The samples were then polished with 3 μm, 1 μm, and 0.5 μm diamond suspensions. EBSD

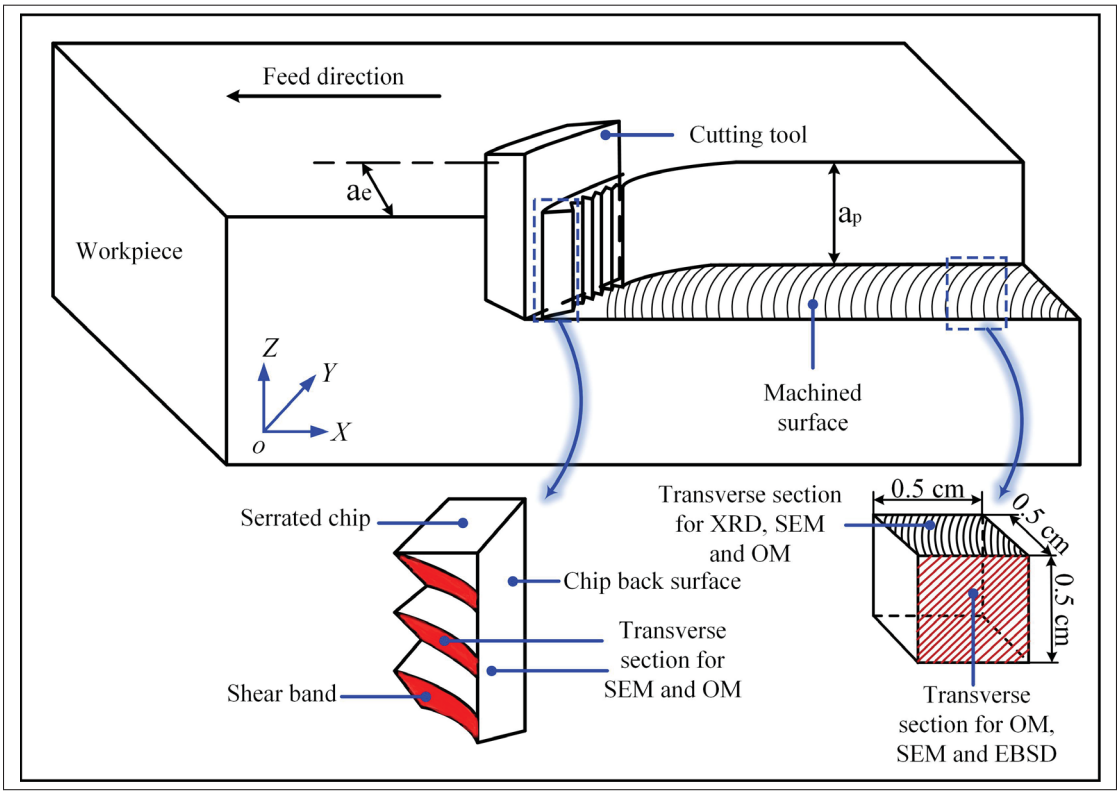

Figure 2.4 Schematic diagram of chip and machined surface layer material characterization

was used to examine grain size evolution. After EBSD analysis, the samples were etched using a solution composed of 6 ml HNO_3, 3 ml HF, and 91 ml distilled water. The OM, SEM and XRD techniques were then utilized to assess the geometrical and microstructural characteristics of the CDZs.

2.2.5 Hardness and Residual stress measurement

A microhardness tester was used to measure the hardness of the cutting deformation zones. The Vickers indenter, with a 136º angle, was employed for the hardness measurements. Fig. 2.5 presents an array of microhardness indentations for both the machined surface and serrated chip cross-sections. The tests were performed under a load of 50 gf applied for 15 seconds. Four indentation arrays were created for the machined surface layer (i.e., two in the vertical direction and two at an angle of 45º). The indentations were spaced 20 μm apart horizontally and 5 μm apart vertically, measured from the top of the machined surface down to the base material. The first hardness measurement was taken directly on the top surface, while the subsequent measurements were performed on the machined subsurface. Similarly, microhardness measurements were taken in the heat-affected zones of the chip, specifically within the shear band and from the chip back surface down to the free surface. The final representative hardness values were determined by averaging the results from these measurements across all cutting conditions.

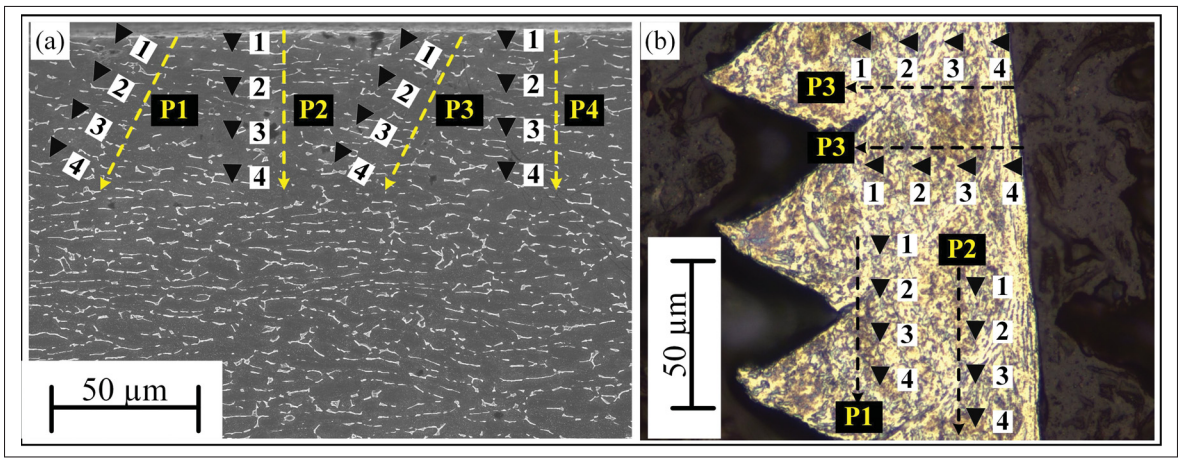

Figure 2.5 Micro-hardness measurement procedure

Similarly, to measure the RS, a macro strain was defined as the total lattice strain generated by the polycrystalline structure of the material. Therefore, measuring lattice strain with elastic mechanics theory and Hooke's law helps determine RS. As expressed in Eq. (2.1), the XRD technique based on Bragg's law can accomplish this function.

$$n\lambda = 2d \sin\theta \tag{2.1}$$

Where n, λ, d, and θ represent the diffraction order, wavelength of an X-ray, the distance between planes in the crystal, and the angle where constructive interference occurs, respectively. For

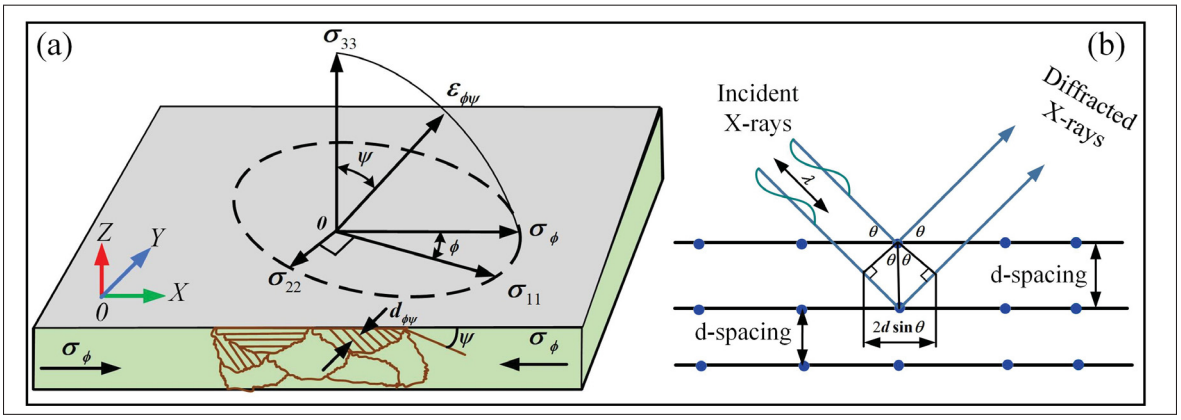

Figure 2.6 Residual stress measurement procedure

measuring the cutting surface layer RS, the stress component normal to the surface (σ33) is considered zero under plane stress assumptions. However, tensile loading along the X-axis induces stress in the transverse direction. Hence, the strain component perpendicular to the surface can be evaluated based on variations in crystal lattice dimensions, which are characterized by angles ϕ and ψ: (as shown in Fig. 2.6) and defined in Eq. 2.2.

$$\varepsilon_{\phi\psi} = \frac{\Delta d}{d_0} = \frac{d_{\phi\psi} - d_0}{d_0} \tag{2.2}$$

Where d_0 is the distance between planes in the crystal.

According to elastic mechanics theory, the following equation can express the lattice strain for the crystallographic plane (i.e., HKL) in the direction of ϕ and ψ:

$$\mathcal{E}_{\varphi\psi}^{hkl} = \left\{\frac{d_{\varphi\psi} - d_0}{d_0}\right\} = \frac{1}{2}S_2^{hkl}\left[\langle\sigma_{11}^s\rangle\cos^2\varphi + \langle\sigma_{12}^s\rangle\sin(2\varphi) + \langle\sigma_{22}^s\rangle\sin^2\varphi\right] + \frac{1}{2}S_2^{hkl}\left[\langle\sigma_{13}^s\rangle\cos\varphi + \langle\sigma_{23}^s\rangle\sin\varphi\right]\sin(2\psi) + S_1^{hkl}\left[\langle\sigma_{11}^s\rangle + \langle\sigma_{22}^s\rangle + \langle\sigma_{33}^s\rangle\right] \quad (2.3)$$

The above equation can be simplified to the plane stress condition as expressed in Eq. (2.4):

$$\varepsilon_{\phi\psi}^{hkl} = \left\{\frac{d_{\phi\psi} - d_0}{d_0}\right\} = S_1\left[\sigma_{11}^s + \sigma_{22}^s\right] + \frac{1}{2}S_2\sigma_\theta\sin^2\psi, \quad (2.4)$$

where S_1 and S_2 are the X-ray elastic constants in a crystallographic plane (213) and can be obtained from the elastic modulus and Poisson's ratio of Ti-6Al-4V alloy, as expressed by Eq. (2.5) and Eq. (2.6), respectively.

$$S_1 = -\frac{v}{E} \quad (2.5)$$

$$S_2 = -\frac{2(1+v)}{E} \quad (2.6)$$

The RS at various locations on the prepared samples was analyzed in both the parallel $\sigma 11$ and perpendicular $\sigma 22$ directions relative to the machined surface at four distinct points. Given the limited penetration depth of X-rays, the samples were incrementally stripped layer by layer using electro-polishing. A solution consisting of 30 ml $HClO_4$, 175 ml $C_4H_{10}O$, and 300 ml CH_3OH was used for this layer removal process. The RS values of the machined surface and subsurface of TC4 titanium alloy were measured using Proto LXRD equipment. The measurements were done on the crystallographic plane (213), where the diffraction peak location was detected at $2\theta = 140.13°$. Data were taken at fifteen different tilt angles ψ within a range of ±45° to produce stress values closer to the average of the material.

2.2.6 Machine surface roughness and particle emission analysis

Among other surface integrity indicators, the machined surface roughness is the most widely used parameter to characterize the geometrical characteristics of the machined parts. In the current investigation, once the machining tests were completed, the surface roughness measurements were taken using a Keyence VR-5200 microscope and a portable profilometer (Surftest SJ-410, Mitutoyo America Corporation, Aurora, IL, USA). The measurement was taken in the cutting and perpendicular directions on the machined part at four different locations, and the results obtained were averaged. Likewise, as shown in Fig. 2.7(b), an Aerodynamic Particle Sizer

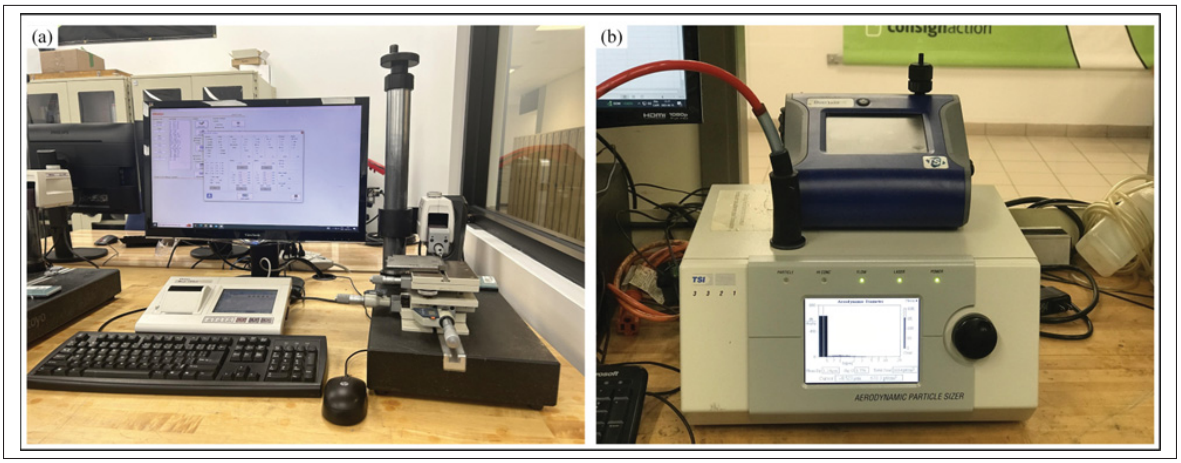

Figure 2.7 Surface roughness measurement and particle collections units

(APS, model 3321, TSI Inc., Shoreview, MN, USA) was exploited to determine the particle number, mass, and specific area concentration based on aerodynamic diameters (μm). The data acquisition duration was 30 s, and the emitted particle data were gathered using a 10-mm suction tube located 10 cm horizontally from the tool/workpiece interface.

2.3 Finite element modeling for the machining process

Modeling and simulating the machining process can not only significantly reduce the time consumption and cost expenditure caused by the cutting experiment but also help to reveal the physical phenomena that are difficult to observe in real-time and directly during the cutting

process. Additionally, it is commonly assumed that during HSM, both the main and secondary cutting edges of the milling tool typically participate in material removal. However, when the main cutting edge involved in the process is significantly longer than the cutting width of the secondary cutting edge, the cutting role of the secondary cutting edge can be neglected (Wang *et al.*, 2016a). Based on these considerations, the three-dimensional milling process can be reasonably simplified to a two-dimensional plane strain model. This simplification allows scholars to enhance their understanding of the deformation behavior of cutting layer materials while significantly improving computational efficiency. Unlike continuous machining operations, milling is not a steady-state process; therefore, two different FE models were developed in the current research work. For microstructure evolution and phase transformation analysis, the model was simplified in a way that considered the trochoidal path as an arc segment. Meanwhile, for RS prediction, the undeformed chip thickness was approximated as a sinusoidal function. The schematic diagram of the developed FE models is depicted in Fig. 2.8. Both models were

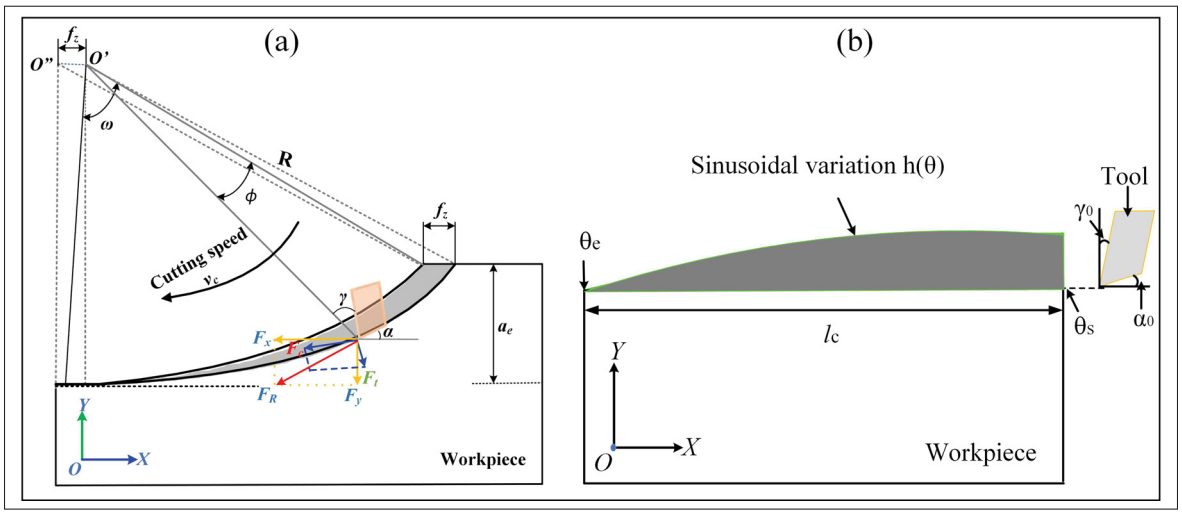

Figure 2.8 Schematic diagrams of simplified FE models build during the research

built in Abaqus/Explicit. The detailed assumptions, governing equations, simplification of a three-dimensional model to a two-dimensional milling model, and the physical phenomenon of the established model are discussed in detail in the following chapters. To accurately predict microstructural evolution, a user-defined subroutine VUSDFLD was developed in FORTRAN and integrated into the cutting simulation via the secondary development interface

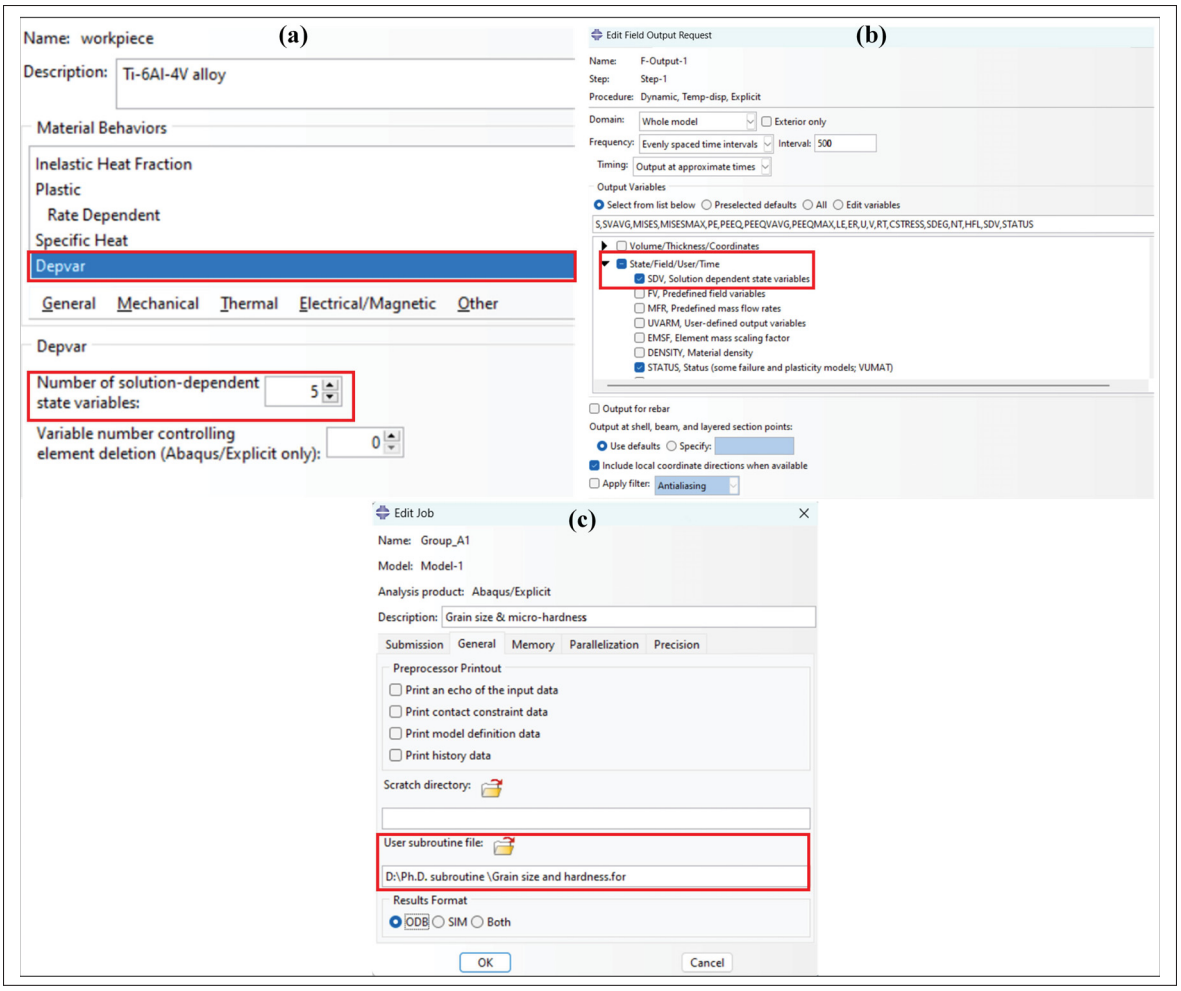

Figure 2.9 Steps for user define subroutine in Abaqus software for microstructure evolution

in Abaqus/Explicit. Within this subroutine, microstructural evolution kinetics were defined as state variables. As illustrated in Fig. 2.9(a), the number of custom state variables assigned in the material properties section must be equal to or greater than those specified in the VUSDFLD subroutine. The customized output state variables can be visualized in the simulation results by selecting SDV (State-Dependent Variables) in the field output settings, as highlighted in the red box in Fig. 2.9(b). Upon job submission, the user subroutine is invoked, enabling synchronized execution with the simulation, as depicted in Fig. 2.9(c).

2.4 Summary

This chapter outlines the research methodology used to investigate the HSM of Ti-6Al-4V, focusing on experimental and computational approaches. The experimental work involved varying machining parameters to assess their effects on surface integrity, including microstructure evolution, mechanical properties, and particle emissions. Cutting forces and temperature were measured using a piezoelectric dynamometer and an infrared thermal camera. Surface characterization included microhardness testing, residual stress analysis via X-ray diffraction, and roughness assessment. Additionally, particle emissions were analyzed using an aerodynamic particle sizer. A FE modeling approach aimed to simulate microstructure evolution and residual stress development. Two different FE models were developed in Abaqus/Explicit, incorporating a user-defined subroutine (VUSDFLD) to predict phase transformation and grain size evolution.

CHAPTER 3

A MULTISCALE FINITE ELEMENT MODELING FOR PREDICTING THE SURFACE INTEGRITY INDUCED BY THERMO-MECHANICAL LOADS DURING HIGH-SPEED MILLING OF TI-6AL-4V

Irfan Ullah [1] , Esther T. Akinlabi[2] , Victor Songmene [1] , Jules Kouam [1] , Morteza Sadeghifar [1]

[1] Department of Mechanical Engineering, , École de Technologie Supérieure, 1100 Notre-Dame Ouest, Montréal, Québec, Canada H3C 1K3
[2] Department of Mechanical and Construction Engineering, Northumbria University, Newcastle Upon Tyne NE1 8ST, United Kingdom

This article is published in *"CIRP Journal of Manufacturing Science and Technology",* Volume 52, June 2024, Pages 246–263, https://doi.org/10.1016/j.cirpj.2024.06.003

Abstract

High-speed milling (HSM) of Ti-6Al-4V is subjected to complex thermo-mechanical loads, leading to alteration in metallurgical conditions within the cutting deformation zones, adversely impacting the mechanical performances of manufactured products. Hence, inclusive insight into microstructural alterations within the Adiabatic Shear Band (ASB) and the milled surface becomes essential for better service performance. This study first developed a Finite Element (FE) milling model to simulate the machining process of Ti-6Al-4V. The proposed FE model is validated through experimental results regarding cutting forces (CFs), cutting temperature (CT), and chip geometry, where the absolute relative error between simulations and experiments was less than 15 %. Secondly, Zenner-Holloman (Z-H) and Hall-Petch (H-P) equations were incorporated into a user-defined subroutine to simulate dynamic recrystallization (DRX) for grain size and microhardness prediction. Simulation results revealed that the grains became finer in the ASB than on the milled surface. In particular, when the cutting speed and feed rate were increased to 350 m/min and 0.30 mm/tooth, the grain size in the ASB decreased from 14 to 0.68 and 0.44 μm, while in the topmost milled surface, it reduced to 7.06 and 6.75 μm, respectively. Conversely, microhardness exhibited an inverse correlation with grain size and increased with cutting speed and feed rate. Furthermore, the impact of increased plastic strain and temperature on the grains during chip segmentation was also examined. Finally, the proposed

FE model validity was established by comparing simulated results with experimental data using advanced characterization techniques. This research significantly contributes to a comprehensive understanding of microstructural evolution and its implications for the mechanical performance of machined titanium components.

Keywords Cutting forces, Cutting temperature, Grain size, High-speed milling, Microhardness, Numerical modeling, Serrated chip, Ti-6Al-4V

3.1 Introduction

High-speed milling (HSM) has attracted substantial adherence in the research community and has been extensively employed in manufacturing industries (Li, Zhang, Zhang, Chen & Zhang, 2018a). It is appropriate for machining a large variety of materials, including soft, difficult-to-cut, and composite materials (Guolong *et al.*, 2023). Recently, various unconventional forming technologies, such as laser processing, powder metallurgy, and 3D printing, have greatly assisted in the improvement and development of the manufacturing industry as science and technology made progress (Bourell *et al.*, 2017). Nonetheless, precision joining and finishing still necessitate additional machining procedures such as high-speed milling. Despite significant application advantages and future development potential, HSM still poses many challenges, especially during the machinability of various difficult-to-cut alloys (Shivpuri, Hua, Mittal, Srivastava & Lahoti, 2002; Zhao *et al.*, 2024). Due to its remarkable blend of characteristics, Ti-6Al-4V is one such material that is widely employed in most critical engineering applications, such as aircraft structural components, because of its high strength-to-weight ratio and outstanding corrosion resistance (Ye, Chen, Xue & Dai, 2014). However, the machining of titanium and its alloy is always problematic because of its inhomogeneity and anisotropic character, making it challenging to manufacture (Zhang, He & Zhang, 2023). Among others, the main challenges that Ti-6Al-4V encountered during machining lie in excessive prevalence in thermo-mechanical loads, which subsequently compromise cutting tool life and substantially deteriorate machined surface integrity (Wang *et al.*, 2021). Material properties and parameters, including thermal conductivity, elastic and inelastic material constitutive parameters, hardness, and so

forth, are generally dependent and functional parameters and strongly influence the material's microstructure. Therefore, the prophecy of microstructural changes and assessing the mechanical properties during milling has become of prime prominence for many researchers, as it is directly related to fatigue life and the strength of the material (Geng *et al.*, 2024).Various experimental and theoretical studies on chips and machined surfaces of Ti-6Al-4V were conducted to evaluate microstructural phenomena, including texture evolution, phase transformations, recrystallization, dislocation density evolution, grain growth, and hardness (Sun *et al.*, 2024; Calistes *et al.*, 2009; Xiao *et al.*, 2020; Li *et al.*, 2018b). Among them, recrystallization and grain growth are two phenomena that have been studied in relation to the properties and service performance of Ti-6Al-4V. However, since the experimental methods are costly and time-consuming, many researchers and scientists have tried to develop FE models, as they require a small number of experiments for validation. For machining simulations, FE models in the literature follow constitutive laws, which can be classified into two classes (i.e., physical-based and phenomenological laws). Physical-based models, such as those based on dislocation density and phase changes, can explicitly assess physical attributes at the microscale to update flow stress continuously (Zhang *et al.*, 2023). While phenomenological laws typically employ a function to illustrate and modernize flow stress as strain, strain rate, and temperature change (Liu *et al.*, 2022a). Based on physical-based law, (Ding, Zhang & Richard Liu, 2014) exploited the grain refinement model following the dislocation-density accumulation during the turning of A16061-T6 alloy. The established model precisely forecasts the microstructural variation under different cutting speeds and tool rake angles. (Melkote, Liu, Fernandez-Zelaia & Marusich, 2015) introduced an improved physically based constitutive model by incorporating the inverse Hall-Petch effect to simulate microstructural evolution in CP-Ti machined chips. The authors described spatial distribution of grains and dislocation density in ASB of segmented chips. Similar approaches (i.e., dislocation-density-based models) were also carried out in the literature to predict the grain size of machining-produced chips (Liu *et al.*, 2015; Estrin, Tóth, Molinari & Bréchet, 1998; Denguir, Outeiro, Fromentin, Vignal & Besnard, 2017). Although, some microstructural features can be exhibited promptly and unequivocally with these models. However, substantial experimental efforts are still mandatory to identify the parameters for such microstructural

evolution models. Furthermore, these models are regulated by an individual deformation mechanism solely considering dislocation mobility and evolution. These models perform inadequately regarding deformation influenced by multi-mechanisms and restricted to single-phase materials (Bruschi *et al.*, 2014; Li, Zhang, Du & Sun, 2022). In addition, many physical parameters that can significantly enhance the computational time and are challenging to identify, make these models less practical in machining industries. As a result, phenomenological models are still widely accepted for treating microstructural alteration as a homogenous variable during the machining process (Xu, Zhang, Outeiro, Xu & Zhao, 2020; Wang, Ren, Zhou & Cai, 2023b; Wang *et al.*, 2016b). In the metal machining process, DRX is the crucial aspect ensuing in grain evolution. For grain size prediction induced by DRX, Johnson-Mehl-Avrami-Kolmogorov (JMAK) and Zenner-Hollomon (Z-H) are usually employed with phenomenological laws. (Arısoy & Özel, 2015) employed JMAK model to calculate DRX and grain size in a three-dimensional turning FE simulation of Ti-6Al-4V. However, the authors ignore the chip formation process during their simulations. Similarly, (Pan *et al.*, 2016) utilize JMAK model for dry cutting of Ti-6Al-4V to explore the cutting speed's effect on grain alteration and phase changes. The authors concluded that increased cutting speed can help to reduce the grain boundaries in the machined subsurface. The impact of machining parameters and tool geometry on machining-induced grain size prediction was studied by (Sadeghifar, Javidikia, Songmene & Jahazi, 2020) by employing various JMAK constants during the orthogonal cutting of Ti-6Al-4V. Similarly, (Yameogo, Haddag, Makich & Nouari, 2019) also exploited the JMAK model during orthogonal cutting of Ti-6Al-4V to forecast the volume fraction of dynamically recrystallized grains. Reasonable agreements regarding chip geometry and machining forces were obtained, with no grain size prediction. Other researchers also employed the JMAK model to forecast grain alterations, dynamic recrystallization, and volume fraction changes within the machined sub-surface (Özel & Arisoy, 2014; Xu, Zhang, Liu, Xu & Zhao, 2021). However, the JMAK model is more multifaceted, as it requires many parameters to be determined, which is relatively complex. In comparison, the Zenner-Holloman (Z-H) equation, based on the recrystallization, is the most widely used model for microstructural forecast, as it is relatively simple, with fewer parameters to be determined, better universality, and a more comprehensive

range of materials. (Li, Zhang, Fang, Wang & Lu, 2019a) employed the Z-H equation to predict the grain size in the machined surface during the hard cutting of H13 steel. Similarly, (Wang *et al.*, 2016b) and (Lv, Li, Ge & Zhang, 2022) anticipated the grains changes in the chip and cutting surface of Ti-6Al-4V using Z-H and H-P equations. The authors reported an inverse relation between grain size and hardness. The above literature indicates that all these findings provide a crucial indication for comprehending the microstructural evolution in metal cutting. However, most studies were related to continuous turning. It's important to highlight that within the milling process, variations in the initial thickness of the chip and other distinct factors swiftly transform into a thermo-mechanical loading sequence. This sequence profoundly impacts the plastic deformation, sustainability of grains, and hardness within the regions undergoing cutting deformation. In addition, a comprehensive analysis of grains and hardness variation, which demonstrated the interrelationship among cutting temperature, equivalent plastic strain, and strain rates, remains inadequately understood. Hence, the current research objectives are to utilize a simplified two-dimensional milling model, which can replicate the actual milling process (i.e., varying chip load with cutting tool advancement) to expand the understanding of microstructure and microhardness prediction within the cutting deformation zones and optimize machining parameters for better surface integrity. With the objectives in mind, first initial grain size and microhardness of the as-received alloy were determined. Subsequently, the material sub-model for Ti-6Al-4V was introduced. Afterward, the developed model was incorporated with a user-defined subroutine to analyze the effect of process parameters on CFs, CT, chip morphology, grain size, and microhardness. Finally, the material sub-model was validated through experimental measurements.

3.2 Description of established model

3.2.1 Simplified milling model

An effective and precise transformation from a 3D milling system to a 2D cutting process can diminish mesh complexity and computational time without compromising the envisioned

outcomes. Moreover, the hypothetical feed rates in the current study are more trivial than the ascribed depth of cut. Therefore, the assumption of plain strain can be appropriate for 2D simulation (Tang, Wang, Hu & Song, 2009; Ullah *et al.*, 2022; Li *et al.*, 2019c). The conversion from the 3D milling process to the 2D cutting process has been indicated in Fig. 3.1.

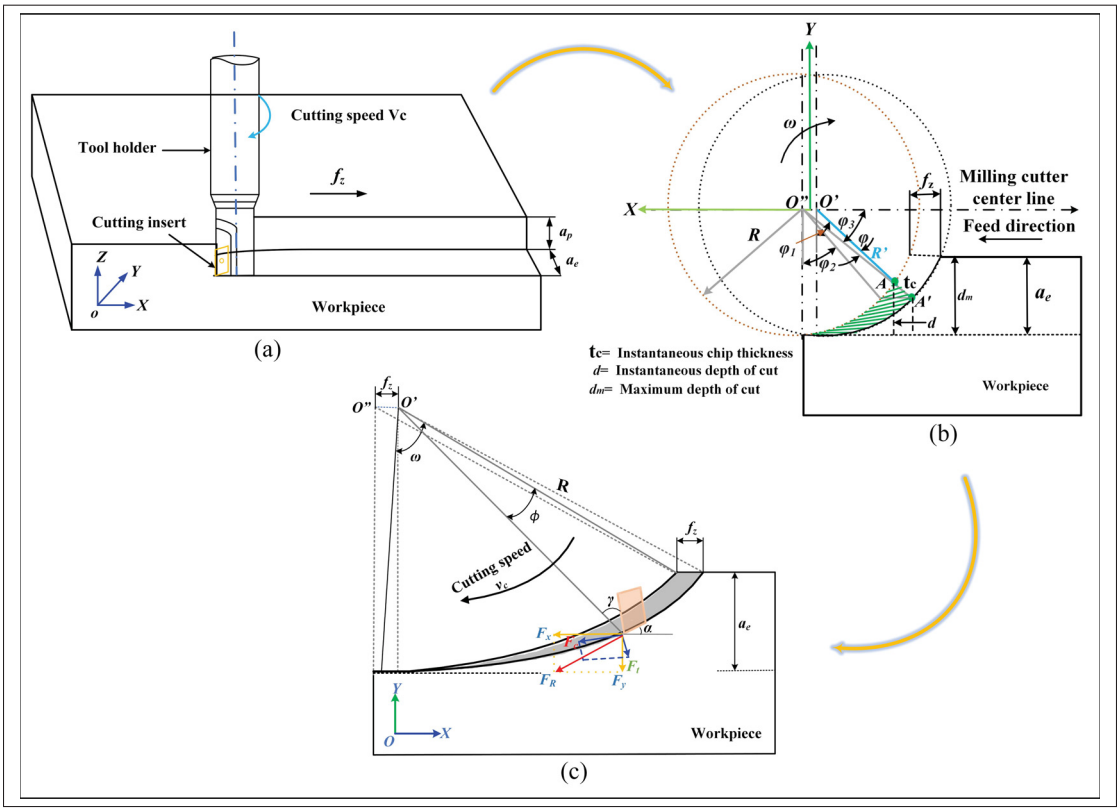

Figure 3.1 Conversion of 3D milling system to simplified 2D milling system: (a) schematic diagram of 3D milling process, (b) conversion of a trochoidal path to cutting arc, and (c) simplified 2D milling model

By rationalizing the trochoidal path as an arc segment and knowing the milling circumstances and the tooth path length, the instantaneous milling chip's thickness for the circular path can be accomplished in the following way (Eq. (3.1)).

$$t_c = R + f_z \sin\varphi_1 - \sqrt{R^2 - f_z^2 \cos^2\varphi_1} \tag{3.1}$$

where R demonstrates the milling cutter's radius, and f_z is the feed rate (Fig. 3.1(b)). The term in Eq. (3.1) represents the angular displacement of the milling cutter, which can be drawn in the following form.

$$\varphi_1 = \sin^{-1}\left(\frac{\sqrt{2Rd - d^2} - f_z}{\sqrt{R^2 - 2f_z\sqrt{2Rd - d^2} + f_z^2}}\right) \tag{3.2}$$

where d is the instantaneous depth of cut. For the actual milling process, the expression under radical in Eq. (3.1) can be approximated to R^2 (Martellotti, 1941); therefore, the modified form of Eq. (3.1) can be written as follows.

$$t_c = f_z \sin\varphi_1 \tag{3.3}$$

Hence, the instantaneous chip thickness can be obtained by substituting Eq. (3.2) into Eq. (3.3) as follows.

$$t_c = f_z \frac{\sqrt{2Rd - d^2} - f_z}{\sqrt{R^2 - 2f_z(2Rd - d^2) + f_z^2}} \tag{3.4}$$

3.2.2 FE model, meshing, and boundary conditions

To evaluate and predict grain refinement and microhardness deviation within cutting deformation zones, a simplified FE milling model was developed in Abaqus/Explicit. The model is composed of a cutting insert (PVD-coated carbide) and workpiece (Ti-6Al-4V) with applied fixed boundary conditions, as depicted in Fig. 3.2. The workpiece is further sub-divided into three parts, including undeformed chip thickness (i.e., Part-B), chip separation layer (i.e., Part-C), and the base material (i.e., Part-D). The cutting insert's clearance and rake angles were kept analogous to those employed during milling experiments. The workpiece and cutting insert were meshed by assigning element type CPE4RT, which combines plain stain quadrilateral with temperature-displacement coupling. To capture the large deformation, shear localization occurrence, and

heat-affected zones, Part-B and Part-C were meshed with consistent elements of about 4 μm. In contrast, Part-D was meshed using a bias ratio to achieve a compact mesh in the vicinity of the chip partition layer. The initial temperature for both the workpiece and cutting insert was considered equivalent to 20 ℃. Heat conversion from the critical regions to the adjacent atmosphere was not considered since the cutting insert engages with the workpiece for a short time due to high rotational speeds.

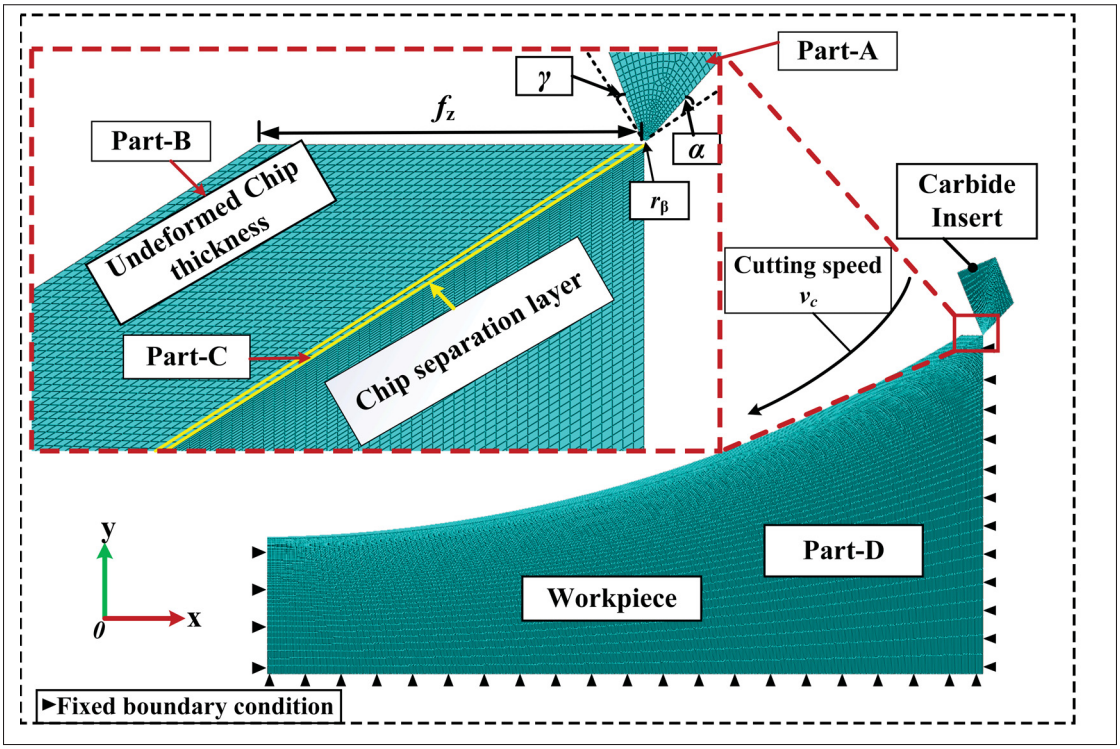

Figure 3.2 Simplified 2D milling simulation model

3.2.3 Material flow stress model

A precise and unwavering constitutive model is critical for describing the dynamic mechanical response during HSM. A Johnson-Cook (J-C) constitutive material model was employed in the current research. The following equation can express the J-C constitutive model (Johnson & Cook,

1985).

$$\sigma = (A + B\varepsilon^n)\left[1 + C\ln\frac{\dot{\varepsilon}}{\dot{\varepsilon}_0}\right]\left[1 - \left(\frac{T - T_{\text{room}}}{T_{\text{melt}} - T_{\text{room}}}\right)^m\right] \tag{3.5}$$

In Eq. (3.5), the parameters σ, ε, $\dot{\varepsilon}$ and $\dot{\varepsilon}_0$ account for equivalent flow stress, plastic strain, strain rate, and reference strain rate, respectively. Meanwhile, as listed in Table 3.1, the terms A is the initial yield strength, B is the strain hardening coefficient, C is the strain rate hardening coefficient, n is the strain rate hardening index, and m is the thermal softening index.

Table 3.1 JC material constitutive model parameters for Ti-6Al-4V Alloy
Taken from Ullah *et al.* (2022)

A(MPa)	B(MPa)	n	m	C	$T_{\text{melt}}(^\circ C)$	$T_{\text{room}}(^\circ C)$
860	683	0.47	1	0.035	1605	20

3.3 Damage and Chip Formulation Model

Due to low thermal conductivity and high chemical reactivity, HSM of Ti-6Al-4V generally generates serrated chips and narrow shear bands. In addition, crack initiation and propagation will result from high shear localization in shallow bands. To realize material failure and chip formulation criterion, the material should be buckled until fracture. Hence, node partition and element obliteration approaches are required to recognize the material malfunction and chip formation process. In this research, a J-C fracture model, which can be described by the variable w, as specified in Eq. (3.6), was implemented for the damage initiation step.

$$w = \sum\left(\frac{\Delta\bar{\varepsilon}^{pl}}{\bar{\varepsilon}_f^{pl}}\right) \tag{3.6}$$

Where $\Delta\bar{\varepsilon}^{pl}$ and $\bar{\varepsilon}_f^{pl}$ symbolize the equivalent plastic strain increment and damage initiation, respectively. The term $\bar{\varepsilon}_f^{pl}$ is linked to stress triaxiality, strain rate, and temperature and can be

illustrated by Eq. (3.7) (Arrazola, Özel, Umbrello, Davies & Jawahir, 2013).

$$\bar{\varepsilon}_f^{pl} = [d_1 + d_2 \exp(-d_3)\eta] \left[1 + d_4 \ln\left(\frac{\dot{\varepsilon}^{pl}}{\dot{\varepsilon}_0}\right)\right] \left(1 - d_5\hat{\theta}\right) \tag{3.7}$$

In Eq. (3.7), the terms d1-d5 symbolize the damage parameters listed in Table 3.2 and $\dot{\varepsilon}_0$ denote the reference strain rate. Meanwhile, η is the stress triaxiality (dimensionless pressure deviatoric stress ratio), equal to p/q (where p is pressure stress and q is Mises stress), and $\hat{\theta}$ is the dimensionless temperature allocation, stated by Eq. (3.8), as follows.

$$\hat{\theta} = \begin{cases} 0 & T < T_{\text{room}} \\ \frac{T - T_{\text{room}}}{T_{\text{melt}} - T_{\text{room}}} & T_{\text{room}} \leq T \leq T_{\text{melt}} \\ 1 & T > T_{\text{melt}} \end{cases} \tag{3.8}$$

As illustrated in Fig. 3.3, when plastic deformation increases, material hardening modulus becomes gradually fragile to the extent of damage, resulting in a declination of material loading capacity at point B. As the damage further intensifies, the stress-strain association no longer precisely signifies the material's response and reaches its ultimate stress volume at point D. As a result, fracture energy is acquired by incorporating the yield stress into the strain function. The fracture energy model's main advantage is controlling material deterioration once the damage has begun and describing high-strain localization even with a small-scale element size. Therefore, in stage 2, the fracture energy model was implemented to describe the damage evolution, expressed by Eq. (3.9).

$$G_f = \int_{\bar{\varepsilon}_{0i}^{pl}}^{\bar{\varepsilon}_f^{pl}} L\sigma_y d\bar{\varepsilon}^{pl} = \int_0^{\bar{u}_f^{pl}} \sigma_y d\bar{u}^{pl} \tag{3.9}$$

where L and $\bar{u}^{pl}$ represent the element's characteristic length and equivalent plastic displacement, respectively. The term $\overline{u}_f^{pl}$ in the above equation denotes the equivalent plastic displacement at failure. For the plain strain hypothesis, G_f (i.e., fracture energy) can be estimated with the help

of fracture toughness (i.e., K_c) as follows (Mabrouki, Girardin, Asad & Rigal, 2008):

$$G_f = \left(\frac{1-v^2}{E}\right) K_c^2 \tag{3.10}$$

Where E and v are Young's modulus and Poisson's ratio of the material, respectively. A material's stiffness degradation in the occurrence of damage evolution can be defined via the variable D as follows:

$$D = \frac{L\bar{\varepsilon}}{\bar{u}_f^{pl}} = \frac{\bar{u}}{\bar{u}_f^{pl}} \tag{3.11}$$

The fracture model is associated with the damage parameter (D) value, as indicated in Fig. 3.3. A complete fracture exists as the D approaches 1.

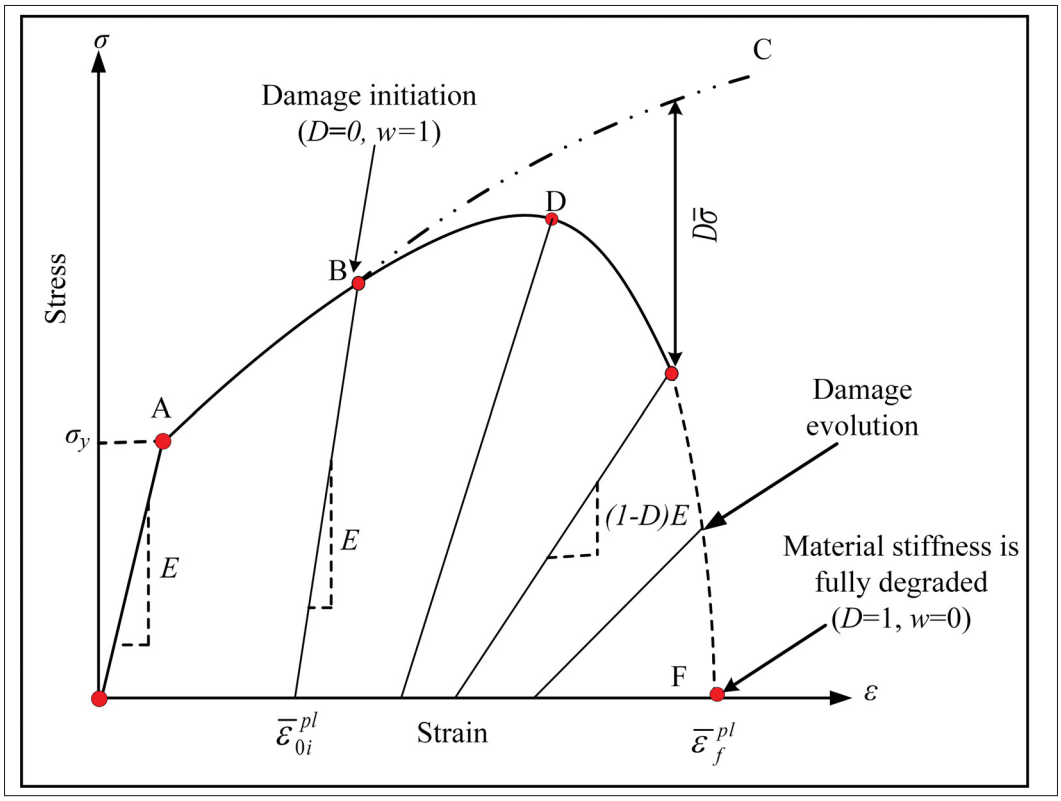

Figure 3.3 Stress-strain curve of the material damage degradation
Taken from Ullah *et al.* (2021b)

Table 3.2 Damage parameter values for Ti-6Al-4V alloy
Taken from Ullah *et al.* (2022)

d_1	d_2	d_3	d_4	d_5
-0.09	0.25	-0.5	0.014	3.87

3.3.1 Contact model

The contact model plays a significant role in thermo-mechanical interaction in machining, directly impacting microstructural evolution. The Zorev model was employed in the current investigation to express the sticking and sliding friction between the tool-chip interface (Ng & Aspinwall, 2002). The sticking and sliding behavior between the tool and workpiece is contingent upon the shear and normal stresses, as determined by Eq. (3.12)

$$\tau_f = \begin{cases} \mu\sigma, & \mu\sigma \leq \tau_{crit} \text{ (sliding zone)} \\ \tau_{crit}, & \mu\sigma \geq \tau_{crit} \text{ (sticking zone)} \end{cases} \tag{3.12}$$

where τ_f, τ_{crit}, μ, and σ are the frictional shearing stress, critical shear stress, friction coefficient, and normal stress, respectively. In the current research, the coefficient of friction was set to 0.24, which can lead to adequate outcomes regarding machining forces, temperature, and chip geometrical characteristics (Ullah *et al.*, 2021b).

3.3.2 Grain size and microhardness prediction model

During milling, the combined action of thermal and mechanical loads results in severe plastic deformation (SPD), subsequently influencing microstructural alteration. Various grain evolution and hardness prediction modeling approaches have been described, fluctuating from combined kinetic and thermodynamic numerical models and continuum-based analytical prescriptions. In the current research, the defined Z parameter was integrated into the kinetics to deliberate the influences of material deformation behavior at higher temperatures and strain rates. Hence, the following two equations describe the Z-H equation and grain size d (μm) (Yanagimoto & Liu,

1999).

$$Z = \dot{\varepsilon} \exp\left(\frac{Q}{RT}\right) \tag{3.13}$$

$$d = d_0 b Z^m \tag{3.14}$$

Where $Q = 376,000$ J/mol (activation energy), $R = 8.3145$ J/K/mol (universal gas constant), $d_0 = 14$ μm (initial grain size), b and m are material constants. Similarly, for DRX (Dynamic Recrystallization) initiation, the critical strain ε_{cr} induced by machining needs to be achieved or surpassed throughout the cutting process. Therefore, to accommodate for DRX, the critical strain value, which is related by constants a and c, was calculated by employing the equations provided by (Abbasi & Momeni, 2011) and (Momeni & Abbasi, 2010), as follows.

$$\varepsilon_{cr} = aZ^c \tag{3.15}$$

Grain refinement substantially impacts the material's physical and mechanical properties, particularly its microhardness, which exhibits an inverse relationship with grain size. Therefore, as articulated in Eq. (3.16), the H-P equation was used to estimate microhardness (HV).

$$HV = C_0 + C_1 . d^{-0.5} \tag{3.16}$$

Where C0= 324 HV (initial hardness), and C1 denotes the material constant. The procedure for grain size and microhardness prediction with the employed user-defined subroutine VUSDFLD, which was written in Fortran, is indicated in Fig. 3.4. In this framework, the strain and temperature values at the conclusion of each incremental step were acquired, enabling the determination of critical strain. When the strain surpasses the critical threshold, it triggers the process of DRX, leading to the adjustment of grains and hardness through Eqs. (3.14) and (3.16), respectively. Other than that, grains and hardness remained unchanged.

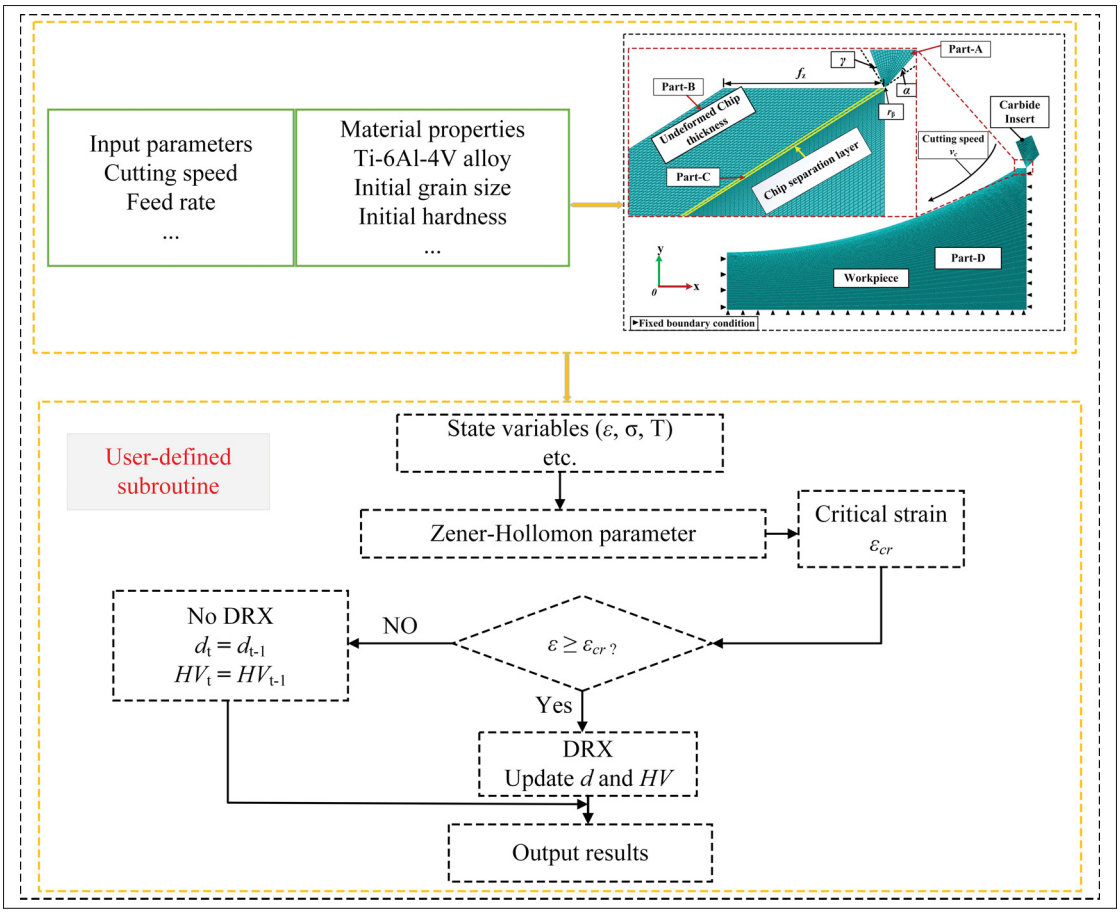

Figure 3.4 Flowchart for predicting GS and M-H during HSM of Ti-6Al-4V

3.4 Experimental validation of the established FE Model

Ti-6Al-4V, with an average grain size of 14 μm (Fig. 3.5), was chosen as an experimental material for HSM to validate the established model. The alloy's nominal chemical composition and thermo-mechanical parameters are shown in Tables 3.3 and 3.4. The oxidation layer was eradicated from the workpiece prior to the machining tests. The tests were accomplished in dry conditions on a 3-axis vertical machining center (Huron K2X10). PVD-coated carbide indexable cutting inserts (XOMX090308TR-M08 F40M), which were held tightly with a milling cutter (R217.69-2020.0-09-3AN), with a diameter of 20 mm, providing an axial rake angle of +10°, clearance angle of −15°, were used during the HSM experiments. To avoid the cutting tool's runout effects, a single new insert was employed during the milling experiments, and every

test was repeated three times to ensure the reliability and consistency of results. Machining forces were measured by utilizing a Kistler piezoelectric dynamometer (type 9255B) under different cutting conditions at a sampling frequency of 10 kHz. The workpiece was fastened tightly to the dynamometer by bolts, and then the dynamometer was fixed to the machine tool with the help of a fixture. The Infrared (IR) thermal imaging camera (VarioCAM®HD head

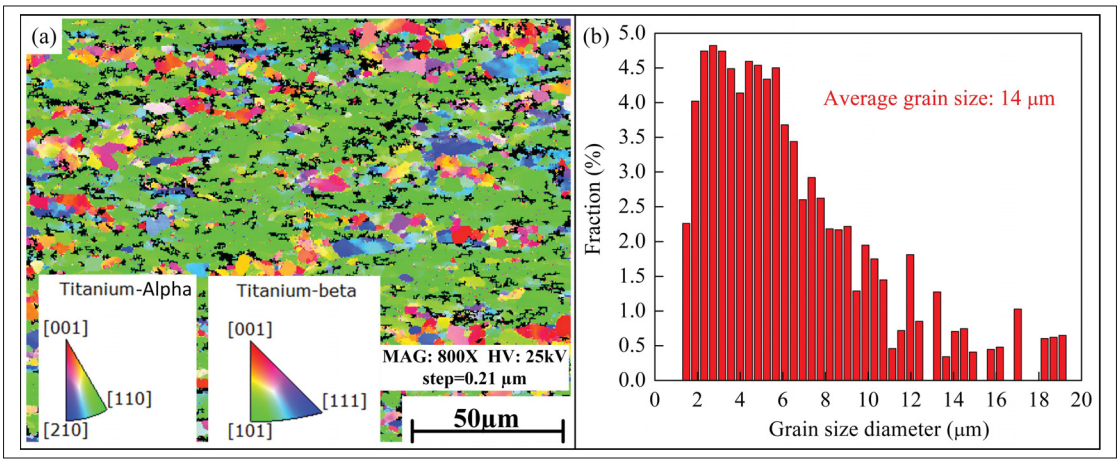

Figure 3.5 EBSD of base alloy: (a) inverse pole (IP) Y-scheme figure, and (b) grain size distribution

900) with IR pixel (2,048 × 1,536) and frame rates with up to 240 Hz was employed to obtain the instantaneous cutting temperature. The camera was sealed in a box and set at a distance of 190 mm from the tool/workpiece interface, as shown in Fig. 3.6. The obtained IRS data files were then analyzed in IRT analyzer 7 software. The actual temperature depends on the material's emissivity, which is a specific apprehension for thermal imaging cameras. In the current investigation, the emissivity of Ti-6Al-4V was set in the range of 0.257-0.286, which was determined following the procedure given in the author's previous work (Ullah *et al.*, 2021b). Details regarding the experimental arrangement and cutting parameters for the milling process are provided in Fig. 3.6 and Table 3.5, respectively.

Table 3.3 Chemical Composition of Ti-6Al-4V Alloy

Element	Al	V	Sn	Fe	Cu	C	O	N	Ti
Wt. %	6.11–6.14	3.89–4.01	1.4–2.6	0.31–1.1	0.34–90	≤0.04	≤0.22	≤0.05	Balance

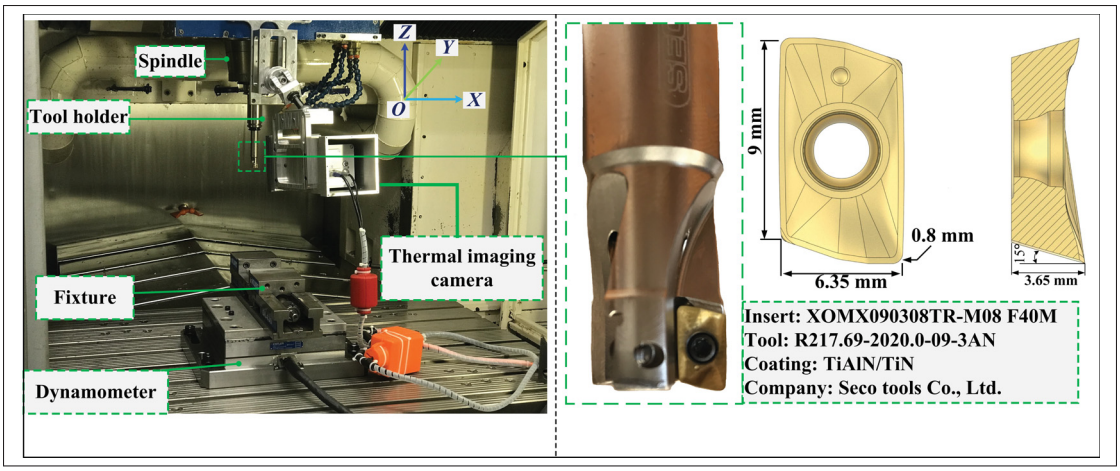

Figure 3.6 Details of high-speed milling experiments

Table 3.4 Physical and temperature-dependent thermo-mechanical Properties of Ti-6Al-4V Alloy
Taken from Wang & Liu (2015)

Density (kg/m^3)	Elastic Modulus (GPa)	Poisson's Ratio	Thermal Conductivity (W/mK)	Inelastic Heat Fraction	Specific Heat Capacity (J/kgK)	Thermal Expansion Coeff. ($10^6/K$)
4430.8	109 (50°C) 91 (250°C) 75 (550°C)	0.34	6.80 (20°C) 7.40 (100°C) 9.80 (300°C) 11.80 (500°C)	0.9	611 (20°C) 624 (100°C) 674 (300°C) 703 (500°C)	9.0

Table 3.5 Machining parameters in experimental tests

Variables	**Constants**
$V_c = 150,\ 250,$ and 350 m/min	$f_z = 0.20$ mm/tooth, $a_e = 1.6$ mm, and $a_p = 1.4$ mm
$f_z = 0.10, 0.20, 0.25, 0.30$ mm/tooth	$V_c = 150$ m/min, $a_e = 1.6$ mm, and $a_p = 1.4$ mm

Once the machining tests were completed, samples were cut from the machined surface using an electric wire machine. The samples were then molded with bakelite, ground with various abrasive papers (600, 1200, and 2000), and polished with 5μm and 3μm diamond suspensions.

A similar procedure was conducted for the chip's geometrical and morphological observation. Optical Microscopy, Scanning Electron Microscopy (SEM), and Electron Backscattered (EBSD) techniques were employed to analyze the microstructural changes in the cutting deformation zones, respectively. Similarly, the microhardness of the machined surface down to unaffected zones was also deliberated by employing a micro-hardness tester under the load of 50 gf for 15 s.

3.5 Validation of simplified milling simulation model

3.5.1 Machining forces and workpiece temperature

Since the material's microstructural evolution is intensely affected by highly integrated thermo-mechanical loading conditions, an adequate uniformity of CFs and temperature between predicted and measured outcomes can emphasize the guarantee of grain and hardness prediction. The precision of the developed FE model was initially confirmed regarding CFs and workpiece temperature. To analyze and to compare the experimental and simulated CFs, a mean of twenty cycles within a single cutting period for maximum chip load was considered for experimentally obtained CFs (Fig. 3.7(a)). In contrast, for simulations, the highest values (i.e., maximum chip load) of CFs were chosen, as specified in Fig. 3.7(b). As depicted in Fig. 3.7(c), the CFs obtained from milling experiments against 150 m/min and 250 m/min in both directions (i.e., X- and Y-direction) are marginally higher than those obtained from the FE model and increase with cutting speed in both directions. In contrast, for a cutting speed of 350 m/min, the predicted CFs dominate the experimental ones. Likewise, the influence of different feed rates on CFs was also examined. Fig. 3.7(d) indicates that CFs demonstrate mixed behavior against feed rates. The simulated and experimentally obtained CF components increased when the feed rate increased from 0.10 mm/tooth to 0.20 mm/tooth. However, when the feed rate increased to 0.25 mm/tooth, the CF in the X-direction decreased, and with a further increase in feed rate (i.e., 0.30 mm/tooth), CF components rose again. Condensed CF tends to be mainly attributed to material softening phenomena triggered by high thermal gradients as the feed rate increases (Liu, Kilic & Altintas, 2022b)[45]. It was perceived that the predicted force components exhibit a precise correlation

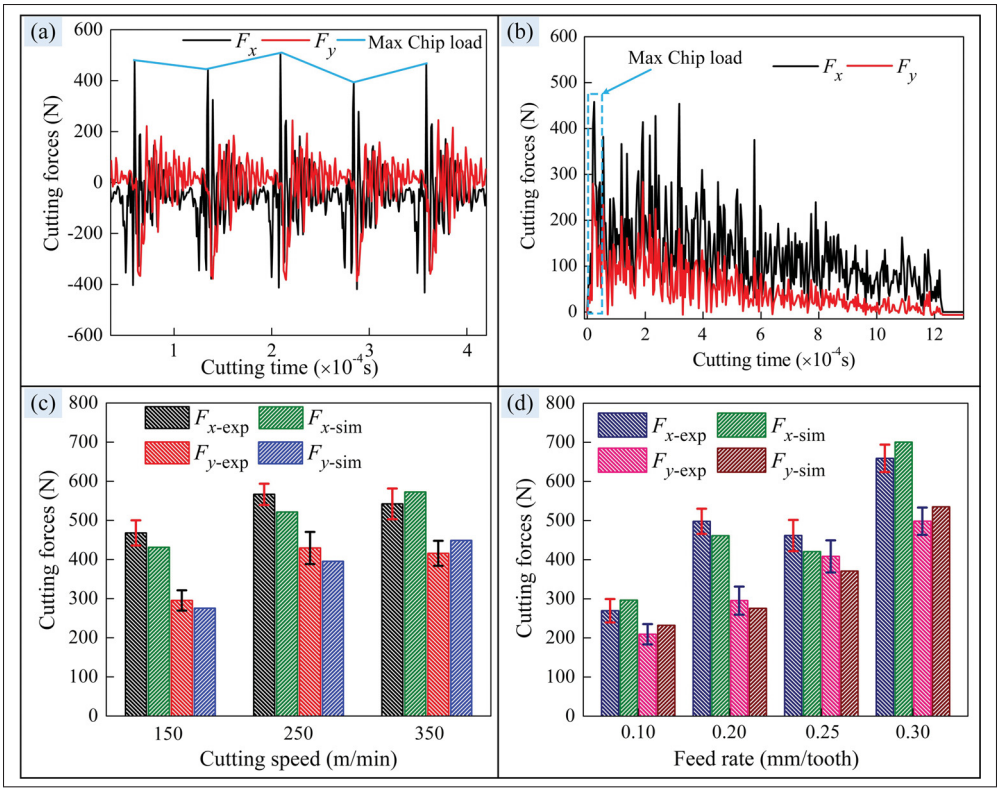

Figure 3.7 Predicted and experimental cutting forces: (a) experimental CFs at 150 m/min, (b) predicted CFs at 150 m/min, (c-d) CFs comparison against various cutting speeds and feed rates

with experimental outcomes for the given machining parameters, demonstrating a relative error of less than 14.2 %. Concurrently, for the assessment of temperature distribution within the workpiece, first two points (i.e., Point-1 and Point-2) were specified at the uppermost milled surface as shown in Fig. 3.8(a), and the obtained results were labeled in Fig. 3.8(b). The temperature of the milled surface remained relatively constant for specified nodes, and once the tool passed the selected nodes, temperature swiftly dropped, ultimately reaching around 60°C. A similar trend can also be observed for temperature encountered during actual machining experiments. As indicated in Fig. 3.8 (c-d), the temperature abruptly increased from ambient temperature to about 420°C, followed by the rapid cooling phase. For a detailed understanding of how machining input parameters influence the workpiece temperature, seven nodes were selected within the milled surface of the developed model, as indicated in Fig. 3.13 and 3.16.

While an average value of the frame-based approach was used for experimentally obtained workpiece temperature, and the obtained results were demonstrated in Fig. 3.9.

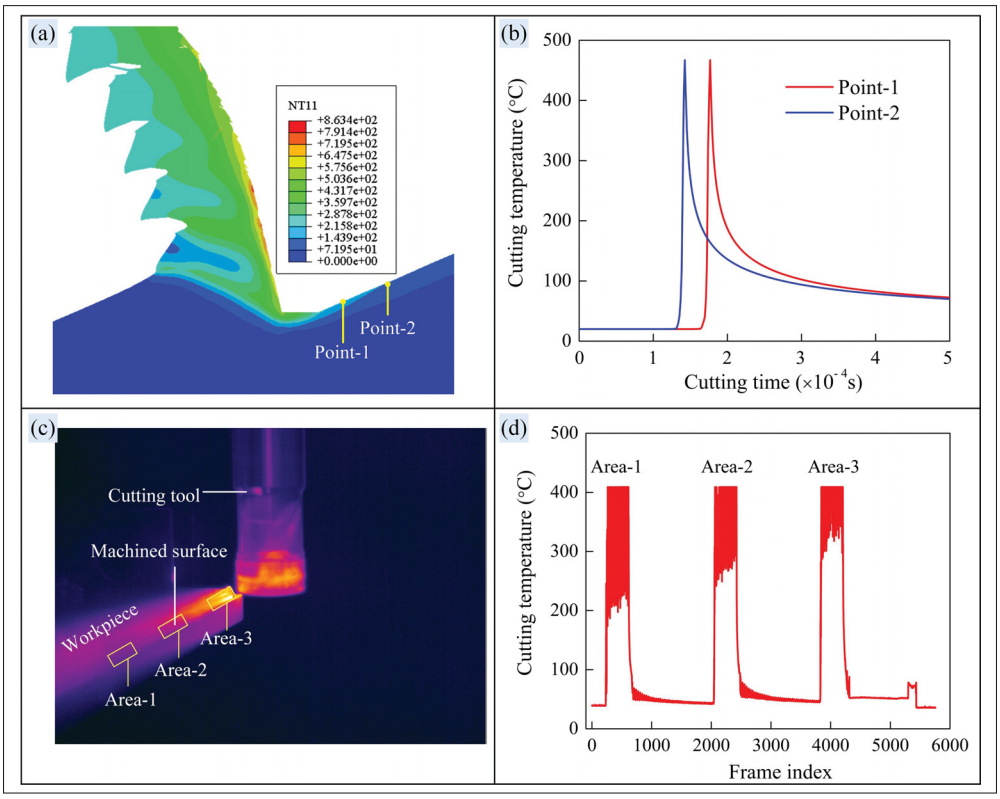

Figure 3.8 Simulated and experimental machined surface temperature for 150 m/min

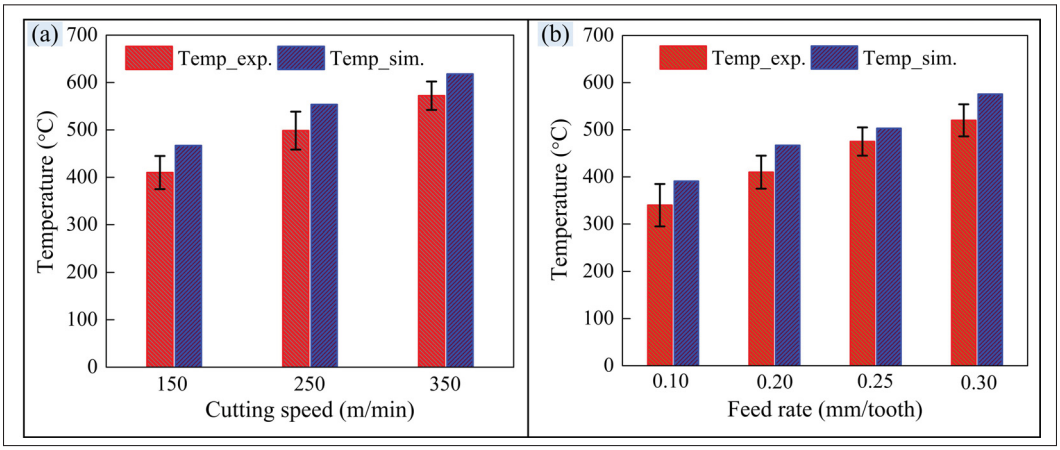

Figure 3.9 Experimental and simulated machined surface temperature: (a) vs. cutting speeds (m/min), (b) vs. feed rates (mm/tooth)

It can be summarized that although the predicted machined surface temperature was found to be marginally higher than the experimental ones. Undoubtedly, the experimentally measured milled surface temperatures in peak values were in promising agreement with predicted ones on utmost milled surfaces, which get sharpened as cutting speeds and feed rates increase.

3.5.2 Morphological Observation of Chip

Since the chip's morphological and metallurgical observations are closely associated with stress, strain, and thermal fields, a proper consistency between simulated and experimentally obtained chip morphological features can further assure the established model's consistency. A steady

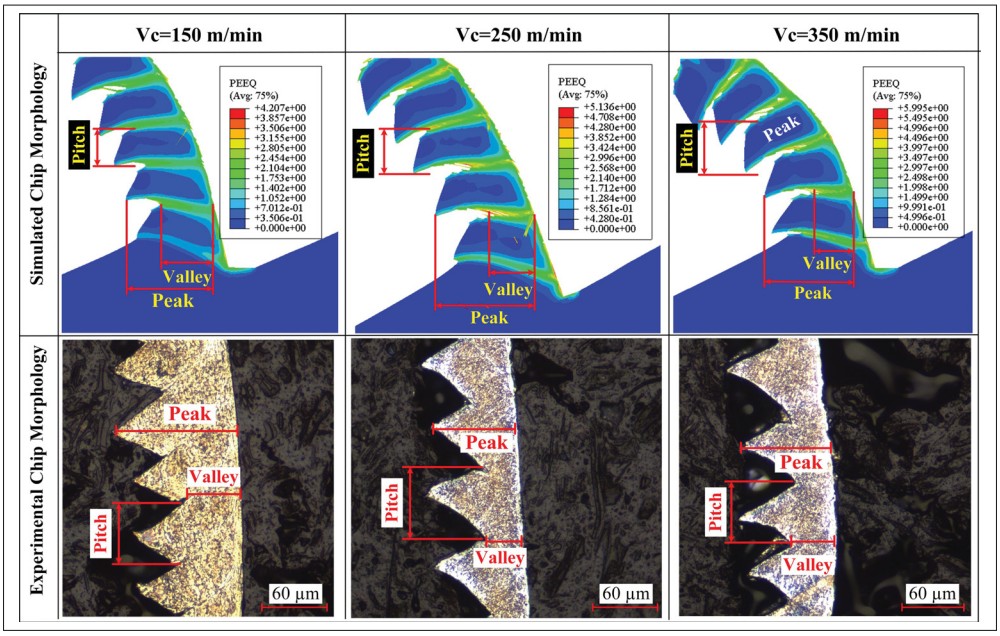

Figure 3.10 Simulated and experimentally obtained chip geometrical characteristics against various cutting speeds

zone (i.e., the obtained chip's mid spot) within a single cutting cycle was chosen to evaluate the simulated and experimentally accomplished chip, as indicated in Fig. 3.10 and 3.11. From these figures, it can be stated that the morphological characteristics of the simulated and experimentally acquired chip are consistent. Further detailed elucidation, statistical outcomes with various measurement places, and averaging of the serrated chip features (i.e., pitch, peak, and valley)

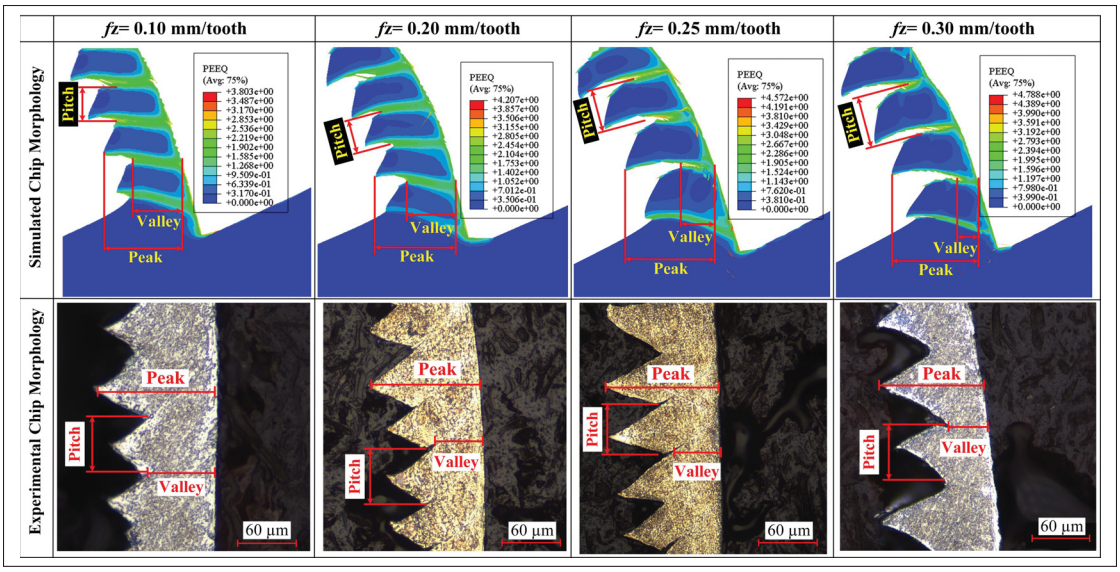

Figure 3.11 Simulated and experimentally obtained chip geometrical characteristics comparison against various feed rates

are demonstrated in Fig. 3.12. After careful observation and analysis, the absolute relative error between experimental and simulated obtained chip's features was found in the range of 5.2-14.36%, designating that established model for HSM of Ti-6Al-4V is reliable and can be implemented for grain size and microhardness prediction.

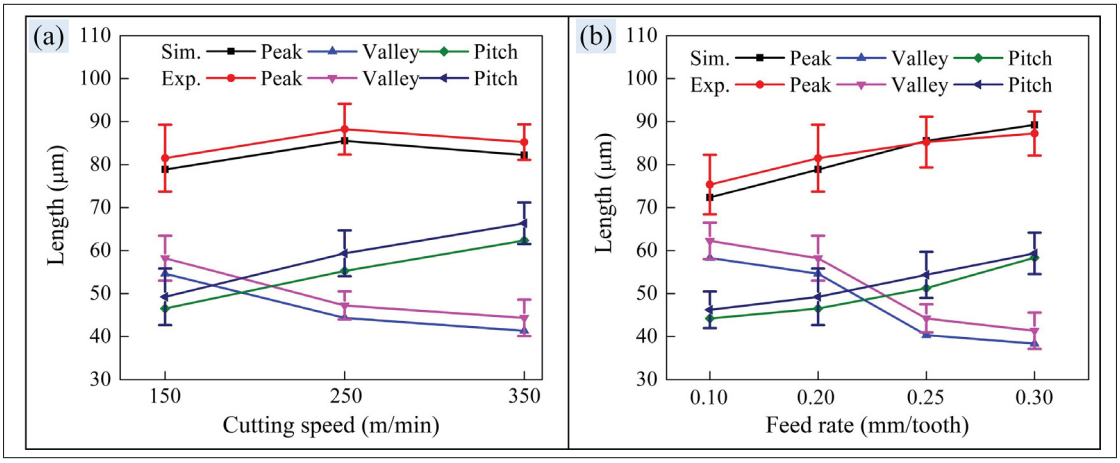

Figure 3.12 Chip morphology comparison: (a) cutting speed, (b) feed rate

3.6 Results and discussions

3.6.1 Grain size and microhardness prediction

The mutual maneuver of high strain, strain rate, and temperature can persuade inhomogeneous plastic deformation (PD) and change in volume fraction, which is considered an essential aspect of grain refinement. Simulation outcomes of equivalent strain (ES), strain rate (SR), and temperature at a cutting speed (i.e., 150, 250, and 350 m/min) are indicated in Fig. 3.13.

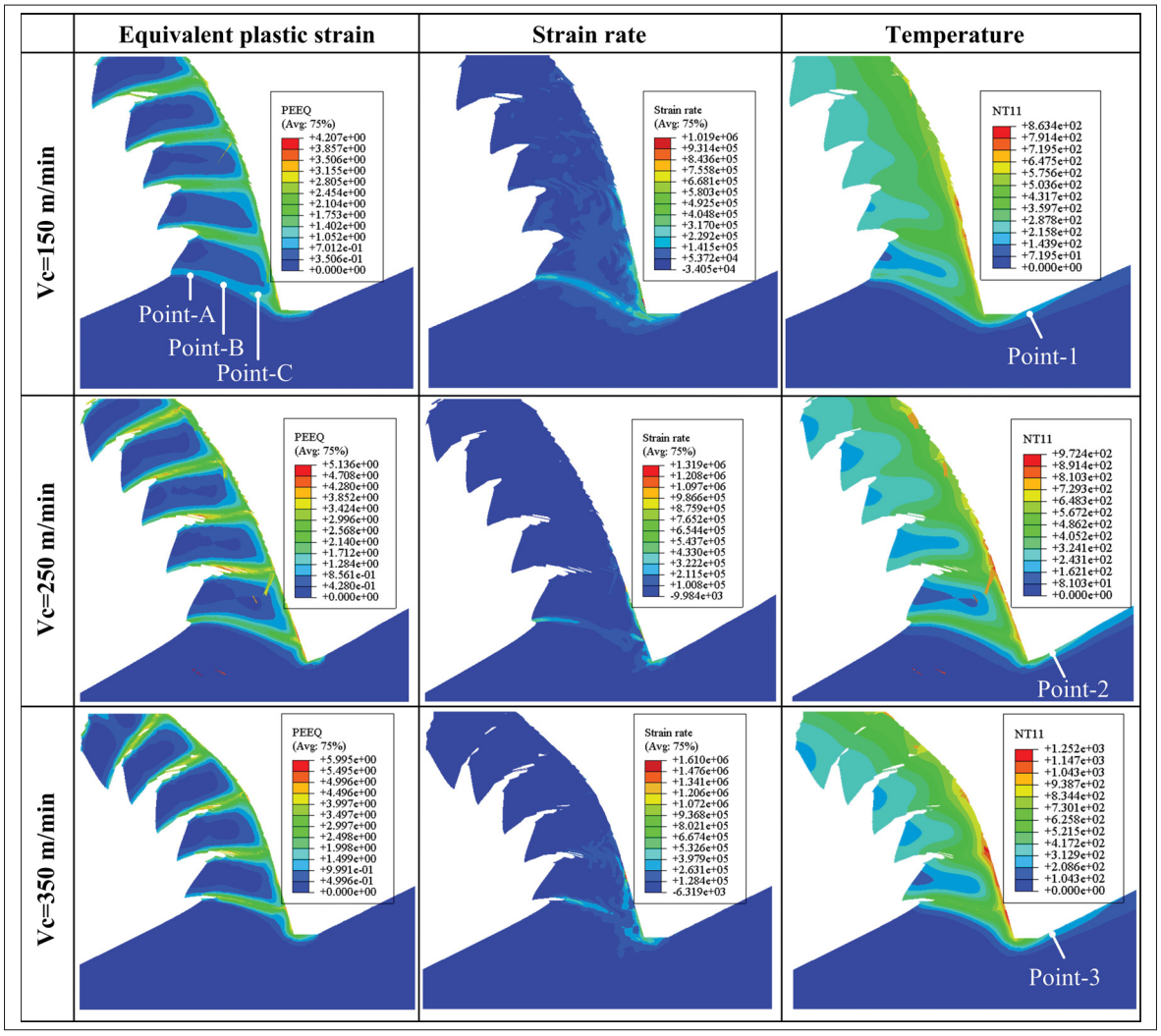

Figure 3.13 Contour plot of equivalent plastic strain, strain rate, and temperature against various cutting speeds

To examine the impact of cutting speeds on ES, SR, and temperature, three points (i.e., points A, B, and C) were chosen within the ASB, as demonstrated in Fig. 3.13, and then averaged. The obtained results are listed in Table 3.6. ES, SR, and temperature fields were all found to increase with the cutting speeds. Furthermore, the silhouette also indicates that ES and SR fields are incredibly high. Generally, during the machining process, an equivalent strain and strain rate of about 0.5-2 μm and $10^3 - 10^5 s^{-1}$ or above are considered extreme conditions for microstructural evolution (Xu *et al.*, 2020). Similarly, higher temperature is another prerequisite for dynamic recrystallization initiation. It can be noted that the peak temperature within the primary deformation zones was about 633 °C, 697 °C, and 763 °C against 150, 250, and 350 m/min, respectively, while the temperature in the secondary deformation zones was much higher, reaching about 1250 °C. As explained above, this phenomenon occurs due to substantial material removal during milling, and elevated temperatures play a dominant role in facilitating material recovery and recrystallization. DRX and grain size evolution kinetic equations linked with

Table 3.6 Average values of equivalent strain, strain rate, and temperature within the ASB of serrated chip

Cutting Speed V_c (m/min)	Equivalent Strain	Equivalent Strain Rate (/s)	Temperature (°C)
150	3.25	8.97×10^5	633.79
250	4.53	1.052×10^6	697.34
350	4.96	1.209×10^6	763.72

Abaqus/Explicit software indicate that significant microstructural alterations occur in the cutting deformation zones. The effect of cutting speeds on grain variations in the milled exaggerated zones has been highlighted in Fig. 3.14. As indicated, grains within the ASB of the serrated chip diminish from about 1.16 μm to 0.68 μm, decreasing by 41.38 % as the speed rises from 150 to 350 m/min. This result could be explained by the fact that Ti-6Al-4V was subjected to high strain, strain rate, and temperatures for a relatively extended time throughout the milling process. For a detailed explanation of how grains alter within the cutting deformation zones, two paths (i.e., Path-1 and 2) were generated within the ASB and from the milled surfaces, and the obtained outcomes were demonstrated in Fig. 3.15. As plotted in Fig. 3.15(a), grains within the ASB of

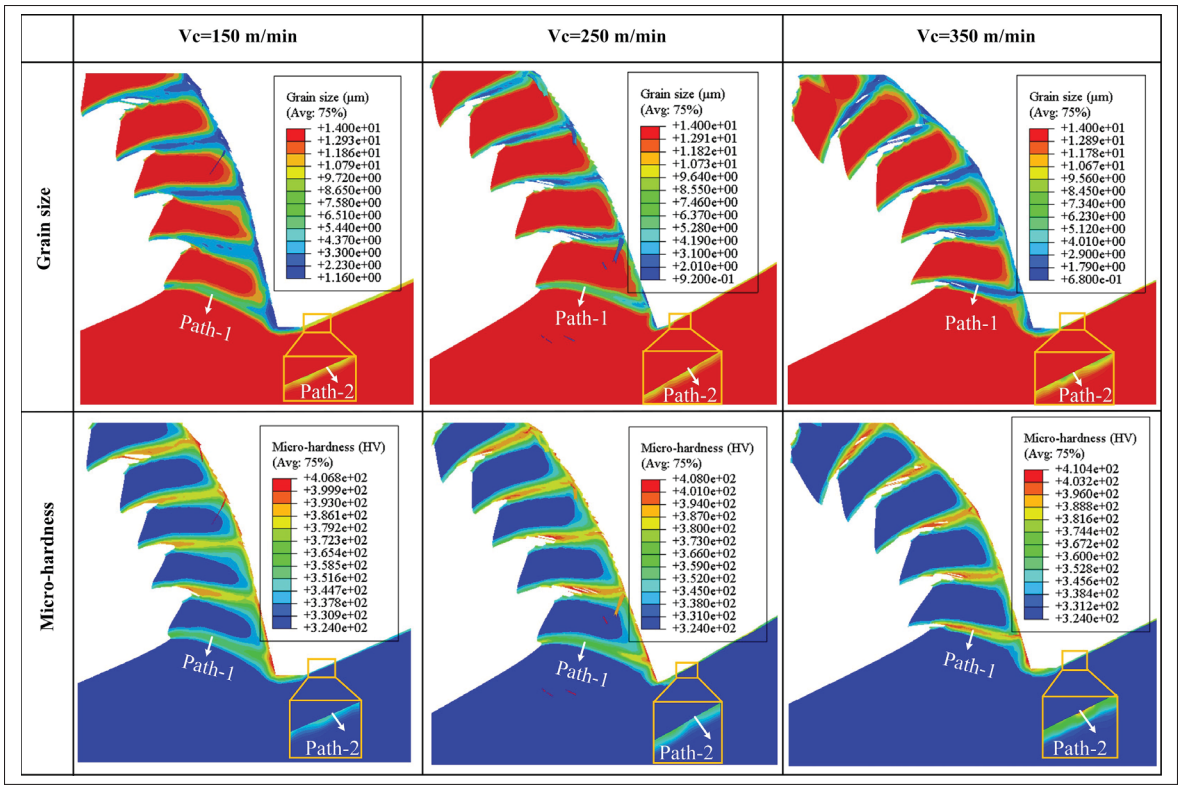

Figure 3.14 Silhouette map of grain size and microhardness distribution against various cutting speeds

serrated chip significantly alter along the designated path (i.e., Path-1) since the narrow shear band experiences extremely high strain rates, increased temperature, and strain localization, which can induce SPD, twining, and dislocation motion. As a result, grain refinement in these regions is becoming more prominent. Comparatively, as depicted in Fig. 3.15(b), the alteration of milled surface grains (i.e., along Path-2) is about two times slighter than the ASB of the serrated chip. Since milled surface temperature, which is considered key for the DRX, is much lower than the primary and secondary deformation zones. Hence, the grains were less refined compared to those in the ASB. Also, from silhouette milled surface and subsurface, exaggerated zone intensity is exceptionally narrow, ranging from 1 to 3 μm. Therefore, these overelaborated zones were further differentiated into various sub-zones: the topmost machined surface (where the grain size is around about 8.43, 7.82, and 7.06 μm against the cutting speeds of 150, 250, and 350 m/min, respectively), inter-zone (where grains distort to a certain degree resulting in

average grain size of roughly 10.27, 10.16, and 9.96 μm), and the bulk zone, which remains undeformed. The prediction of such a refined grain within the milled surface can positively impact the functional amalgamation of ductility and strength (Geng *et al.*, 2024). Furthermore, these characteristics can also improve the milled surface mechanical properties, especially the wear resistance of machined implants. The influence of grain refinement on microhardness, which is believed to coincide with the material's strength, is also explored in this investigation. Based on the H-P equation, the hardness of cutting deformation zones is associated with a new grain. As specified in Fig. 3.15(c), the microhardness of ASB and milled surface intensifies with cutting speed. It can also be observed from the mapping in Fig. 3.14 that the hardness of the cutting deformation zones is more significant than that of the bulk region. This hardness gradient indicates that the material experiences inhomogeneous plastic deformation during HSM. The

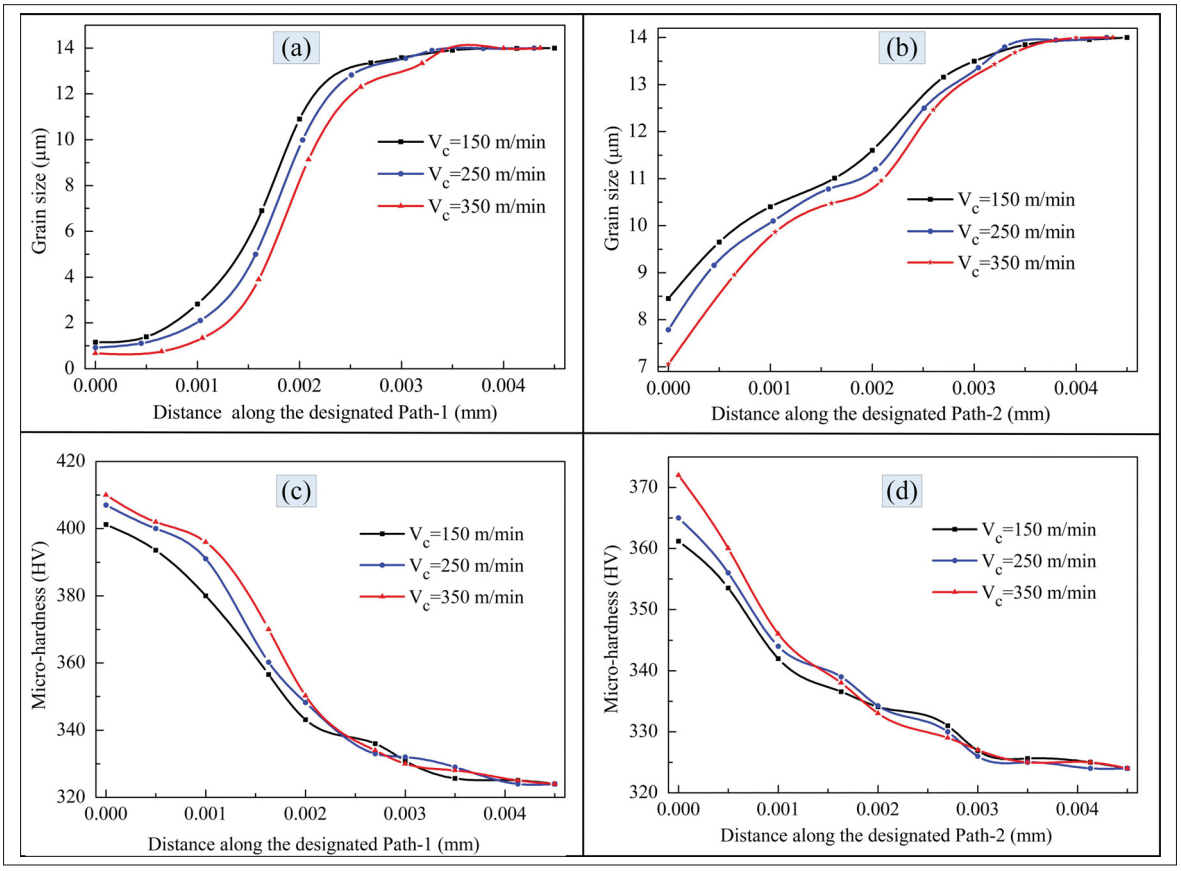

Figure 3.15 Grain size and microhardness distribution within the cutting deformation zones

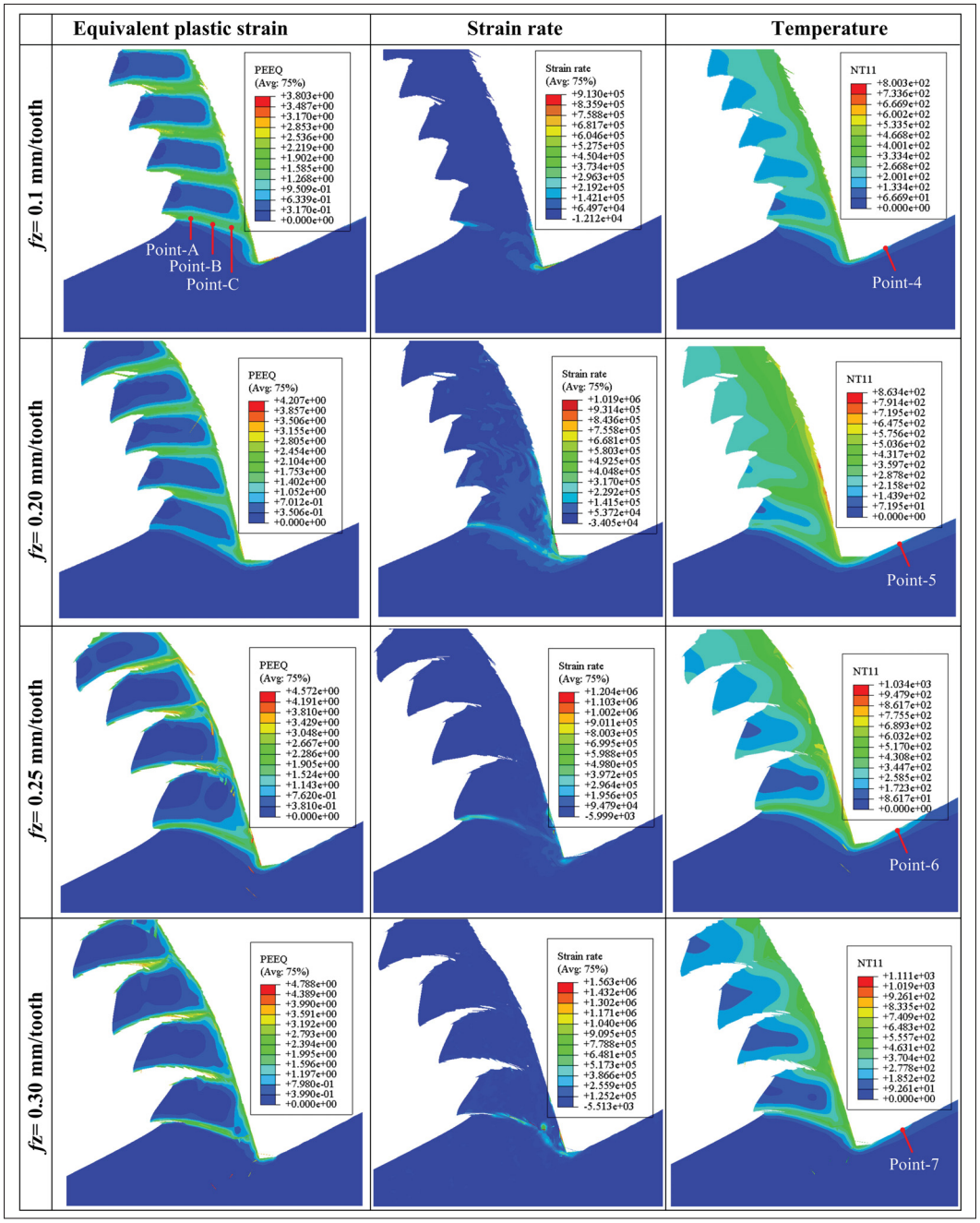

Figure 3.16 Contour plot of equivalent plastic strain, strain rate, and temperature against various feed rates

results also designated that when the cutting speed was raised from 150 to 350 m/min, ASB's hardness fluctuated from about 401.06 to 409.63 HV, which is much higher than the milled surface hardness (361.82-372.93 HV). As mentioned above, the grain refinement within the

ASB is much more evident than the milled part; hence, the hardness of ASB is more significant compared to milled surface. Additionally, when the material is removed during the milling process, the hardness is influenced by the material's microstructure and work hardening. Hence, the hardness significantly improves after milling. Analogous to the results indicated in Fig. 3.13 and 3.14, the impact of different feed rates on ES, SR, temperature, grain size, and microhardness was also analyzed. As indicated in Fig. 3.16, ES, SR, and temperature synchronously increase with feed rates. From Fig. 3.16, the peak values of ES, SR, and temperature within the ASB of the serrated chip at a higher feed rate (i.e., 0.30 mm/tooth) reach about 4.16, 1.319 ×106 s-1, and 746.96 °C, respectively, which is slightly lower than the cutting speeds. Nevertheless, these values are adequate for DRX initiation.

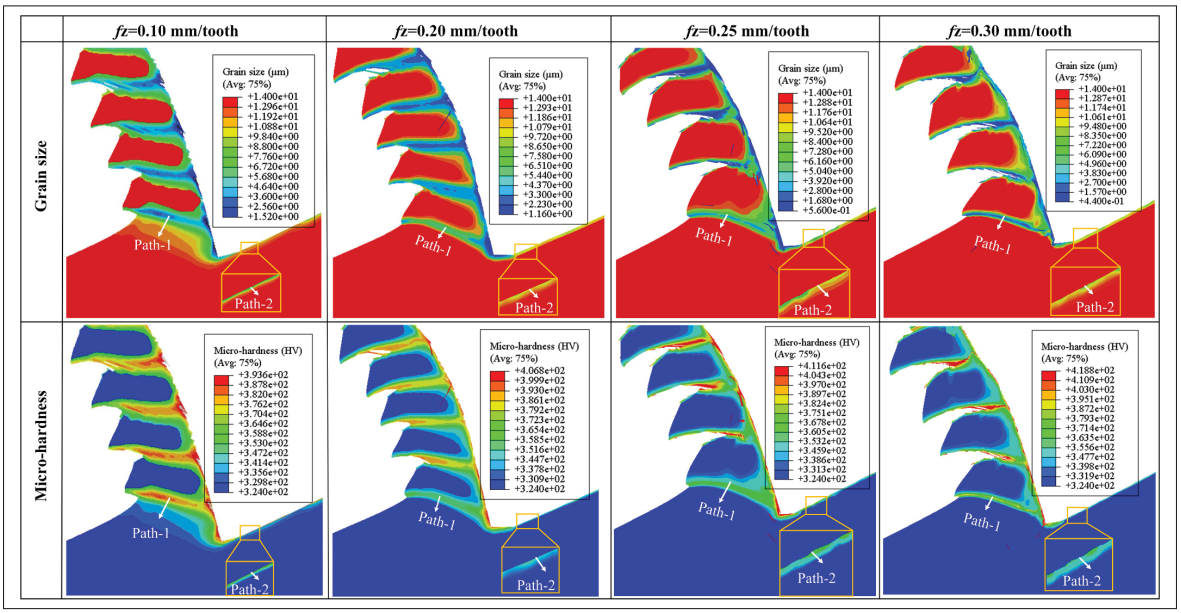

Figure 3.17 Silhouette map of grain size and micro-hardness distribution against various feed rates

The grain size reduces gradually as the feed rate intensifies (Fig. 3.17). The expected grain propagation in ASB and the milled surface is dependable on the heat effect zones characterized by high temperature and SPD. Interestingly, as demonstrated in Fig. 3.18, although the grains within ASB of serrated chip and topmost milled surface show similar trends (i.e., decreases with the increased feed rates) to the cutting speeds; however, within the inter-zone, it shows

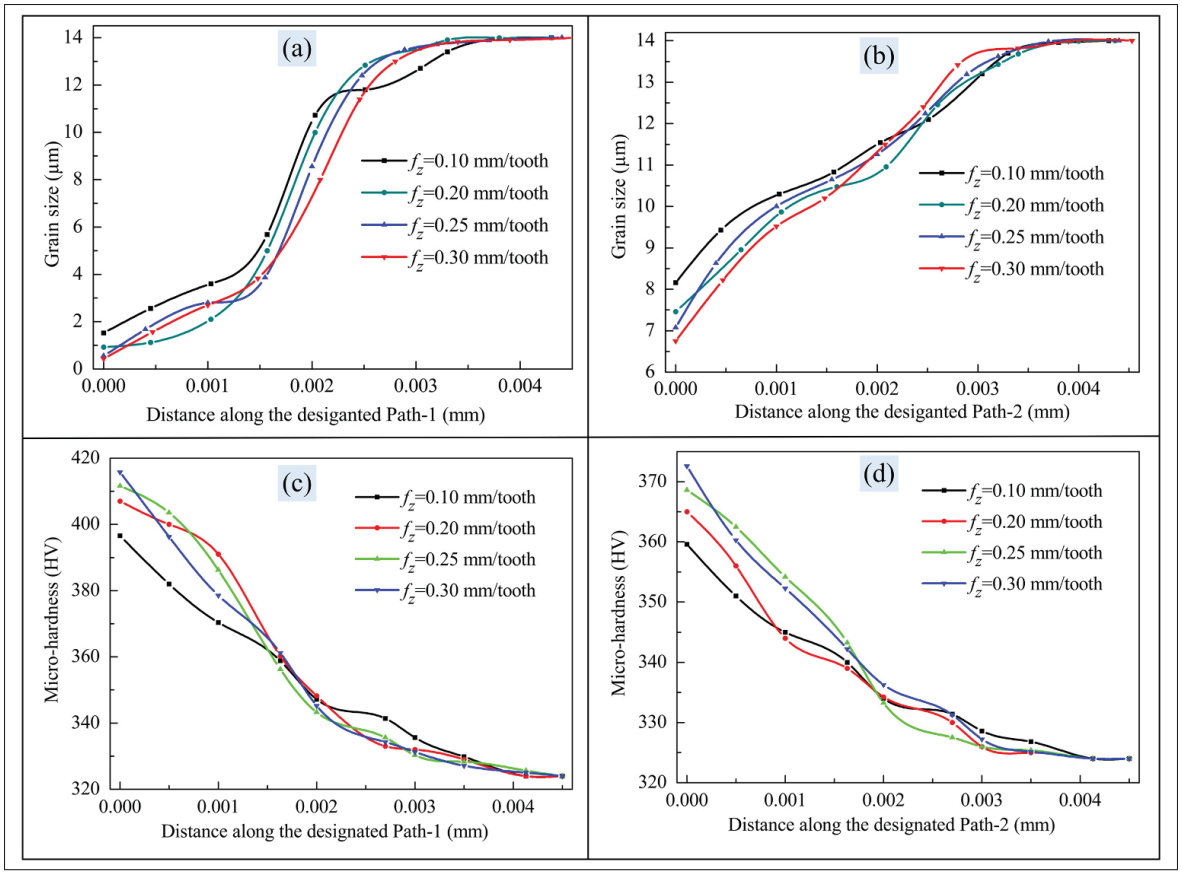

Figure 3.18 Grain size and microhardness distribution within the cutting deformation zones against various feed rates

mixed behavior. This could be described as, for low feed rates, the material around the cutting tool becomes softer, requiring more mechanical work; consequently, more dwindling grains are produced. Similarly, the effect of various feed rates on hardness distribution along the specified paths in Fig. 3.17 was depicted in Fig. 3.18(c-d). As revealed, feed rates also influence the hardness of the cutting deformation zones. The immediate decline in microhardness in intense narrow sections indicates an abrupt gradient for increased temperature and strain rate intensity existed. In addition, the comparison values also confirmed that the ASB's hardness is higher than the machined surface and gradually increases as the feed rates rise from 0.10 mm/tooth to 0.30 mm/tooth.

3.6.2 Effect of thermo-mechanical loads on grain size evolution during chip formation stages

This section analyzed the effect of the different stages of serrated chip formation – namely damage initiation, propagation, and catastrophic failure - on equivalent plastic strain, temperature, and grain size. As shown in Fig. 3.19(a1), shear damage initially occurs simultaneously on the tool-workpiece and the workpiece-free surface and penetrates deep into the primary shear zone (Fig. 3.19(a2)). Eventually, a localized pinch in material flow stress triggers the formation of a serrated chip, culminating in catastrophic failure (Fig. 3.19(a3)). This devastating failure occurs when thermal softening offsets the work-hardening induced by high strain and temperature (Li *et al.*, 2019c; Wang *et al.*, 2016a). Furthermore, as shown in section 4.1, during the serrated chip formation, both thermal and mechanical loads exhibit a cyclical fluctuation, significantly influencing the plastic deformation condition and thereby altering the microstructure status. Therefore, to deepen the understanding of how the serrated chip formation stimulus the plastic strain, temperature, and the resultant grain size, analysis was focused on the stages portraying the formation of one chip segment. To do that, a path was drawn within the ASB during three different stages of a single chip segmentation, as shown in Fig. 3.19(a1-a3), and the obtained results were presented in Fig. 3.19(b1-d3). As indicated, during stage-1(i.e., the damage initiation), when the cutting speed increased from 150 to 350 m/min, the plastic strain within the ASB enhanced from 0.58 to 1.2 (Fig. 3.19(b1)) and the temperature was increased from 413.72 to 481.10 °C (Fig. 3.19(c1)). However, no apparent changes were observed in the grain refinement (Fig. 3.19(d1)). The absence of considerable changes in grain refinement indicates that the primary factor influencing these alterations lies in the strain rate sensitivity of the material (Zhang *et al.*, 2023).

As the damage progressed to stage-2 of serrated chip formation, the plastic strain and temperature increased continuously, eventually reaching 1.43 and 1.95 (Fig. 3.19(b2)) and 482.67 and 515.28 °C (Fig. 3.19(c2)), respectively, and the grain size was reduced to 9.97 and 8.37 μm (Fig. 3.19(d2)). This development underlines the continued influence of strain rate sensitivity on material behavior under high-cutting conditions. On the one hand, the increased plastic

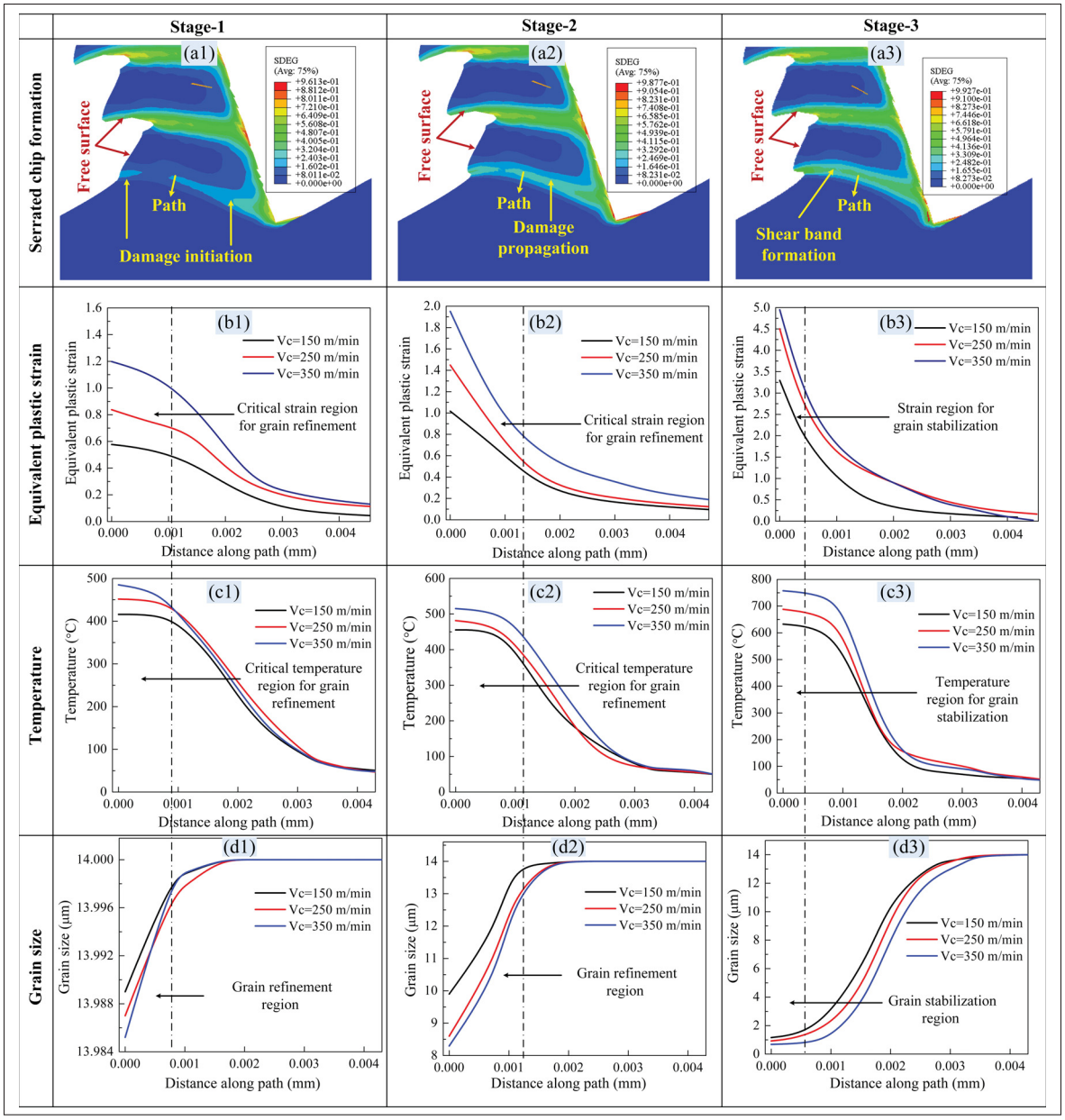

Figure 3.19 Effect of cutting speeds on the equivalent plastic strain, temperature, and grain size on the stages portraying the formation of a single chip segment

strain and temperature indicate an increased deformation process within the ASB driven by the increased strain rate. On the other hand, the simultaneous reduction in grain size suggests that the DRX process becomes more pronounced with increasing deformation and thermal effects. Finally, during catastrophic failure (i.e., stage-3) of a single segment, both the equivalent

plastic strain and temperature reach 4.61 and 4.94 (Fig. 3.19(d1)) and 633.79 and 763.53°C (Fig. 3.19(d2)), respectively, with a concomitant decrease in grain size to approximately 1.2 and 0.68 μm (Fig. 3.19(d3)). Interestingly, the grains progressively stabilize in this stage, indicating a balance between deformation-induced grain refining and the subsequent static recrystallization process. The considerable increase in plastic strain and temperature emphasizes the intense deformation and thermal conditions encountered during the catastrophic failure event, illustrating the convergence of strain rate-induced effects, which leads to more grain refinement.

3.6.3 Effect of increased Strain and Temperature on grain size evolution

This section examined the impact of increased strain and temperature on grain size evolution. As shown in Fig. 3.20, grain refinement is most prominent in regions where higher strain and temperature are induced (i.e., primary and secondary deformation zones and at the tool-workpiece interface).

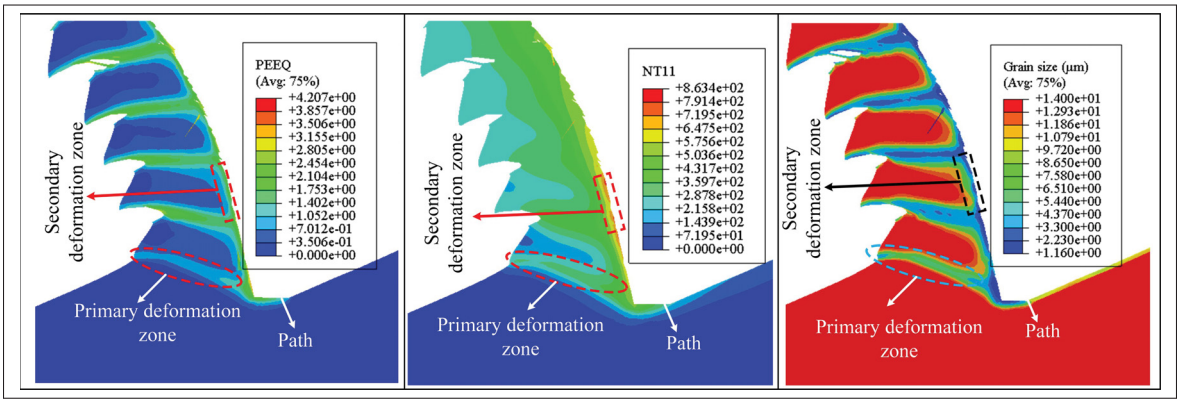

Figure 3.20 Mapping relationship between equivalent strain, temperature, and grain size

The grain is stumbling and distorting in these regions because of shearing and squeezing phenomena provoked by inhomogeneous plastic deformation during milling. To quantitatively examine the effect of increased strain and temperature on grain distribution within the milled subsurface, paths were generated near the tool-workpiece, and the obtained results were plotted in Fig. 3.21. As labeled, the grain started to shrink promptly when the strain and temperature

approaches the critical values of about 1.1, and 450 °C. Once the strain and temperature increase up to 3.5 and 525 °C, the grains gradually stabilize, resulting in stability between grain nucleation and progression, which is significantly dependent on deformation condition. Furthermore, from these plots, it can also be concluded that increased strain and temperature can lead to dislocation accumulations and enhance atomic mobility and nucleation, facilitating recrystallization and grain refinement.

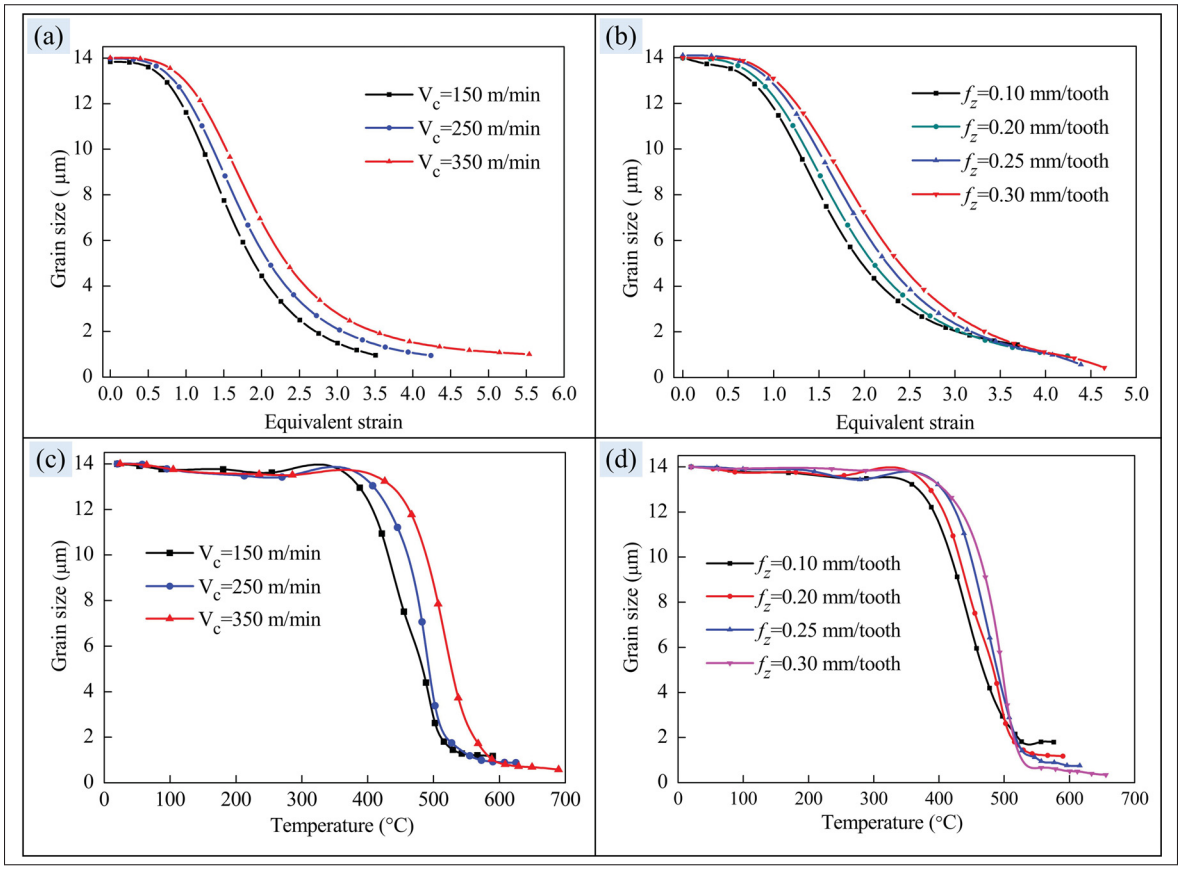

Figure 3.21 Grain size evolution with increased strain and temperature

3.6.4 Experimental validation of Grain size and microhardness

In this section, experimental findings for grain size and microhardness are provided to demonstrate the efficiency of the FE model. Although, as shown above, the removed chip offers valuable insights regarding the machining operation, the scientific research community focuses on

machined surface integrity. Hence, only grains and microhardness of the cutting surface layer are displayed. EBSD analysis was conducted to analyze the grain refinement in machined affected regions. As indicated in inverse pole (IP) Y-scheme figures (Fig. 3.22 (a-c)), the orientations and structures of the grains were affected by cutting speeds. At the cutting speed of 150 m/min (Fig. 3.22(a)), more elongated grains were observed in the milled affected zones. However, when the cutting speed increased further, elongated grains were reduced in size and became more equiaxed forms (Fig. 3.22 (b-c)). Furthermore, the observed IP figures also indicated that the HSM deformation process was mainly connected with Ti-6Al-4V hexagonal-packed triggered basal slip systems. As mentioned above, a rise in temperature and a relatively high strain rate during HSM can increase dislocation density and produce a subsequent cellular structure inside the material microstructures. This step is followed by the DRX phenomenon, which results in grain refinement within the material microstructure near the milled surface.

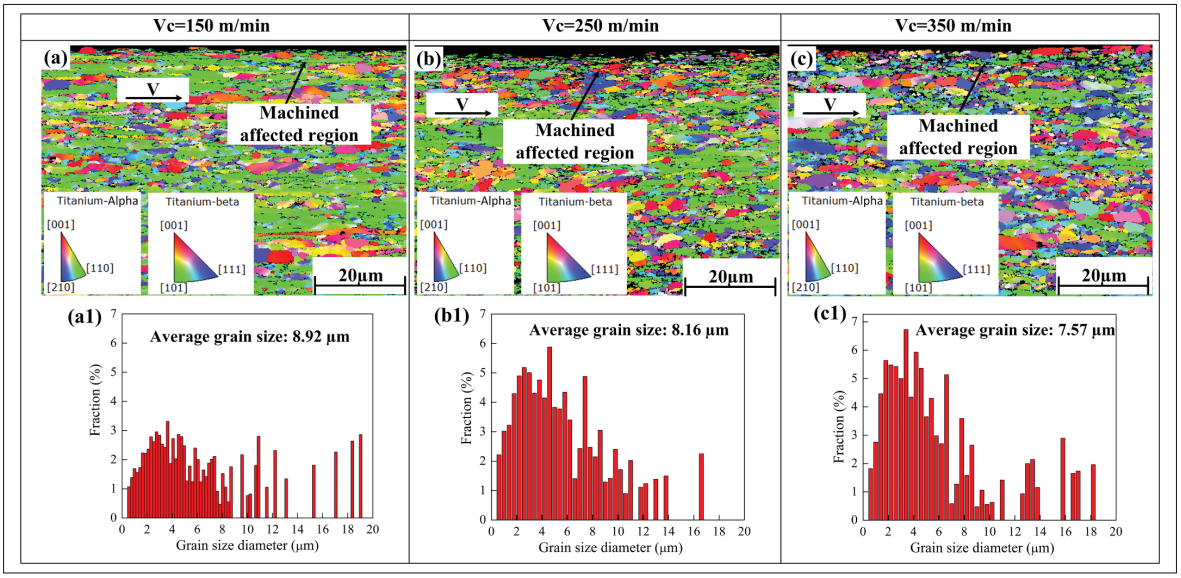

Figure 3.22 EBSD results of the machined surface layer: (a-c) inverse pole (IP) figures and (a1-c1) grain size distribution

The results in Fig. 3.22 (a1-c1) illustrate the average grain size within the cutting surface layer resulting from cutting speeds of 150, 250, and 350 m/min, respectively. Notably, the average grain sizes within the machined subsurface were 8.92, 8.16, and 7.57 μm for the corresponding cutting speeds. These measurements are closely aligned with the results obtained from the FE

model, which yielded 8.43, 7.82, and 7.06 μm grain sizes for cutting speeds of 150, 250, and 350 m/min, respectively. Moreover, when contrasted with the EBSD-derived average grain size of 14 μm for the Ti-6Al-4V matrix, it becomes evident that the machined subsurface grain size of the Ti-6Al-4V alloy undergoes refinement, leading to a reduction in size. In alignment with the outcomes delineated in Fig. 3.22, the influence of varying feed rates on grain size is similarly elucidated in Fig. 3.23. As depicted in the corresponding IP figures (Fig. 3.23(a-c)), the grains within the cutting surface layer exhibit discernible alterations in response to the feed rates. Notably, when contrasted with the matrix, the machined subsurface reveals a prevalence of more refined grains. Specifically, the average grain size within the cutting surface layer for feed rates of 0.10, 0.25, and 0.30 mm/tooth was determined to be 9.87, 7.82, and 7.67 μm, respectively, findings which exhibit congruence with the simulation outcomes (i.e., 8.16, 7.08, and 6.75 μm, correspondingly). Similarly, the simulated and experimental microhardness for

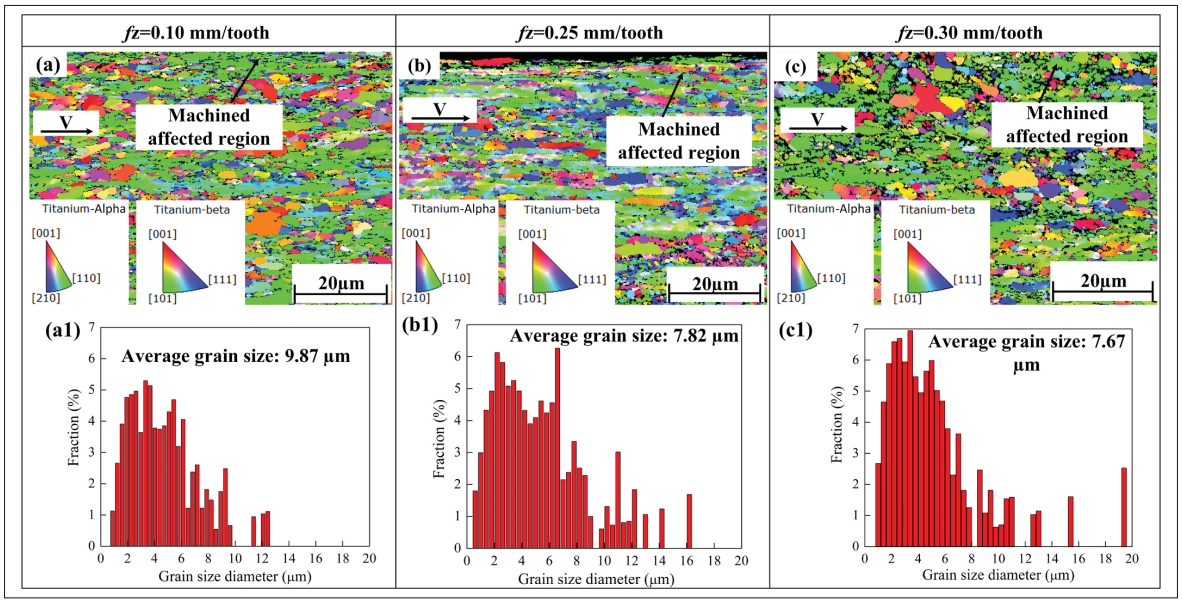

Figure 3.23 EBSD results of the machined surface layer: (a-c) inverse pole (IP) figures and (a1-c1) grain size distribution

machined surfaces were also compared. It is important to note that due to uncut chip thickness variation, the microhardness of the cutting surfaces was recorded at various locations for both experiments and simulation and then averaged, and the obtained results are presented in Fig. 3.24.

As displayed, the microhardness of the milled surfaces improves with increasing cutting speed, and feed rates, which correlates to the tiny grains in the milled affected zone, as seen in Fig. 3.22 and 3.23. However, the impacted layer thickness in the simulation at various milling input parameters deviates slightly from the actual results. Notably, the simulated values exhibit a slight predominance over the experimental counterparts at a 150 m/min cutting speed. However, as the cutting speed intensifies, the measured hardness supersedes the predicted values. Likewise,

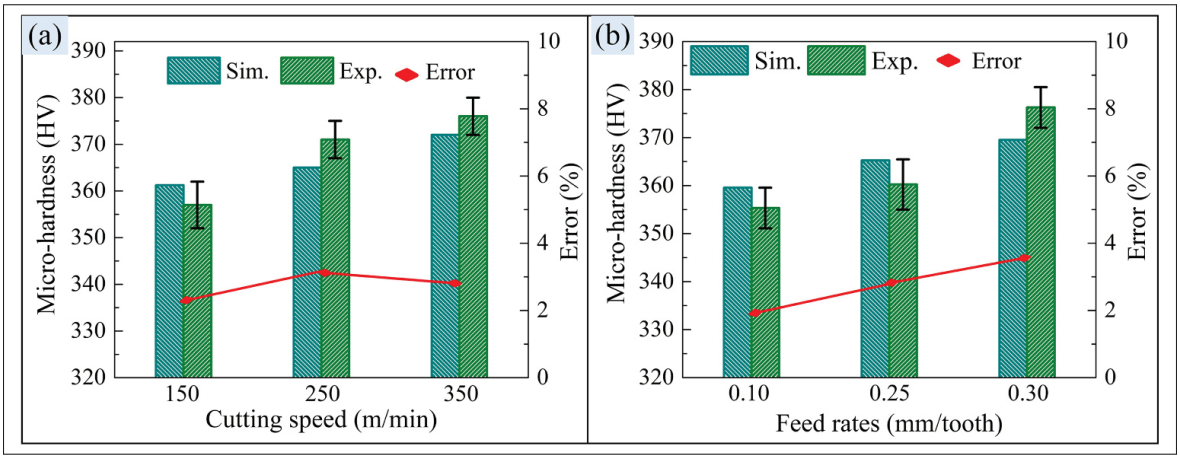

Figure 3.24 Machined surface microhardness comparison: (a) cutting speeds and (b) feed rates

concerning feed rates of 0.10 and 0.25 mm/tooth, the simulated microhardness prevails over the experimental values on the uppermost machined surfaces. Nonetheless, with a subsequent augmentation in feed rates (i.e., 0.30 mm/tooth), the measured hardness surpasses the simulated values. The extra grain boundaries within small grain impede dislocation movement, making it more difficult for dislocations to move, resulting in higher microhardness. Although, due to work hardening impact, there is some discrepancy between the simulated and experimental results which is not considered in the H-P equation. Nonetheless, there was excellent stability between observed and simulated values, with an absolute relative error of less than 3.78%.

3.7 Conclusions

In the current study, a multiscale FE model for milling of Ti-6Al-4V was introduced to explore grain refinement due to dynamic recrystallization and microhardness variation in the cutting deformation zones. At first, the established model regarding CFs, temperature, and chip morphology was verified experimentally. Afterward, Z-H and H-P equations were incorporated into a user-defined subroutine for grain size and microhardness prediction within the cutting deformation zones. Based on the obtained results, the following conclusions can be drawn:

1. The simulated and measured CFs component, temperature, and chip geometrical features were consistent, with a relative error of less than 14.2 %, 13.7%, and 14. 36%, respectively, indicating that the developed FE model can accurately predict the machining process of Ti-6Al-4V.
2. The simulation results demonstrate that grains within the ASB of the serrated chip became more refined compared to the milled surface. Inside the ASB, grain size diminished from 14 μm to 1.16, 0.92, and 0.68 μm, while in the milled surface, it reduced to 8.43, 7.76, and 7.06 μm, against the cutting speed of 150, 250, and 350 m/min, respectively. Similarly, the grain refinement at the topmost milled surface in terms of feed rate exhibited similar trends to cutting speed; however, within the inner deformation zones, a mixed behavior is observed.
3. The simulation results also indicated that the microhardness of the cutting deformation zones was highly improved. The ASB hardness was found to enhance from 324HV to 401.06, 405.3, and 409.63 HV, while the milled surface hardness increased to 361.82, 365.05, and 372.93 HV against the cutting speed of 150, 250, and 350 m/min, respectively. Similarly, the hardness of ASB and the milled surface was gradually improved with feed rates.
4. The effect of thermo-mechanical loads on chip formation stages reveals that no apparent changes were observed in the grain refinement during the initial stage. However, the grains were found to start shrinking as the strain and temperature approached the critical values during the damage propagation stages, and once the strain and temperature exceeded the critical values, the grains gradually stabilized due to nucleation.

5. The EBSD analysis indicated that compared to as-receiver material microstructures, the machined subsurface grains were elongated, reduced in size, and became more equiaxed forms as the cutting speed increased. The experimental average grain size in the milled subsurface were 8.92, 8.16, and 7.57 μm against cutting speeds of 150, 250, and 350 m/min, respectively, which demonstrate a close alignment with the results obtained from the FE model, which yielded grain sizes of 8.43, 7.82, and 7.06 μm respectively. Similar results were also obtained when the feed rates were enhanced from 0.10 to 0.30 mm/tooth.
6. It is also observed that the hardness of the milled surface was highly improved and had an inverse relation to grain size. The simulated microhardness at the topmost milled surface was in reasonably good agreement with the experimentally obtained microhardness, with an absolute relative error of less than 3.78% for all the milling input parameters, and was found to increase with both the cutting speeds and feed rates.

CHAPTER 4

THERMO-METALLO-MECHANICAL BASED PHASE TRANSFORMATION MODELING FOR HIGH-SPEED MILLING OF TI-6AL-4V THROUGH STRESS-STRAIN AND TEMPERATURE EFFECTS

Irfan Ullah [1] , Esther T. Akinlabi[2] , Victor Songmene [1]

[1] Department of Mechanical Engineering, , École de Technologie Supérieure, 1100 Notre-Dame Ouest, Montréal, Québec, Canada H3C 1K3
[2] Department of Mechanical and Construction Engineering, Northumbria University, Newcastle Upon Tyne NE1 8ST, United Kingdom

This article is published in *"Journal of Materials Research and Technology",* Volume 30, March 2024, Pages 894–909 https://doi.org/10.1016/j.jmrt.2024.03.096

Abstract

The optimization of machining parameters, tool longevity, and surface quality in High-Speed Milling (HSM) of Ti–6Al–4V relies immensely on understanding the local phase transformation. This study endeavors to build a Finite Element (FE) model capable of forecasting phase alterations during the rapid thermal fluctuations intrinsic to Ti–6Al–4V machining. Dynamic phase transformation models were initially introduced to capture rapid heating and cooling phenomena. Using a user-defined subroutine, the phase transitions predictive models were integrated into the HSM simulation within Abaqus/Explicit. Simulation outcomes unveiled phase transitions primarily occurring within the serrated chip and at the tool-workpiece interface. Notably, during rapid heating, when the cutting speed increased to 350 m/min, the β-phase volume fraction surged from 7.5 to 96.38%. A similar trend was observed with feed rate adjustments (i.e., 0.15–0.25 mm/tooth), where β-phase increased from 7.5 to 67.84%. Rapid cooling facilitated the reversion of the transformed β-phase back into the α'-phase. Finally, some advanced characterization techniques were employed to validate the developed thermo-metallomechanical coupled FE model for phase transformation. The simulation results verified by the experimental data promotes a better understanding of phase alteration mechanisms and microstructural evolution in HSM of Ti–6Al–4V. The current research is also beneficial for crucial insights into optimizing the machining conditions and their impact on tool-material

interactions and surface integrity.

Keywords: Finite element method, High-speed milling, Material characterization, Phase transformation, Ti–6Al–4V

4.1 Introduction

Ti-6Al-4V, a dual-phase alloy, has been broadly devoted in various sectors, including biomedical, aerospace, die, and mold, due to its enhanced mechanical strength and high corrosion resistance at elevated thermal conditions (Sun, Shan, Zong, Dong & Jing, 2021; Ullah *et al.*, 2021a). However, the machining of Ti-6Al-4V presents several challenges due to its low thermal conductivity, high chemical reactivity, and the tendency for serrated chip production (Che-Haron & Jawaid, 2005). These characteristics contribute to the appearance of complex behaviors during machining, such as increased temperatures, intense plastic deformation, alteration in grain structure, and phase transition. On the one hand, the heat and stresses triggered in the cutting deformation zones can lead to phase changes that have an unfavorable consequence on the surface integrity, which can cause the work hardening and lead to white layer formation. On the other hand, these thermo-mechanical loading histories have the potential to influence the stress state through phenomena such as thermal softening and thermal strains (Chen, Ren, Zhang, Cui & Li, 2013). Additionally, they can also impact the metallurgical conditions of material in accordance to the phase transformation kinetics. Previous research has repeatedly mentioned the occurrence of phase transformation during the manufacturing of titanium and its alloys. However, it is difficult to characterize the phase transformation by standard methods, as the highly coupled behavior of thermal and mechanical loads and energy conversion in the HSM is a typically nonlinear problem. Numerous research studies have been undertaken to explore the occurrence of phase transformation of titanium in friction stir welding (Buffa, Ducato & Fratini, 2013), (Luo *et al.*, 2020)hot forging, and laser sintering processes (Ribamar *et al.*, 2016). However, while machining, the prediction of phase transformation becomes more challenging as it simultaneously involves multi-faceted stress, high strain rates, and thermal loading history. In the late 90s, (Bayoumi & Xie, 1995) realized the non-diffusional phase transition occurrence within the Adiabatic Shear Band

(ASB) of Ti-6Al-4V. However, contradictory results (i.e., no phase transformation in the shear band) were presented by (Velásquez *et al.*, 2007). By utilizing Transmission Electron Microscopy (TEM), (Wan *et al.*, 2012) analyzed the existence of martensitic phase transition during the rapid cooling process. However, the authors could not detect any β-phase in their observations. The absence of the β-phase was attributed to the post-cooling experiments, a stage during which the β-phase had converted back into the α-phase. Similarly, Wang et al. discovered a gradual variation in the microstructures between the matrix and the center of ASB during the machining of 30CrNi3MoV, which may have undergone a martensitic phase change. Although substantial experimental work regarding the phase transformation of titanium and its alloys is available in the published literature. Nevertheless, most of the published research is related to conventional heat treatment. Unlike conventional methods, the phase transformation during the machining process is generally associated with mechanical load, severe plastic deformation, and rapid heating and quenching process. In addition, no systematic investigation has been conducted to investigate how machining factors explicitly impact the phase transition in Ti-6Al-4V. Since predicting phase transition in mechanical machining is challenging to capture, the finite element (FE) model is becoming the most popular among researchers and industries for predicting phase transformation. (Wang, Liu, Yang & Mohsan, 2017b) developed an FE model for predicting the phase alteration during machining of Ti-Al-4V and concluded that cutting speeds significantly influence the rapid heating and cooling process. Using cutting temperature as the determining factor, (Zhang *et al.*, 2014) developed an FE model to predict phase changes in Ti-6Al-4V machining. Although the authors explored the phase transition behavior in machining deformation zones. However, their study relied on a steady-state phase transition assumption, which may inevitably lead to specific prediction errors. (Ramesh & Melkote, 2008) developed a 2D FE model for predicting the white layer during orthogonal cutting of AISI52100 steel and concluded that the white layer is directly related to residual stress formation. Similarly, contemplating stress-strain effects, (Li *et al.*, 2018a) elaborated on the phase transformation in the hard cutting of H13 steel. They anticipated the austenite volume fraction in the chip backsurface. Like the cutting process, (Bailey, Katinas & Shin, 2017) presented a three-dimensional FE model for predicting phase transformation during direct laser deposition. Considering various cooling

stages during wire laser additive manufacturing of Ti-6Al-4V, (Sun *et al.*, 2021) recently applied a density-based constitutional model for predicting phase transformation. They concluded that the increased temperature and decreased cooling rates significantly impact the formation process of α'-phase (with hexagonal structure). Taking Ni-Ti alloy as a research objective, (Kaynak, Manchiraju, Jawahir & Biermann, 2020) presented an FE model for phase transformation based on Helmholtz free energy. However, the authors only considered the layer subjected to twinnning for model validation. Although few researchers have observed and verified phase transformation as a fundamental mechanism during machining with complex stress states, a well-established theoretical model for high-stress-strain-assisted transformation mechanisms is still lacking in predicting phase transformations. In addition, the existing research also indicates that the relationship between increased thermal history and phase transformation is still scant in most studies. Hence, a multi-scale FE model is required for HSM to assess how stress-strain and thermal fields affect phase changes within the material. Consequently, limited research has focused on establishing an FE model for the milling process, particularly one that encompasses phase transitions for both phases. Hence, the current research objective is to investigate the phase transformation in two different stages during the HSM of Ti-6Al-4V. In the first stage (i.e., rapid heating), Avrami and Clapeyron-Clapeyron (C-C) type equations were implemented to predict α- to β-phase conversion by considering the stress-strain and temperature effects. While in stage two (i.e., rapid cooling), an empirical equation was implemented for the prediction of decomposed β-phase to α'-phase. The structured phase transitions model was implemented into the user-define VUSDFLD subroutine, employing a simplified FE model. Finally, experiments were conducted on the HSM to validate and correlate the established thermo-metallo-mechanical model.

4.2 Phase transformation kinetics

Since the temperature history, higher stresses and cooling rates induced by HSM have considerably influenced the phase transformation in Ti-6Al-4V. Therefore, to realize the effect of heating and rapid cooling process separately, two sub-models for HSM of Ti-6Al-4V were carried

out in the current investigation. Generally, temperature and increased stress are considered the fundamental aspects assisting the phase transformation of Ti-6Al-4V during the heating stage (Liu *et al.*, 2022a). In contrast, abrupt temperature change rates are the main factor preceding phase conversion in rapid cooling (Wang *et al.*, 2021). Detailed implementation of these two processes (i.e., rapid heating and cooling) are described below.

4.2.1 Rapid heating process

Generally, as the temperature ascends to the initial point of the transition temperature, the α-phase undergoes a gradual conversion to the β-phase until it reaches 100% at the transus temperature, which is approximately 982.5 °C. Moreover, in Ti-6Al-4V, conversion from α-phase to β-phase requires the inauguration of β-phase from α-matrix and growth of β-phase through diffusion. Hence, to describe the β-phase volume fraction and the machining-induced cutting temperature, the Avrami model was implemented (Avrami, 1940), which is expressed by Eq. (4.1).

$$V_\beta = 1 - \exp\left[A.\left(\frac{T - T_i}{T_c - T_i}\right)^D\right] \tag{4.1}$$

Where T, T_i, and T_c are the current deformation temperature, starting temperature for β-Ti transformation, and the complete phase transition temperature, respectively. Ti-6Al-4V starting and complete phase transition temperatures were set at 600 °C and 982.5 °C, respectively. Similarly, the terms A and D in Eq. (4.1) are the material constants that were set at -1.86 and 4.35, respectively (Wang *et al.*, 2017b; Pan *et al.*, 2016). Besides thermal history, the material phase transformation is also associated with the mechanical loads, which can categorically influence the formation of β-phase) . Since the β-phase) development within the α-matrix is a non-diffusion transformation process similar to martensite phase transformation (Ahmed & Rack, 1998). Therefore, owing to linked proceedings of thermo-mechanical loads on Ti-6Al-4V during HSM, the transition of α- to β-phase) is regarded as a martensite phase transformation. The quantitative relation between critical temperature and the critical stress as an external mechanical load of the initial phase transformation is expressed by employing the Clausius-Clapeyron type

equation (Liu, Mahmud, Kursawe & Nam, 2008), as described in Eq. (4.2).

$$\frac{d\sigma}{dT_i} = -\frac{\rho \Delta H_{tr}}{T_0 \varepsilon_t} \tag{4.2}$$

In Eq. (4.2), ρ represents the mass density, ΔH_{tr} is the latent heat of transformation from α-Ti to β-Ti (taken as 4.18 kJ/mol) (LaGrange, Campbell, Turchi & King, 2007), T_0 is the equilibrium temperature, and ε_t is the transformation strain in the uniaxial stress direction.

4.2.2 Rapid cooling process

As the cutting tool advances into the workpiece material, the removed chips and machined surface go into the rapid cooling stage, and the volume of β-phase decomposition could result in a martensite with a microstructure of α' (with hexagonal structure) or α'' (with orthorhombic structure) depending on the cooling rates. If the cooling rate is greater than or equal to 410°C/s and the temperature (T) is less than martensitic transformation temperature (T_{Ms}), the α' with martensite microstructure will form. In the current simulation, the critical cooling rate was set equal to 410 °C s^{-1}, notably slower than the cooling rates during the HSM (105 °C s^{-1}). Hence, it is assumed that α' will form. As a result, as described in Eq. (4.3), an empirical formula was adopted to estimate the volume fraction of α'-phase with an orthorhombic structure (Li *et al.*, 2018a; Deng, 2009).

$$V_{\alpha'} = (V_\beta) \cdot (1 - \exp(1 - X(T_{MS} - T))) \tag{4.3}$$

where V_β and T_{MS} demonstrate the amount of β-phase available for martensitic transformation following the heating process and the martensitic transformation temperature, respectively. X is the material constant, demonstrating the martensitic transition rate. The researchers have proven that approximately 10% of the β-phase remained unchanged, irrespective of the cooling rate, once the β-phase had undergone cooling to ambient temperature (Malinov, Guo, Sha & Wilson, 2001; Fan, Cheng, Yao, Yang & Egland, 2005). As a result, the value of X is set to 0.005.

4.2.3 Implementation of phase transformation models

The user-defined subroutine VUSDFLD was utilized to integrate rapid heating and cooling stages transition models into the simplified milling model. Fig 4.1 illustrates a flow chart showcasing the sequential stages of submodules within the computational system. The phase transitions

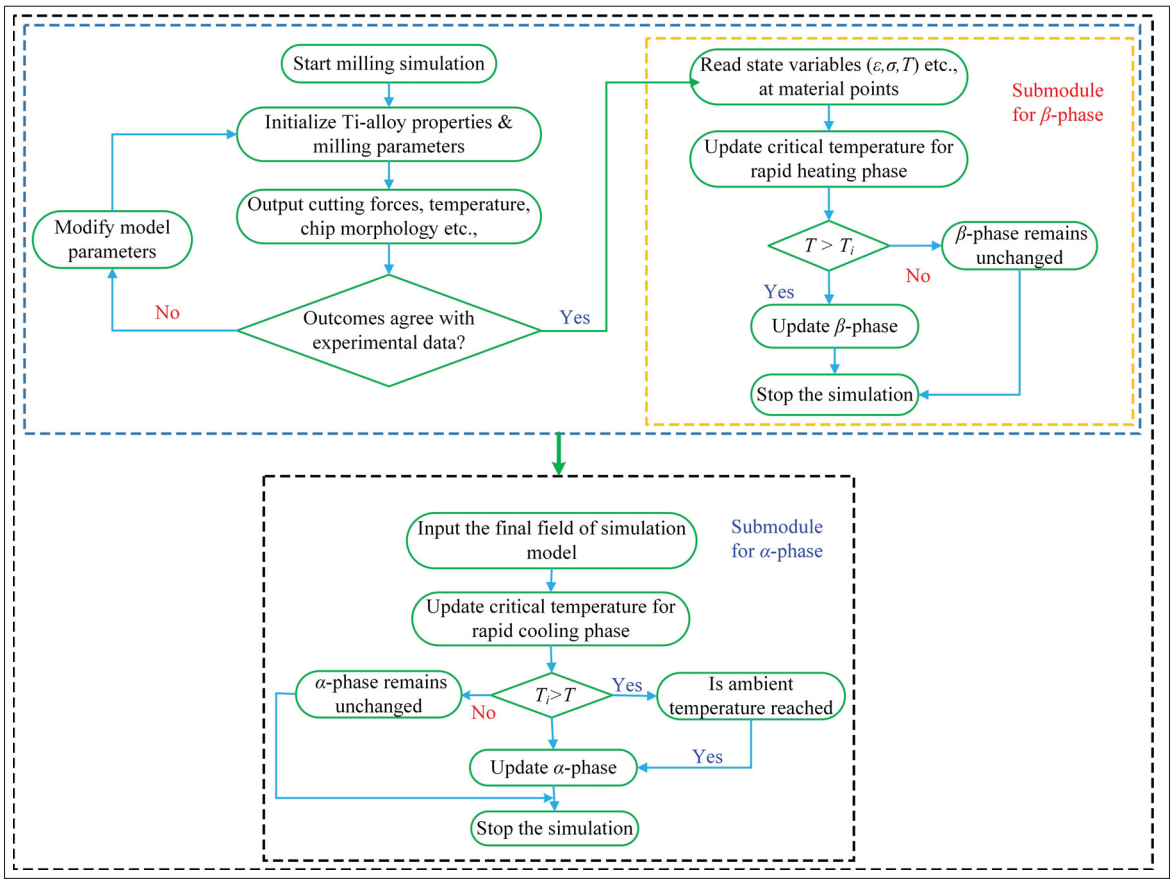

Figure 4.1 Flowchart for predicting the phase transition during rapid heating and cooling process

simulation was achieved by utilizing two user subroutines. The temperature stress-strain field distributions for Ti-6Al-4V were retrieved from a validated simulated model during the rapid heating process. Subsequently, the volume fraction of β-phase) was determined utilizing Eq. (4.1) and Eq. (4.2), respectively. Finally, the concluding field states from the heating stage were introduced to the cooling process model, and the volume percentage of α'-phase was determined using Eq. (4.3).

4.3 FE Model descritpion

4.3.1 Material constitutive model for Ti-6Al-4V

In this study, the Johnson-Cook (JC) constitutive material model (Eq. (4.4)) was employed to simulate the plastic behavior of Ti-6Al-4V. This model states the equivalent flow stress (σ) as a function of plastic strain (ε), strain rate ($\dot{\varepsilon}$), reference strain rate ($\dot{\varepsilon}_0$), and temperature (T) (Liu, Ni, Wang, Zhu & Zheng, 2023). Similarly, a J-C fracture model was utilized for the chip formation process, as described in Eq. (4.5).

$$\sigma = (A + B\varepsilon^n)\left[1 + C\ln\frac{\dot{\varepsilon}}{\dot{\varepsilon}_0}\right]\left[1 - \left(\frac{T - T_{\text{room}}}{T_{\text{melt}} - T_{\text{room}}}\right)^m\right] \tag{4.4}$$

$$\bar{\varepsilon}_f^{pl} = [d_1 + d_2\exp(-d_3)\eta]\left[1 + d_4\ln\left(\frac{\dot{\varepsilon}^{pl}}{\dot{\varepsilon}_0}\right)\right]\left(1 - d_5\hat{\theta}\right) \tag{4.5}$$

In Eq. (4.4), the terms A, B, C, n, and m are the initial yield strength, hardening modulus, strain rate sensitivity, strain rate hardening exponent, and thermal softening coefficient, respectively. While in Eq. (4.5), the terms d_1–d_5 are the failure factors, η represents the deviatoric stress ratio, and $\hat{\theta}$ is a dimensionless thermal partition. Table 4.1 displays the values attributed to the J-C constitutive model along with the consequent failure parameters pertinent to the Ti-6Al-4V material.

Table 4.1 JC material constitutive model and failure parameters for Ti-6Al-4V
Taken from Ullah *et al.* (2022)

A (MPa)	B (MPa)	n	m	C	T_{room} (°C)	T_{melt} (°C)
860	683	0.47	1	0.035	20	1605
d_1	d_2	d_3	d_4	d_5		
-0.09	0.25	-0.5	0.014	3.87		

4.3.2 Initial boundaries conditions and meshing

A precise FE model is crucial for accurately capturing and comprehending the phase changes in Ti-6Al-4V. Fig. 4.2 depicts a developed milling model that has been verified in the author prior research (Ullah *et al.*, 2022). As indicated, the workpiece was constrained from three sides, and the physical parameters and geometry of the cutting tool remained identical to those utilized in the machining tests. The workpiece and cutting insert were meshed by assigning element type CPE4RT, which combines plain stain quadrilateral with temperature-displacement coupling. The initial temperature for the workpiece and cutting insert was equivalent to 20 ℃, and the inelastic heat fraction was set as 0.9 to describe the heat flux flows into the chip. Since the HSM

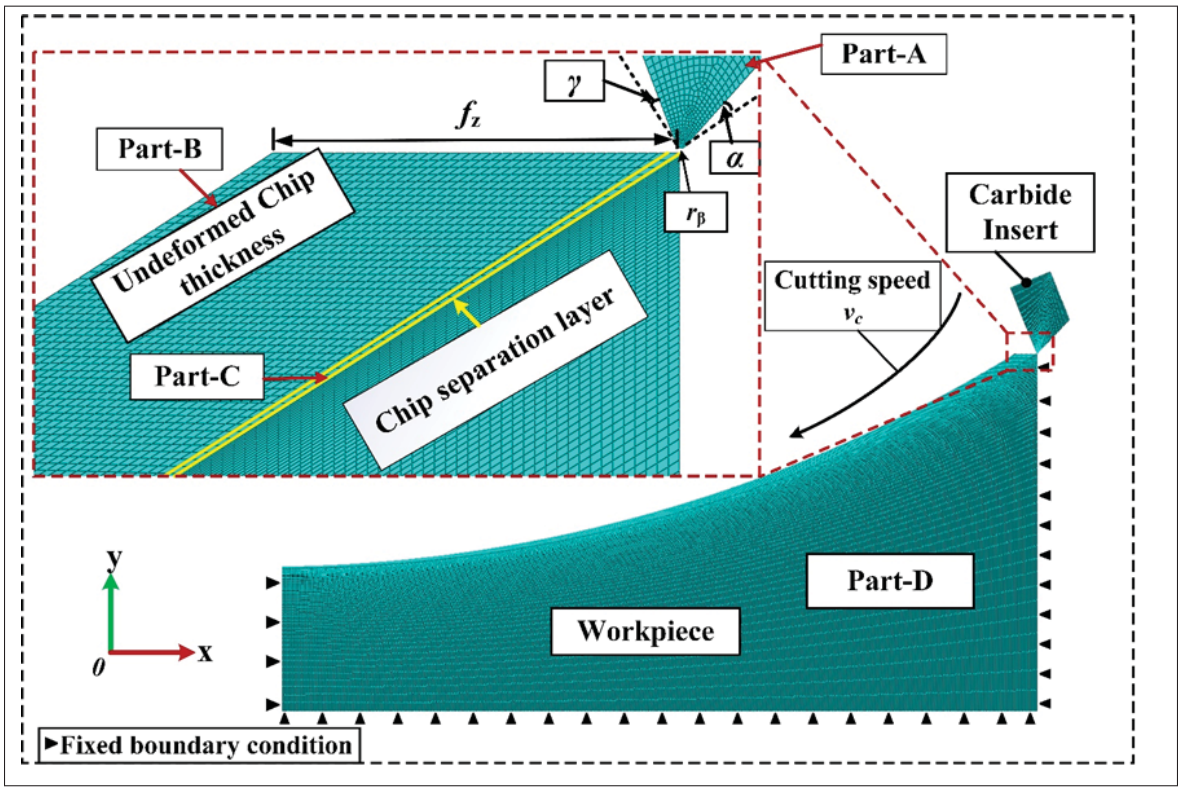

Figure 4.2 Simplified FE model for HSM of Ti-6Al-4V

involves complex physical phenomena, including material deformation, chip formation, and heat generation. Therefore, an accurate contact model is required to represent the interaction between the workpiece and the cutting tool. A Zorev model was incorporated in the current simulation to

illustrate the sliding and sticking behavior between the chip-tool interface (Wang *et al.*, 2016a).

$$\tau_f = \begin{cases} \mu\sigma, & \mu\sigma \leq \tau_{crit} \text{ (sliding zone)} \\ \tau_{crit}, & \mu\sigma \geq \tau_{crit} \text{ (sticking zone)} \end{cases} \tag{4.6}$$

Where τ_f, τ_{crit}, μ, and σ are the frictional shearing stress, critical shear stress, friction coefficient, and normal stress, respectively. In the current research, the coefficient of friction was set at 0.24, according to the author's previous research (Ullah *et al.*, 2022).

4.4 Experimental work

Ti-6Al-4V with chemical composition of 6.11-6.14 wt% Al, 3.89-4.01 wt% V, 1.4-2.6 wt% Sn, 0.31-1.1 wt% Fe, 0.34-90 wt% Cu was employed as a material test for the HSM. Tests were carried out in a dry environment on a 3-axis vertical machining center (Huron K2X10). A Kistler piezoelectric dynamometer (type 9255B) and thermal imagining camera were employed to record the cutting forces and temperature. As depicted in Fig. 4.3(a), A PVD-coated carbide insert, held tightly with a milling cutter, was used during machining tests. To mitigate the impact of tool wear on surface integrity, a new milling insert was utilized for every experiment. Upon completion of the milling experiments, samples measuring 7 mm^3 in dimensions were

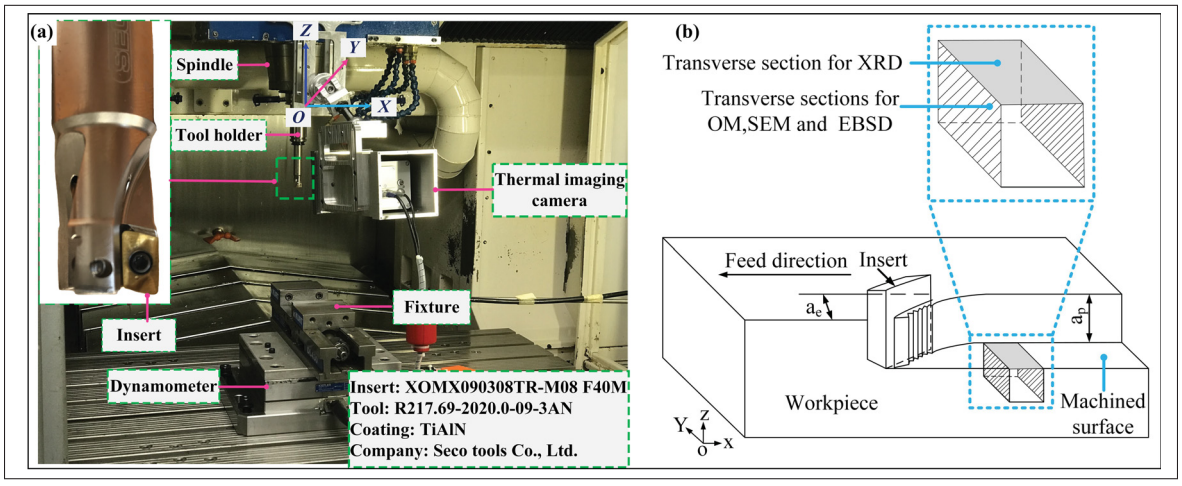

Figure 4.3 Experimental setup for HSM: (a) machining setup, (b) metallographic test areas

extracted from the machined surface for subsequent metallographic observation, as delineated in Fig. 4.3(b). Finally, a combination of advanced characterization instruments such as optical microscopy (OM), Electron Backscattered Diffraction (EBSD), scanning electron microscopy (SEM), and X-ray diffraction analysis (XRD) were utilized for comprehensive analysis and observation. These were used to assess the geometrical and microstructural state of the machined surface and removed chips.

4.4.1 Base material microstructural and phase compositions

Fig. 4.4 depicts the microstructures and phase composition of as-received Ti6Al4V. This alloy was received in the form of plates which were obtained by cold rolling. XRD and EBSD analysis

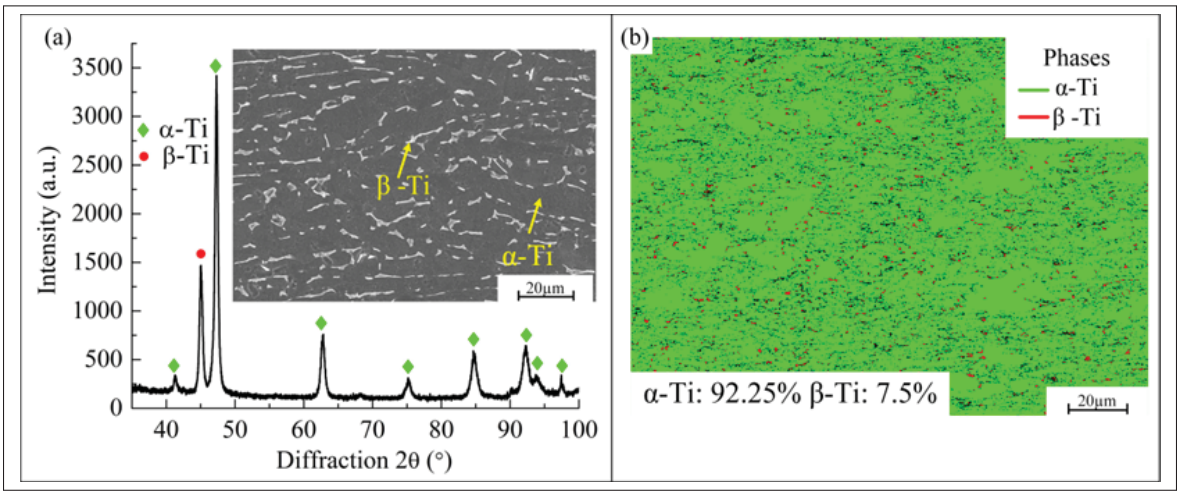

Figure 4.4 Initial microstructural and phase composition of the base material

indicated that the base material mainly comprised 92.25% α – Ti and 7.5% β – Ti. The α-phase has a hexagonal-close-packed (HCP) crystal structure, while the crystal structure of the β-phase is a body-centered cubic (BCC).

4.4.2 FE model validation

To validate the accuracy of an established model, six experimental trials were selected (given in Table 4.2). First, the developed model was verified regarding chip geometrical characteristics(

Table 4.2 Detailed experimental setup for HSM of Ti-6Al-4V

Exp. Nos	Cutting Speed v_c (m/min)	Radial Depth of Cut a_c (mm)	Axial Depth of Cut a_p (mm)	Feed per tooth f_z (mm/z)
1#	150	1.6	1.4	0.20
2#	250	1.6	1.4	0.20
3#	350	1.6	1.4	0.20
4#	150	1.6	1.4	0.15
5#	150	1.6	1.4	0.20
6#	150	1.6	1.4	0.35

i.e., peak, valley, and spacing). As shown in Fig. 4.5, a serrated chip was consistently observed for all the experimental trials, and the simulated chip morphology was adequately coherent with the experimental findings. For a detailed elucidation of chip morphology, the geometrical

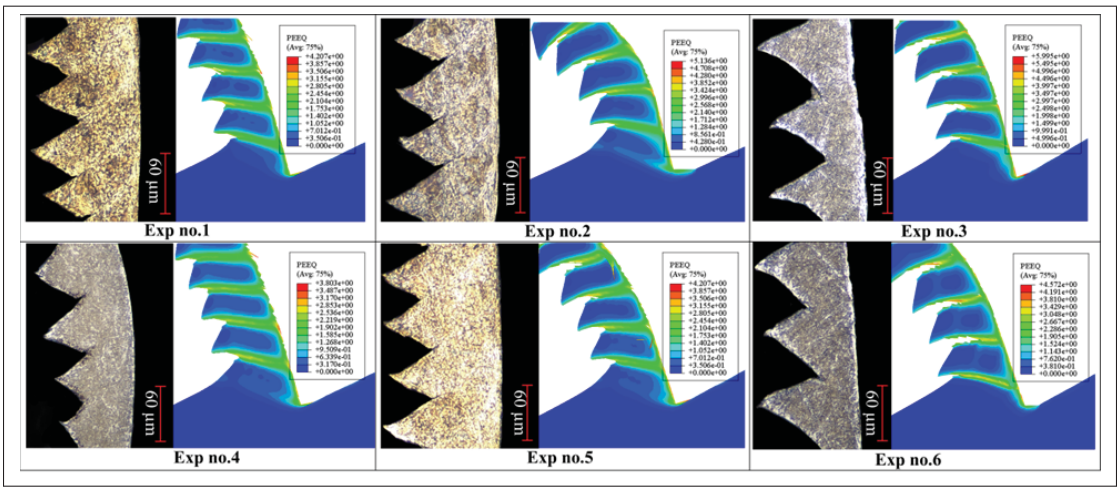

Figure 4.5 Chip morphology comparison between experiment and simulation

features of serrated chips were determined and analyzed, and the obtained results are documented in Table 4.3. As listed, the average relative error of the three features (i.e., peak, valley, and spacing) obtained through simulation and experiment is less than 13 %, which proves the reliability and precision of the established FE model. Similarly, to further verify the developed model, the simulated and experimental cutting forces values were compared in Fig. 4.6. As presented in Fig. 4.6(a) and (b), the experimental cutting forces in X and Y direction for Exp nos. 1, 2, and 4 are slightly higher than the simulated ones. In contrast, for Exp nos. 3, 5, and 6,

Table 4.3 Detailed comparative results of chip geometrical characteristics

Exp Nos.	Value	Chip Morphology (μm)		
		Average Peak	Average Valley	Average Spacing
1#	Simulated	76.86	54.63	62.13
	Experimental	80.56	59.23	56.47
	Relative error (%)	6.03	8.42	9.11
2#	Simulated	82.53	46.36	60.91
	Experimental	88.23	51.67	57.77
	Relative error (%)	6.90	11.45	5.15
3#	Simulated	82.23	42.36	65.26
	Experimental	87.74	37.36	73.39
	Relative error (%)	6.7	11.80	12.46
4#	Simulated	73.36	56.30	45.23
	Experimental	77.16	52.26	49.39
	Relative error (%)	5.42	7.17	9.19
5#	Simulated	76.86	54.63	62.13
	Experimental	80.56	59.23	56.47
	Relative error (%)	6.03	8.42	9.11
6#	Simulated	85.53	40.36	68.82
	Experimental	79.23	45.23	74.56
	Relative error (%)	7.36	12.06	8.34
Footnote: Relative error % = |(simulated value – experimental value)/simulated value|				

the simulated cutting forces dominated the experimental ones in the X-direction, while opposite trends were absorbed for cutting forces in the Y-direction. Furthermore, it was also observed

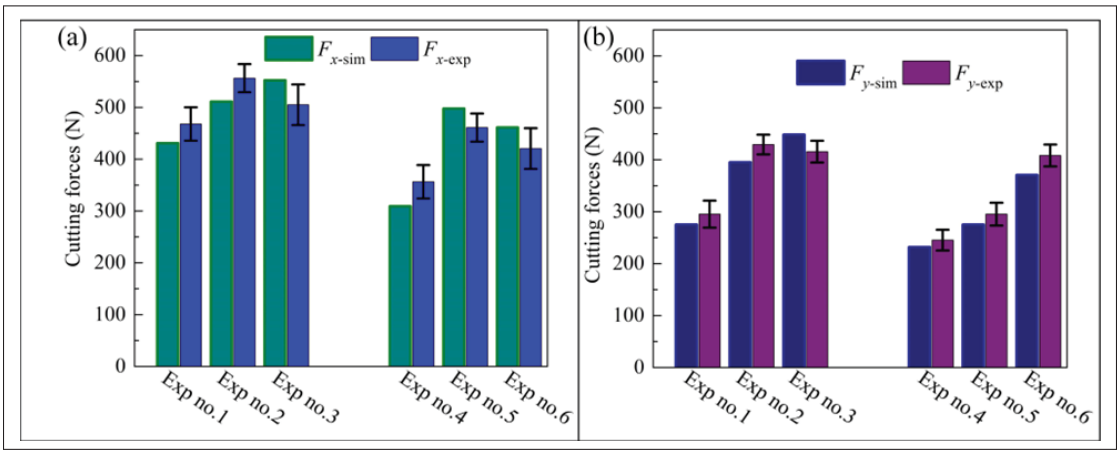

Figure 4.6 Experimental and simulated cutting forces comparison

that experimental cutting forces in the X-direction first increased with cutting speed (i.e., Exp nos. 1 and 2) and feed rates (i.e., Exp nos. 4 and 5) and then declined with further increase in cutting speed (Exp no.3) and feed rate (Exp no.6). The percentage relative to cutting forces in both directions was less than 14.2%. These analyses indicated that the developed FE model of Ti-6Al-4V is accurate and reliable. Therefore, it can simulate phase transformation under a coupled thermo-metallo-mechanical effect.

4.5 Results and discussion

4.5.1 Analysis of phase transformation during rapid heating

The simulated outcomes for equivalent plastic strain, von Mises stress, temperature, and β-phase) volume fraction for three experimental trials are demonstrated in Fig. 4.7. As indicated in Fig. 4.7 (a-c), the predicted maximum equivalent plastic strain were about 4.2, 5.15, and 5.99 for Exp nos. 1,2, and 3, respectively. On the one hand, the plastic strain was relatively higher in the primary and secondary deformation zones and at the tool-workpiece interface. On the other hand, the plastic strain at the milled surface is significantly lower compared to that observed at the shear plane and chip back surface. The higher plastic strain is mainly contributed by severe plastic deformation (Wang *et al.*, 2023a). Fig. 4.7 (d-f) shows that the highest stress values were concentrated within the primary shear zone, reaching approximately 1941 MPa, 2219 MPa, and 2372 MPa for Exp nos. 1, 2, and 3, respectively. Furthermore, it can also be observed from the silhouette that the maximum stress values on the machined surface were limited to 500 MPa for all the experiments. Meanwhile, in machined subsurface zones, the stress values lie in the range of 970 MPa to around about 1780 MPa for all the experiments. Similarly, higher temperatures are another prerequisite for assisting the phase transitions. The simulation outcomes of temperature fields during the HSM of Ti-6Al-4V have been indicated in Fig. 4.7 (g-i). As shown, when the tool crosses the shear plane of the material, the temperature significantly rises from room temperature. The extreme heat generation can be primarily attributed to severe shear plastic deformation, leading to higher temperatures in the cutting

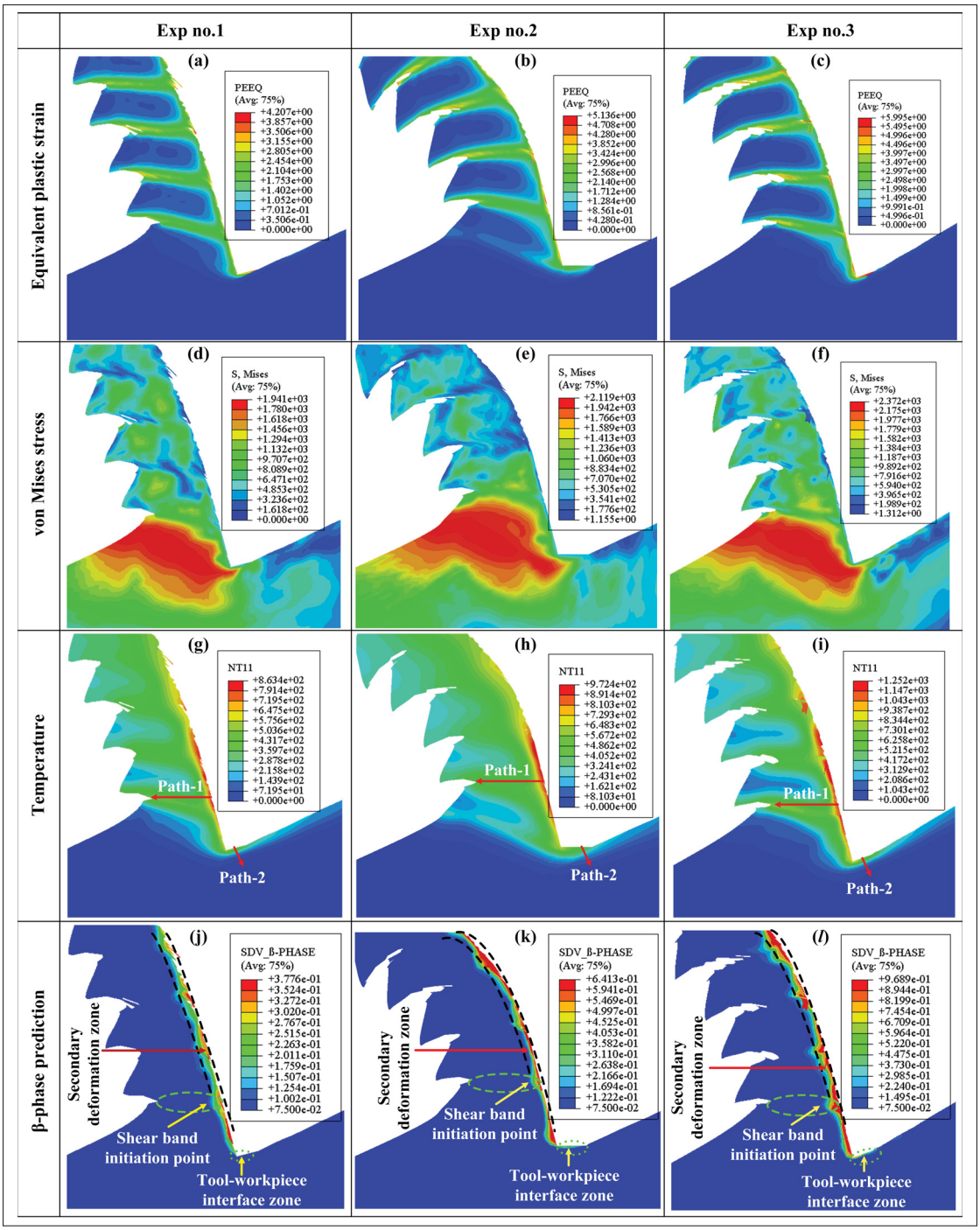

Figure 4.7 Prediction of plastic stain, von Mises stress, temperature, and β-phase field for Exp no. 1,2 and 3

deformation zones (Li, Zhang, Hu & Zhang, 2020). For a detailed understanding of temperature

distribution within the cutting deformation zones, two paths (i.e., Path-1 and Path-2) were generated within the shear band and at the tool-workpiece interface, as shown in Fig. (g-i), and the obtained results were plotted in Fig. 4.8 (a and b). As displayed in Fig. 4.8(a), the maximum

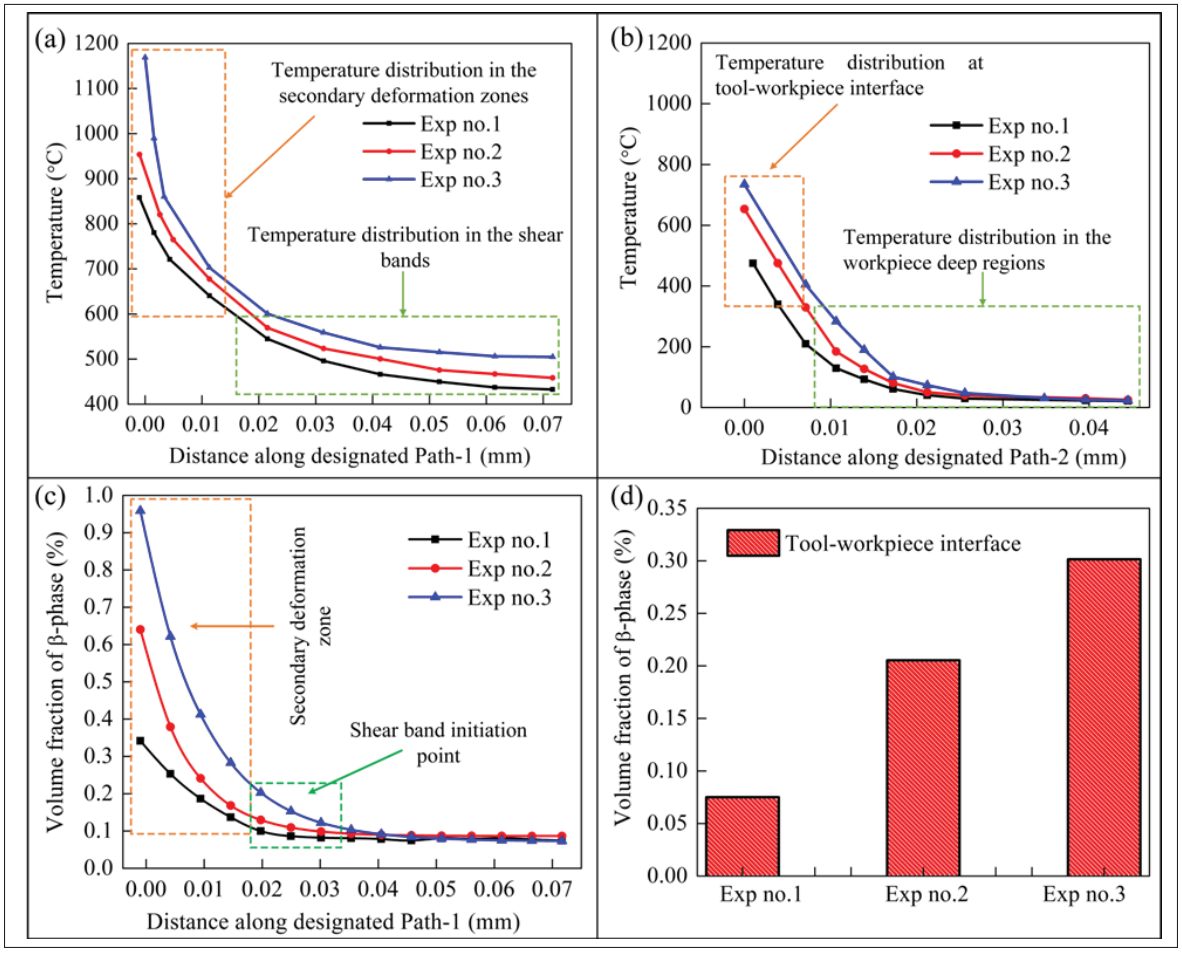

Figure 4.8 Temperature and corresponding β-phase for Exp nos. 1,2 and 3: (a-b) temperature variation along path-1 and path-2, and (c-d) volume fraction of β-phase along path-1 and path-2

temperature was allocated in the secondary deformation zones (i.e., chip back surface). It can be seen that temperature dramatically enhances from ambient temperature to 863.4 °C (Exp no.1), 972.4 °C (Exp no.2), and 1252 °C (Exp no.3), respectively, and decreases cyclically within the shear band. Similarly, as indicated in Fig. 4.8(b), the maximum temperature at the tool-workpiece interface was about 474.7 °C (Exp no.1), 653.5 °C (Exp no.2), and 734.7 °C, respectively. The predicted phase transformation (i.e., from α- to β-phase) has been indicated

in Fig. 4.7(j-l). Notably, the primary volume percent of β-phase was adjusted, equivalent to 7.5%. According to the results shown in Fig. 4.7(j-l), a shallow layer in the chip back surface has undergone a phase transformation (i.e., α- to β-phase). As mentioned earlier, thermal history has a predominant role in phase transformation. Therefore, as seen in Fig. 4.8(c), when the temperature in the chip back surface was about 863.4 °C (for Exp no.1), the volume percentage of β-phase was increased from 7.5 % to about 33.5 %. In comparison, when the temperature reached 972.4 °C, the β-phase volume fraction was enhanced to 63.56 % (Exp no.2). Similarly, with further increase in cutting speed (i.e., 350 m/min (Exp no.3)), the temperature in chip back surface rises to 1252 °C and almost all of the α-phase has been transformed into β-phase (Fig. 4.8(c)). Similarly, as indicated in Fig. 4.8(d), when the peak temperature at the tool-workpiece interface was about 471.72 °C, no changes in β-phase were detected for Exp no.1, while for Exp nos. 2 and 3, when the peak temperature at the tool-workpiece interface reaches 653.58 °C, and 754.65 °C, the volume fraction of β-phase was increased to 20.53 % and 30.14 %, respectively. Three additional tests (i.e., Exp no. 4,5 and 6) were conducted to further understand the consequence of feed rates on phase transition, and the obtained results were plotted in Fig. 4.9. It can be seen that the feed rates also affect the plastic strain, von Mises stress, temperature, and volume fraction of β-phase. As depicted in Fig. 4.9(a-c), when the feed rates were enhanced from 0.15 (Exp no.4) to 0.25 (Exp no.6), the plastic strain was increased from 3.80 to 4.57, and the von Mises stress was augmented from 1825 MPa to 2042 MPa (Fig. 4.9(d-f)), respectively. Fig. 4.9(g-i) indicates that the feed rates also influence the temperature. Again, the highest temperature was observed in the secondary deformation zones for all the experiments. As revealed in Fig. 4.10 (a-b), the peak temperature at the chip's back surface (i.e., along Path-1) was about 789.53 °C, 858.05 °C, and 953.75 °C for Exp nos. 1,2 and 3, respectively. In contrast, the tool-workpiece interface temperature (along Path-2) was about 414.72 °C, 474.72 °C, and 659.65 °C, respectively. The distribution of β-phase) against various feed rates has been demonstrated in Fig. 4.9 (j-l). On the one hand, when the temperature increased to 789.53 °C (Exp no.4), the β-phase volume fraction increased to 22.41%. Similarly, when the temperature surges to 858.05 °C (Exp no. 5) and 953.75 °C (Exp no.6), the volume percentage of β-phase proceeded to 33.5 % and 67.84 %, respectively, as shown in

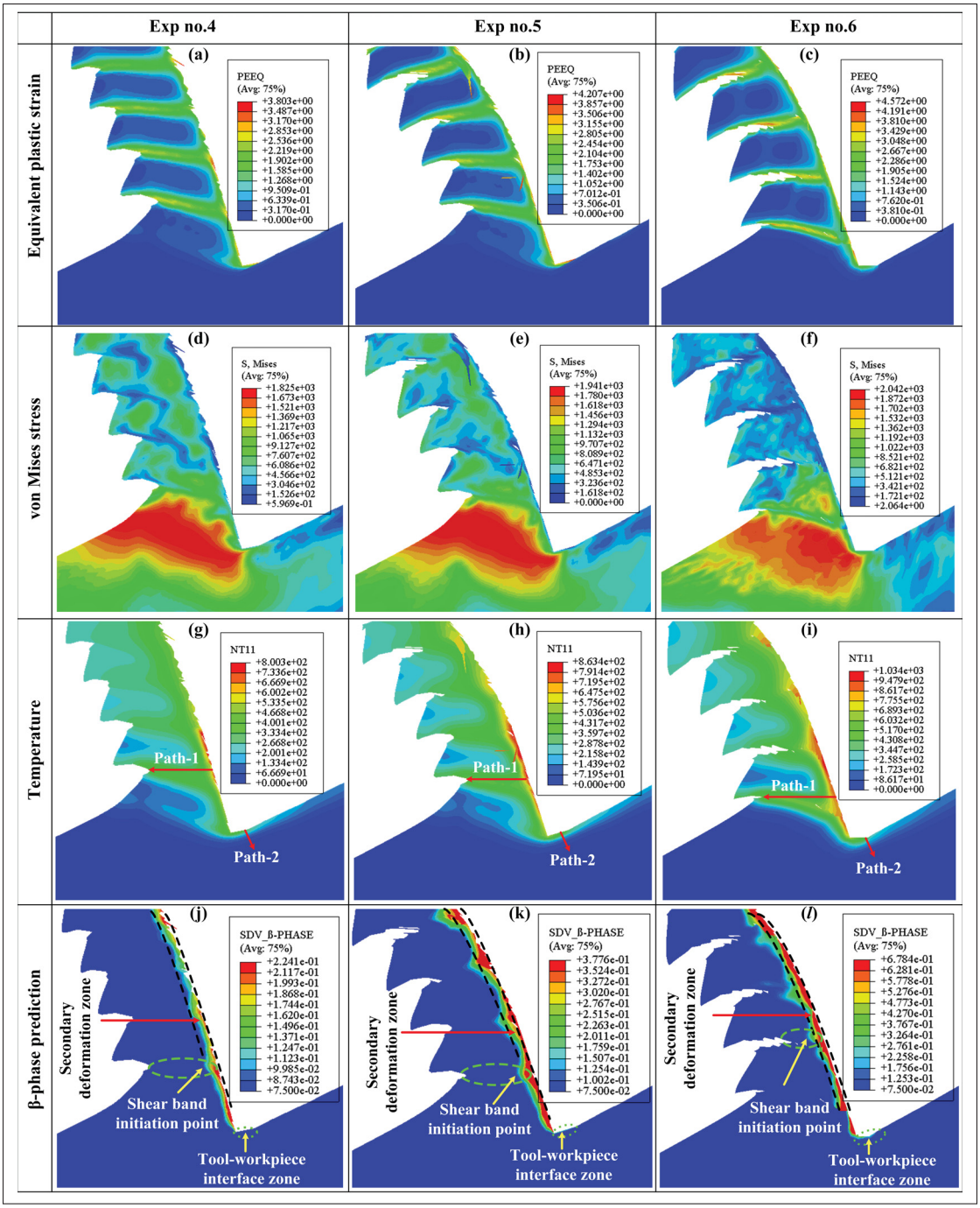

Figure 4.9 Prediction of plastic stain, von Mises stress, temperature, and β-phase field for Exp no. 4,5, and 6

Fig. 4.10(c). On the other hand, when the temperature at the tool-workpiece interface was about 414.72 °C (Exp no.4) and 474.72 °C (Exp no.5), respectively, no phase transformation occurred.

However, when the temperature at the tool-workpiece interface increased to 659.65 °C for Exp no.6, the volume percentage of β-phase was increased to 17.5% (Fig. 4.10(d)). As depicted

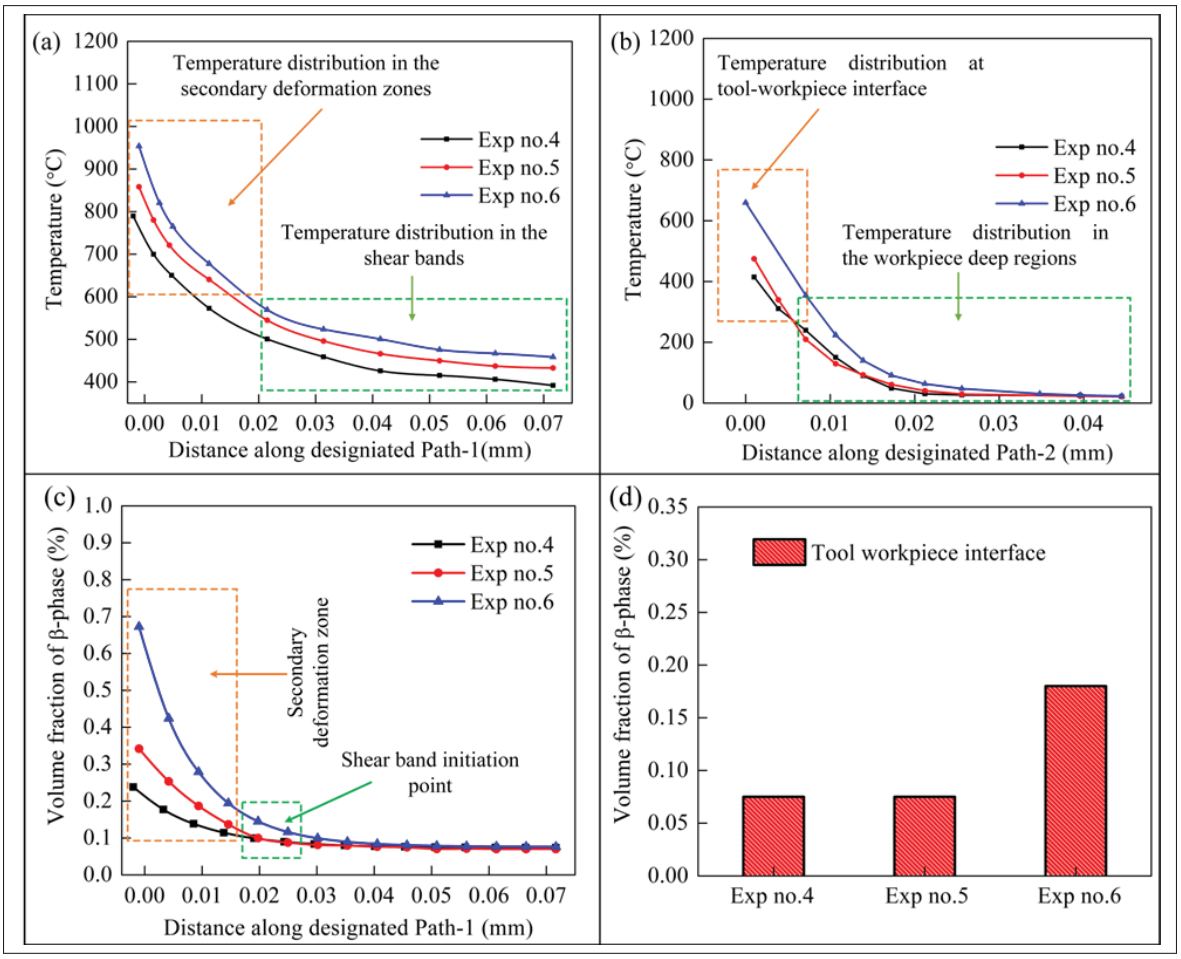

Figure 4.10 Temperature and corresponding β-phase for Exp nos. 4,5, and 6: (a-b) temperature variation along path-1 and path-2, and (c-d) volume fraction of β-phase along path-1 and path-2

in Fig. 4.11, a reasonably good correlation existed between the simulated β-phase and the cutting temperature distribution. The distinct stress, strain, and cutting temperature distributions within the cutting deformation zones likely contributed to the inhomogeneous distribution of β-phase across different deformation zones due to their combined effects. Moreover, no phase transformation was identified in the milled surface. This is because the machined surface is below the initial phase transformation temperature. As depicted in Fig. 4.12 (a), the maximum machined surface simulation temperature for Exp no. 1,2, and 3 was 451.26 ° C, 524.77° C, and

574.37° C, respectively. In contrast, the temperature observed during the milling tests for these experiments was approximately 406.72°C, 479.21°C, and 561.05°C, respectively. Similarly, the maximum simulated temperature of the machined surface for Exp nos. 4, 5, and 6 was 365.39°C, 451.25 °C, 515.11°C, while the maximum experimental machined surface temperature was 341.86°C, 406.72°C, and 490.44°C, respectively. As observed, the simulated machined surface

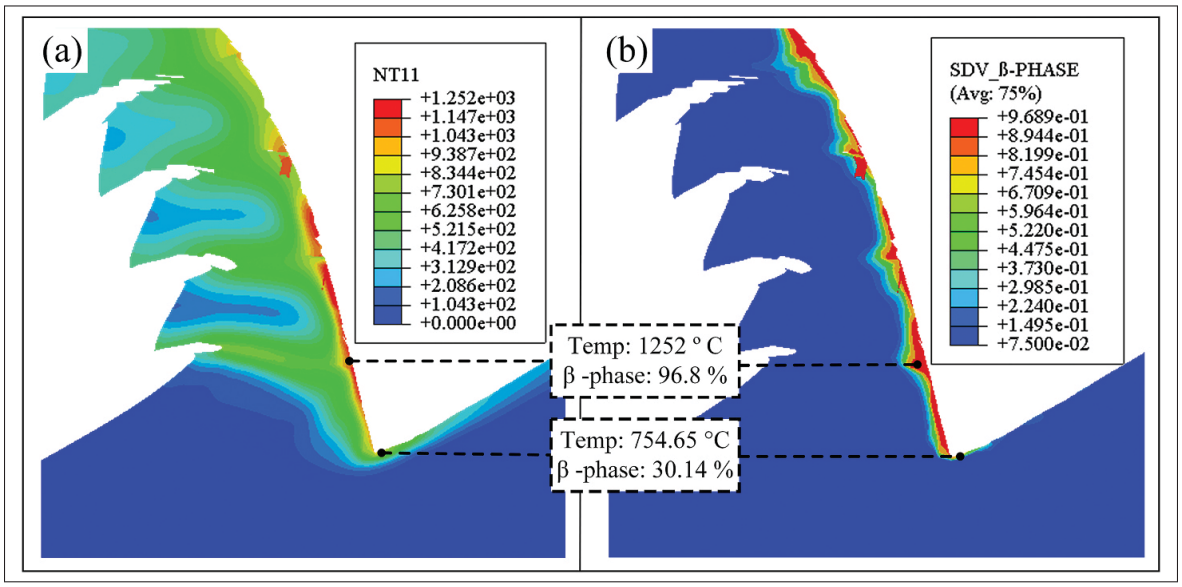

Figure 4.11 Mapping relationship between β-phase field and temperature for the rapid heating stage

temperature dominates the experimental ones for all the tests. Nevertheless, the machined surface temperature for both experimental and simulated temperatures is below the martensitic phase transformation temperature. Generally, the proportion of total heat transferred into a workpiece varied from 1% to 20%, which is significantly lower than the 74% to 96% thermal energy ratios blown away by the chip (Li, Zhang & Zhang, 2019b). In contrast to the chip, the stress and plastic strain distributions are relatively lower on the machined surface. Consequently, these combined conditions diminish the probability of the machined surface undergoing a phase transition.

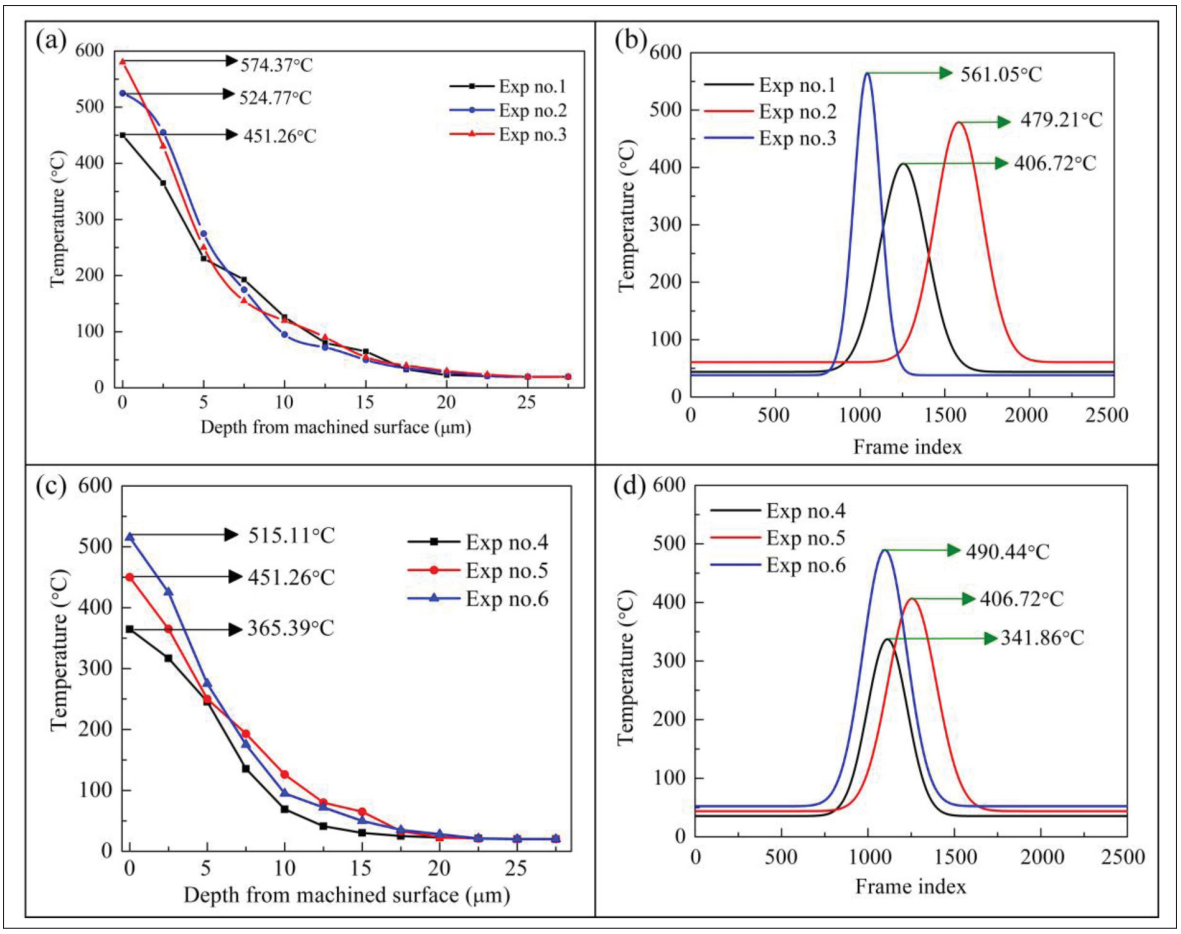

Figure 4.12 Simulated and experimental machined surface temperature comparison

4.5.2 Analysis of phase transformation during rapid cooling

Following the rapid heating stage, the volume percentage of α'-phase during the rapid cooling stage for various milling experiments has been conducted (Fig. 4.13). In the simulation results, the red regions represent the volume fraction of α-phase, while the blue areas indicate the volume fraction of α'-phases. Notably, all experiments consistently witnessed a substantial volume fraction of α'-phase in the chip's back surface. However, for Exp no.1, 4, and 5, no α'-phase was detected at the tool-workpiece interface since, for these experiments, the β-phase did not change during the first stage. It can be seen that the α'-phase distributes homogeneously in the secondary deformation zones. For Exp no.1, the volume fraction of α'-phases was about

9.5% at the chip back surface region, while for Exp no.2 and 3, the volume fraction of α'-phases reduced to 8.76 and 7.81 %, respectively.

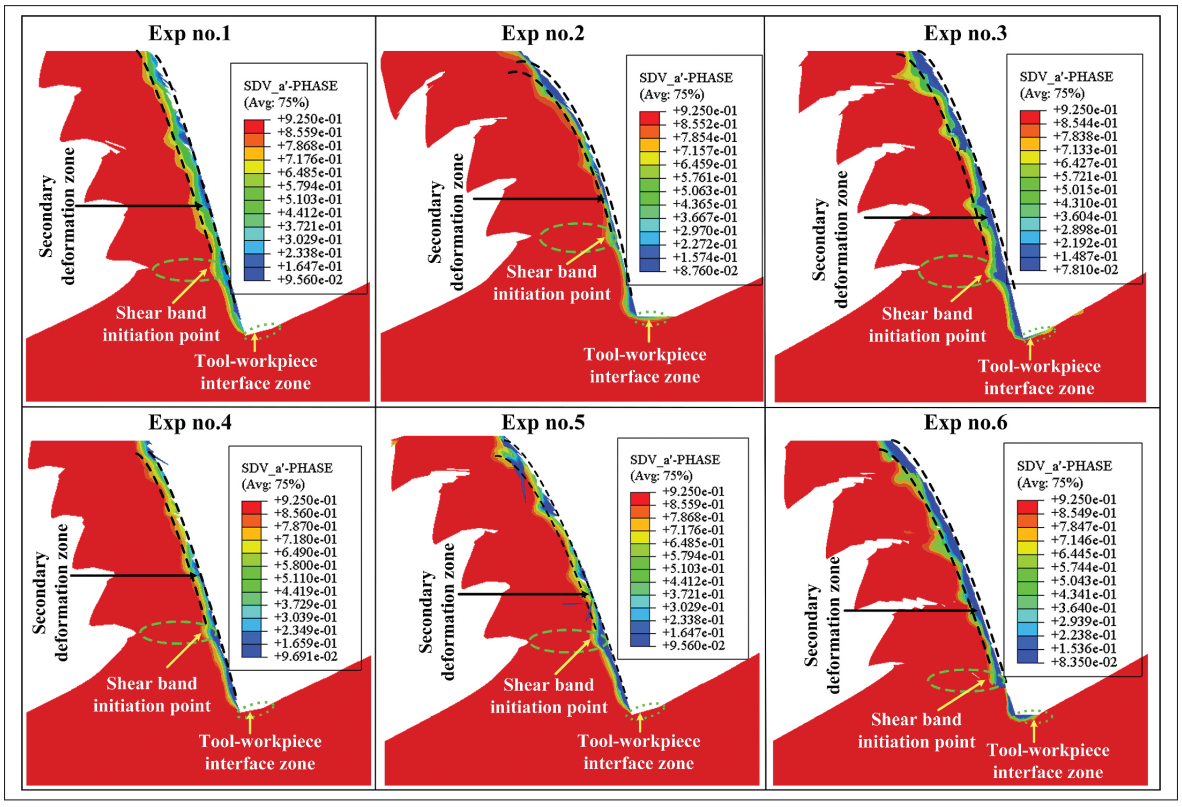

Figure 4.13 Evolution of α'-phases volume fraction during the rapid cooling process

Similarly, when the feed rate increased from 0.15 to 0.25 mm/tooth (i.e., Exp no.4 to Exp no.5), the percentage volume fraction of α'-phases was reduced from 9.69 to 8.35, respectively. On the one hand, the increased heat generation due to higher cutting speeds (Exp nos. 1-3) can shorten the time available for phase transformation and significantly change the kinetics and completeness of martensitic transformation, specifically the volume fraction of α' phase. On the other hand, increased feed rates cause more frictional forces between the cutting tool and the workpiece, resulting in more heat energy, which surges the transformation process. However, the decreased period for phase transition may slow down the complete reconversion of the β-phase , resulting in a smaller volume percent of the α'-phases. Furthermore, higher feed rates originate sharp heat gradients within the material, altering diffusion rates and microstructural

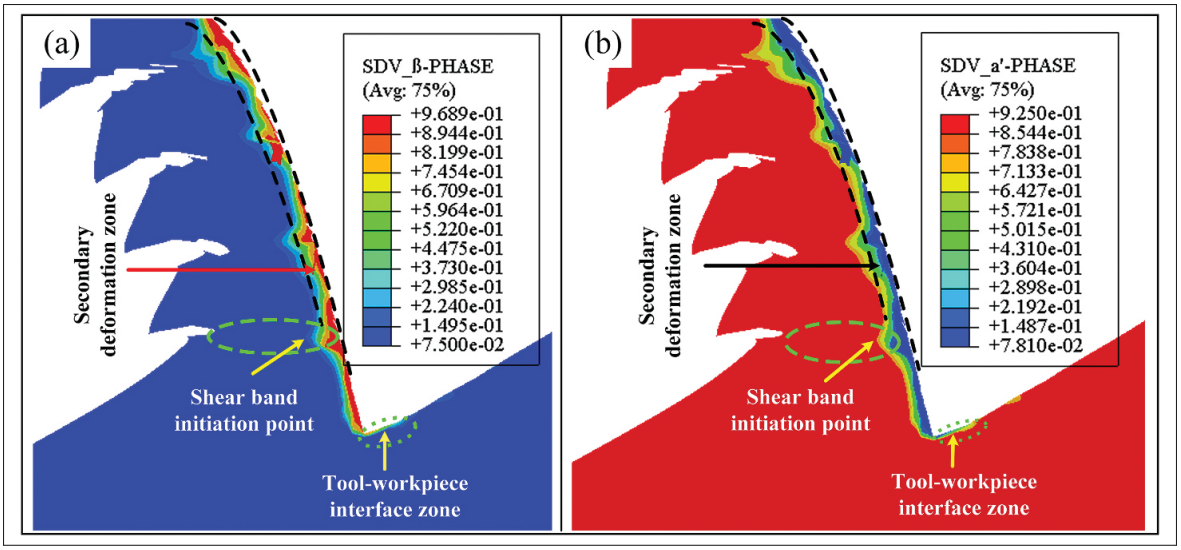

Figure 4.14 Mapping correlations between β-phase and α'-phases for Exp no.3

development, which affects martensitic grain nucleation and growth. A mapping illustration in Fig. 4.14 showed a vital observation. As demonstrated, the regions where the β-phase encountered during the heating stage were reconverted back into α'-phases during the subsequent rapid cooling step. This finding emphasizes the dynamic character of the material's behavior during machining under various thermal conditions. The reversible transition from β-phase to α'-phases throughout the heating and cooling stages provides information on the material's sensitivity to thermal fluctuations, offering vibrant insights into the structural modifications of Ti-6Al-4V during the machining process.

4.5.3 Experimental validation of the developed model

Due to severe plastic deformation, Ti-6Al-4V experiences rapid heating in the cutting plane and subsequently undergoes quick cooling once the cutting insert advances into the workpiece. Consequently, the phase transformations occur in two stages within an extremely short period: first, the conversion from α- to β-phase during heating, followed by the reverse transformation. Owing to the transient approach of high-speed milling, the β-phase within the cutting deformation zones is challenging to analyze directly during the actual machining experiments. Therefore, the

simplified milling model was validated only during the rapid cooling stage in the current research by employing some advanced characterization techniques. XRD analysis was conducted on the machined surface for all the selected experiments, and the results obtained were plotted in Fig. 4.15. Contrast to a base alloy, although the machined surface's phase compositions and relative peak intensities vary with changing milling input parameters; specifically, the peak intensities for the β-phase decreased, leading to a corresponding diminution in the volume fraction of β-phase . These peak intensities owing to the reduced crystalline size and perhaps nano-sized grains caused by the severe plastic deformation at the machined subsurface (Liang, Liu, Wang, Wang & Ren, 2020). Furthermore, the material's grain size can affect the XRD

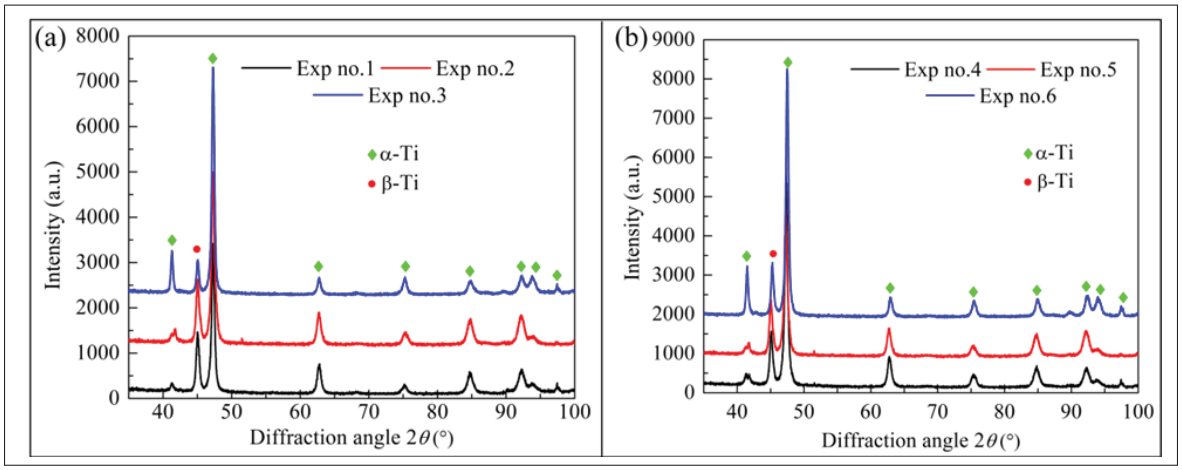

Figure 4.15 XRD analysis of machined surfaces: (a) phase composition for Exp nos. 1, 2, and 3, (b) phase composition for Exp nos. 4, 5, and 6

peaks' full width at half maximum (FWHM) (Vashista & Paul, 2012). Smaller grain sizes generally result in broader diffraction peaks, while larger grain sizes produce sharper peaks. This is because smaller grains lead to a more pronounced distribution of diffraction angles due to crystallite orientation and size variations within the sample. Nonetheless, the peak intensity positions remain consistent, which suggests that the machined surface has not significantly altered the crystallographic phases. Further microscopic analyses were conducted to understand any potential microstructural changes induced by machining, even if they're not instantly apparent in the XRD pattern. As shown in the SEM images in Fig. 4.16 (a-c), the microstructure of the machined subsurface undergoes substantial plastic deformation. The grains were rotated

and elongated in the cutting directions, indicating severe plastic deformation in the machined subsurfaces. Increased cutting parameters can transform the material's microstructure primarily due to intensified temperatures triggered by elevated friction during the machining process. Furthermore, the rapid heating and cooling cycles can also lead to amended material properties, including altered grain structures. Moreover, the accelerated strain rates at higher machining

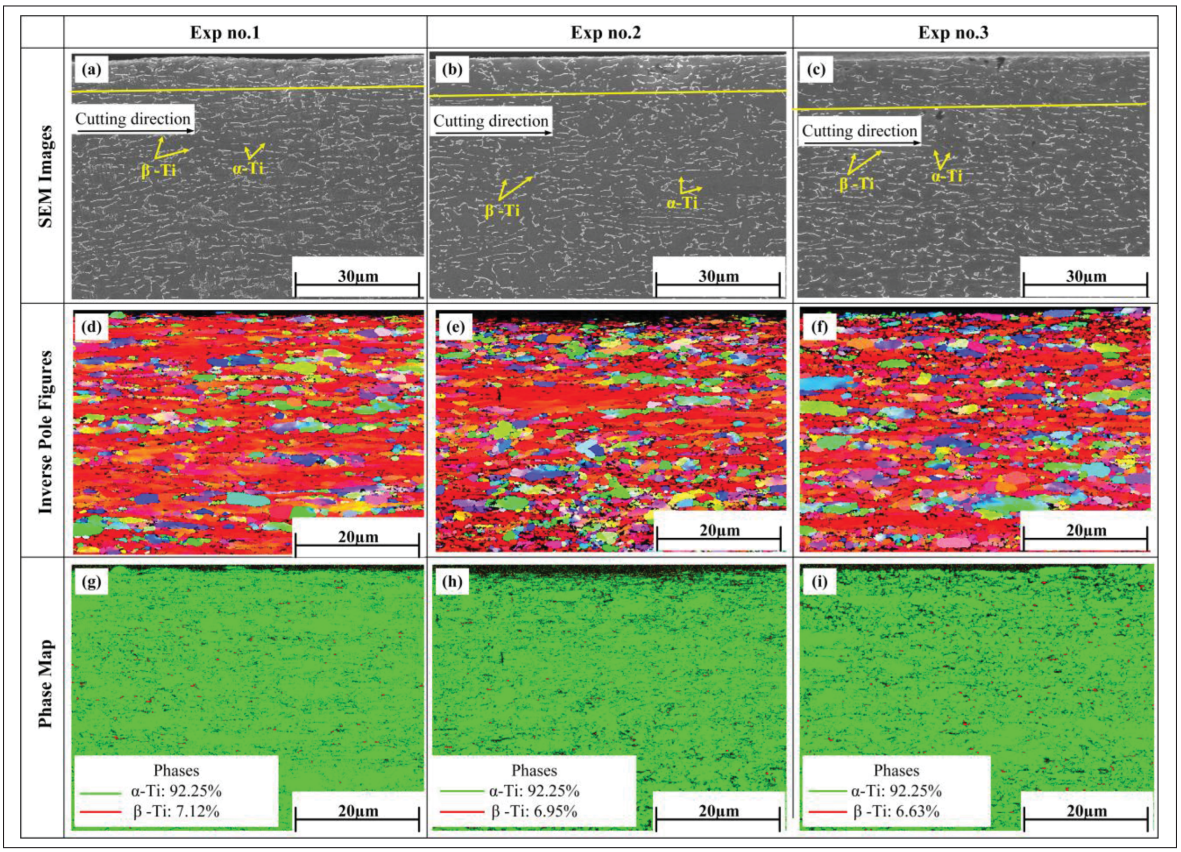

Figure 4.16 SEM and EBSD results of machined surface layer: (a-c) SEM images, (d-f) Inverse pole figures for grain size evolution, and (g-i) phase map

input parameters can impact deformation mechanisms, influencing grain size, orientation, and texture within the material. As shown in the inverse pole figures, initially, at a lower cutting speed (i.e., Exp no.1), the grains were elongated along the cutting direction. This elongation occurs because the material experiences significant stress and strain in the cutting direction. However, with further increases in the cutting speed (i.e., Exp no. 2 and 3), the deformation causes the grains to break and reduce in size within the machined subsurface. The corresponding

statistical data of grain refinement has been displayed in Fig. 4.17. As illustrated, the average

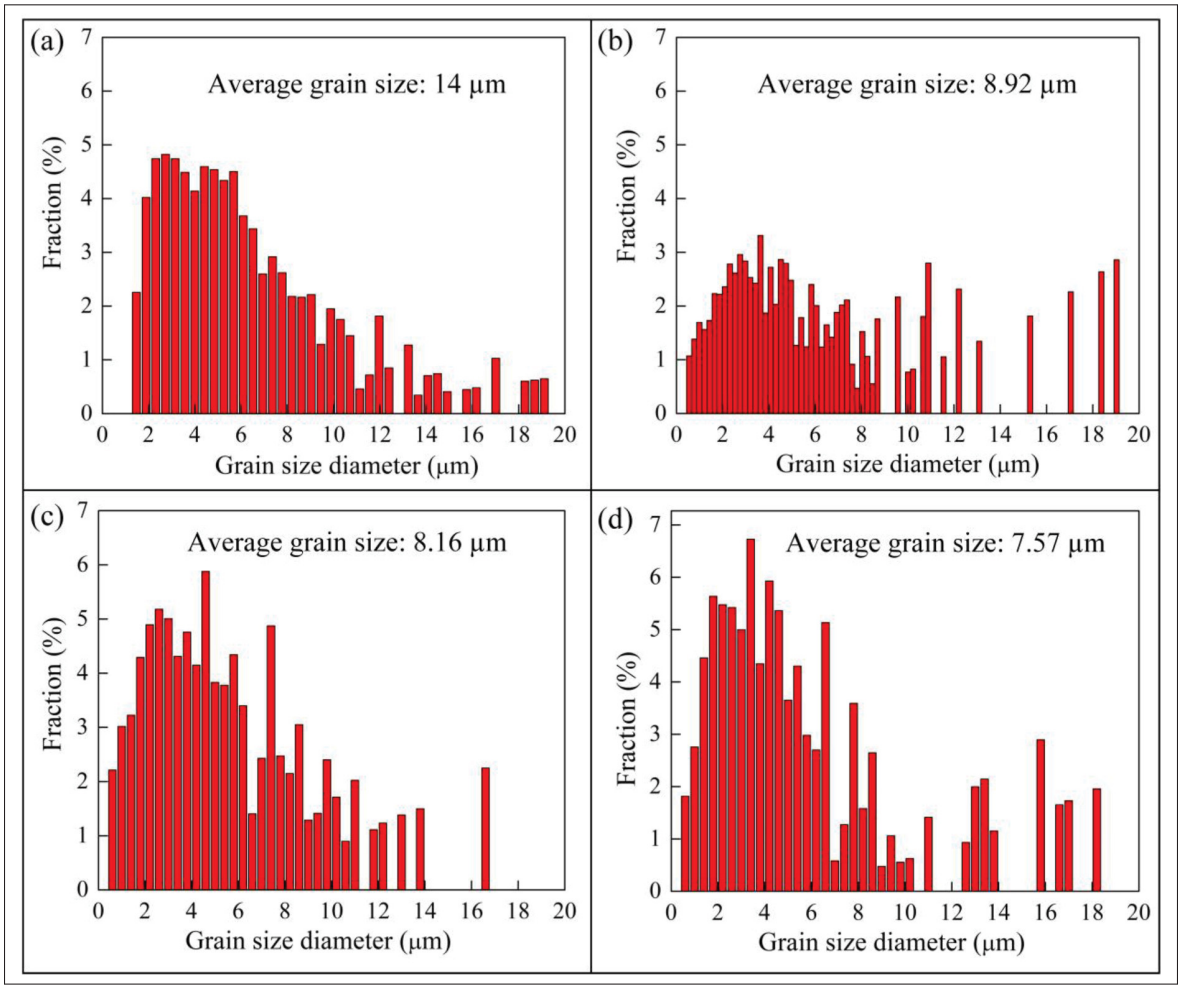

Figure 4.17 Grain size statistical representation: (a) matrix average grain size, (b) average grain size for Exp no.1, (c) average grain size for Exp no.2, and (d) average grain size for Exp no.3

grain size within the machined subsurface was 8.92, 8.16, and 7.57 μm for Exp no.1, 2, and 3, respectively. Moreover, when contrasted with the EBSD-derived average grain size of 14 μm for the Ti-6Al-4V matrix, it becomes evident that the machined subsurface grain size of the Ti-6Al-4V alloy undergoes refinement. The reduction in grain size results from the intense shearing and deformation forces acting on the material during machining, leading to fragmentation and refinement of the grains within the surface layer of the workpiece (Zhang & Bai, 2023)[35]. The phase map (Fig. 4.16(g-i)) obtained through EBSD analysis indicated that the volume fraction

of β-phase slightly decreased with increasing machining input parameters. For Exp no.1, the volume fraction of β-phase decreased from 7.5 % to 7.12 %. While for Exp no. 2 and 3, 6.95% and 6.63 % of the volume fraction of β-phase was retained, respectively. On the one hand, the decrease in the β-phase after rapid cooling supports the potential of cooling-induced phase changes. On the other hand, Rapid cooling can change the phase composition of material by favoring the production of the more stable phases from the metastable β-phase. Because of friction and distortion, the material experiences increased temperatures during machining. Following machining, fast cooling causes a quenching effect, forcing the material to harden quickly. This rapid cooling may limit the β-phase's stability, causing it to change into the α'-phase or other more stable phases at lower temperatures.

4.6 Conclusions

The present study implemented a thermo-metallo-mechanical coupled model that relied on phase transformation kinetics to anticipate and forecast phase transitions during the rapid heating and cooling stages in the context of HSM of Ti-6Al-4V. OM, SEM, EBSD, and XRD analyses were accomplished to recognize the accuracy of the developed model. The following conclusions can be drawn based on the obtained results.

1. The developed model's chip geometrical features and cutting forces predictions aligned well with experimental data. The percentage relative error for chip geometrical parameters and cutting forces fell within the 5.15% to 14.2% range. This suggests that the Ti-6Al-4V simulation model can accurately represent the stress-strain and temperature conditions during HSM and can provide a suitable framework for phase transformation analysis.
2. The simulation results showed that as the temperature at the chip's back surfaces for Exp nos. 1, 2, and 3 increased to 863.4, 972.4, and 1252°C, respectively, the volume fraction of β-phase increased from 7.5% to 33.5, 63.56, and 96.89. Similarly, in the feed rate ranges from 0.15 mm/tooth to 0.25 mm/tooth (Exp nos. 4-6), the volume fraction of β-phase increased from 7.5% to 67.84%.

3. The predicted results also confirm that Exp nos. 1, 4, and 5 did not exhibit any phase transition at the tool-workpiece interface due to temperatures remaining considerably below the initial phase transformation temperature. However, for Exp nos. 2, 3, and 6, the volume percentage of the β-phase at the tool-workpiece interface increased from 7.5% to 20.53%, 30.14%, and 17.5%, respectively. In addition, all the experimental trials detected no phase transition at the machined surface.
4. During the rapid cooling phase, regions that experienced the β-phase during heating were converted back to α'-phases. Within the 150–350 m/min cutting speed range and feed rates of 0.15-0.25 mm/tooth, the volume fraction of α'-phases in the phase transformation regions increased to approximately 9.5%.
5. The XRD analysis indicated that no new peaks were obtained, confirming the absence of phase transformation on the machined surface. SEM and EBSD analyses revealed substantial plastic deformation in the machined subsurface. Elongated grains were observed at lower cutting speeds, but at higher cutting speeds, the deformation led to grain breakage and reduction in size within the machined subsurface.

CHAPTER 5

NUMERICAL ANALYSIS OF CYCLIC RESIDUAL STRESS INDUCED BY THERMO-MECHANICAL LOADS IN HIGH-SPEED MILLING OF TC4 TITANIUM ALLOY

Irfan Ullah [1] , Esther Titilayo Akinlabi[2] , Mehmet Aydin [3] , Victor Songmene [1]

[1] Department of Mechanical Engineering, , École de Technologie Supérieure, 1100 Notre-Dame Ouest, Montréal, Québec, Canada H3C 1K3
[2] Department of Mechanical and Construction Engineering, Northumbria University, Newcastle Upon Tyne NE1 8ST, United Kingdom

[3] Department of Industrial Design, Bilecik Şeyh Edebali University, Türkiye

This article is submitted to *" journal of Machining Science and Technology",* in Jan 2025,

Abstract

The machining-induced residual stress significantly impacts the fatigue life of machined components, including geometrical stability and service performance. This study presents a fully coupled thermo-mechanical two-dimensional (2D) Finite Element (FE) model to investigate residual stress distributions induced by High-Speed Milling (HSM) of TC4 titanium alloy. The effectiveness of the developed model was demonstrated by comparing the predictions with experimental data on chip segmentation, cutting forces, and temperatures, and the relative errors were found within the range of 6.85–12.40%. In addition to the verification of the cutting model, the periodic fluctuations of plastic strain and residual stress in the machined surface and subsurface regions were simulated. The results revealed that the tensile stress was dominated at a lower cutting speed (i.e.,150m/min), while compressive stress emerged at higher speeds (i.e., 450 m/min), particularly for $\sigma 11$. The subsurface residual stress profiles exhibited hook-shaped distributions, where compressive stress peaked at depths of 7–10 μm and gradually diminished to zero beyond 22 μm. Furthermore, a strong alignment was found between the experimental and simulated results; the subsurface stress was consistently compressive in both directions and exhibited higher magnitudes with increasing cutting speeds and feed rates. Accordingly, thermal loads predominantly influence the residual stress on the machined surface, whereas

mechanical loads govern the subsurface stress. The present research provides a comprehensive understanding of residual stress distributions in milled components, highlighting their critical influence on the fatigue life and overall service performance of machined parts.
Keywords: Chip segmentation degree, FE Model, HSM, Residual stresses, Thermo-mechanical loads, TC4 titanium alloy

5.1 Introduction

Due to its exceptional strength-to-weight ratio, corrosion resistance, and high-temperature performance, TC4 titanium alloy has become critical in various industries, especially in aerospace, automotive, biomedical, and energy sectors (Sun & Guo, 2009). These desirable properties allow for producing lighter and more durable components, such as aircraft engine parts, medical implants, and turbine blades, where longevity and resilience are paramount under demanding conditions. However, the high toughness and low thermal conductivity of TC4 titanium alloy pose machining challenges, often resulting in excessive tool wear and surface integrity issues (Sarıkaya *et al.*, 2021). Among other indicators of machining quality, the residual stress of the machined surface and subsurface is one of the foremost characteristics, as it significantly influences the fatigue life, corrosion resistance, and overall mechanical performance of the machined component (Yang *et al.*, 2016). Tensile residual stress is often regarded as detrimental to the service performance of a component, as it can lead to fracture initiation, shorten fatigue life, and compromise overall structural integrity (Ullah *et al.*, 2022). In contrast, compressive residual stress is beneficial since it enhances fatigue resistance, delays fracture propagation, and extends the service life of the product. HSM, known for its high efficiency, adaptability, and precision, is widely used in many industries. However, controlling and understanding residual stress during HSM remains a critical and pressing challenge within these fields. Extensive experimental studies have been carried out to explore the relationship between machining conditions and residual stress. In prior investigations, (Mantle & Aspinwall, 2001) analyzed the residual stress induced during the machining of gamma titanium aluminides. The results indicated that cutting speed was the most influential factor affecting residual

stress. (Huang, Sun, Li, Han & Xiong, 2013) conducted an experimental investigation on HSM of 7050-T7451 Aluminum Alloy and found that mechanically induced compressive stress decreased with increasing cutting speeds and decreased with feed rate. This finding contradicts the results of (Salahshoor & Guo, 2011), who observed that high cutting speeds combined with low feed rates could produce substantial compressive stress. Similarly, (Khaliq, Zhang, Jamil & Khan, 2020) examined the effects of different cutting speeds and feed rates on residual stress during the machining of additively manufactured titanium alloy under dry and minimum quantity lubrication conditions. They found that compressive residual stresses tended to decrease as cutting speed and feed rate increased. Besides cutting speed and feed rate, the effect of tool geometry on machining-induced residual stress also considerably influenced surface residual stress. For instance, (Denkena, Nespor, Böß & Köhler, 2014) reported that during the ball end milling of titanium alloy, the cutting edge radius has a five times more significant impact on the residual stress formation compared to other process parameters. (Chen *et al.*, 2004) found that when machining titanium alloy, tool wear ranging from 0.03 mm to 0.2 mm caused a shift in residual stress from compressive to tensile. (Liang & Liu, 2017) observed similar results during the machining of titanium alloy. Some empirical models were also developed to predict residual stresses in machining processes. (Robles, Aurrekoetxea, Plaza, Llanos & Zelaieta, 2022) developed an empirical model to estimate residual stresses produced by face milling of titanium alloy, achieving lower error values than those found from X-ray diffractometry and an R-squared (R2) value greater than 90%. (Tan, Zhang, Yao, Wu & Zhang, 2017) established an empirical model for milling with shot peening to assess compressive residual stress profiles of TC17 alloy using exponential and sinusoidal decay functions, achieving highly accurate predictions with an R2 > 97%. (Jiang, Kong, He & Wu, 2021) proposed an empirical model to analyze the effects of thermo-mechanical loads on residual stress. Their findings indicated that thermal load has a more significant impact on tensile residual stress, while mechanical load influences both compressive and tensile residual stress. Although empirical models can be valuable guides for regulating machining-induced residual stresses, their applicability is restricted since they are regulated to specific cutting circumstances (Wan, Ye, Wen & Zhang, 2019). Furthermore, imprecise assumptions or interpretations of physical circumstances during

machining might compromise the validity of these empirical methods. As a result, there is a substantial research interest in establishing high-reliability simulation models for more accurate prediction of residual stresses. Numerous high-quality research studies have utilized FE analysis to predict residual stresses during machining processes (Xu *et al.*, 2023; Pan, Liang & Garmestani, 2019; Paschoalinoto, Bordinassi, Bortolussi, Leonardi & Delijaicov, 2021). However, few studies have focused on modeling residual stresses induced by the milling of titanium and its alloys. (Wang, Zhou, Ren & Shu, 2023c) developed a three-dimensional FE model to predict residual stresses during the machining of titanium alloy, reporting a good agreement between the simulated and experimental residual stresses. (Yang *et al.*, 2016) utilized a sine attenuation function combined with an FE model to analyze the relationship between process parameters and residual stresses. (Ullah *et al.*, 2022) developed a simplified milling model to predict the correlation between white layer formation and residual stresses during the milling of Ti-6Al-4V alloy. Similarly, (Xu, Outeiro, Zhang, Li & Zhao, 2024) proposed a framework based on coupled Eulerian and Lagrangian approaches to study the effect of tool wear on residual stresses in the machining of Ti-6Al-4V alloy. (Rao *et al.*, 2011) observed that an increase in flank wear leads to a reduction in maximum residual stress. They also found that higher feed rates resulted in compressive residual stress. Similar research findings have been also reported in the literature (Aydin, 2017; Liu *et al.*, 2021). Furthermore, it is also reported that sequential cuts significantly affects residual stress distribution but has a minimal impact on cutting forces and temperature (Song, Li, Lv, Lv & Zhao, 2019; Ruitao, Linfeng, Jiawei, Xiuli & Meiliang, 2021). According to the literature study on machining-induced residual stress, the majority of investigations have focused on the turning process, which produces reasonably homogenous and uniform chips. In contrast, few research has investigated residual stress formation during the milling process. Unlike turning, milling includes variable undeformed chip thickness, resulting in variations in thermo-mechanical loads that have a substantial impact on the residual stress distribution inside machined parts. However, the link between thermo-mechanical loads and residual stress generation in milling remains inadequately understood, and further investigation is required. Hence, this work aims to look into how undeformed chip thickness variation and thermo-mechanical loading history affect machined surface and subsurface residual stress

during HSM of TC4 titanium alloy. The main objective of the present research is several folds. First, a simplified 2D milling model was developed, where the undeformed chip thickness is approximated as a sinusoidal function. The model was subsequently validated by comparing simulated and experimental results for chip segmentation, cutting temperature, and cutting forces. Second, the periodic fluctuations of plastic strain and residual stress during milling were unveiled. Finally, the simulated residual stress profiles for the machined surface and subsurface were compared with experimental measurements, and the influence of thermo-mechanical loads on residual stress formation was thoroughly analyzed.

5.2 FE Model Formulation

5.2.1 Development of a 2D Cutting Model for Milling Process

The milling process involves the periodic engagement and disenchantment of the cutting tool, resulting in sinusoidal variation in undeformed chip thickness. This makes the modeling process significantly complex compared to the turning process (Li, Jing & Chen, 2009). Furthermore, 3D FE models for the milling process are computationally intensive; thus, a 2D FE model can be implemented to efficiently investigate the residual stress formation within the machined surfaces (Tounsi & El-Wardany, 2022). By rationalizing the trochoidal tool path, the undeformed chip thickness can be approximated as a sinusoidal function for a 2D model as expressed in Eq. 5.1:

$$h(\theta) = f_z \sin(\theta) \tag{5.1}$$

where f_z is the feed per tooth, and θ is the angular position of the cutting tool.

Fig. 5.1 shows the geometrical conversion of machining processes. As can be seen from the figure, θ_s and θ_e are the entry and exit angles, respectively. The entry angle (θ_s) and the cutting

length (l_c) can be determined by employing Eqs. (5.2) and (5.3):

$$\theta_s = \arccos\left(1 - \frac{a_e}{R}\right) \tag{5.2}$$

$$l_c = R \cdot \arccos\left(1 - \frac{a_e}{R}\right) \tag{5.3}$$

where a_e is the radial depth of cut, and R represents the cutting tool radius.

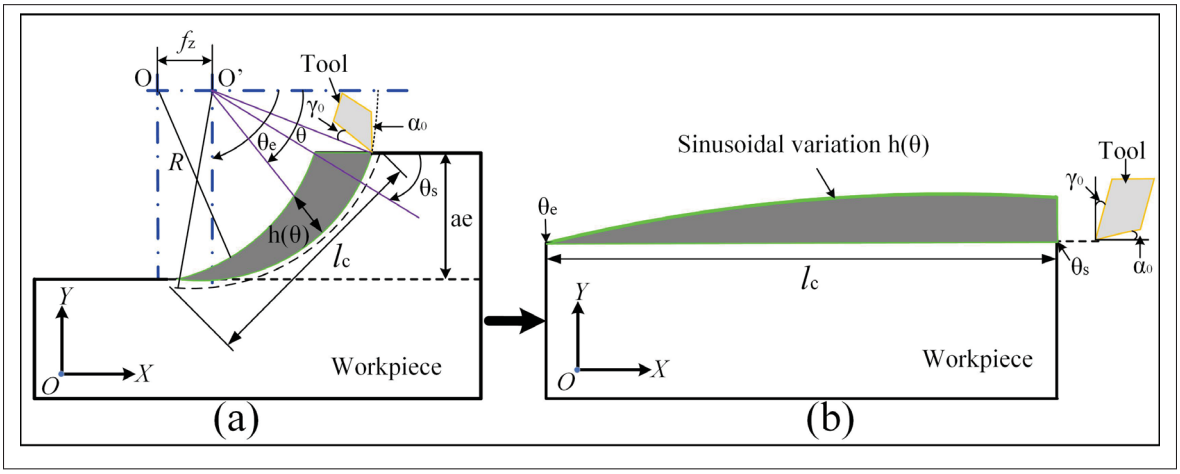

Figure 5.1 Geometrical conversion of milling processes: (a) 3D milling model, and (b) 2D cutting

5.2.2 Numerical Model Establishment for Residual Stress

To capture the residual stress induced during machining, a detailed 2D cutting model was implemented in Abaqus/Explicit (v 6.14) (Fig. 5.2) . The workpiece is composed of TC4 titanium alloy, which is further subdivided into undeformed chip thickness, chip separation layer, and base material. The chip separation layer was defined as the failure zone and was finely meshed with an element size of 3 μm, while a biased mesh was used for the base material to focus on the head-affected zones near the machined surface. The cutting tool was modeled as an analytical rigid body. The numerical model uses an initial temperature of 20 $^{\circ}C$ with an inelastic heat fraction of 0.9, representing the heat flux flow of plastic deformation.

During the machining process, the flow stress, at which the plastic deformation is mainly affected by a complex thermo-mechanical coupling process followed by relatively large plastic strain and strain rate, makes selecting a constitutive model for the cutting process challenging. Therefore, a Johnson-Cook (J-C) constitutive model was implemented (Johnson & Cook, 1985), which describes the large strains, high strain rates, and thermal-dependent viso-plasticity. The equivalent plastic flow stress is presented in Eq. (5.4).

$$\begin{cases} \sigma = [A + B \cdot \varepsilon^n] \cdot [1 + C_0 \cdot \ln(\dot{\varepsilon}^*)] \cdot [1 + T^{*m}] \\ \dot{\varepsilon}^* = \frac{\dot{\varepsilon}}{\varepsilon_0} \quad \text{and} \quad T^{*m} = \frac{T - T_0}{T_m - T_0} \end{cases} \tag{5.4}$$

where σ is the flow stress, $A = 860\,\text{MPa}$, $B = 683\,\text{MPa}$, $C_0 = 0.035$, $n = 0.47$, and $m = 1$ are the material constants, respectively (Ullah *et al.*, 2021b). Meanwhile, as listed in Eq. (5.4), the terms $\dot{\varepsilon}^*$ and T are the homologous strain rate and current temperature, respectively. Similarly, the $T_0 = 20\,^\circ\text{C}$ is the room temperature, $T_m = 1605\,^\circ\text{C}$ is the melting temperature, and $\varepsilon_0 = 1\,\text{s}^{-1}$ is the reference strain rate. Similarly, during the metal cutting simulation, the chip separation criterion is a physical standard based on tool-tip elemental nodes such as stress and strain. When the value of a given physical quantity exceeds the physical condition of the material, it is considered that the unit node is separated (Li, Pang, Zhao, Zang & Wang, 2017). The present simulation uses a J-C fracture model for damage initiation, which is based on the calculation of damage parameter w, defined by Eq. (5.5), and updated in every FE analysis solving step. Elements are assumed to fail and be deleted when the damage parameter exceeds unity.

$$\omega = \sum \left(\frac{\Delta \bar{\varepsilon}^{pl}}{\bar{\varepsilon}_f^{pl}} \right) \tag{5.5}$$

In the above equation, $\Delta \bar{\varepsilon}^{pl}$ is the increment of equivalent plastic strain, and $\bar{\varepsilon}_f^{pl}$ is the plastic strain at failure, described by Eq. (5.6):

$$\bar{\varepsilon}_f^{pl} = \left[d_1 + d_2 \exp\left(d_3 \frac{\sigma_p}{\sigma} \right) \right] \left[1 + d_4 \ln\left(\frac{\dot{\varepsilon}^{pl}}{\dot{\varepsilon}_0} \right) \right] (1 + d_5 \times T^{*m}) \tag{5.6}$$

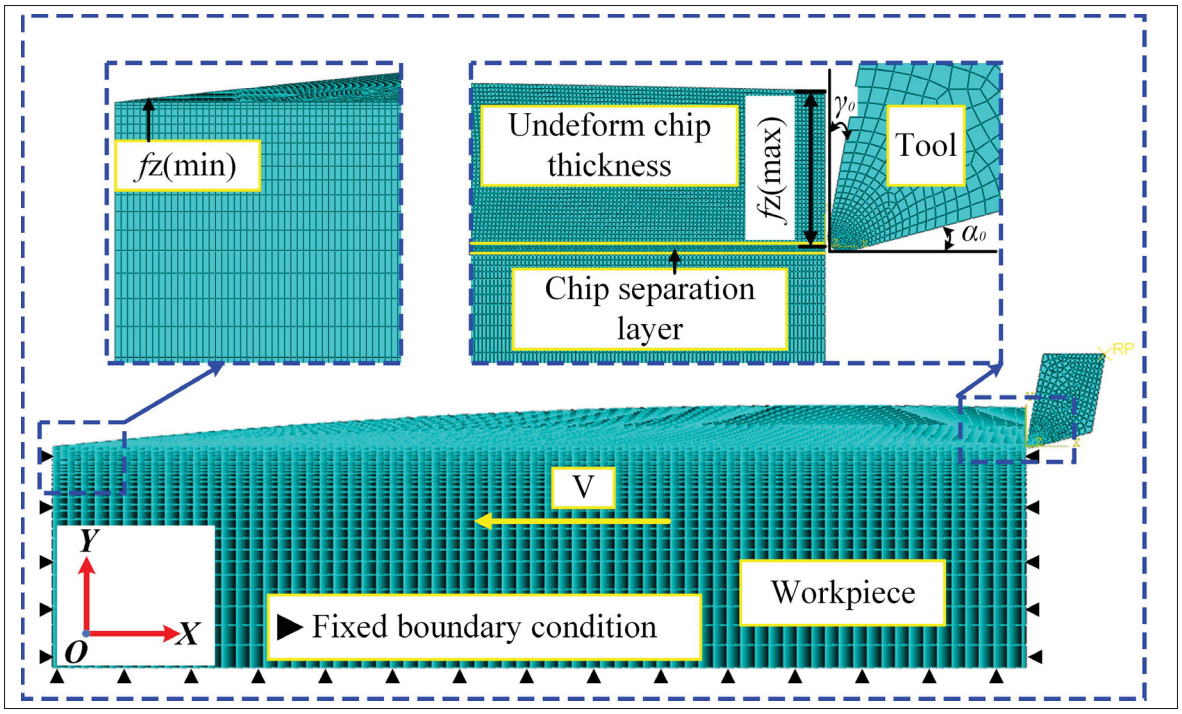

Figure 5.2 2D FE model and boundaries conditions for the milling of TC4 titanium alloy

where σ_p is the hydrostatic stress. $d_1 = -0.09$, $d_2 = 0.25$, $d_3 = -0.5$, $d_4 = 0.014$, $d_5 = 3.87$ represents the damage parameters.

In addition to the flow stress and fracture model, the contact model also has a noticeable impact on mechanical and thermal behaviors, thus affecting the residual stress distribution within the workpiece material. The stick-slip friction contact model proposed by Zorev, as represented by Eq. (5.7), was utilized in the present research. This model represents the tool-chip contact, divided into regions: sticking friction is the contact behavior near the cutting edge, and sliding friction occurs far away from the cutting edge, as follows:

$$\tau_f = \begin{cases} \mu\sigma, & \mu\sigma \le \tau_{crit} \text{ (sliding zone)} \\ \tau_{crit}, & \mu\sigma \ge \tau_{crit} \text{ (sticking zone)} \end{cases} \tag{5.7}$$

where τ_f is the frictional shearing stress, μ is the friction coefficient, σ is frictional normal stress, and τ_{crit} is critical shear stress.

5.2.3 Procedure for Predicting Residual Stresses from the FE Model

In order to extract the residual stresses from the FE model, after the cutting tool was retracted, it was completely stopped, and the loads applied to the workpiece boundaries during the cutting step were removed. Due to the serrated chip formation and the sinusoidal variation of undeformed chip thickness, the residual stress is inhomogeneously distributed in the workpiece. Therefore, paths were drawn on the machined surface and subsurface layer to extract the residual stresses. Then, the obtained results were averaged and compared with the experimentally found residual stress values.

5.3 Experimental Work

HSM experiments were performed on a vertical machining center (Huron K2X10) in a dry environment, as shown in Fig. 5.3(a). The workpiece material, a dual-phase (α+ β) TC4 titanium alloy, whose microstructures and phase composition are indicated in Fig. 5.3(b), was machined using fresh PVD-coated inserts for each experimental trial. The physical and mechanical properties of the workpiece and cutting inserts can be found in the authors' previous research work (Ullah, Akinlabi, Songmene, Kouam & Sadeghifar, 2024a). During the milling experiments, the forces and temperatures were measured by employing a Kistler dynamometer (type 9255B) and an Infrared (IR) thermal imaging camera (VarioCAM®HD head 900). The cutting speed was varied: 150 m/min and 450 m/min. The feed rate was also varied: 0.10 mm/tooth, 0.2 mm/tooth, and 0.30 mm/tooth. The radial and axial depths of the cut were kept constant to 1.6 mm and 1.4 mm, respectively. Chip samples were collected for chip geometrical observation using scanning electron microscopy (SEM) and optical microscopy (OM). The experimental residual stress values of the machined surface and subsurface of TC4 titanium alloy were measured using Proto LXRD equipment. The measurements were done on the crystallographic plane (213), where the diffraction peak location was detected at 2θ = 140.13°.

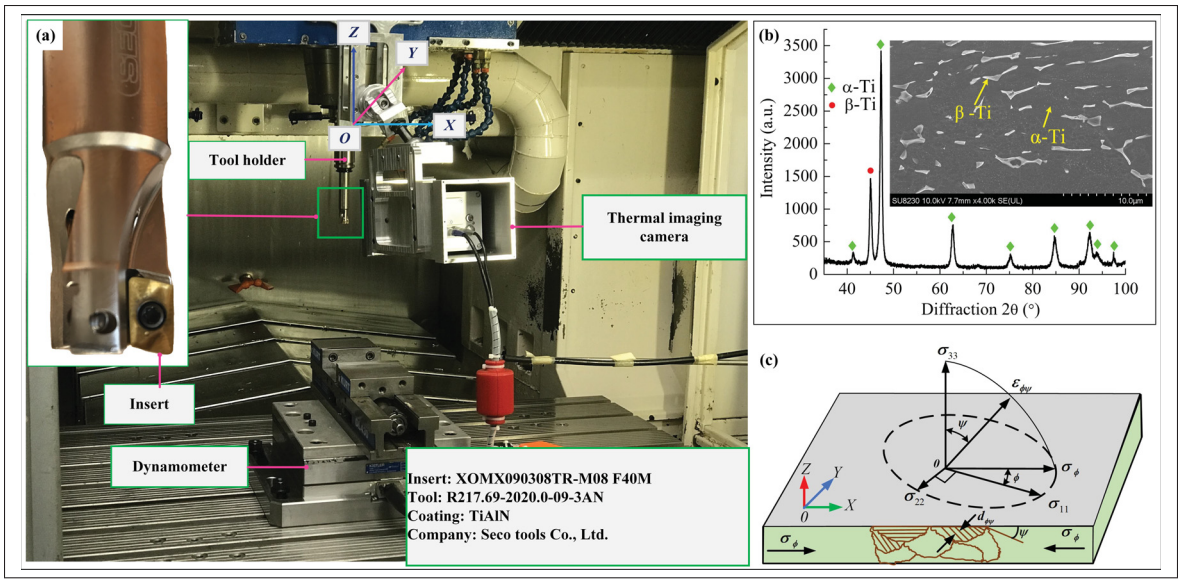

Figure 5.3 Experimental procedure and methods: (a) HSM setup, (b) microstructure and phase composition of workpiece material, and (c) schematic diagram of residual stress coordinated system

Data were taken at fifteen different tilt angles (ψ) within a range of ±45° to produce stress values closer to the average of the material. The strain component, perpendicular to the surface, was calculated in terms of crystal lattice dimensional changes defined by angle ϕ and ψ (depicted in Fig. 5.3(c)) as expressed in Eq. (5.8).

$$\varepsilon_{\psi\psi}^{hkl} = \left\{ \frac{d_{\psi\psi} - d_0}{d_0} \right\} = S_1 \left[\sigma_{11}^s + \sigma_{22}^s \right] + \frac{1}{2} S_2 \sigma_\psi \sin^2 \psi \tag{5.8}$$

where σ_ψ is the surface stress in ϕ direction, d_0 is the unstressed interplanar spacing, and $d_{\psi\psi}$ is interplanar spacing obtained from the position of the diffraction peak. σ_{11}^s and σ_{22}^s denote the normal stress components in the plane of the surface. Similarly, $S_1 = -2.83 \times 10^{-3}$ and $\frac{1}{2}S_2 = 11.68 \times 10^{-6}\,\text{MPa}^{-1}$ are the elastic constants of X-ray in the Miller (hkl) crystallographic plane, which are expressed by Eq. (5.9):

$$\begin{cases} S_1 = -\frac{\nu}{E} \\ S_2 = \frac{2(\nu+1)}{E} \end{cases} \tag{5.9}$$

where ν and E are the Poisson's ratio and Young's modulus of the material, respectively.

5.4 Results and Discussion

5.4.1 FE Model Validation

Generally, machining forces, temperatures, and chip segmentation degree are frequently used as potential indicators to verify the accuracy and reliability of the established cutting simulation model. Initially, the validity of the developed FE model was demonstrated through the degree of segmentation (G_s), i.e., the dimensions of serrated chip peak (H) and valley (h), which is frequently used for validation (Chen, Ren, Yang, Jin & Guo, 2011; Wang & Liu, 2014) as described by Eq. (5.10).

$$G_s = \frac{H - h}{H} \tag{5.10}$$

The SEM and OM micrographs of an experimentally obtained chip at a cutting speed of 150 m/min are illustrated in Fig. 5.4. Fig. 5.4(a1) demonstrates a detailed view of the chip segmentation structure, which is characteristic of HSM of TC4 titanium alloy and contributes to the formation of saw-tooth patterns. Fig. 5.4(a2) provides a closer look at the shearing process, highlighting the shear slip surface, where plastic deformation primarily occurs, leading to segmentation. In Fig. 5.4(a3), the undeformed surface and the slipping surface are even more visible, indicating the material flow direction during chip formation. Similarly, the simulation results of the chip formation at the same cutting speed are presented in Fig. 5.4(b). It can be concluded that the predicted segmentation characteristics closely resemble those observed in

Fig. 5.4(a1). The quantitative comparison of chip segmentation (G_s) between experimental and simulation outcomes at various machining input parameters is demonstrated in Fig. 5.4(c). As illustrated, the average (G_s) for the experimental and simulated chip morphology under the given cutting conditions are in reasonably good agreement. It can also be seen that when the cutting speed and feed rates are enhanced from 150 to 450 m/min and from 0.10 to 0.30 mm/tooth, respectively, the (G_s) values significantly increased, indicating that at critical cutting conditions, the adjacent segments of serrated chips will be wholly separated. Furthermore, considering the

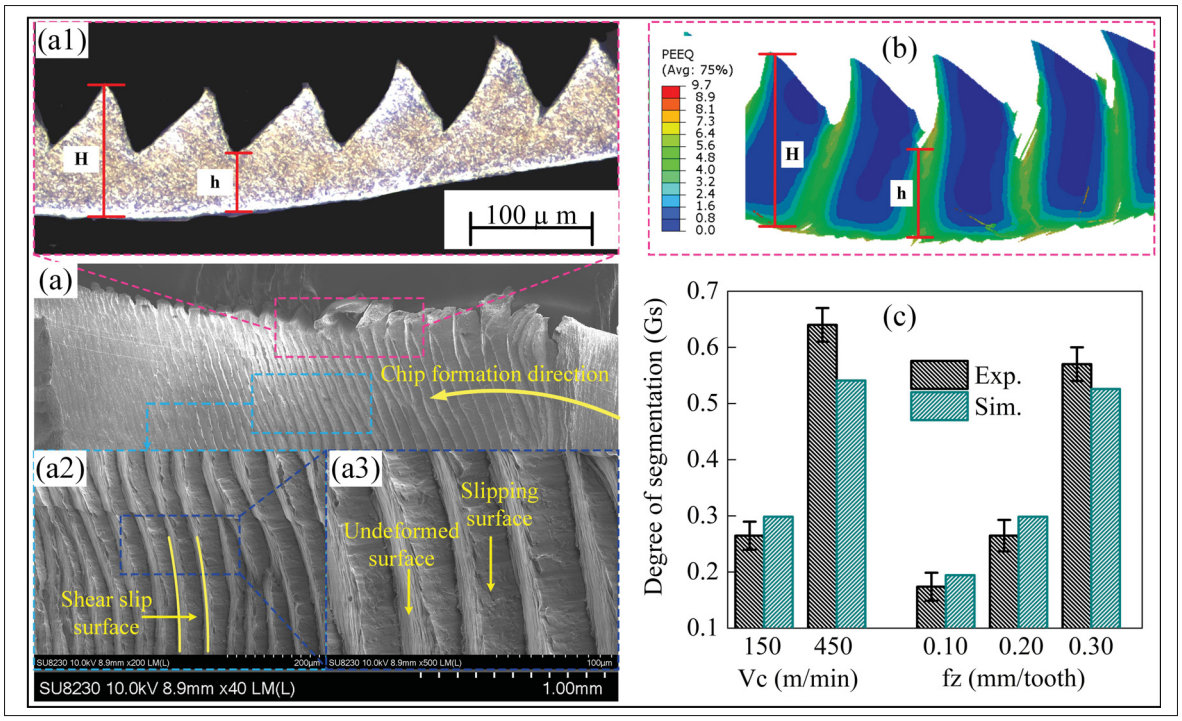

Figure 5.4 Comparison of experimental and simulated chips: (a-a3) experimental chip characteristics, (b) simulated chip, and (c) chip segmentation degree comparison

vital role of thermal and mechanical loads on the residual stresses during machining, the FE model was further verified against cutting temperatures and cutting forces obtained from the authors' previous work (Ullah *et al.*, 2024a). Fig. 5.5(a-b) demonstrates the actual temperature encountered during the milling experiments and the simulated temperature at a 150 m/min cutting speed. As illustrated, the maximum temperature at the tool-workpiece interface for the experimental trial reached approximately 435.6°C. In contrast, the recorded temperature at the

tool-workpiece interface for the simulation is about 456.7°C, further demonstrating the efficiency of the FE model in capturing the thermal dynamics. Fig. 5.5(c-d) provides a comparative analysis of cutting temperatures between the experimental and simulation results for various cutting speeds and feed rates. It should be noted here that the cutting temperature values were recorded at five different places and then averaged for both experimental and simulation. As shown in Fig. 5.5(c), when the cutting speed increases from 150 to 450 m/min, both experimental and simulated temperatures rise significantly. Although the FE model slightly overestimates the experimental temperatures, the trends remain consistent with a relative percentage error of about 4.84-8.06%. Similarly, Fig. 5.5(d) indicates the temperature variation against various feed rates, where higher feed rates result in elevated temperatures. Similarly, to further verify the

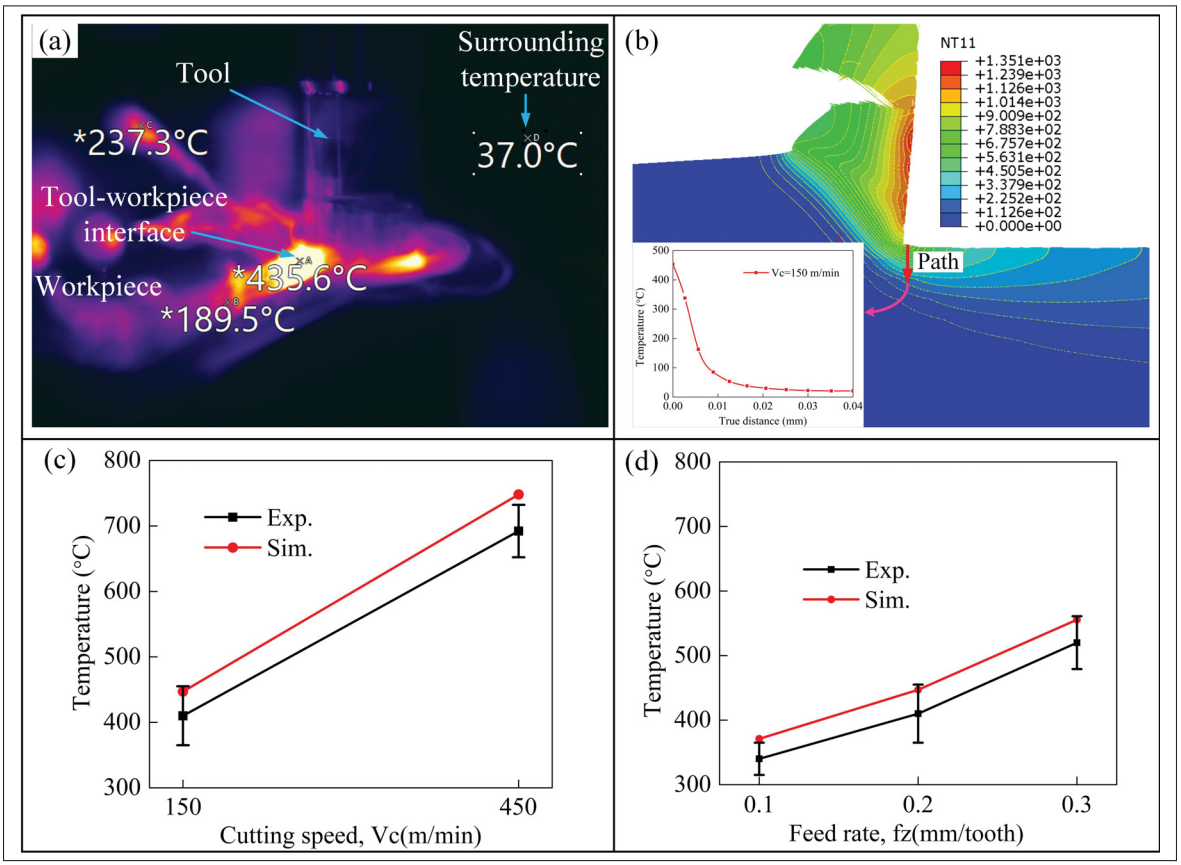

Figure 5.5 Comparison of experimental and simulated cutting temperature: (a) experimental cutting temperatures, (b) simulated cutting temperatures, (c) and (d) variation of cutting temperature against various cutting speeds and feed rates

accuracy of the FE model, the average values of the experimental and simulated cutting forces are compared and documented in Table 5.1. It can be seen that the measured cutting forces are slightly higher in magnitude than simulated ones; however, the relative error is in the range of 4.23-12.40 %, demonstrating the reliability of the cutting model across all machining conditions. These analyses revealed that the developed FE model used for cutting TC4 titanium alloy is accurate and reliable and can be utilized for residual stress prediction.

Table 5.1 Detailed comparative results of experimental and simulated cutting forces

Cutting parameters	Values	Average cutting forces	
		Fx(N)	Fy(N)
Vc=150 m/min	Experimental	467.86	295.26
	Simulated	448.08	265.3
	Relative error (%)	4.23	10.15
Vc=450 m/min	Experimental	622.03	481.67
	Simulated	592.7	452.46
	Relative error (%)	4.72	6.06
Fz= 0.10 mm/tooth	Experimental	269.25	209.23
	Simulated	242.89	183.29
	Relative error (%)	9.79	12.40
Fz= 0.20 mm/tooth	Experimental	467.86	295.26
	Simulated	448.08	265.3
	Relative error (%)	4.23	10.15
Fz= 0.30 mm/tooth	Experimental	528.84	388.19
	Simulated	498.29	348.95
	Relative error (%)	5.78	10.11
Footnote: Relative error % = $\left\lvert\frac{\text{(Experimental value-Simulated value)}}{\text{Experimental value}}\right\rvert$			

5.4.2 Simulated Machined Surface and Subsurface Plastic Strain and Residual Stress Profiles

Fig. 5.6 illustrates the simulation results for the equivalent plastic strain distributions during the machining of TC4 titanium alloy, highlighting the effects of cutting speeds on the machined surface and subsurface. The contour plot in Fig. 5.6(a) provides an overview of the spatial distributions of equivalent plastic strain. As can be seen from the figure, Path-1 and Path-2 were

designated for further quantitative analysis. Path-1 corresponds to the cutting direction along the topmost machined surface, while Path-2 is located beneath the machined surface to capture subsurface effects. Fig. 5.6(b) depicts that the plastic strain on the topmost machined surface (i.e., along Path-1) exhibits a cyclic behavior due to the periodic engagement and disengagement of the cutting tool, which induces localized plastic deformation during serrated chip formation. It can also be observed that the cyclic amplitude at a cutting speed of 450 m/min is nearly double compared to that at a cutting speed of 150 m/min, indicating that higher cutting speeds intensify the localized deformation due to increased mechanical and thermal loads. Similarly, as shown in Fig. 5.6(c), in the subsurface region (i.e., along Path-2), the plastic strain decreases in magnitude but remains cyclic, influenced by mechanical loads that extend into the workpiece depth. The simulation results of residual stress distribution along the X-direction ($\sigma 11$) and

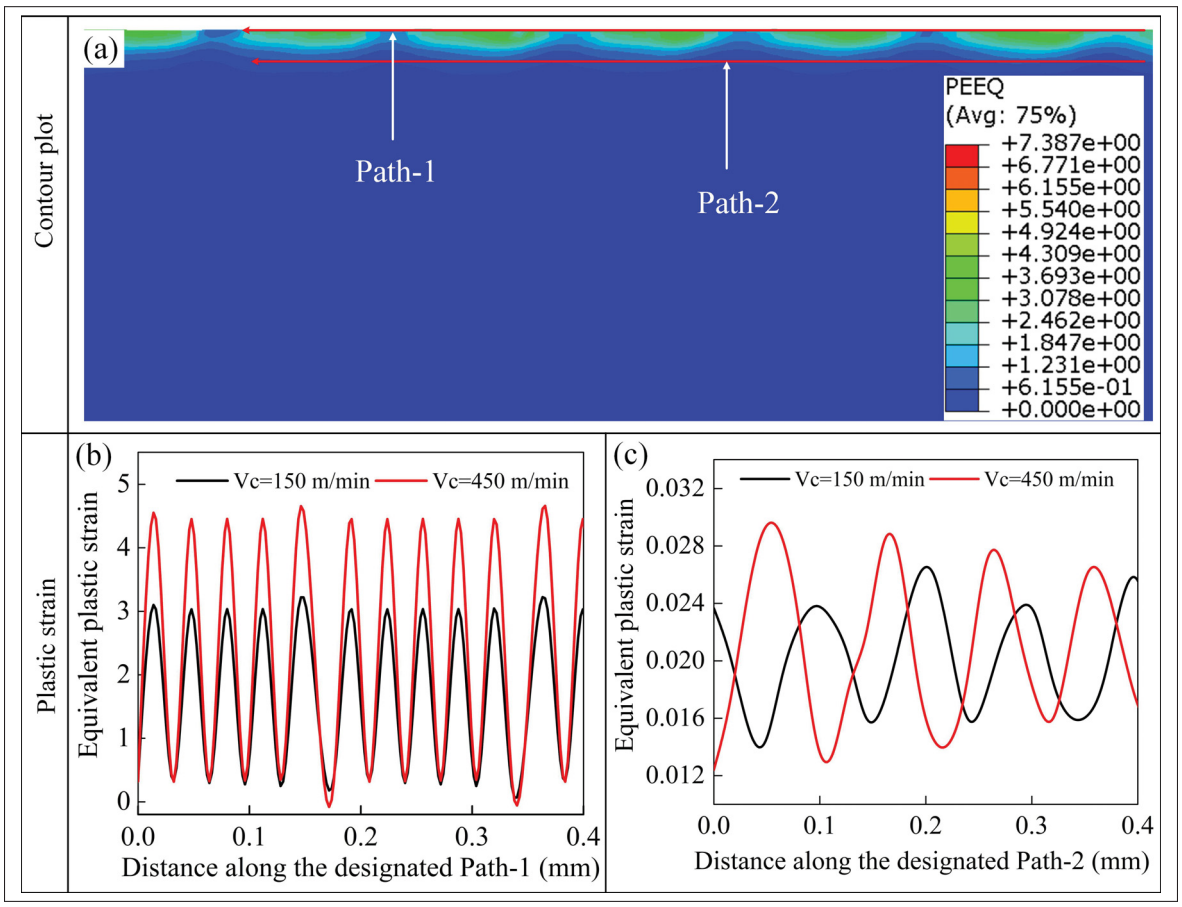

Figure 5.6 Simulated cyclic plastic strain distribution in the machined surface and subsurface regions

Y-direction (σ22) for the machined surface and subsurface are indicated in Fig. 5.7. The contour plots in Fig. 5.7 (a-b) display the spatial distributions of stress in the cutting direction and perpendicular to the cutting direction, respectively. To further enhance the understanding of residual stresses, the stress distribution along the topmost machined surface (Path-1) and the machined subsurface (Path-2) were plotted in Fig. 5.7(a1-a2), and Fig. 5.7(b1-b2), respectively. Fig. 5.7(a1-b1) represents the residual stress along Path-1, which shows a cyclic distribution for both σ11 and σ22. This periodic nature of the residual stresses can be attributed to the intermittent contact and release cycles between the cutting tool and workpiece. Furthermore, it can also be observed that at lower cutting speed (i.e., 150 m/min), the amplitude of σ11 and σ22 is tensile in nature. However, when the cutting speed was increased to 450 m/min, both compressive and tensile stresses were observed for the σ11, while the stress state still remained tensile for σ22. Similarly, Fig. 5.7(a2) and (b2) display the residual stress distributions in the subsurface region (i.e., along Path-2). It can be observed that the subsurface residual stress (i.e., σ11 and σ22) also exhibits a cyclic pattern, though with different magnitudes and less pronounced peaks. The stress values in the subsurface are predominantly compressive, reflecting the nature of subsurface deformation, which is primarily influenced by mechanical interactions rather than direct tool impact. Furthermore, it can also be seen that the compressive stresses are slightly higher in both directions at a cutting speed of 450 m/min. Generally, the increased mechanical loads at higher cutting speeds can promote plastic deformation of the machined subsurface. Also, higher strain rates associated with increased cutting speeds can result in work hardening, further contributing to the generation of compressive stresses (Zhang, Wu & Liu, 2011). As a result, slightly higher compressive stress was achieved. Similarly, the residual stress profiles from the machined surfaces down to the bulk are also demonstrated in Fig. 5.8. The σ11 stresses against cutting speeds of 150 and 450 m/min are depicted in Fig. 5.8(a). It can be observed that the residual stress on the machined surface at a cutting speed of 150 m/min is initially tensile and reaches approximately 93.56 MPa. However, as the depth increases, the stress shifts toward a compressive state, with a peak value of about -325 MPa at around 6 μm below the surface. Then, the stress then gradually reduces in magnitude, stabilizing toward the bulk material region. When the cutting speed was enhanced to 450 m/min, the residual

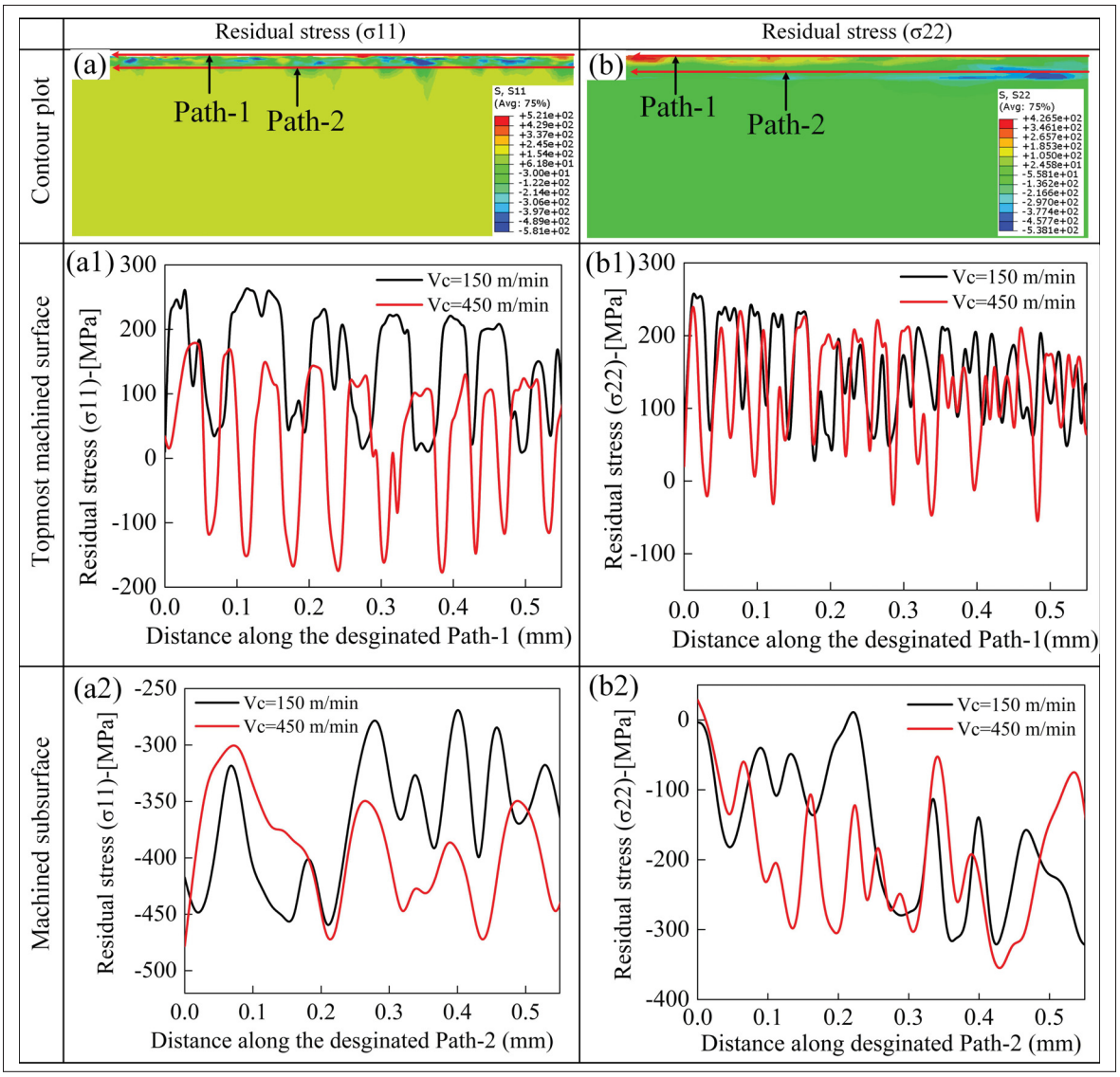

Figure 5.7 Simulation result of cyclic residual stress distribution for machined surface and subsurface

stress was compressive, reaching about -107.65 MPa, and the compressive stress reached a peak value of about -389.27 MPa at a depth of about 7.5 μm. The reduction in the magnitude of residual stress at higher cutting speeds can be attributed to increased thermal softening, which diminishes the mechanical deformation intensity. Similarly, as indicated in Fig. 5.8(b), the σ22 stress also exhibits a similar pattern. At 150 m/min, the residual stress is tensile on the machined surface, reaching approximately 138.73 MPa, and transitions to a compressive peak value of

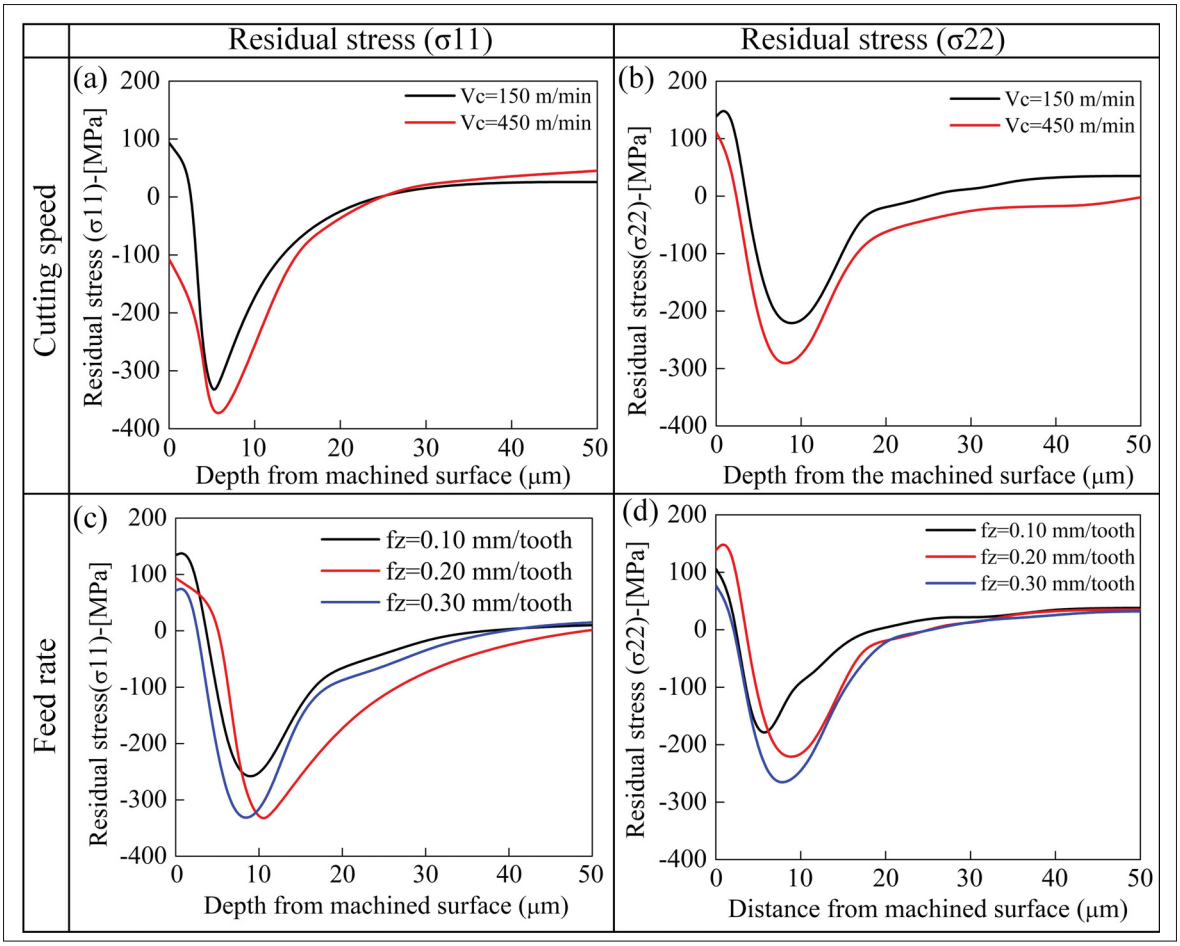

Figure 5.8 Simulation results of residual stress profiles from machined surfaces to the bulk region at various cutting speeds and feed rates

about - 229.69 MPa. For a cutting speed of 450 m/min, the tensile stress on the machined surface is slightly reduced to 111 MPa and then becomes compressed peak values of approximately -297.99 MPa in the machined subsurface. The reduced compressive stress at higher cutting speeds suggests that increased thermal effects dominate over mechanical interactions, leading to trivial plastic deformation in the subsurface. Analogous to the results indicated in Fig. 5.8(a-b), the influence of feed rate on residual stress was also analyzed. As shown in Fig. 5.8(c-d), when the feed rate was increased from 0.10 to 0.30 mm/tooth, no noticeable difference was observed in the residual stress distributions $\sigma 11$ and $\sigma 22$ on the machined surface. However, in the machined subsurface, the compressive residual stress varies significantly.

5.4.3 Comparison of Experimental and Simulated Residual Stress Distributions for Machined Surface and Subsurface

An in-depth understanding of residual stress distribution is crucial to enhance the fatigue life of service components. Fig. 5.9 compares the experimentally measured and simulated residual $\sigma 11$, and $\sigma 22$ stresses for the topmost machined surface and subsurface under various cutting parameters. Since the residual stress profile in milling is inherently non-uniform due to uncut chip thickness variations, therefore the whole machined surface and subsurface region were calculated and then averaged. Then, the simulation results were compared with the experimentally measured residual stresses. Fig. 5.9(a-b) exhibits the effect of cutting speeds on the average residual stress $\sigma 11$ and $\sigma 22$ for the topmost machined surface. It can be observed that at lower cutting speed (i.e., 150 m/min), the machined surface residual stress is predominantly tensile in nature. The experimental values of $\sigma 11$ and $\sigma 22$ reach approximately 125±22 MPa and 113.23±29 MPa, respectively. The simulated values are slightly lower than the experimental one for $\sigma 11$, while it override the experimental one for $\sigma 22$. The differences between the experimental and simulated residual stresses are due to the influences of the FE model's boundary conditions and thermal assumptions. When the cutting speed is enhanced to 450 m/min, the machined surface stress tends to decrease significantly, and the $\sigma 11$ stress is transformed into the compressive state. For instance, the simulated $\sigma 11$ value is approximately -87.49 MPa, while the experimental data shows a similar trend with the maximum compressive stress of about -109.23 ±26 MPa. The changing trend in stress magnitude at higher speed is likely due to increased thermal loads, which enhance the intensity of plastic deformation during machining. Similarly, the effects of feed rate on machined surface and subsurface residual stress is also investigated. As labeled in Fig. 5.9(a-b), when feed rate was increased from 0.10 mm/tooth to 0.30 mm/tooth, the $\sigma 11$ stress decreased continuously, almost becoming neutral, with simulated and experimental values roughly matched. This is because higher feed rates induce more thermal loads, resulting in more severe plastic deformation due to shorter tool-material contact durations. Fig. 5.9(c-d) shows the simulated and experimental $\sigma 11$ and $\sigma 22$ stress distribution in the machined subsurface regions, where the stresses are compressive due to plastic deformation virtuously resulting from mechanical loading, as the thermal impact cannot infiltrate severely into the workpiece. As

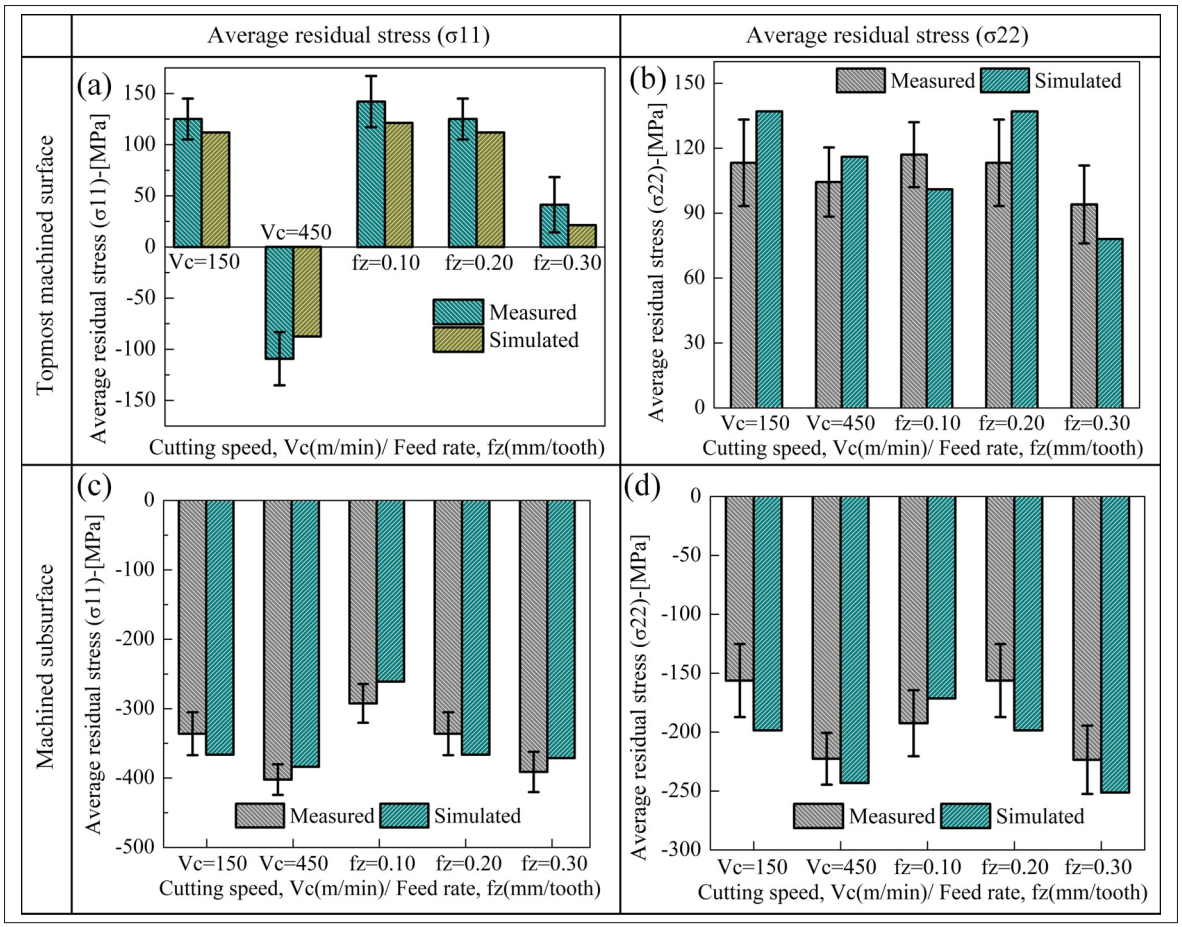

Figure 5.9 Comparison of experimental and simulated residual stress for machined surfaces and subsurface

demonstrated in Fig. 5.9(c), at a cutting speed of 150 m/min, the simulated $\sigma 11$ stress value is around -366.30 MPa, which is consistent with the experimental results (i.e., -336.23±32 MPa). In contrast, the simulated $\sigma 22$ stress value is about -198.53 MPa compared to the experimental value of about -156.23±36 MPa. Similarly, when the cutting speed was increased to 450 m/min, the compressive stress values in both directions significantly enhanced, and the percentage relative errors between experimental measured and simulated residual stresses were 5.79 % and 10.37 %, respectively. A similar trend was obtained for varying feed rates. As indicated in Fig. 5.9(c-d), when the feed rate was increased from 0.10 mm/tooth to 0.30 mm/tooth, the simulated $\sigma 11$ stress values increased from about -261.03 MPa to -371.30 MPa, while the experimental $\sigma 11$ enhanced from about -292.35 MPa to -391.2 MPa, respectively.

At the same time, the simulated compressive $\sigma 22$ stress values are about -171.42 MPa and -251.30 MPa, while the experimental $\sigma 22$ stress values are about -192.45 MPa and -223.52 MPa, respectively. It is worth noting that there are some differences between the simulated and experimental residual stress distributions within the machined surface and subsurface, which may be due to measurement inaccuracies, model simplifications, or assumptions about thermal and mechanical boundary conditions. Nonetheless, the findings highlight the importance of machining conditions in managing residual stress distributions and improving the fatigue life and performance of machined components.

5.4.4 Correlation Between Thermo-Mechanical Loads and Residual Stresses

In machining, residual stress formation is a complex phenomenon driven by the combined effects of thermo-mechanical loading history and microstructural changes such as phase transformation, which induces volumetric changes. Generally, the residual stresses on the machined surface are predominantly influenced by thermal loads due to the intense heat generated during the cutting process. In contrast, subsurface residual stresses are primarily influenced by mechanical loading, as the thermal effects diminish significantly with increasing depth into the workpiece. Hence, understanding the interplay between these factors is critical for optimizing machining parameters to achieve desired residual stress profiles that improve machined components' performance and fatigue life. This section explicitly examines the impact of thermal loads on surface residual stress and mechanical loads on subsurface residual stress. Fig. 5.10(a,b) depicts the variation of the residual stress (i.e., $\sigma 11$ and $\sigma 22$) on the machined surface with feed rate and temperature, respectively. It is evident that higher temperatures significantly influence the surface residual stresses. As indicated in Fig. 5.10(a), at a feed rate of 0.10 mm/tooth, the experimentally obtained cutting temperature is approximately 340°C and the $\sigma 11$ stress is tensile, which is around 142.03 MPa, while the simulated temperature and stress are slightly lower, around 371°C, and 121.23 MPa, respectively. However, when the feed rate was increased to 0.30 mm/tooth, both the experimental and simulated temperatures increased significantly, while the residual stress became less tensile, which reflects a reduction in the thermal impact due to the reduced

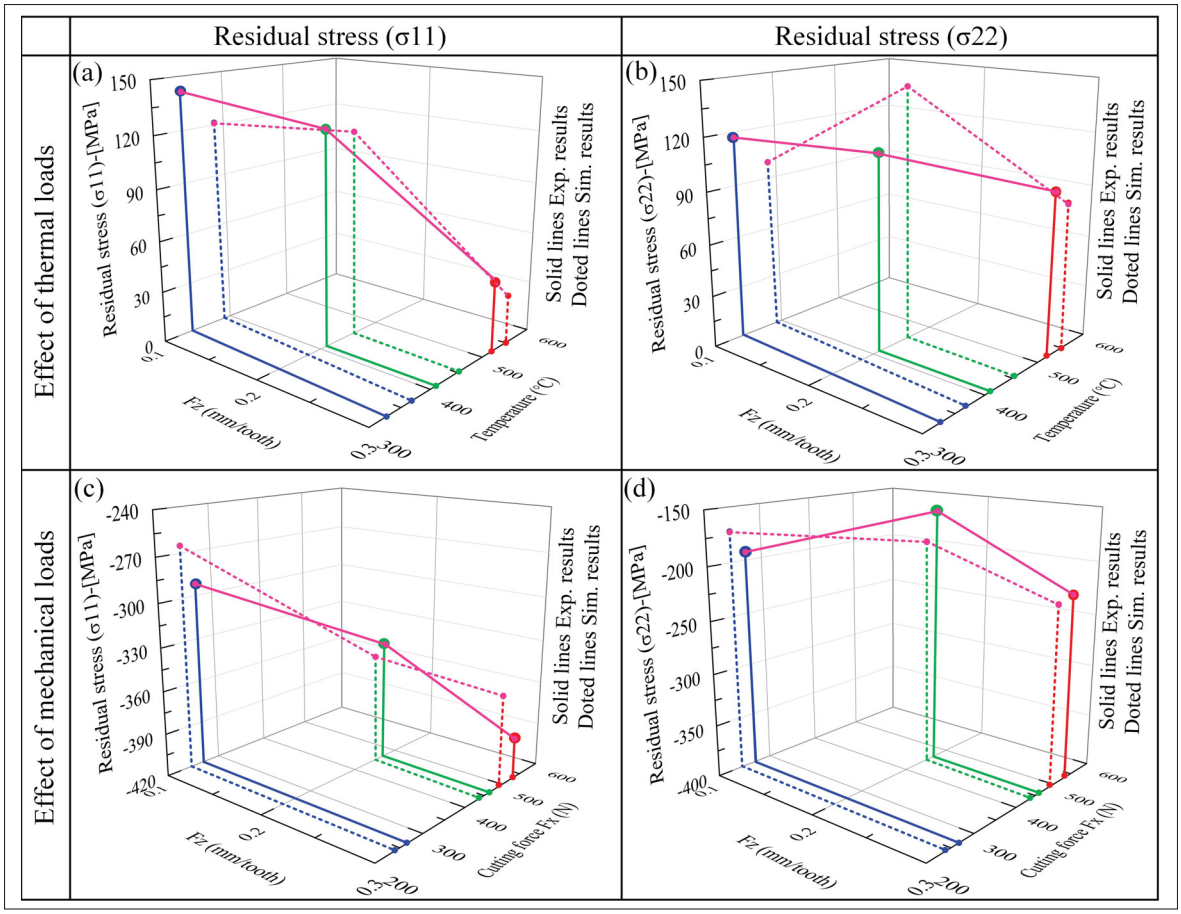

Figure 5.10 Correlation between thermo-mechanical loading history and residual stresses for machined surfaces and subsurfaces

cutting zone engagement time. Similarly, the experimental $\sigma 22$ stresses decrease slightly with increasing temperature. However, when it comes to the simulated $\sigma 22$ stress, it first increases with an increase in feed rate and temperature; with a further increase in feed rate, the temperature continues to enhance, and the residual stress tends to decrease. Similarly, the effect of mechanical load on the subsurface residual stress is indicated in Fig. 5.10 (c-d). Unlike surface stresses, subsurface residual stresses are compressive due to the dominance mechanical load of plastic deformation. At a feed rate of 0.10 mm/tooth, the measured cutting force is about 269.25 N, and the $\sigma 11$ stress value is roughly -292.35 MPa, which nearly matches the predicted values of 242.89 N and -261.03 MPa, respectively. When the feed rate was increased to 0.30 mm/tooth, the measured cutting forces increased further, reaching about 528.84 N, and the $\sigma 11$ stress value

became more compressive, ultimately reaching about -391.23 MPa. In contrast, the simulated cutting force and $\sigma 11$ stress values are about 498.29 N and -371.30MPa, respectively. Similarly, for the stresses in the Y-direction, when the feed rate first increased from 0.10 mm/tooth to 0.20 mm/tooth, the measured $\sigma 22$ stress increased slightly at first, and with further increase in feed rate (i.e., 0.30 mm/tooth), the $\sigma 22$ stress decreased to around -223.52 MPa. Similar results can also be seen in the simulation results. These analyses show that the residual stress change trends are associated with increasing/decreasing patterns of the thermo-mechanical loading histories, as approximately a linear relation between thermo-mechanical loading histories and residual stresses was obtained.

5.5 Conclusions

This study develops a simplified 2D thermo-mechanical coupled FE model to predict the residual stress distributions induced by HSM of TC4 titanium alloy. Based on the findings, the following conclusions can be drawn:

1. The simulated degree of chip segmentation closely aligns with the experimental observations, demonstrating an increasing trend with higher cutting speed and feed rates. This indicates that high machining parameters promote a complete separation of serrated chip segments. The developed FE model also demonstrated a high predictive accuracy, with percentage relative errors ranging from 6.85% to 9.12% and 4.23% to 12.40%, for cutting temperature and forces across all machining conditions, respectively.
2. The simulation results revealed that plastic strain exhibits a cyclic pattern for the machined surface and subsurface, with its intensity increasing at higher cutting speed. The simulated residual stresses ($\sigma 11$ and $\sigma 22$) demonstrated a similar cyclic behavior. At lower cutting speed (i.e., 150 m/min), both $\sigma 11$ and $\sigma 22$ stresses on the machined surface were tensile. However, at higher cutting speed (i.e., 450 m/min), $\sigma 11$ stress was transformed into the compressive stress, while $\sigma 22$ stress remained as tensile. In addition, experimental and simulated $\sigma 11$ and $\sigma 22$ stresses demonstrated good agreement

3. Residual stress profiles showed a hook-shaped distribution. Both $\sigma 11$ and $\sigma 22$ stresses reached their maximum compressive state at a depth of 7–10 μm below the surface, then gradually approached zero at depths of approximately 22–35 μm. This reflects the inhomogeneous distribution of residual stress influenced by thermal-mechanical interactions.
4. It is also observed that the increased feed rate caused minor changes in surface stress, with $\sigma 11$ and $\sigma 22$ stresses predominantly tensile. In contrast, subsurface residual stresses were compressive in both directions and tended to increased with feed rates.
5. The effect of thermo-mechanical loads on residual stress indicated that thermal loads predominantly affect the residual stresses on the machined surface, while mechanical loads govern the residual stresses in the subsurface region. Higher feed rates reduced surface tensile stresses and enhanced subsurface compressive stresses, thus improving fatigue resistance.

CHAPTER 6

A COMPREHENSIVE EXPERIMENTAL INVESTIGATION ON THE CORRELATION BETWEEN CHIP FORMATION, MACHINED SURFACE INTEGRITY, AND PARTICLE EMISSIONS DURING HIGH-SPEED MILLING OF TC4 TITANIUM ALLOY

Irfan Ullah [1] , Esther Titilayo Akinlabi[2] , Jules Kouam [1] , Victor Songmene [1]

[1] Department of Mechanical Engineering, , École de Technologie Supérieure, 1100 Notre-Dame Ouest, Montréal, Québec, Canada H3C 1K3
[2] Department of Mechanical and Construction Engineering, Northumbria University, Newcastle Upon Tyne NE1 8ST, United Kingdom

This article is published in *"The International Journal of Advanced Manufacturing Technology"*, Volume 136, January 2025, Pages 3285-3301 https://doi.org/10.1007/s00170-025-15039-3

Abstract

In today's industry, machining processes must not only meet technical and economic requirements but also prioritize sustainability in terms of environmental impact and operator safety. Recently, particle emissions have gained significant attention due to their detrimental effects on the environment, operator health, workpiece quality, and energy efficiency. Hence, the current research aims to investigate particle emissions, their correlations with machining parameters, and machined part surface integrity. First, high-speed milling (HSM) experiments were conducted under various cutting parameters in a dry environment, and the effect of cutting parameters on chip formation, machined subsurface microstructure evolution, burr formation, particle emissions, and surface roughness was analyzed. The experimental results revealed that parameters such as cutting speed initially increased chip serration, deformed layer thickness, particle emissions, and surface roughness, followed by a subsequent decrease. In contrast, it consistently increased with feed rates and depth of cuts. Finally, the correlation between particle emissions and machined surface integrity was obtained and discussed. The current research can provide more valuable insights for designing sustainable and safe machining processes that balance efficiency with reduced environmental impact and improved operator safety.

Keywords: Burr formation, Chip formation , Fine particle emission , High-speed milling , Microstructure evolution , Surface roughness , TC4 titanium alloy

6.1 Introduction

HSM of TC4 titanium alloy is a critical process in aerospace and biomedical industries due to its exceptional mechanical properties, such as its high strength-to-weight ratio, corrosion resistance, and biocompatibility (Ezugwu *et al.*, 2007; Sun & Guo, 2009; Ullah *et al.*, 2021a). However, the machining of TC4 titanium alloy presents significant challenges, including high cutting forces, rapid tool wear, and heat generation, which can adversely affect the machined surface integrity (Gupta *et al.*, 2023; Ullah, Akinlabi & Songmene, 2024b). Despite the recent enhancement in developing high-performance and improved machine tools, HSM still poses many challenges, especially to the machine operators and the surrounding working environment. Among other challenges, fine and ultrafine particle emissions are receiving increased attention due to their adverse effects on the machine shop environment, the health of machinists, and machining products. On the one hand, these tiny particles have the potential to remain suspended in the air for an extended period. On the other hand, these particles can adversely affect the operator's health, primarily through skin contact and inhalation (Hands, Sheehan, Wong & Lick, 1996). The detrimental effects of dust generated during the machining entering the respiratory system are contingent upon various factors, including type of materials, machining conditions, and tool geometries (Khettabi, Fatmi, Masounave & Songmene, 2013). To date, research on the machinability of the TC4 titanium alloy has primarily focused on the surface integrity of machined parts, encompassing aspects such as microstructural evolution, surface roughness, residual stress prediction, and enhancement of cutting tool life (Ulutan & Ozel, 2011; Abbasi *et al.*, 2016; Sharma & Meena, 2020). However, the potential hazards posed by fine and ultrafine particles during machining operations can equally contribute to performance criteria. Therefore, a detailed assessment of the particle emission sources and their relationship with the cutting deformation zones during mechanical machining becomes essential to optimize machining parameters, improve surface integrity, ensure environmental safety, and achieve

cost efficiency, contributing to sustainable manufacturing practices. In general, all machining processes generate aerosols (solid, liquid, or mixt forms), which can be harmful to operator health and the environment (Khettabi, Songmene & Masounave, 2010a; Zhao *et al.*, 2023). Solid aerosols are produced during dry and wet machining, whereas liquid aerosols are generated when cutting fluids are applied (Zhao *et al.*, 2023). Several insightful studies have documented particle emissions during the machining of metallic and non-metallic materials. (Sokolović, Höflinger, Sokolović, Sokolović & Sakulski, 2013) conducted experimental work on aerosol/mist formed from three different metalworking operations with varying concentrations of oil-in-water emulsions. They discovered that increasing the oil concentration in the emulsion led to an increase in both particle concentration and size. (Sutherland, Kulur, King & Von Turkovich, 2000) analyzed the particle emissions during machining of gray cast iron at various cutting speeds and observed that the particle concentration during wet cutting was 12 to 80 times higher than that during dry turning. However, (Songmene, Balout, & Masounave, 2008) reported that cutting fluids can lower particle generation by 40 to 50% compared to dry machining. (Zaghbani, Songmene & Khettabi, 2009) distinguished fine and ultrafine particles during HSM of 6061-T6 aluminum alloys and observed that the mass concentration of particles in the size range of 0.5–1 μm was 5 to 30 times higher during wet milling than dry milling. However, for particles in the 1–10 μm size range, the mass concentration was significantly lower during wet milling compared to dry milling. (Li, Aghazadeh, Hatipkarasulu & Ray, 2003) carried out a detailed assessment of different categories of oil mist particles and found that 95% of the oil mist particles generated during the milling process were less than 3 μm in diameter. Besides, some scholars analyze the effect of cutting tool coatings and tool geometry on the intensity of dust formation during the turning and milling process of brittle materials. (Arumugam *et al.*, 2003) experimentally analyzed the effect of PCD and CVD coated inserts, feed rates, and depth of cut on particle emission during dry cutting of aluminum-silicon alloys and found that feed rate and depth of cut for PCD inserts and speed and feed rate for CVD inserts significantly affected aerosol concentration. Similarly, (Djebara *et al.*, 2013) used TiCN and TiCN/Al2O3/TiN coated tools in dry slot milling of 2024-T351, 6061-T6, and 7075-T6 aluminum alloys to analyze the specific surface area of PM2.5, and found that cutting speed and tool coating were the most important

factors influencing the specific surface area of the ultrafine particles. (Khettabi *et al.*, 2007) examined the tool geometry and cutting conditions effects on particle emission during the turning process of 4140 steel, 1018 steel and 6061-T6 aluminum alloy. They concluded that the cutting speeds at which particle emissions is high are sensitive to the lead angle for the 1018 steel and 6061-T6 aluminum alloy, compared to 4140 steel. Some analytical models were also presented for quantifying particle emissions under various cutting conditions. An analytical model based on Needelman-Lemond's for particle emission was proposed by (Khettabi *et al.*, 2010b), which took into consideration tool-chip friction and the material's plastic deformation. Similarly, (Chen, Atmadi, Stephenson, Liang & Patri, 2000) developed an analytical model for the prediction of aerosol generation resulting from the metal cutting fluids. The model examines the primary mechanisms of spin-off, splash, and diffusion to formulate the airborne particulate concentration and size distribution in quantitative terms of fluid properties, fluid application conditions, cutting process parameters, and machining time. (Rautio *et al.*, 2007) developed an empirical model for particle emission by considering the average chip thickness and found that the fraction of particles generated is inversely proportional to the chip thickness. However, the developed model was only applicable for medium-density fiberboard materials. From the above literature, it is evident that earlier research endeavors have examined various materials but neglected to incorporate titanium and its alloys. The manner in which chips are formed, and particles are released from titanium and its alloys diverges from that of other materials. Furthermore, the existing research also indicated that most dust-generated studies were carried out on turning and grinding processes and were conducted in lubrication conditions. It is important to note that conventional cutting fluids always require considerable energy and resource consumption, which can be considered divergent to an environmentally friendly society. Therefore, this research conducted HSM experiments of TC4 titanium alloy in a dry environment. The main objectives of this research are several folds. First, the effect of a wide range of cutting conditions on the chip serration was studied. Secondly, the machined surface layer microstructure evolution and burr formation was analyzed. Thirdly, the machining-induced particle emission was investigated. Subsequently, the machined surface roughness was also examined. Finally, the correlation between particle emission and machined surface integrity was presented.

6.2 Material and Methods

6.2.1 Workpiece, Cutting Tool, and Machining Setup

TC4 titanium alloy having a chemical composition of 6.11-6.14 wt% Al, 3.89-4.01 wt% V, 1.4-2.6 wt% Sn, 0.31-1.1 wt% Fe, 0.34-90 wt% Cu was used as a material test for the HSM. The as-received alloy's microstructures, phase composition, and thermo-mechanical properties are shown in Fig. 6.1(d) and Table 6.1, respectively. A 3-axis computerized numerical control high-speed milling machine (Huron K2X10: 50 Nm torque, 28000 rpm max spindle speed) was used to machine TC4 titanium alloy specimens. PVD-coated carbide indexable cutting inserts

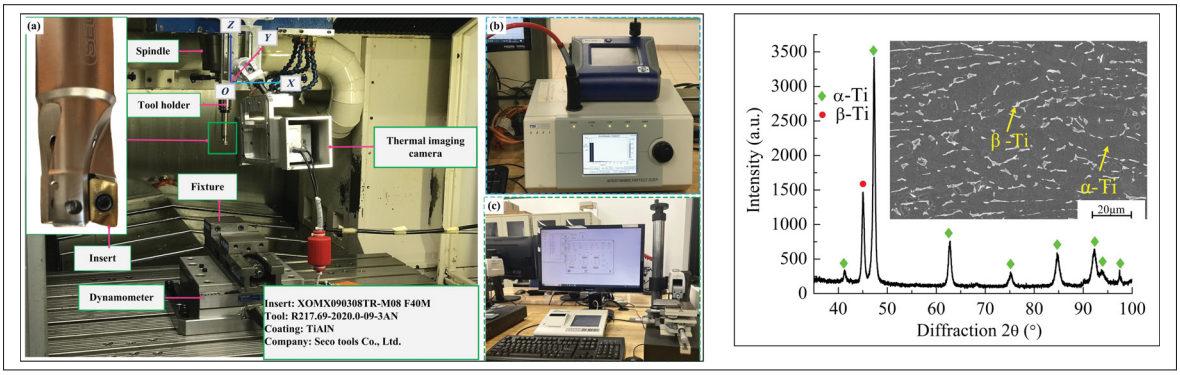

Figure 6.1 Experimental setup. (a) Machining setup, (b) particle collection unit, (c) surface roughness measurement setup, and (d) microstructure and the phase composition of as-received material

(XOMX090308TR-M08 F40M) which were held tightly with a milling cutter (R217.69-2020.0-09-3AN), were utilized during the milling tests. A new insert was employed for each experiment, and every experiment was repeated three times to ensure the reliability and consistency of results. Details of the cutting parameters for the milling process are listed in Table 6.2.

Table 6.1 Thermo-mechanical properties of TC4 titanium alloy at ambient temperature

Density (kg/m^3)	Thermal Conductivity ($W/m°C$)	Elastic Modulus (GPa)	Yield Strength (MPa)	Poisson's Ratio	Specific Heat ($J/kg°C$)	Melting Point (°C)
4430.8	6.80	109	880	0.34	611	1610

Table 6.2 Matrix of experiments used for the HSM of TC4 titanium alloy

Exp. Nos	Cutting Speed v_c (m/min)	Radial Depth of Cut a_c (mm)	Axial Depth of Cut a_p (mm)	Feed per tooth f_z (mm/z)
1#	150	1.6	1.4	0.20
2#	250	1.6	1.4	0.20
3#	350	1.6	1.4	0.20
4#	150	1.6	1.4	0.10
5#	150	1.6	1.4	0.20
6#	150	1.6	1.4	0.30
7#	150	1.6	1.4	0.20
8#	150	1.9	1.4	0.20
9#	150	2.2	1.4	0.20

6.2.2 Measurement Procedure and Sample Preparation

A Kistler piezoelectric dynamometer (type 9255B) was employed in the milling trials to measure the cutting force components in three directions (Fx, Fy, and Fz). The workpiece was firmly secured to the dynamometer with bolts, and the dynamometer was then attached to the machine tool using a fixture. Similarly, as depicted in Fig. 6.1(b), an Aerodynamic Particle Sizer (APS, model 3321, TSI Inc., Shoreview, MN, USA) was used to measure particle number concentration, mass concentration, and specific area concentration as a function of aerodynamic diameters (μm). The data acquisition time was set to 30 seconds, and the emitted particles were sucked through a 10 mm suction tube positioned 10 cm horizontally from the tool/workpiece interface. After completing the milling experiments, surface roughness measurements were taken on machined surfaces using a Keyence VR-5200 microscope and a portable profilometer (Surftest SJ-410, Mitutoyo America Corporation, Aurora, IL, USA), which can generate various roughness parameters (Ra, Rq, Rt, Rz, etc.). Finally, samples with dimensions 0.5 cm^3 were cut from the milled surface for subsurface microstructural investigation. These samples were molded with bakelite, ground with abrasive papers (600, 1200, and 2000 grit), polished with 5μm and 3μm diamond suspensions, and etched with Kroll's reagent. For chip segmentation analysis, the obtained chips were ultrasonically cleaned to remove dust and other impurities. Scanning

electron microscopy (SEM) and optical microscopy (OM) were used to analyze microstructural changes, burr formation, and chip segmentation.

6.3 Results and Discussion

6.3.1 Effect of Cutting Parameters on Chip-Free Surface

During metal cutting, shear degeneration and slippage of the workpiece material can cause friction between the shearing surface and the slip layers, leading to particle emission from the primary deformation zone. Similarly, friction generated due to the plastic degeneration of chip material in the secondary deformation zone can also result in particle emissions (Zhao *et al.*, 2023). Therefore, a detailed analysis of chip cross-sectional morphology can provide more insights into particle emissions. To analyze the chip formation mechanism, SEM images of chip-free surfaces at various cutting speeds are shown in Fig. 6.2. It can be observed that the free surface of the obtained chip primarily consists of lamellar structures caused by the shearing mechanism, with each slice forming a sawtooth segment across all cutting speeds. As shown in Fig. 6.2 (a-a1) and (b-b1), for Exp No.1 and 2, the slipping and undeformed surfaces of a segmented chip are more uniform compared to Exp no.3, where these surfaces exhibit irregular heights, small interstices, and irregular shear initiations. At higher magnification, the difference is even more evident; as indicated in Fig. 6.2 (a2-c2), increasing the cutting speed leads to a higher number of slipping and undeformed surfaces, indicating a lower shear band frequency. Additionally, some microvoids and shear dimples were observed for Exp nos.1 and 2, indicating that ductile fracture occurred at the chip-free surface. The shear dimples were more uniform at lower cutting speeds (Exp. no.1). However, with increased cutting speed (Exp. no 2), the shear dimples became elongated, indicating predominantly ductile behavior due to high thermal and mechanical loads. These shear dimples are mainly caused by the formation and coalescence of microvoids, involving severe localized plastic deformation due to frictional heat at the tool-chip interface (Chen, Ge, Lu, Liu & Ren, 2021). When the cutting speed increased further (Exp no.3), a few cracks appeared on the chip-free surface. These cracks are likely due to heat effects,

high strain rates, stress concentration, reduced plastic deformation, and possible tool wear. The

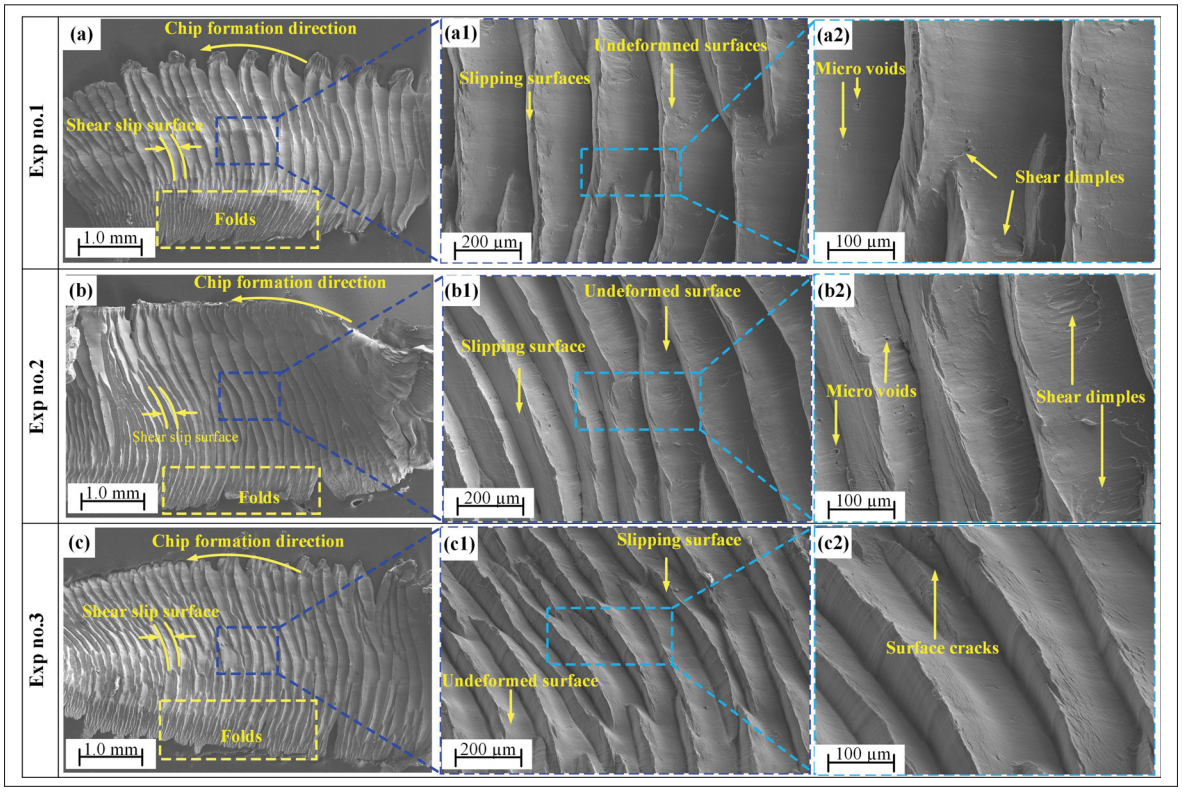

Figure 6.2 SEM images of chip-free surface at various cutting speeds: (a-a2) 150 m/min, (b-b2) 250 m/min, and (c-c2) 350 m/min

absence of micro voids and shear dimples implies a brittle fracture process, which is common in high-speed machining with intense thermal and mechanical loads (Wang, Li, Liu & Zhang, 2022). Similarly, by analyzing the lower half of the chip-free surface, a zigzag chip layer structure that transitions to a banded shape fold structure was observed. The comparison indicated that when the cutting speed increased from 150 to 250 m/min, the number of folds was reduced; with a further increase in cutting speed to 350 m/min (Exp no.3), the number of folds was enhanced again. The reduction in folds at a cutting speed of 250 m/min can be attributed to thermal softening and more uniform material flow, facilitating smoother chip formation. However, at higher cutting speed (Exp no.3), the increased thermal effects, higher strain rates, and greater tool wear lead to more complex and unstable material flow, resulting in increased folds in the chip. Similar to the results displayed in Fig. 6.2, the effect of feed rates on chip-free surfaces has

also been analyzed. As shown in Fig. 6.3, the feed rates significantly influenced the chip-free surface. At lower feed rates (i.e., Exp no. 4), no prominent slipping and undeformed surfaces were observed (Fig. 6.3 (a-a1)). However, the microvoids and shearing dimples were more severe for this experimental trial, as displayed in Fig. 6.3(a2). The smoother surface results from the controlled and uniform plastic deformation, while the severity of microvoids and shearing dimples is due to the localized intense shear and stress experienced by the material during the cutting process. Similarly, at lower feed rates, it can also be observed that the material being cut is insufficient to cause any apparent folds. As the feed rate increased (i.e., Exp no.5), the chip serration increased significantly, with more slipping and undeformed surfaces, and an increased pattern of folds can be observed. However, similar to Exp no.3, when the feed rate reaches 0.30 mm/tooth, limited folds were observed. The effect of the radial depth of cut on the chip-free

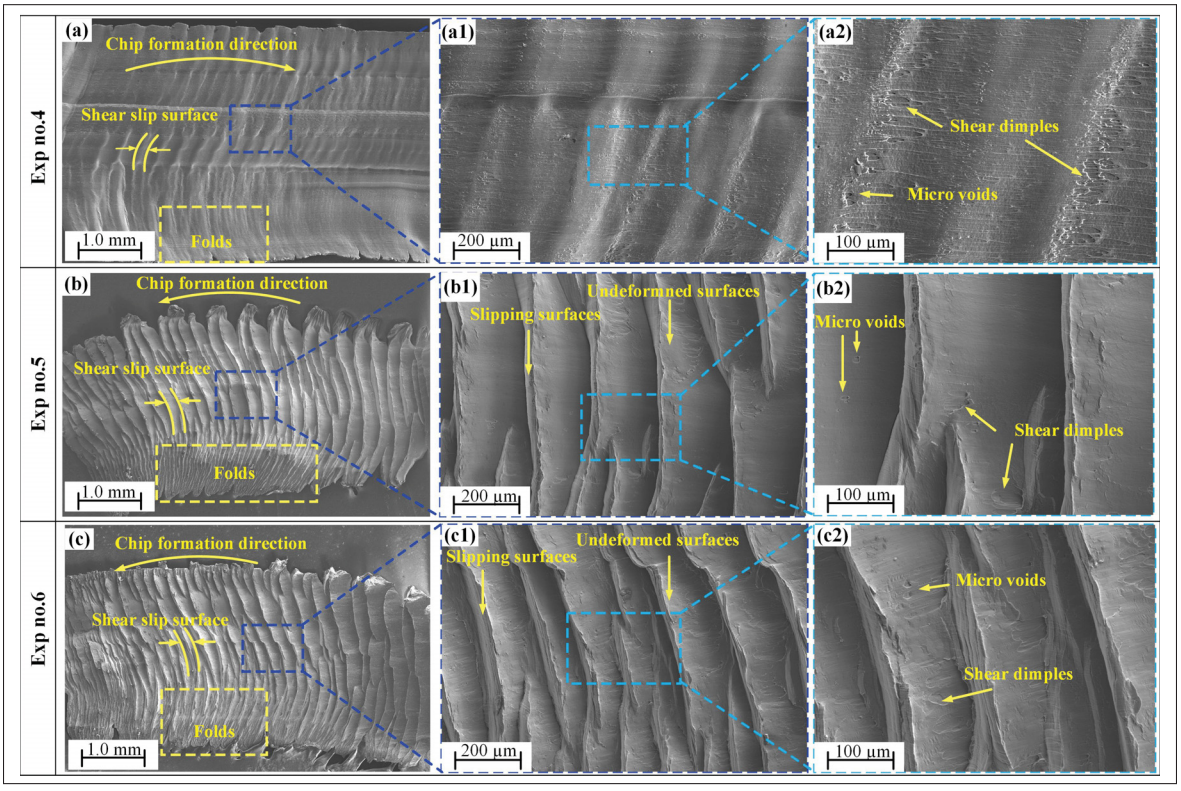

Figure 6.3 SEM images of the chip-free surface at various feed rates: (a-a2) 0.10 mm/tooth, (b-b2) 0.20 mm/tooth, and (c-c2) 0.30 mm/tooth

surface is demonstrated in Fig. 6.4. Strong evidence of serrated chips across all the experimental

trials can be observed. Initially, a more uniform slice of lamellar structure can be observed for Exp nos. 7 and 8. However, when the depth of cut was increased further (i.e., Exp no. 9), resulting in significant increases in slipping and undeformed surfaces. Furthermore, for Exp no.9, a periodic occurrence of segmentation and micro-cracks initiated in front of the shear zone was observed. This is more visible in Fig. 9 (c1), where the discontinuous lamellae on the lower part of the chip-free surface were generated by the adiabatic shear in the primary cutting zone. Furthermore, it can also be observed that the chip serration is significantly increased as the radial depth was enhanced.

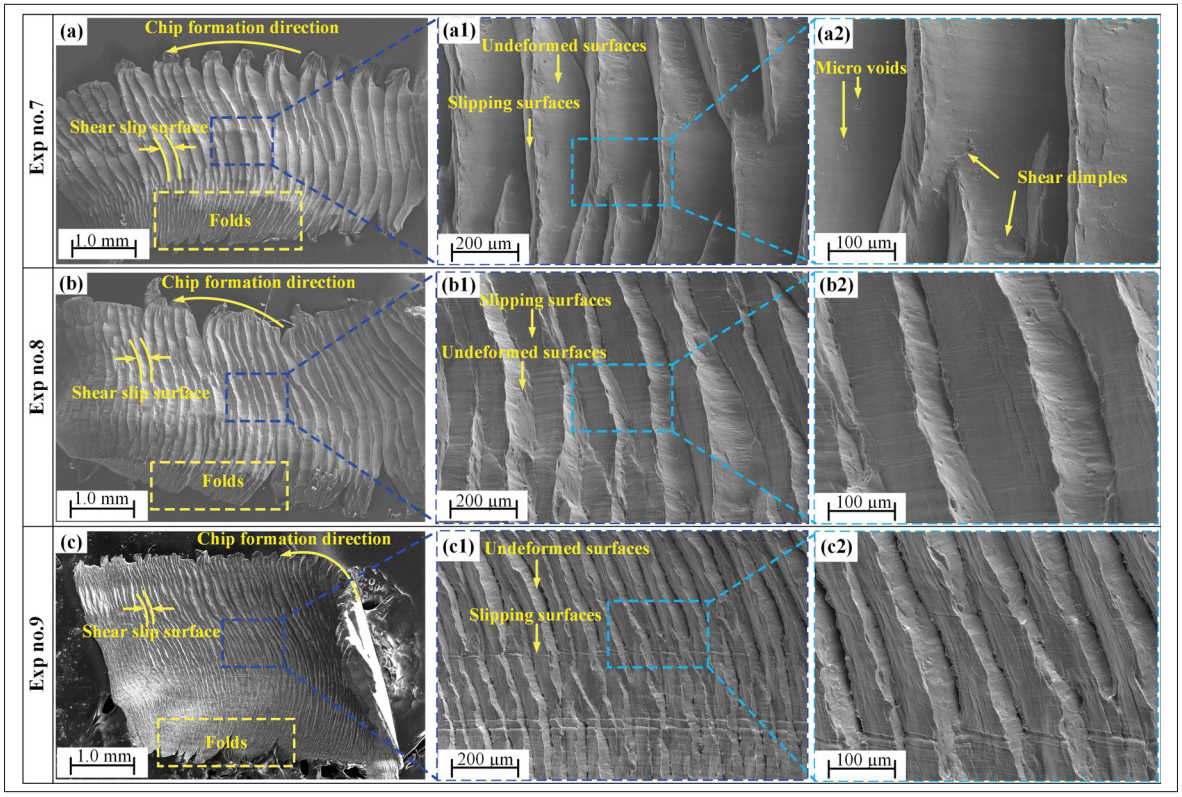

Figure 6.4 SEM images of chip-free surface at various radial depths of cuts: (a-a2) 1.6 mm, (b-b2) 1.9 mm, and (c-c2) 2.2 mm

6.3.2 Effect of Cutting Parameters on Microstructure Evolution and Burr Formation

The plastic deformation of the workpiece and burr formation, resulting from extrusion and friction at the contact interface between the workpiece and the cutting insert flank face, serve as additional indicators of particle emissions. As a result, this section gives a thorough examination of the machined subsurface microstructure and burr development during the HSM of TC4 titanium alloy. The SEM micrographs of machined subsurface microstructure and burr formation at various cutting speeds have been demonstrated in Fig. 6.5. It can be seen from Fig. 6.5 (a-c),

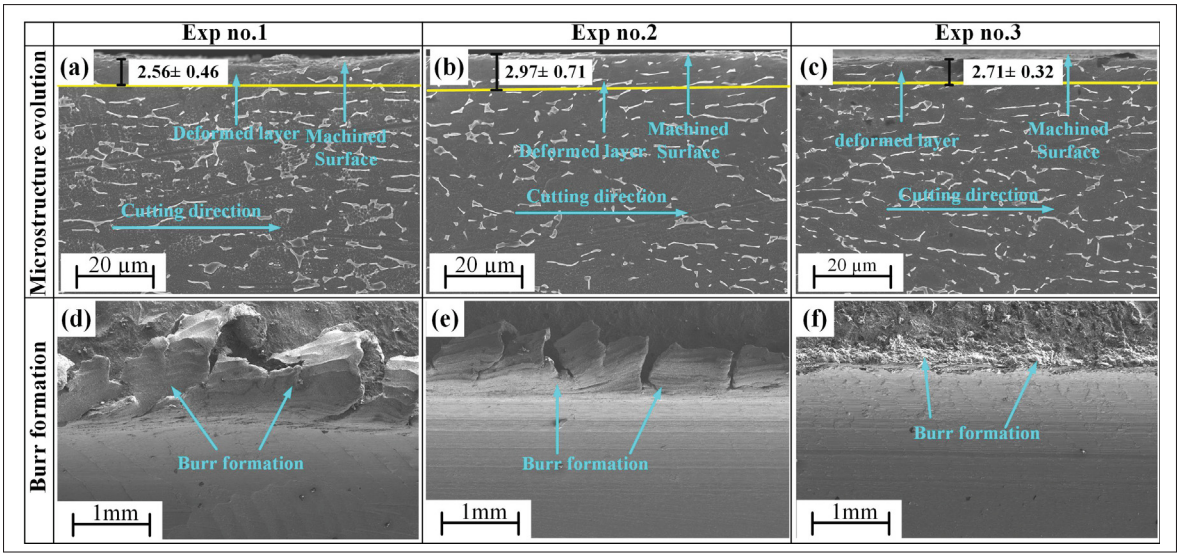

Figure 6.5 Microstructure evolution of the machined surface layer and burr formation analysis at varying cutting speed. (a–c) microstructures of machined surface layer (d-f) burr formation

initial at a cutting speed of 150 m/min (i.e., Exp no.1) a fragile deformed layer of about 2.56 μm was observed, in which the β-Ti is rotated in the cutting direction. When the cutting speed increased to 250 m/min (i.e., Exp no.2), the depth of plastic deformation increased further, ultimately reaching about 2.97 μm. However, when the cutting speed approaches 350 m/min (i.e., Exp no.3), the thickness of the deformed layer is reduced to 2.71 μm. The reduction in a deformed layer can be attributed to higher cutting temperatures in the tertiary deformation zone and reduced contact time at the tool-workpiece interface. Furthermore, the variation in deformed layer thickness is highly correlated with mechanical loading history (i.e., cutting forces). As

shown in Fig. 6.8, when the resultant cutting force increases, the deformed layer thickness increases due to increased stress and energy input, causing the material to deform plastically to a more considerable extent. In contrast, when the resultant cutting force is decreased (Exp no.3), the lower stress and energy input result in a shallower deformation zone. It is also observed for Exp no.3 that the volume fraction of β-Ti becomes very small and almost disappears in the near milled surface. The plastic deformation of the workpiece and burr formation, resulting from extrusion and friction at the contact interface between the workpiece and the cutting insert flank face, serve as additional indicators of particle emissions. As a result, this section gives a thorough examination of the machined subsurface microstructure and burr development during the HSM of TC4 titanium alloy. The SEM micrographs of machined subsurface microstructure

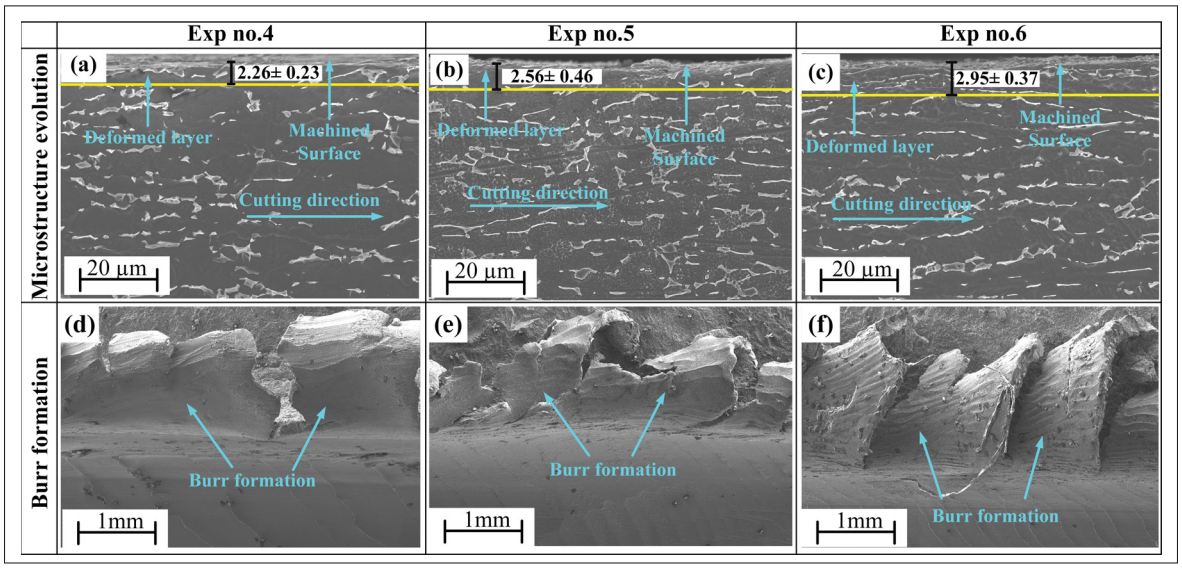

Figure 6.6 Machined surface layer microstructure evolution and burr formation analysis at varying feed rates. (a–c) microstructures of machined surface layer, and (d-f) burr formation

and burr formation at various cutting speeds have been demonstrated in Fig. 6.5. It can be seen from Fig. 6.5 (a-c), initial at a cutting speed of 150 m/min (i.e., Exp no.1) a fragile deformed layer of about 2.56 μm was observed, in which the β-Ti is rotated in the cutting direction. When the cutting speed increased to 250 m/min (i.e., Exp no.2), the depth of plastic deformation increased further, ultimately reaching about 2.97 μm. However, when the cutting speed approaches

350 m/min (i.e., Exp no.3), the thickness of the deformed layer is reduced to 2.71 μm. The reduction in a deformed layer can be attributed to higher cutting temperatures in the tertiary deformation zone and reduced contact time at the tool-workpiece interface. Furthermore, the variation in deformed layer thickness is highly correlated with mechanical loading history (i.e., cutting forces). As shown in Fig. 6.8, when the resultant cutting force increases, the deformed layer thickness increases due to increased stress and energy input, causing the material to deform plastically to a more considerable extent. In contrast, when the resultant cutting force is decreased (Exp no.3), the lower stress and energy input result in a shallower deformation zone. It is also observed for Exp no.3 that the volume fraction of β-Ti becomes very small and almost disappears in the near milled surface. Similarly, the effect of cutting speeds on burr formation has been depicted in Fig. 6.5 (d-f). Generally, burr formation occurs due to three possible mechanisms: bending of the chip, tearing of the chip from the workpiece, and lateral extrusion of material (Zannoun & Schoop, 2023; Gillespie, 1973). The current research focuses on the first and second mechanisms. It can be seen that burr height and width vary irregularly with changing cutting speeds. At a cutting speed of 150 m/min (i.e., Exp no.1), both the width and height of the bur formation are more significant than at a cutting speed of 250 m/min (i.e., Exp no.2). As discussed above, at lower cutting speed, the material exhibits substantial plastic deformation, resulting in more burrs. As the cutting speed increases to 250 m/min, thermal softening of the material minimizes distortion, resulting in smaller burrs. Similarly, as depicted in Fig. 6.5(e), no apparent burr formation was found for Exp no.3. This phenomenon can be explained by the combination of high temperatures and quick cutting, which produces effective chip creation with limited material adhesion, almost eliminating burr development. Fig. 6.6 reveals the effect of various feed rates on the machined subsurface microstructures and burr formation during HSM of TC4 titanium alloy. It can be seen that feed rates significantly influence the deformed layer thickness and burr formation. As indicated in Fig 6 (a), at a feed rate of 0.10 mm/tooth (i.e., Exp no.4), the machined subsurface exhibited a thin deformed layer thickness of about 2.26 μm, where the grains rotate in the cutting direction. When the feed rate was increased to 0.20 mm/tooth and 0.30 mm/tooth (i.e., Exp no.5 and 6), respectively, as depicted in Fig. 6.6 (b) and (c), the depth of deformed layer thickness extended to about 2.56 μm and 2.95 μm, respectively.

It should be highlighted that a higher feed rate requires more mechanical work during the cutting process, generating comparatively higher cutting temperatures on the machined surface due to enhanced deformed layer thickness (Liao *et al.*, 2021). Furthermore, it was also observed that increasing trends of deformed layer thickness against feed rates are also associated with the increased pattern of mechanical load (Fig. 6.8). Similarly, the SEM micrographs of burr

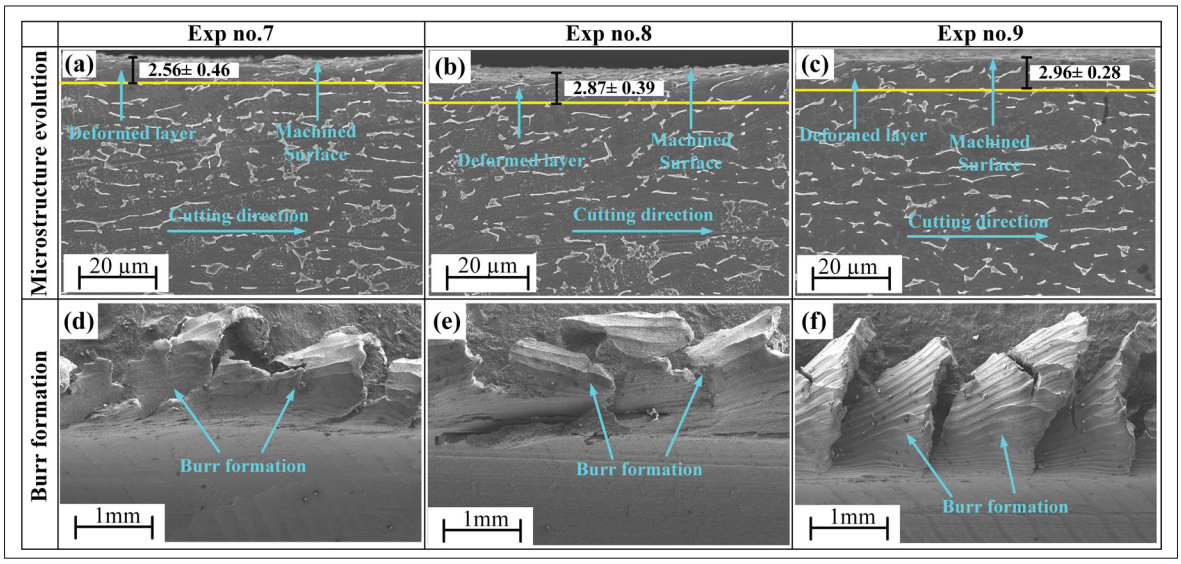

Figure 6.7 Machined surface layer microstructure evolution and burr formation analysis at varying depths of cut (a–c) microstructures of machined surface layer, and (d-f) burr formation

formation against various feed rates have been depicted in Fig. 6.6 (d-f). It can be seen that for Exp no.4 and 5, sizeable irregular rollover burrs were formed. While for Exp no.6, the width and height of the burr become regular. As the feed rate increases, more material is removed per unit time, resulting in higher cutting forces and increased plastic deformation of the workpiece. This, along with increased heat output, weakens the material and makes it more sensitive to deformation and burr development. Furthermore, increased feed rates diminish the shear plane angle, resulting in larger undeformed chips and more aggressive material push-out at the cut edges. These combined factors can create more prominent and noticeable burrs at higher feed rates. Analogous to the results shown in Fig. 6.5 and 6, the effect of radial depth of cut on machined subsurface microstructure and burr formation is analyzed in Fig. 6.7. As indicated in

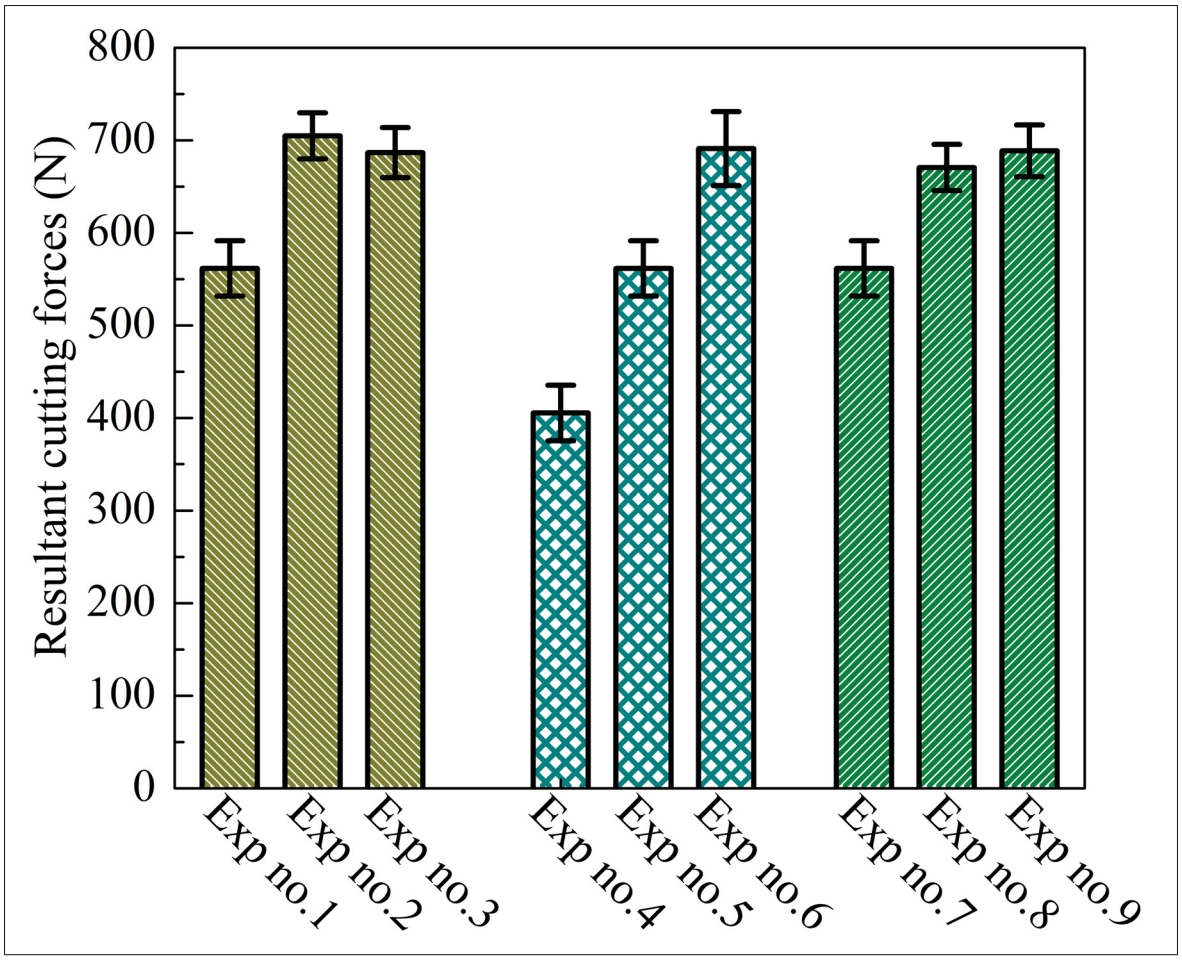

Figure 6.8 Resultant cutting forces for the selected milling experiments

Fig. 6.7(a-b) when the cutting speed and feed rate remain unchanged, and the radial cutting depth increases from 1.6 mm to 1.9 mm, the deformed layer thickness beneath the milled surfaces gradually increases from about 2.56 to 2.87 μm. Furthermore, the most considerable deformed layer thickness was observed at a radial depth of cut of 2.2 mm (i.e., Exp no.9). It can be inferred that under this cutting condition, the thermal-mechanical coupling load reaches the maximum value and significantly influences the evolution of the milled subsurface microstructure. Fig. 6.7 (d-f) illustrates the variation in burr formation against various radial cutting depths. As the radial cutting depth increased from 1.6 mm to 2.2 mm (i.e., Exp no. 7-9), both burr height and width increased. This increase is primarily attributed to greater material engagement and higher cutting forces. On the one hand, when the radial cutting depth increases, more material is

removed per unit volume, resulting in higher stresses at the cutting edge and increased material deformation. This leads to larger burr formation as more material is plastically deformed and displaced. On the other hand, the increased cutting depth can cause more heat generation, further enhancing the material's plasticity and contributing to burr growth.

6.3.3 Effect of Cutting Parameters on Particle Emission

Generally, particles with an aerodynamic diameter ≤10 μm (PM10) could harm machine operators' health more than those induced by particles with a diameter >10 μm [12, 30]. Therefore, in the current research, the PM10 is further subdivided into two categories: fine particles (diameter of ≤ 2.5 μm), which can cause respiratory diseases, and coarse particles (diameter; 2.5 μm – 10 μm), which might induce asthma. Fig. 6.9 demonstrates the total particle number, surfaces, and mass concentration as a function of particle diameters obtained through the dust collection unit. To better understand the effect of various input milling parameters on fine and coarse particles, the particles in the range of 0.5-2.5 μm and 2.5-10 μm were added for each experimental trial, and the obtained results were plotted in Fig. 6.10. As demonstrated in Fig. 6.10 (a) when the cutting conditions were increased from low to higher, the fine particles in terms of number concentrations were consistently increased. In contrast, the coarse particles showed a trend opposite to fine particles. On the one hand, higher cutting conditions impart more energy, leading to extensive material fragmentation and the formation of fine particles. On the other hand, higher energy and higher temperatures soften or melt the material in the micron range, increasing the formation of fine particles. Hence, the observed trend results from increasing energy, thermal effects, tool wear, and aerodynamic considerations. It is also revealed that the total particle number concentration (i.e., a combination of fine and coarse particles) increased when the cutting speed was increased from 150 m/min (Exp no. 1) to 250 m/min (Exp no. 2) but decreased with a further increase in cutting speed (Exp no. 3). This trend can be explained by considering the balance between particle generation and removal dynamics. An increased cutting speed can initially surge the chip serration and plastic deformation of the machined subsurface, resulting in a higher total particle number concentration. However, at even

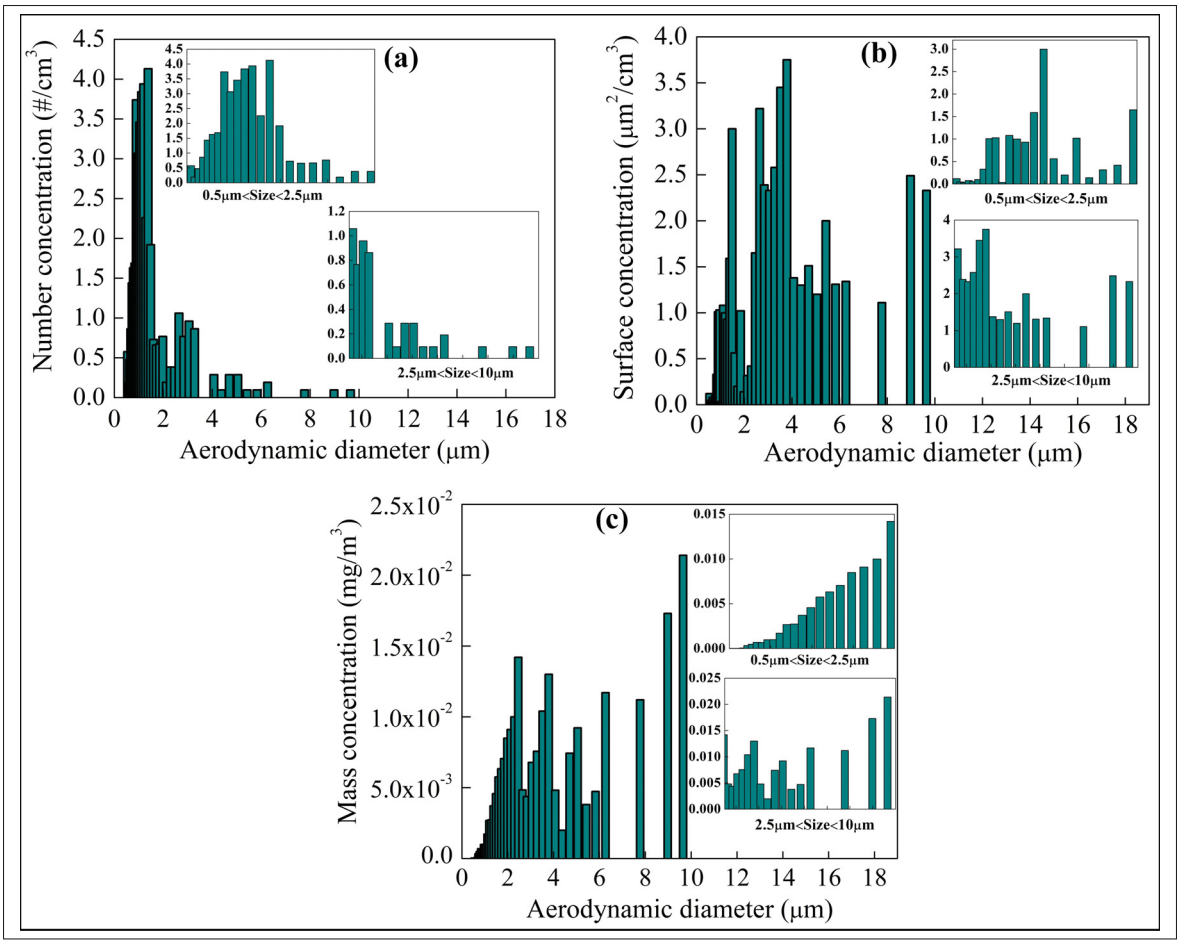

Figure 6.9 Particle emission against aerodynamic diameters for Exp no.3: (a) particle number concentration, (b) surface concentration, and (c) mass concentration

higher cutting speeds, other factors such as more efficient particle ejection, stabilization of the temperature in the cutting zone, or changes in material behavior may come into play, leading to a decrease in the total particle number concentration. These higher cutting speeds could create conditions where the particles are more effectively carried out of the cutting zone or where the material properties change, reducing the rate of new particle formation. The analysis also indicates that the total number of particle concentrations increases with feed rates (Exp no.4-6) and depth of cuts (Exp no. 7-9). This tendency occurs because increasing the feed rate and depth of cut improves material removal, resulting in more intense cutting conditions and higher energy input. This increased energy produces more widespread material fragmentation, resulting in

more particles. Furthermore, more particles are produced overall when the volume of material being cut increases. As a result, higher feed rates and deeper cuts increase the particle number concentration. Similarly, the effect of cutting conditions on particle surface concentration has

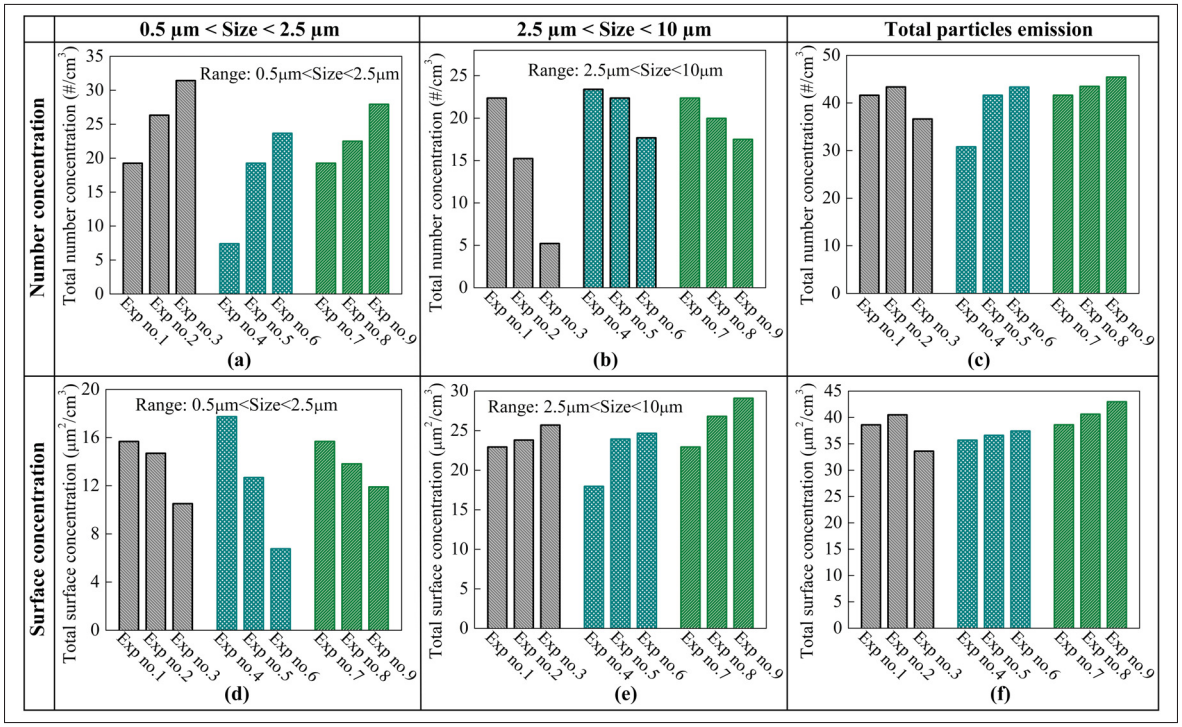

Figure 6.10 Fine, coarse, and total particle emissions: (a-c) particle number concentration, and (d-f) surface concentration

been depicted in Fig. 6.10 (d-e). It was found that the surface concentration in terms of fine and coarse particles exhibits an opposite trend to that of particle number concentrations. When the cutting conditions were increased from lower to higher, the particle surface concentration continuously decreased in the range of 0.5-2.5 μm (fine particles), while it increased in the range of 2.5-10 μm (coarse particles) for all the cutting conditions. The observed trends in particle surface concentration under varying cutting conditions can be explained by material removal and particle generation dynamics. As cutting speeds (Exp no. 1-3), feed rates (Exp no. 4-6), and depths of cut (Exp no. 7-9) increase, the energy input into the material also increases, leading to more aggressive cutting and greater material removal rates. This results in higher temperatures and forces, which tend to break the material into coarser particles (2.5-10

μm). Consequently, the concentration of fine particles (0.5-2.5 μm) decreases as the formation

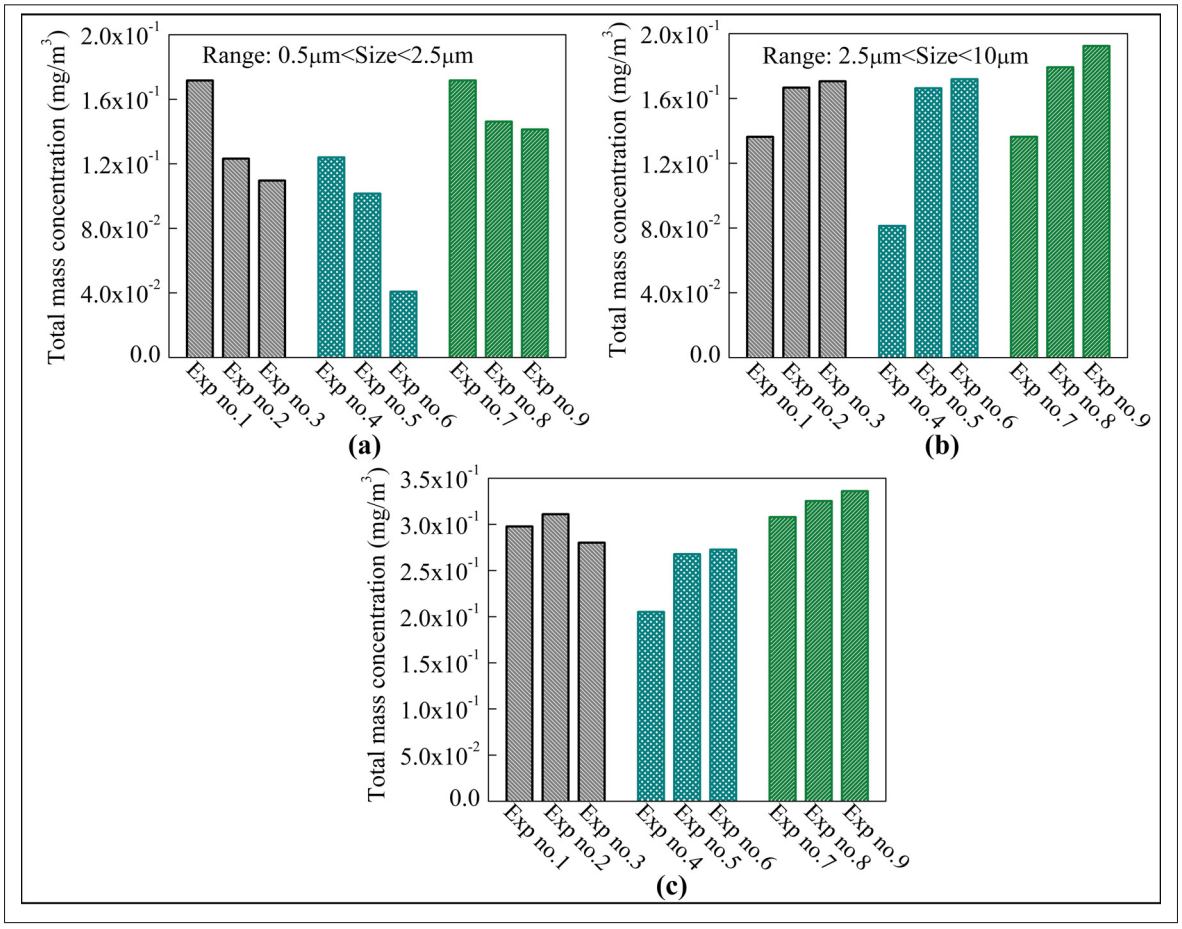

Figure 6.11 Mass concentration against various cutting parameters; (a) fine particle, (b) coarse particle, and (c) total mass concentration

of coarser particles becomes more dominant. Furthermore, the overall surface concentration (i.e., a combination of fine and coarse particles) follows a similar trend to the particle number concentration since both are influenced by the distribution of particle sizes. Similarly, mass concentration is another crucial indicator of particle emissions and is highly relevant for assessing health impacts associated with particle exposure. Fig. 6.11 shows the effect of cutting conditions on mass concentration during HSM of TC4 titanium alloy. As cutting conditions intensify, the mass concentration of emitted particles typically decreases within the range of 0.5-2.5 μm (i.e., fine particles), which shows similar trends to particle number concentration. In contrast, it tends to increase in the coarse particle range (i.e., 2.5-10 μm), as shown in Fig. 6.11 (b). Furthermore,

as demonstrated in Fig. 6.11(c), the overall mass concentration increased when the cutting speed was increased from 150 m/min (i.e., Exp no.1) to 250 m/min (Exp no.2), with further increase in cutting speed (i.e., Exp no.3), it tends to decrease. On the one hand, when the cutting speed first increased from 150 m/min to 250 m/min, the energy input is sufficient to generate a high number of fine and coarse particles, resulting in a higher mass concentration. As cutting speed increases beyond a certain point, the particles tend to fragment into even finer sizes or become dispersed more effectively, leading to a decrease in mass concentration. On the other hand, higher feed rates (i.e., Exp nos. 4-5) and depths of cut (i.e., Exp nos. 7-9) increase the material removal rate, producing more particles across all size ranges and thereby raising the mass concentration.

6.3.4 Effect of Cutting Parameters on Surface Roughness

The quality of the machined surface finish is regarded as one of the prime parameters in ensuring the performance requirements of final products (Yan, Chibowski & Szcześ, 2017). Therefore, this section analyzed the effect of different cutting conditions on surface roughness. The impact of cutting speeds (Exp nos. 1, 2, and 3) on machined surface roughness, along with the roughness parameters: Ra (average roughness), Rq (root mean square roughness), Rz (maximum height), and Rt (peak valley difference) calculated over the entire measured array for the machined surface, is shown in Fig. 6.12. As depicted the values of Ra, Rq, Rz, and Rt first increased when the cutting speed increased to 250 m/min (i.e., Exp no.2). However further increase in cutting speed (i.e., Exp no.3), the roughness values decreased. The observed trend in surface roughness parameters (Ra, Rq, Rz, and Rt) with varying cutting speeds can be attributed to changes in the dynamics of the cutting process. Initially, as the cutting speed increases from 150 to 250 m/min, the increased heat generation and higher material removal rate cause more tool wear and thermal expansion, leading to a rougher surface. However, when the cutting speed is further increased to 350 m/min (Exp no.3), the cutting process may enter a regime where the higher speed promotes more stable and efficient material shearing. This higher speed can reduce cutting forces and lower vibration, resulting in a smoother surface finish. Thus, the initial increase in roughness values is due to the detrimental effects of heat and wear, while

the subsequent decrease at higher speeds is due to improved cutting stability and efficiency. Similarly, Fig. 6.13 indicates the effect of feed rates on machined surface roughness. As expected,

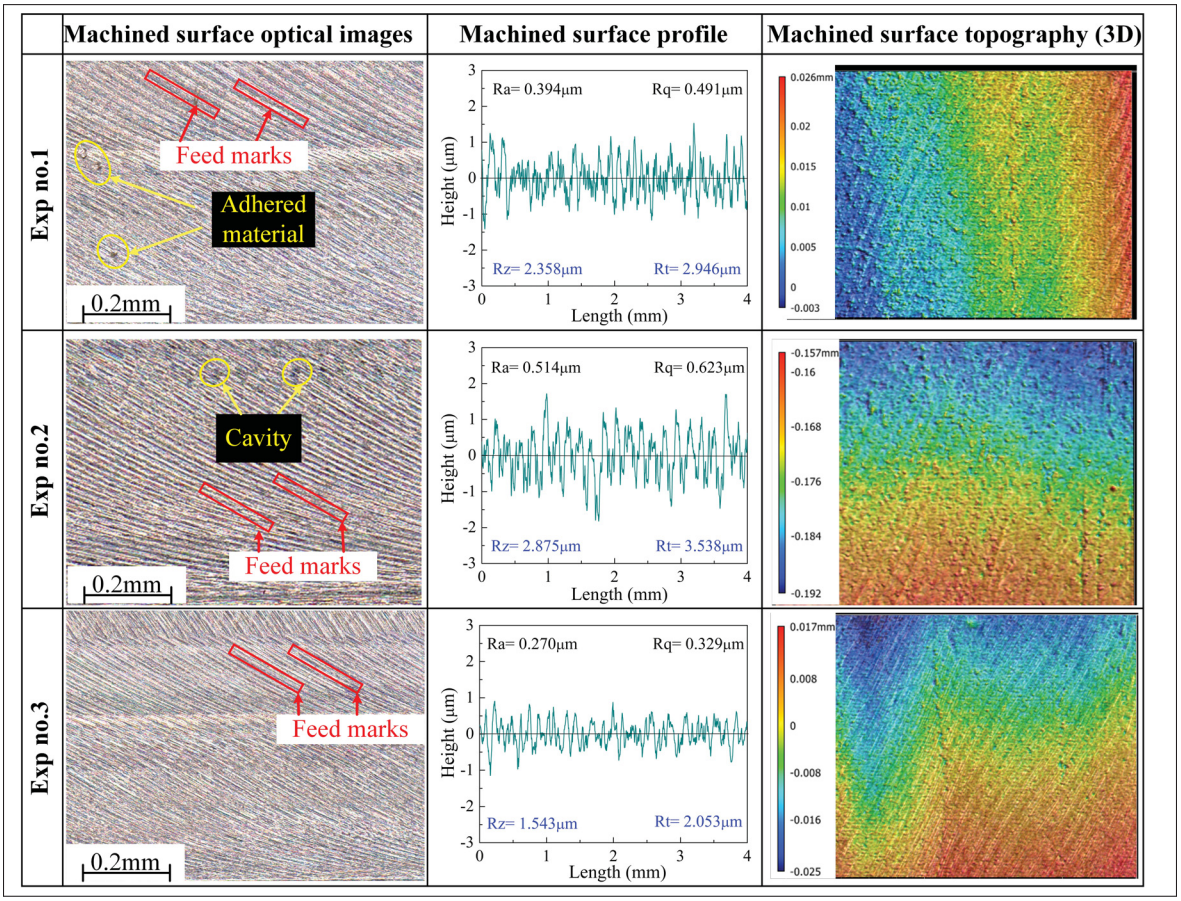

Figure 6.12 Machined surface roughness analysis against various cutting speeds

feed rates significantly influence the machined surface roughness. When the feed rates increased from lower to higher (i.e., Exp no. 4-6), the surface roughness parameters (Ra, Rq, Rz, and Rt) gradually increased. Generally, as discussed above, the cutting tool removes a larger volume of material at a higher feed rate, resulting in more pronounced tool marks and irregularities on the machined surface. In addition, this increased material removal per tooth generates higher cutting forces and vibrations, which can further deteriorate the surface finish. Furthermore, at higher feed rates, there is less time for heat dissipation, leading to increased thermal effects that can affect the surface integrity (Wang *et al.*, 2021). Consequently, these combined effects of higher material removal rates, increased cutting forces, vibrations, and thermal influences

contribute to the rougher surface texture observed at higher feed rates. Likewise similar to

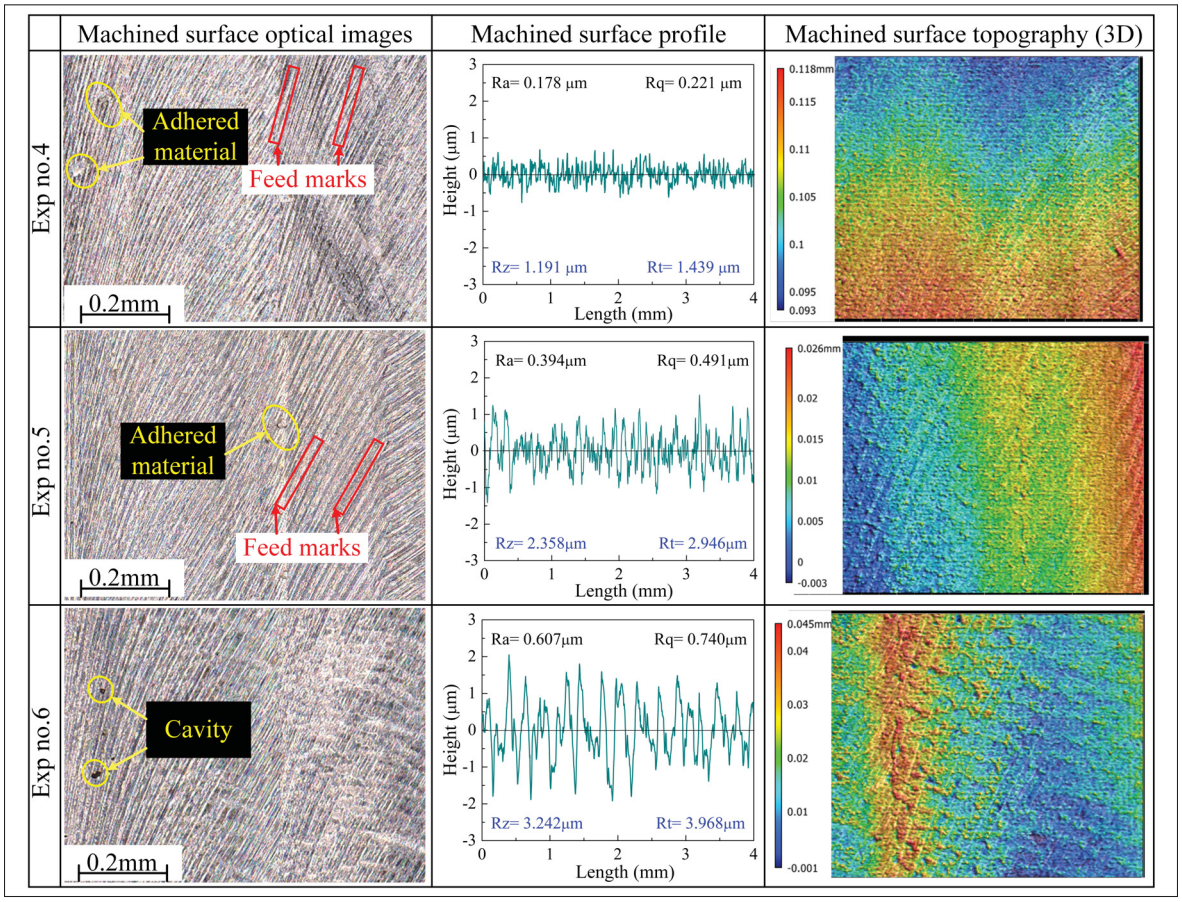

Figure 6.13 Machined surface roughness analysis against various feed rates

the results indicated in Figs. 12 and 13, the effect of radial depth of cut on machined surface roughness is presented in Fig. 6.14. The minimum surface roughness parameters (Ra, Rq, Rz, and Rt) were found for Exp no.7 (i.e., ae=1.6 mm). When the radial depth of the cut was further increased while keeping other machining parameters constant, all the roughness parameters were found to increase continuously. This rise in surface roughness can be attributed to several factors. As the radial depth of the cut increases, the engagement of the cutting tool with the material also increases, leading to higher cutting forces and greater tool deflection. The enhanced interaction between the tool and the workpiece can lead to more noticeable tool marks and surface irregularities, thereby increasing the roughness parameters. Additionally, a deeper cut generates more heat and induces higher vibration levels, further deteriorating the surface

finish. Consequently, maintaining a lower radial depth of cut helps achieve a smoother surface by minimizing these adverse effects.

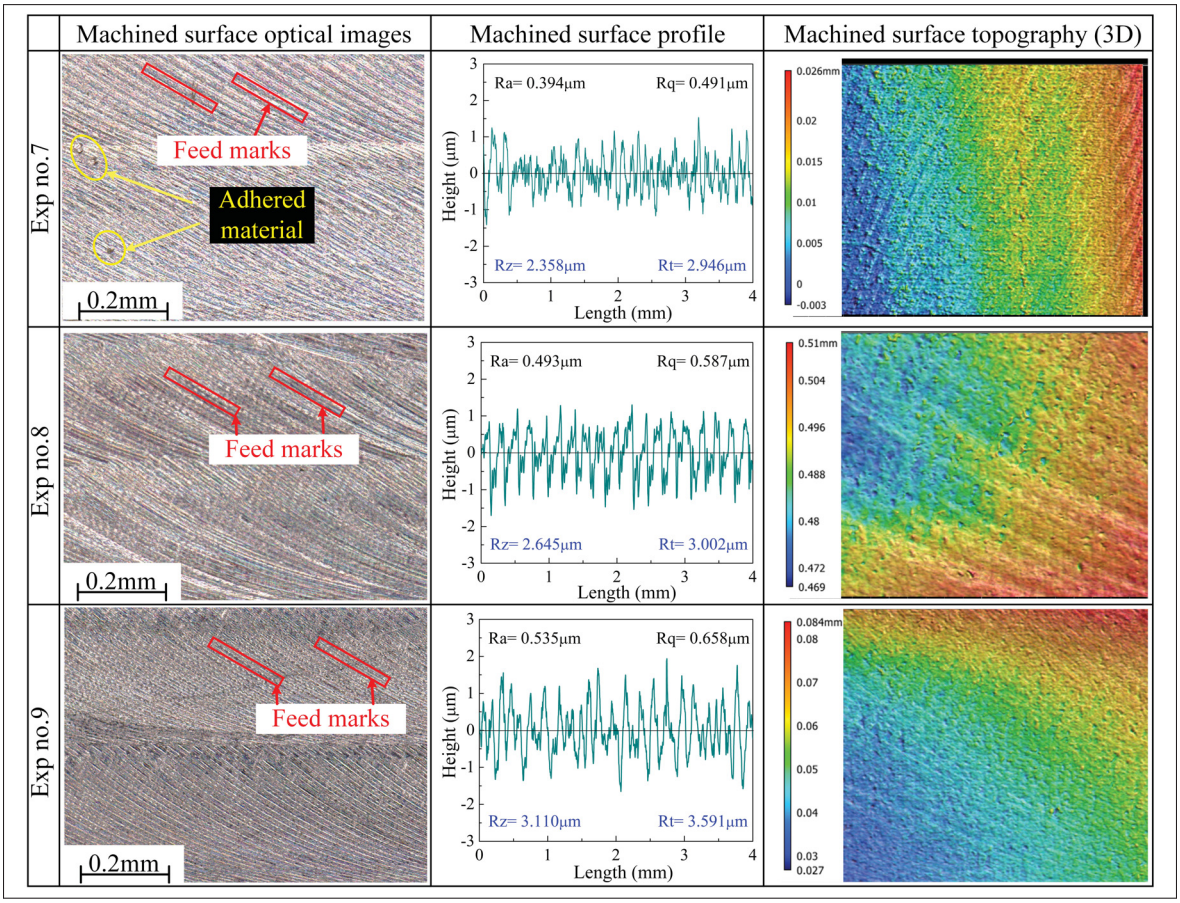

Figure 6.14 Machined surface roughness analysis against various radial depths of cuts

6.3.5 Correlation Between Particle Emission and Machined Surface Integrity

The correlation between particle emissions (i.e., particle number and surface concentration), depth of deformed layer thickness, and surface roughness has been described in Fig. 6.15. The observed results demonstrate a consistent relationship among particle emissions, the depth of deformed layer, and surface roughness during the milling process. As depicted in Fig. 6.15(a), when the cutting speed increased from 150 m/min (Exp no.1) to 250 m/min (Exp no.2), there was a consistent increase in particle emissions, depth of plastic deformation, and surface

roughness. This can be attributed to the higher energy input associated with the increased cutting speed, which exacerbates material removal and deformation. However, when the cutting speed was further increased to 350 m/min (Exp no.3), a reduction in particle emissions, deformed layer thickness, and surface roughness was observed. This phenomenon can be explained by the thermal softening of the material at higher speeds, which leads to smoother cutting and shrink-deformed layer thickness. Consequently, while an initial increase in cutting speed enhances the severity of machining effects, beyond a certain threshold, further increases in cutting speed result in a more efficient and refined cutting process. Similarly, Fig. 6.15 (b-c)

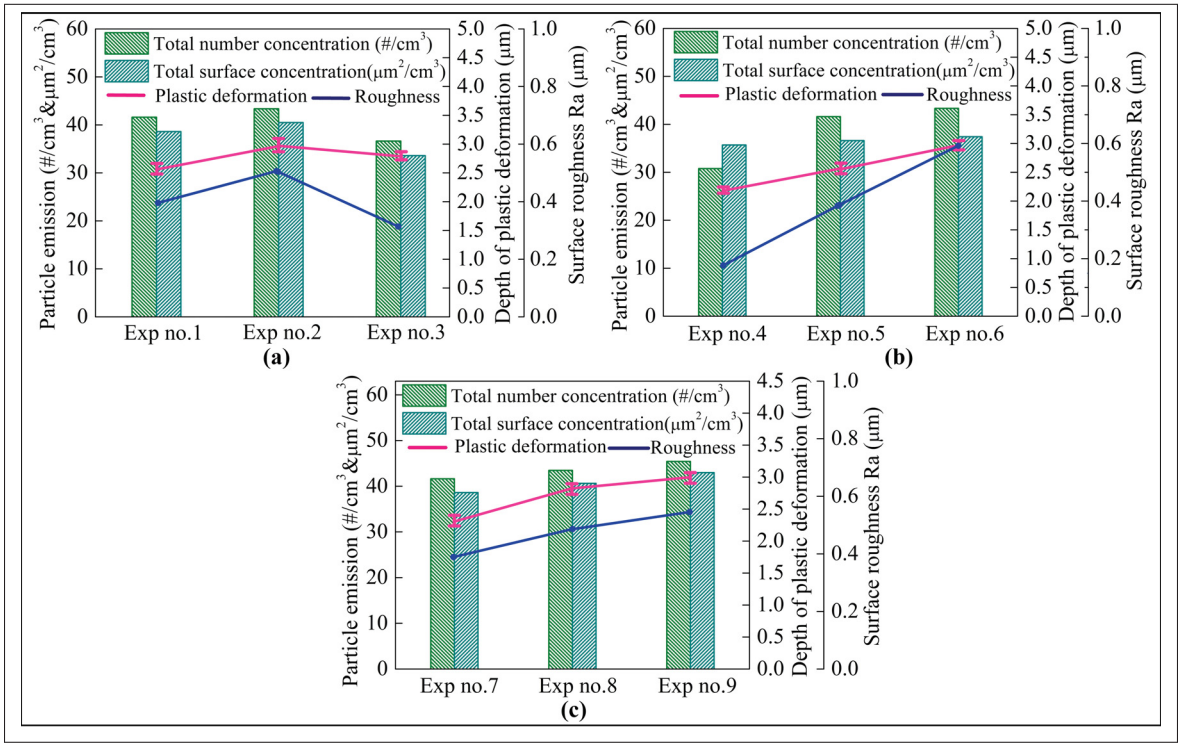

Figure 6.15 Correlation among particle emission and machined surface integrity: (a) Exp nos. 1-3, (b) Exp nos. 4-6, and (c) Exp nos. 7-9

demonstrates the correlation between particle emissions and machined surface integrity against various feed rates and radial depths of cut. It is evident that the variation in particle emissions is associated with the increasing pattern of deformed layer thickness and surface roughness. As discussed above higher feed rates and depths of cut introduce greater mechanical loads to the machined surface, resulting in more increased plastic deformation and surface roughness.

Subsequetly, elevated thermal loads further contribute to the formation of a thicker deformed layer and increased surface roughness, which in turn results in higher particle emissions.

6.4 Conclusions

This study conducted experimental research work to analyze the effects of machining parameters on machined surface integrity and metallic particle emission during HSM of TC4 titanium alloy. The main conclusions of this study are listed as follows:

1. The experimental results revealed that the chip-free surface consists of lamellar structures, with slipping and undeformed surfaces being more uniform at lower and moderate machining parameters. At lower cutting parameters, some microvoids and shear dimples were observed, indicating ductile behavior, while higher speeds resulted in cracks indicative of brittle fracture. Variations in feed rates and radial depth of cut similarly affected chip morphology, with lower values producing smoother surfaces and higher values causing more pronounced slipping, undeformed surfaces, and complex fold patterns.
2. The experimental results indicate that the milled subsurface undegoes plastic deformation. As the cutting speed increased from 150 m/min to 250 m/min, the deformed layer thickness rose from approximately 2.56 μm to 2.97 μm. However, with further increases in cutting speed, it decreased to about 2.71 μm. Furthermore, the deformed layer thickness was found to increase with higher feed rates and radial depth of cuts. These variations in deformed layer thickness are closely correlated with the changing patterns of resultant cutting forces.
3. The analysis of burr formation reveals that increasing the cutting speed from 150 to 350 m/min results in decreased burr height and width. Conversely, increasing the feed rate from 0.10 mm/tooth to 0.30 mm/tooth and the radial depth of cut from 1.6 mm to 2.2 mm leads to an increase in burr width and height.
4. The particle emission analysis reveals that fine particles, in terms of number concentrations, consistently increased with the cutting parameters. In contrast, coarse particles exhibited the opposite trend. Overall, the total particle concentration (i.e., a combination of fine and coarse particles) initially increased with cutting speed and then decreased, whereas

it consistently increased with feed rates and radial depths of cut. Similarly, for surface and mass concentrations, fine particles decreased as cutting parameters increased, whereas coarse particles showed an upward trend. The overall surface and mass concentrations demonstrated behavior similar to that of the number concentrations.

5. It was also observed that the milled surface roughness initially increased with the cutting speed and then decreased with a further increase in the cutting speed. In contrast, milled surface roughness was found to consistently increase with the feed rates and radial depth of cuts.
6. Finally, the correlation between particle emissions and machined surface integrity was obtained, revealing that particle emissions are directly related to machined subsurface plastic deformation and surface roughness.

CONCLUSION AND RECOMMENDATIONS

7.1 Conclusions

This work employed both modeling and experimental approaches to investigate the influence of machining parameters on surface integrity and metallic particle emissions during high-speed milling (HSM) of Ti-6Al-4V. Initially, a simplified two-dimensional (2D) milling model was developed using the Johnson-Cook (J-C) constitutive model alongside an energy density-based failure criterion. Subsequently, a computational framework incorporating user-defined subroutines was established to simulate microstructural evolution, particularly grain refinement and phase transformations, within the cutting deformation zones of Ti-6Al-4V. HSM experiments were conducted to validate the results, with cutting speeds ranging from 150 to 550 m/min, feed rates ranging from 0.10 to 0.30 mm/tooth, axial depths of cut ranging from 1.0 to 1.8 mm, and radial depths of cut ranging from 1.0 to 2.2 mm. The predicted cutting forces, temperatures, and chip morphologies exhibited strong agreement with the experimental results. Moreover, advanced characterization techniques confirmed the model's accuracy in predicting grain size and phase transformations. Additionally, the cyclic behavior of RS in the machined surface layer was also investigated through both simulations and experiments. Finally, an experimental analysis was performed to assess the impact of process parameters on particle emissions, establishing a clear correlation between surface integrity and particle emission levels. Based on the findings, the following conclusions are drawn:

1. **Finite Element Modeling of Grain Size and Microhardness Evolution**

   The multi-scale numerical model developed in this study effectively designed the milling process for optimized grain refinement. By incorporating cutting speed and feed rate as variable functions, the model accurately predicted grain refinement within both the adiabatic shear band and the machined surface. The findings indicate that microstructural alterations in the chip were predominantly driven by extremely high strain rates, elevated temperatures,

and strain localization, which collectively induced SPD, twinning, and dislocation motion. As a result, the most significant grain refinement occurred within the ASB. In contrast, the degree of grain refinement in the machined surface was approximately half that observed in the ASB, primarily due to lower temperatures in this region. Furthermore, the influence of grain refinement on microhardness was examined, revealing that the cutting deformation zones exhibited significantly higher hardness compared to the bulk material. This hardness gradient reflects the presence of inhomogeneous plastic deformation during HSM.

2. **Finite Element Modeling of Phase Transformation in High-Speed Milling**

   A coupled thermo-metallo-mechanical FE model was developed to analyze the effects of high strain rates, stress, and temperature on phase transformation during the rapid heating and cooling stages of Ti-6Al-4V cutting. Simulation results revealed that phase transformation primarily occurred at the back surface of the serrated chip and at the tool-workpiece interface. During rapid heating, as the temperature reached the phase transformation threshold, the α-phase progressively transformed into the β-phase. At a 150 m/min cutting speed, the secondary deformation zone temperature reached approximately 863.4°C, increasing the β-phase volume fraction from 7.5% to 33.5%, at a higher cutting speed of 350 m/min, where the temperature exceeded the transus temperature, nearly all available α-phase transformed into β-phase. Similarly, increasing the feed rate from 0.15 mm/tooth to 0.25 mm/tooth led to an increase in the β-phase volume fraction from 7.5% to 67.84%. During the rapid cooling phase, regions that had undergone β-phase transformation reverted to α'-phase.

3. **Residual Stress Modeling and Measurement**

   A simplified milling model was introduced to investigate in-depth RS in the machined Ti-6Al-4V alloy. Simulation results demonstrated that plastic strain exhibited a cyclic pattern on the machined surface and subsurface, intensifying at higher cutting speeds. A similar cyclic behavior was observed in the simulated residual stress profile. At a 150 m/min cutting speed, residual stresses were tensile on the machined surface. However, at 450 m/min, the

stress in the X-direction transitioned to compressive, while the Y-direction stress remained tensile. The model was validated through experimental results, confirming its accuracy. The analysis of thermo-mechanical loads indicated that thermal loads predominantly influenced RS on the machined surface, while mechanical loads governed subsurface RS. Higher cutting speeds and feed rates reduced surface tensile stress and enhanced subsurface compressive stress, offering a potential strategy to optimize residual stress profiles for improved fatigue resistance.

4. **Experimental Investigation of Particle Emission During HSM of Ti-6Al-4V**

   A series of high-speed milling experiments were conducted in a dry environment to assess the impact of process parameters on chip formation, subsurface microstructure evolution, and burr formation. The study further analyzed particle emissions and surface roughness. Results indicated that fine particle emissions, in terms of number concentration, consistently increased with cutting parameters, while coarse particle emissions showed an opposite trend. The total particle concentration initially increased with cutting speed before decreasing, whereas it consistently increased with feed rate and radial depth of cut. Similarly, surface and mass concentrations of fine particles decreased with increasing cutting parameters, whereas coarse particle concentrations exhibited an upward trend. The overall surface and mass concentration trends followed those of the number of concentrations. A correlation analysis between machined surface integrity and particle emissions revealed that emissions were directly related to subsurface plastic deformation and surface roughness.

The current research thoroughly explains how machining parameters, surface integrity, and particle emissions interact during high-speed milling of Ti-6Al-4V. The presented models and experimental data provide valuable insights for optimizing milling parameters to achieve appropriate microstructural characteristics, RS distributions, and emission control, improving component performance and sustainability in advanced manufacturing.

7.2 Main Contributions

(1) The development of a multi-scale FE milling model for microstructure evolution under high strain, strain rate, and temperature gradients. This model captures grain refinement in the cutting deformation zones and reveals the influence of thermal and mechanical loads on GS evolution during chip formation stages (i.e., crack initiation, propagation, and catastrophic failure).

(2) A thermo-metallo-mechanical FE model development to investigate phase transformation during rapid heating and cooling phases. The developed model not only predicts phase transitions but also enhances the accuracy of material behavior during HSM of Ti-6Al-4V alloy.

(3) A simplified 2D cutting model is proposed for predicting RS during the milling process. In this model, undeformed chip thickness is approximated as a sinusoidal function. The established model effectively predicts the cyclic behavior of thermo-mechanical loads, chip serration, and the distribution of RS.

(4) Quantitative analysis and digital characterization of the microstructure and mechanical properties of the cutting sub-surface layer were conducted from the milled surface to the bulk region. The evolution mechanism of serrated chips and the sub-surface microstructure under the combined influence of mechanical, thermal, and metallurgical fields was revealed.

(5) A detailed experimental investigation was conducted to establish the correlation between machined surface integrity and metallic particle emissions. The effects of various milling parameters on surface integrity and emissions were analyzed, leading to an understanding of their interdependence.

7.3 Future Recommendations

Based on the findings of this thesis, further research into microstructure evolution, surface integrity, and particle emissions during the machining process is recommended for the following areas:

1. **Incorporating Tool Vibration and Wear in Finite Element Modeling**

   To enhance the accuracy of FE simulations in HSM, the influence of tool vibration and wear on chip formation, subsurface microstructural evolution, and mechanical properties should be considered. Developing an FE model that accounts for these factors will make the simulations more representative of actual machining conditions.

2. **Modeling the Impact of Surface Integrity on Component Performance**

   The effect of surface integrity on machined components' functional performance and longevity remains insufficiently understood. A predictive model should be developed to assess fatigue fracture initiation and propagation rates quantitatively while considering microstructural features such as GS, interfacial energy, and slip bandwidth.

3. **Influence of Tool Edge Micro-Geometry on Surface Integrity**

   The effect of tool edge micro-geometry on machined surface integrity should be a primary focus of future research. A comprehensive FE model should be developed to capture the influence of various tool edge geometries on subsurface microstructure evolution, residual stress distribution, and hardness variations. To accurately predict localized deformation and phase transformations induced by different edge geometries, the model should integrate advanced material behavior laws and microstructural evolution mechanisms.

4. **Machine Learning for Predicting Particle Emissions in Metal Machining**

   A machine learning-based approach could be proposed to improve the prediction and understanding of particle emissions during metal machining. Advanced artificial intelligence models, such as deep learning or ensemble learning techniques, can be trained on experimental and numerical datasets to predict emission characteristics based on machining

parameters, tool wear, and material properties. Feature selection methods can identify key influencing factors, while real-time sensor data integration with machine learning models can enable adaptive control strategies to minimize emissions.

BIBLIOGRAPHY

Abbasi, S. A., Feng, P., Ma, Y., Zhang, J., Yu, D. & Wu, Z. (2016). Influence of microstructure and hardness on machinability of heat-treated titanium alloy Ti-6Al-4V in end milling with polycrystalline diamond tools. *The International Journal of Advanced Manufacturing Technology*, 86, 1393–1405.

Abbasi, S. & Momeni, A. (2011). Effect of hot working and post-deformation heat treatment on microstructure and tensile properties of Ti-6Al-4V alloy. *Transactions of Nonferrous Metals Society of China*, 21(8), 1728–1734.

Ahmed, T. & Rack, H. (1998). Phase transformations during cooling in α+ β titanium alloys. *Materials Science and Engineering: A*, 243(1-2), 206–211.

Amuda, M. O. H. & Mridha, S. (2012). Comparative evaluation of grain refinement in AISI 430 FSS welds by elemental metal powder addition and cryogenic cooling. *Materials & Design*, 35, 609–618.

Arisoy, Y. M. & Özel, T. (2015). Machine learning based predictive modeling of machining induced microhardness and grain size in Ti–6Al–4V alloy. *Materials and Manufacturing Processes*, 30(4), 425–433.

Arısoy, Y. M. & Özel, T. (2015). Prediction of machining induced microstructure in Ti–6Al–4V alloy using 3-D FE-based simulations: Effects of tool micro-geometry, coating and cutting conditions. *Journal of Materials Processing Technology*, 220, 1–26.

Arrazola, P. J., Özel, T., Umbrello, D., Davies, M. & Jawahir, I. S. (2013). Recent advances in modelling of metal machining processes. *Cirp Annals*, 62(2), 695–718.

Arumugam, P. U., Malshe, A. P., Batzer, S. A. & Bhat, D. G. (2003). Study of airborne dust emission and process performance during dry machining of aluminum-silicon alloy with PCD and CVD diamond-coated tools. *Journal of manufacturing processes*, 5(2), 163–169.

Avrami, M. (1940). Kinetics of phase change. II transformation-time relations for random distribution of nuclei. *The Journal of chemical physics*, 8(2), 212–224.

Aydin, M. (2017). Prediction of cutting speed interval of diamond-coated tools with residual stress. *Materials and Manufacturing Processes*, 32(2), 145–150.

Bailey, N. S., Katinas, C. & Shin, Y. C. (2017). Laser direct deposition of AISI H13 tool steel powder with numerical modeling of solid phase transformation, hardness, and residual stresses. *Journal of Materials Processing Technology*, 247, 223–233.

Balout, B., Songmene, V. & Masounave, J. (2007). An experimental study of dust generation during dry drilling of pre-cooled and pre-heated workpiece materials. *Journal of manufacturing processes*, 9(1), 23–34.

Bayoumi, A. & Xie, J. (1995). Some metallurgical aspects of chip formation in cutting Ti-6wt.% Al-4wt.% V alloy. *Materials Science and Engineering: A*, 190(1-2), 173–180.

Bourell, D., Kruth, J. P., Leu, M., Levy, G., Rosen, D., Beese, A. M. & Clare, A. (2017). Materials for additive manufacturing. *CIRP annals*, 66(2), 659–681.

Brown, M., Crawforth, P., M'Saoubi, R., Larsson, T., Wynne, B., Mantle, A. & Ghadbeigi, H. (2019). Quantitative characterization of machining-induced white layers in Ti–6Al–4V. *Materials Science and Engineering: A*, 764, 138220.

Bruschi, S., Altan, T., Banabic, D., Bariani, P. F., Brosius, A., Cao, J., Ghiotti, A., Khraisheh, M., Merklein, M. & Tekkaya, A. E. (2014). Testing and modelling of material behaviour and formability in sheet metal forming. *CIRP Annals*, 63(2), 727–749.

Buffa, G., Ducato, A. & Fratini, L. (2013). FEM based prediction of phase transformations during friction stir welding of Ti6Al4V titanium alloy. *Materials Science and Engineering: A*, 581, 56–65.

Calamaz, M., Coupard, D., Nouari, M. & Girot, F. (2011). Numerical analysis of chip formation and shear localisation processes in machining the Ti-6Al-4V titanium alloy. *The International Journal of Advanced Manufacturing Technology*, 52, 887–895.

Calamaz, M., Coupard, D. & Girot, F. (2008). A new material model for 2D numerical simulation of serrated chip formation when machining titanium alloy Ti–6Al–4V. *International Journal of Machine Tools and Manufacture*, 48(3-4), 275–288.

Calistes, R., Swaminathan, S., Murthy, T., Huang, C., Saldana, C., Shankar, M. & Chandrasekar, S. (2009). Controlling gradation of surface strains and nanostructuring by large-strain machining. *Scripta Materialia*, 60(1), 17–20.

Che-Haron, C. & Jawaid, A. (2005). The effect of machining on surface integrity of titanium alloy Ti–6% Al–4% V. *Journal of materials processing technology*, 166(2), 188–192.

Chen, G., Ren, C., Yang, X., Jin, X. & Guo, T. (2011). Finite element simulation of high-speed machining of titanium alloy (Ti–6Al–4V) based on ductile failure model. *The International Journal of Advanced Manufacturing Technology*, 56, 1027–1038.

Chen, G., Ren, C., Zhang, P., Cui, K. & Li, Y. (2013). Measurement and finite element simulation of micro-cutting temperatures of tool tip and workpiece. *International Journal of Machine Tools and Manufacture*, 75, 16–26.

Chen, G., Ge, J., Lu, L., Liu, J. & Ren, C. (2021). Mechanism of ultra-high-speed cutting of Ti-6Al-4V alloy considering time-dependent microstructure and mechanical behaviors. *The International Journal of Advanced Manufacturing Technology*, 113, 193–213.

Chen, L., El-Wardany, T. & Harris, W. (2004). Modelling the effects of flank wear land and chip formation on residual stresses. *CIRP Annals*, 53(1), 95–98.

Chen, Z., Atmadi, A., Stephenson, D. A., Liang, S. Y. & Patri, K. V. (2000). Analysis of cutting fluid aerosol generation for environmentally responsible machining. *CIRP Annals*, 49(1), 53–56.

Deng, D. (2009). FEM prediction of welding residual stress and distortion in carbon steel considering phase transformation effects. *Materials & Design*, 30(2), 359–366.

Denguir, L., Outeiro, J., Fromentin, G., Vignal, V. & Besnard, R. (2017). A physical-based constitutive model for surface integrity prediction in machining of OFHC copper. *Journal of materials processing technology*, 248, 143–160.

Denkena, B., Nespor, D., Böß, V. & Köhler, J. (2014). Residual stresses formation after re-contouring of welded Ti-6Al-4V parts by means of 5-axis ball nose end milling. *CIRP Journal of Manufacturing Science and Technology*, 7(4), 347–360.

Ding, H. & Shin, Y. C. (2012). A metallo-thermomechanically coupled analysis of orthogonal cutting of AISI 1045 steel. *Journal of Manufacturing Science and Engineering*, 134, 051014.

Ding, H., Shen, N. & Shin, Y. C. (2011). Modeling of grain refinement in aluminum and copper subjected to cutting. *Computational Materials Science*, 50(10), 3016–3025.

Ding, L., Zhang, X. & Richard Liu, C. (2014). Dislocation density and grain size evolution in the machining of Al6061-T6 alloys. *Journal of Manufacturing Science and Engineering*, 136(4), 041020.

Djebara, A., Songmene, V. & Bahloul, A. (2013). Effects of machining conditions on specific surface of PM 2.5 emitted during metal cutting. *Health*, 2013, 8.

Duan, C., Kong, W., Hao, Q. & Zhou, F. (2013). Modeling of white layer thickness in high speed machining of hardened steel based on phase transformation mechanism. *The International Journal of Advanced Manufacturing Technology*, 69, 59–70.

Ducobu, F., Rivière-Lorphèvre, E. & Filippi, E. (2014). Numerical contribution to the comprehension of saw-toothed Ti6Al4V chip formation in orthogonal cutting. *International Journal of Mechanical Sciences*, 81, 77–87.

Estrin, Y., Tóth, L., Molinari, A. & Bréchet, Y. (1998). A dislocation-based model for all hardening stages in large strain deformation. *Acta materialia*, 46(15), 5509–5522.

Ezugwu, E. O., Bonney, J., Da Silva, R. B. & Çakir, O. (2007). Surface integrity of finished turned Ti–6Al–4V alloy with PCD tools using conventional and high pressure coolant supplies. *International Journal of Machine Tools and Manufacture*, 47(6), 884–891.

Fan, Y., Cheng, P., Yao, Y. L., Yang, Z. & Egland, K. (2005). Effect of phase transformations on laser forming of Ti–6Al–4V alloy. *Journal of applied physics*, 98(1), 013518.

Fanfoni, M. & Tomellini, M. (1998). The johnson-mehl-avrami-kohnogorov model: a brief review. *Il Nuovo Cimento D*, 20, 1171–1182.

Fang, N. & Wu, Q. (2009). A comparative study of the cutting forces in high speed machining of Ti–6Al–4V and Inconel 718 with a round cutting edge tool. *Journal of materials processing technology*, 209(9), 4385–4389.

Geng, D., Sun, Z., Liu, Y., Liu, L., Ying, E., Cai, J., Jiang, X. & Zhang, D. (2024). Unravelling the influence of vibration on material removal and microstructure evolution in ultrasonic transversal vibration-assisted helical milling of Ti-6Al-4V holes. *Journal of Materials Processing Technology*, 326, 118320.

Gillespie, L. K. (1973). The formation and properties of machining burrs. -, -.

Ginting, A. & Nouari, M. (2009). Surface integrity of dry machined titanium alloys. *International Journal of Machine Tools and Manufacture*, 49(3-4), 325–332.

Guo, Y., Li, W. & Jawahir, I. (2009). Surface integrity characterization and prediction in machining of hardened and difficult-to-machine alloys: a state-of-art research review and analysis. *Machining Science and Technology*, 13(4), 437–470.

Guolong, Z., Lianjia, X., Liang, L., Zhang, Y., Ning, H. & Hansen, H. N. (2023). Cutting force model and damage formation mechanism in milling of 70wt% Si/Al composite. *Chinese Journal of Aeronautics*, 36(7), 114–128.

Gupta, M. K., Niesłony, P., Korkmaz, M. E., Kuntoğlu, M., Królczyk, G., Günay, M. & Sarikaya, M. (2023). Comparison of tool wear, surface morphology, specific cutting energy and cutting temperature in machining of titanium alloys under hybrid and green cooling strategies. *International Journal of Precision Engineering and Manufacturing-Green Technology*, 10(6), 1393–1406.

Haber, R. E., Jiménez, J. E., Peres, C. R. & Alique, J. R. (2004). An investigation of tool-wear monitoring in a high-speed machining process. *Sensors and Actuators A: Physical*, 116(3), 539–545.

Han, S., Melkote, S. N., Haluska, M. S. & Watkins, T. R. (2008). White layer formation due to phase transformation in orthogonal machining of AISI 1045 annealed steel. *Materials Science and Engineering: A*, 488(1-2), 195–204.

Hands, D., Sheehan, M. J., Wong, B. & Lick, H. B. (1996). Comparison of metalworking fluid mist exposures from machining with different levels of machine enclosure. *American Industrial Hygiene Association Journal*, 57(12), 1173–1178.

Henriksen, E. K. (1951). Residual stresses in machined surfaces. *Transactions of the American Society of Mechanical Engineers*, 73(1), 69–76.

Hojati, F., Daneshi, A., Soltani, B., Azarhoushang, B. & Biermann, D. (2020). Study on machinability of additively manufactured and conventional titanium alloys in micro-milling process. *Precision Engineering*, 62, 1–9.

Hosseini, S., Ryttberg, K., Kaminski, J. & Klement, U. (2012). Characterization of the surface integrity induced by hard turning of bainitic and martensitic AISI 52100 steel. *Procedia CIRP*, 1, 494–499.

Huang, X., Sun, J., Li, J., Han, X. & Xiong, Q. (2013). An experimental investigation of residual stresses in high-speed end milling 7050-T7451 aluminum alloy. *Advances in Mechanical Engineering*, 5, 592659.

Jafarian, F., Umbrello, D. & Jabbaripour, B. (2016). Identification of new material model for machining simulation of Inconel 718 alloy and the effect of tool edge geometry on microstructure changes. *Simulation Modelling Practice and Theory*, 66, 273–284.

Jiang, F., Yan, L. & Rong, Y. (2013). Orthogonal cutting of hardened AISI D2 steel with TiAlN-coated inserts—simulations and experiments. *The International Journal of Advanced Manufacturing Technology*, 64, 1555–1563.

Jiang, X., Kong, X., He, S. & Wu, K. (2021). Modeling the superposition of residual stresses induced by cutting force and heat during the milling of thin-walled parts. *Journal of Manufacturing Processes*, 68, 356–370.

Johnson, G. R. & Cook, W. H. (1985). Fracture characteristics of three metals subjected to various strains, strain rates, temperatures and pressures. *Engineering fracture mechanics*, 21(1), 31–48.

Junior, A. M. J., Guedes, L. H. & Balancin, O. (2012). Ultra grain refinement during the simulated thermomechanical-processing of low carbon steel. *Journal of Materials Research and Technology*, 1(3), 141–147.

Kaynak, Y., Manchiraju, S. & Jawahir, I. (2015). Modeling and simulation of machining-induced surface integrity characteristicsof NiTi alloy. *Procedia Cirp*, 31, 557–562.

Kaynak, Y., Manchiraju, S., Jawahir, I. & Biermann, D. (2020). Chip formation and phase transformation in orthogonal machining of NiTi shape memory alloy: microstructure-based modelling and experimental validation. *CIRP Annals*, 69(1), 85–88.

Kaynak, Y., Taşcıoğlu, E., Sharif, S., Suhaimi, M. & Benefan, O. (2022). The effect of cooling on machining and phase transformation responses of Ni-rich NiTiHf high-temperature shape memory alloy. *Journal of Manufacturing Processes*, 75, 1144–1152.

Keller, C. & Hug, E. (2017). Kocks-Mecking analysis of the size effects on the mechanical behavior of nickel polycrystals. *International Journal of Plasticity*, 98, 106–122.

Khaliq, W., Zhang, C., Jamil, M. & Khan, A. M. (2020). Tool wear, surface quality, and residual stresses analysis of micro-machined additive manufactured Ti–6Al–4V under dry and MQL conditions. *Tribology International*, 151, 106408.

Khettabi, R., Songmene, V. & Masounave, J. (2007). Effect of tool lead angle and chip formation mode on dust emission in dry cutting. *Journal of Materials Processing Technology*, 194(1-3), 100–109.

Khettabi, R., Fatmi, L., Masounave, J. & Songmene, V. (2013). On the micro and nanoparticle emission during machining of titanium and aluminum alloys. *CIRP Journal of Manufacturing Science and Technology*, 6(3), 175–180.

Khettabi, R., Songmene, V. & Masounave, J. (2010a). Effects of speeds, materials, and tool rake angles on metallic particle emission during orthogonal cutting. *Journal of materials engineering and performance*, 19, 767–775.

Khettabi, R., Songmene, V., Zaghbani, I. & Masounave, J. (2010b). Modeling of particle emission during dry orthogonal cutting. *Journal of materials engineering and performance*, 19, 776–789.

Kim, W. & Kwon, P. (2002). Phase transformation and its effect on flank wear in machining steels. *J. Manuf. Sci. Eng.*, 124(3), 659–666.

Kumar, S. S. & Kumar, S. R. (2021). Ionic liquids as environmental friendly cutting fluids-a review. *Materials today: PROCEEDINGS*, 37, 2121–2125.

LaGrange, T., Campbell, G., Turchi, P. & King, W. (2007). Rapid phase transformation kinetics on a nanoscale: Studies of the $\alpha \rightarrow \beta$ transformation in pure, nanocrystalline Ti using the nanosecond dynamic transmission electron microscope. *Acta materialia*, 55(15), 5211–5224.

Le, W., Caixu, Y., Xianli, L., Ming, L., Yongshi, X. & Liang, S. Y. (2024). Conventional and micro scale finite element modeling for metal cutting process: A review. *Chinese Journal of Aeronautics*, 37(2), 199–232.

Li, A., Pang, J., Zhao, J., Zang, J. & Wang, F. (2017). FEM-simulation of machining induced surface plastic deformation and microstructural texture evolution of Ti-6Al-4V alloy. *International Journal of Mechanical Sciences*, 123, 214–223.

Li, B., Zhang, S., Zhang, Q., Chen, J. & Zhang, J. (2018a). Modelling of phase transformations induced by thermo-mechanical loads considering stress-strain effects in hard milling of AISI H13 steel. *International Journal of Mechanical Sciences*, 149, 241–253.

Li, B., Zhang, S., Fang, Y., Wang, J. & Lu, S. (2019a). Effects of cutting parameters on surface quality in hard milling. *Materials and Manufacturing Processes*, 34(16), 1803–1815.

Li, B., Zhang, S. & Zhang, J. (2019b). Plastic deformation and grain refinement in surface layer induced by thermo-mechanical loads for hard milling process. *Proceedings of the Institution of Mechanical Engineers, Part B: Journal of Engineering Manufacture*, 233(10), 2033–2046.

Li, B., Zhang, S., Zhang, Q. & Li, L. (2019c). Simulated and experimental analysis on serrated chip formation for hard milling process. *Journal of Manufacturing Processes*, 44, 337–348.

Li, B., Zhang, S., Hu, R. & Zhang, X. (2020). Dislocation density and grain size evolution in hard machining of H13 steel: Numerical and experimental investigation. *Journal of Materials Research and Technology*, 9(3), 4241–4254.

Li, B., Zhang, S., Du, J. & Sun, Y. (2022). State-of-the-art in cutting performance and surface integrity considering tool edge micro-geometry in metal cutting process. *Journal of Manufacturing Processes*, 77, 380–411.

Li, J., Jing, L. & Chen, M. (2009). An FEM study on residual stresses induced by high-speed end-milling of hardened steel SKD11. *Journal of Materials Processing Technology*, 209(9), 4515–4520.

Li, J., Wang, B., Huang, H., Fang, S., Chen, P. & Shen, J. (2018b). Unified modelling of the flow behaviour and softening mechanism of a TC6 titanium alloy during hot deformation. *Journal of Alloys and Compounds*, 748, 1031–1043.

Li, K., Aghazadeh, F., Hatipkarasulu, S. & Ray, T. G. (2003). Health risks from exposure to metal-working fluids in machining and grinding operations. *International Journal of Occupational Safety and Ergonomics*, 9(1), 75–95.

Liang, X. & Liu, Z. (2017). Experimental investigations on effects of tool flank wear on surface integrity during orthogonal dry cutting of Ti-6Al-4V. *The International Journal of Advanced Manufacturing Technology*, 93, 1617–1626.

Liang, X., Liu, Z., Wang, Q., Wang, B. & Ren, X. (2020). Tool wear-induced microstructure evolution in localized deformation layer of machined Ti–6Al–4V. *Journal of Materials Science*, 55(8), 3636–3651.

Liao, Z., la Monaca, A., Murray, J., Speidel, A., Ushmaev, D., Clare, A., Axinte, D. & M'Saoubi, R. (2021). Surface integrity in metal machining-Part I: Fundamentals of surface characteristics and formation mechanisms. *International Journal of Machine Tools and Manufacture*, 162, 103687.

Liu, D., Ni, C., Wang, Y., Zhu, L. & Zheng, Z. (2023). Modified material constitutive model with activation energy for machining of selective laser melted Ti6Al4V alloys fabricated by different scanning strategies. *Journal of Materials Research and Technology*, 24, 9612–9629.

Liu, H., Zhang, J., Xu, X. & Zhao, W. (2018). Experimental study on fracture mechanism transformation in chip segmentation of Ti-6Al-4V alloys during high-speed machining. *Journal of Materials Processing Technology*, 257, 132–140.

Liu, H., Xu, X., Zhang, J., Liu, Z., He, Y., Zhao, W. & Liu, Z. (2022a). The state of the art for numerical simulations of the effect of the microstructure and its evolution in the metal-cutting processes. *International Journal of Machine Tools and Manufacture*, 177, 103890.

Liu, R., Salahshoor, M., Melkote, S. & Marusich, T. (2015). A unified material model including dislocation drag and its application to simulation of orthogonal cutting of OFHC Copper. *Journal of Materials Processing Technology*, 216, 328–338.

Liu, S. & Shin, Y. C. (2019). Additive manufacturing of Ti6Al4V alloy: A review. *Materials & Design*, 164, 107552.

Liu, Y., Xu, D., Agmell, M., Ahadi, A., Stahl, J.-E. & Zhou, J. (2021). Investigation on residual stress evolution in nickel-based alloy affected by multiple cutting operations. *Journal of Manufacturing Processes*, 68, 818–833.

Liu, Y.-P., Kilic, Z. M. & Altintas, Y. (2022b). Monitoring of in-process force coefficients and tool wear. *CIRP Journal of Manufacturing Science and Technology*, 38, 105–119.

Liu, Y., Mahmud, A., Kursawe, F. & Nam, T.-H. (2008). Effect of pseudoelastic cycling on the Clausius–Clapeyron relation for stress-induced martensitic transformation in NiTi. *Journal of Alloys and Compounds*, 449(1-2), 82–87.

Luo, S., Yao, J., Zou, G., Li, J., Jiang, J. & Yu, F. (2020). Transformation characteristics of temperature and phases within Ti-6Al-4V aeroengine drum in hot forging and air cooling procedures. *Journal of Materials Research and Technology*, 9(4), 8235–8244.

Lv, M., Li, A., Ge, D. & Zhang, R. (2022). Step-dependent grain refinement and micro-harness evolution during chip formation process in orthogonal cutting of titanium alloy Ti-6Al-4V. *The International Journal of Advanced Manufacturing Technology*, 1–18.

Ma, N., Aviv, D., Guo, H. & Braham, W. W. (2021). Measuring the right factors: A review of variables and models for thermal comfort and indoor air quality. *Renewable and Sustainable Energy Reviews*, 135, 110436.

Mabrouki, T., Girardin, F., Asad, M. & Rigal, J.-F. (2008). Numerical and experimental study of dry cutting for an aeronautic aluminium alloy (A2024-T351). *International Journal of Machine Tools and Manufacture*, 48(11), 1187–1197.

Mahnken, R., Wolff, M. & Cheng, C. (2013). A multi-mechanism model for cutting simulations combining visco-plastic asymmetry and phase transformation. *International Journal of Solids and Structures*, 50(20-21), 3045–3066.

Malinov, S., Guo, Z., Sha, W. & Wilson, A. (2001). Differential scanning calorimetry study and computer modeling of $\beta \Rightarrow \alpha$ phase transformation in a Ti-6Al-4V alloy. *Metallurgical and materials transactions A*, 32, 879–887.

Mantle, A. L. & Aspinwall, D. K. (2001). Surface integrity of a high speed milled gamma titanium aluminide. *Journal of materials processing technology*, 118(1-3), 143–150.

Martellotti, M. (1941). An analysis of the milling process. *Transactions of the American Society of Mechanical Engineers*, 63(8), 677–695.

Massin, N., Bohadana, A., Wild, P., Goutet, P., Kirstetter, H. & Toamain, J. (1996). Airway responsiveness, respiratory symptoms, and exposures to soluble oil mist in mechanical workers. *Occupational and environmental medicine*, 53(11), 748–752.

Melkote, S. N., Liu, R., Fernandez-Zelaia, P. & Marusich, T. (2015). A physically based constitutive model for simulation of segmented chip formation in orthogonal cutting of commercially pure titanium. *Cirp Annals*, 64(1), 65–68.

Mohamed-Amine, A., Mohamed, D., Abdelhakim, D. & Victor, S. (2021). Predictive analytical modeling of thermo-mechanical effects in orthogonal machining. *Materials*, 14(24), 7876.

Momeni, A. & Abbasi, S. (2010). Effect of hot working on flow behavior of Ti–6Al–4V alloy in single phase and two phase regions. *Materials & Design*, 31(8), 3599–3604.

Mondelin, A., Valiorgue, F., Rech, J., Coret, M. & Feulvarch, E. (2013). Modeling of surface dynamic recrystallisation during the finish turning of the 15-5PH steel. *Procedia Cirp*, 8, 311–315.

Moussaoui, K., Mousseigne, M., Senatore, J., Chieragatti, R. & Monies, F. (2013). Influence of milling on surface integrity of Ti6Al4V—study of the metallurgical characteristics: microstructure and microhardness. *The International Journal of Advanced Manufacturing Technology*, 67, 1477–1489.

Nagashima, F., Yoshino, M. & Terano, M. (2018). Microstructure control of pure iron by utilizing metal cutting method. *Procedia Manufacturing*, 15, 1541–1548.

Narutaki, N., Murakoshi, A., Motonishi, S. & Takeyama, H. (1983). Study on machining of titanium alloys. *CIRP Annals*, 32(1), 65–69.

Neugebauer, R., Bouzakis, K.-D., Denkena, B., Klocke, F., Sterzing, A., Tekkaya, A. E. & Wertheim, R. (2011). Velocity effects in metal forming and machining processes. *CIRP annals*, 60(2), 627–650.

Ng, E.-G. & Aspinwall, D. K. (2002). Modelling of hard part machining. *Journal of materials processing technology*, 127(2), 222–229.

Özel, T. & Arisoy, Y. (2014). Experimental and numerical investigations on machining induced surface integrity in Inconel-100 nickel-base alloy. *Procedia CIRP*, 13, 302–307.

Özel, T. (2006). The influence of friction models on finite element simulations of machining. *International journal of machine tools and manufacture*, 46(5), 518–530.

Pan, Z., Liang, S. Y., Garmestani, H. & Shih, D. S. (2016). Prediction of machining-induced phase transformation and grain growth of Ti-6Al-4 V alloy. *The International Journal of Advanced Manufacturing Technology*, 87, 859–866.

Pan, Z., Liang, S. Y. & Garmestani, H. (2019). Finite element simulation of residual stress in machining of Ti-6Al-4V with a microstructural consideration. *Proceedings of the Institution of Mechanical Engineers, Part B: Journal of Engineering Manufacture*, 233(4), 1103–1111.

Paschoalinoto, N. W., Bordinassi, E. C., Bortolussi, R., Leonardi, F. & Delijaicov, S. (2021). The effect of process parameters and cutting tool shape on residual stress of SAE 52100 hard turned steel by high speed machining. *Proceedings of the Institution of Mechanical Engineers, Part B: Journal of Engineering Manufacture*, 235(1-2), 290–300.

Pramanik, A. (2014). Problems and solutions in machining of titanium alloys. *The International Journal of Advanced Manufacturing Technology*, 70, 919–928.

Pramanik, A. & Littlefair, G. (2015). Machining of titanium alloy (Ti-6Al-4V)—theory to application. *Machining science and technology*, 19(1), 1–49.

Ramesh, A. & Melkote, S. N. (2008). Modeling of white layer formation under thermally dominant conditions in orthogonal machining of hardened AISI 52100 steel. *International Journal of Machine Tools and Manufacture*, 48(3-4), 402–414.

Rao, B., Dandekar, C. R. & Shin, Y. C. (2011). An experimental and numerical study on the face milling of Ti–6Al–4V alloy: Tool performance and surface integrity. *Journal of Materials Processing Technology*, 211(2), 294–304.

Rautio, S., Hynynen, P., Welling, I., Hemmilä, P., Usenius, A. & Närhi, P. (2007). Modelling of airborne dust emissions in CNC MDF milling. *Holz Roh Werkst (2007) 65: 335–341*, 335–341.

Research, P. (2024). Machining Market Size To Worth Around USD 755.66Bn By 2034. *Precedence Research*. Retrieved from: https://www.precedenceresearch.com/machining-market.

Ribamar, G. G., Mouráo dos Santos, L. P., Coelho, H. L., Jardini, A., Gomes da Silva, M. J., Gomes de Abreu, H. F. & Béreš, M. (2016). Study of Phase Transformation in Ti-6Al-4V Alloy Produced by Direct Metal Laser Sintering. *Proceedings of the 13th World Conference on Titanium*, pp. 1295–1298.

Robles, A., Aurrekoetxea, M., Plaza, S., Llanos, I. & Zelaieta, O. (2022). Empirical modeling of residual stress profiles in Ti6Al4V after face-milling. *Procedia Cirp*, 108, 362–366.

Rotella, G. & Umbrello, D. (2014). Finite element modeling of microstructural changes in dry and cryogenic cutting of Ti6Al4V alloy. *Cirp Annals*, 63(1), 69–72.

Ruitao, P., Linfeng, Z., Jiawei, T., Xiuli, F. & Meiliang, C. (2021). Application of pre-stressed cutting to aviation alloy: The effect on residual stress and surface roughness. *Journal of Manufacturing Processes*, 62, 501–512.

Sadeghifar, M., Sedaghati, R., Jomaa, W. & Songmene, V. (2018). A comprehensive review of finite element modeling of orthogonal machining process: chip formation and surface integrity predictions. *The International Journal of Advanced Manufacturing Technology*, 96, 3747–3791.

Sadeghifar, M., Javidikia, M., Songmene, V. & Jahazi, M. (2020). Finite element simulation-based predictive regression modeling and optimum solution for grain size in machining of Ti6Al4V alloy: Influence of tool geometry and cutting conditions. *Simulation Modelling Practice and Theory*, 104, 102141.

Salahshoor, M. & Guo, Y. (2011). Surface integrity of biodegradable orthopedic magnesium–calcium alloy by high-speed dry face milling. *Production Engineering*, 5, 641–650.

Sarıkaya, M., Gupta, M. K., Tomaz, I., Pimenov, D. Y., Kuntoğlu, M., Khanna, N., Yıldırım, Ç. V. & Krolczyk, G. M. (2021). A state-of-the-art review on tool wear and surface integrity characteristics in machining of superalloys. *CIRP Journal of Manufacturing Science and Technology*, 35, 624–658.

Sartkulvanich, P., Altan, T. & Göcmen, A. (2005). Effects of flow stress and friction models in finite element simulation of orthogonal cutting—a sensitivity analysis. *Machine Science and Technology*, 9(1), 1–26.

Schulze, V., Uhlmann, E., Mahnken, R., Menzel, A., Biermann, D., Zabel, A., Bollig, P., Ivanov, I. M., Cheng, C., Holtermann, R. et al. (2015). Evaluation of different approaches for modeling phase transformations in machining simulation. *Production Engineering*, 9, 437–449.

Sharma, S. & Meena, A. (2020). Microstructure attributes and tool wear mechanisms during high-speed machining of Ti-6Al-4V. *Journal of Manufacturing Processes*, 50, 345–365.

Shivpuri, R., Hua, J., Mittal, P., Srivastava, A. & Lahoti, G. (2002). Microstructure-mechanics interactions in modeling chip segmentation during titanium machining. *CIRP annals*, 51(1), 71–74.

Shnfir, M., Kouam, J. & Songmene, V. (2020). Ultrafine particle emission during high-speed milling of hardened AISI 1045 steel. *The International Journal of Advanced Manufacturing Technology*, 110, 617–627.

Shu, A., Ren, J., Zhou, J. & Wang, Z. (2024). Grain refinement mechanism in chip and the machined subsurface during high-speed machining of Inconel 718 alloy. *Materials Characterization*, 207, 113559.

Shuang, F., Chen, X. & Ma, W. (2018). Numerical analysis of chip formation mechanisms in orthogonal cutting of Ti6Al4V alloy based on a CEL model. *International Journal of Material Forming*, 11, 185–198.

Singh, N., Hameed, P., Ummethala, R., Manivasagam, G., Prashanth, K. & Eckert, J. (2020). Selective laser manufacturing of Ti-based alloys and composites: Impact of process parameters, application trends, and future prospects. *Materials today advances*, 8, 100097.

Sokolović, D. S., Höflinger, W., Sokolović, R. M. Š., Sokolović, S. M. & Sakulski, D. (2013). Experimental study of mist generated from metalworking fluids emulsions. *Journal of aerosol science*, 61, 70–80.

Song, X., Li, A., Lv, M., Lv, H. & Zhao, J. (2019). Finite element simulation study on pre-stress multi-step cutting of Ti-6Al-4V titanium alloy. *The International Journal of Advanced Manufacturing Technology*, 104, 2761–2771.

Songmene, V., Balout, B., & Masounave, J. (2008). Clean machining: Experimental investigation on dust formation: Part II: Influence of machining strategies and drill condition. *International Journal of Environmentally Conscious Design & Manufacturing*, 14(1), 17–33.

Sujova, E. (2012). Contamination of the working air via metalworking fluids aerosols. *Engineering Review: Međunarodni časopis namijenjen publiciranju originalnih istraživanja s aspekta analize konstrukcija, materijala i novih tehnologija u području strojarstva, brodogradnje, temeljnih tehničkih znanosti, elektrotehnike, računarstva i građevinarstva*, 32(1), 9–15.

Sun, J. & Guo, Y. (2009). A comprehensive experimental study on surface integrity by end milling Ti–6Al–4V. *Journal of materials processing technology*, 209(8), 4036–4042.

Sun, S., Brandt, M. & Dargusch, M. (2009). Characteristics of cutting forces and chip formation in machining of titanium alloys. *International Journal of Machine Tools and Manufacture*, 49(7-8), 561–568.

Sun, W., Shan, F., Zong, N., Dong, H. & Jing, T. (2021). A simulation and experiment study on phase transformations of Ti-6Al-4V in wire laser additive manufacturing. *Materials & Design*, 207, 109843.

Sun, Z., Geng, D., Guo, H., Zhang, Q., Liu, Y., Liu, L., Jiang, X. & Zhang, D. (2024). Introducing transversal vibration in twist drilling: Material removal mechanisms and surface integrity. *Journal of Materials Processing Technology*, 325, 118296.

Sutherland, J., Kulur, V., King, N. & Von Turkovich, B. (2000). An experimental investigation of air quality in wet and dry turning. *Cirp Annals*, 49(1), 61–64.

Tan, L., Zhang, D., Yao, C., Wu, D. & Zhang, J. (2017). Evolution and empirical modeling of compressive residual stress profile after milling, polishing and shot peening for TC17 alloy. *Journal of Manufacturing Processes*, 26, 155–165.

Tang, D., Wang, C., Hu, Y. & Song, Y. (2009). Finite-element simulation of conventional and high-speed peripheral milling of hardened mold steel. *Metallurgical and Materials Transactions A*, 40, 3245–3257.

Tounsi, N. & El-Wardany, T. (2022). Finite element analysis of the effects of process representations on the prediction of residual stresses and chip morphology in the down-milling of Ti6Al4V: part I: milling of small uncut chip thicknesses in the micrometer range with finite cutting edge radius. *Journal of Manufacturing Science and Engineering*, 144(1), 011010.

Ullah, I., Zhang, S., Zhang, Q. & Li, B. (2021a). Microstructural and mechanical property investigation of machined surface layer in high-speed milling of Ti-6Al-4V alloy. *The International Journal of Advanced Manufacturing Technology*, 116(5), 1707–1719.

Ullah, I., Zhang, S., Zhang, Q. & Wang, R. (2021b). Numerical investigation on serrated chip formation during high-speed milling of Ti-6Al-4V alloy. *Journal of Manufacturing Processes*, 71, 589–603.

Ullah, I., Zhang, S. & Waqar, S. (2022). Numerical and experimental investigation on thermo-mechanically induced residual stress in high-speed milling of Ti-6Al-4V alloy. *Journal of Manufacturing Processes*, 76, 575–587.

Ullah, I., Akinlabi, E. T., Songmene, V., Kouam, J. & Sadeghifar, M. (2024a). A multiscale finite element modeling for predicting the surface integrity induced by thermo-mechanical loads during high-speed milling of Ti-6Al-4V. *CIRP Journal of Manufacturing Science and Technology*, 52, 246–263.

Ullah, I., Akinlabi, E. T. & Songmene, V. (2024b). Thermo-metallo-mechanical based phase transformation modeling for high-speed milling of Ti–6Al–4V through stress-strain and temperature effects. *Journal of Materials Research and Technology*, 30, 894–909.

Ulutan, D. & Ozel, T. (2011). Machining induced surface integrity in titanium and nickel alloys: A review. *International Journal of Machine Tools and Manufacture*, 51(3), 250–280.

Umbrello, D. & Filice, L. (2009). Improving surface integrity in orthogonal machining of hardened AISI 52100 steel by modeling white and dark layers formation. *CIRP annals*, 58(1), 73–76.

Umbrello, D., Rizzuti, S., Outeiro, J., Shivpuri, R. & M'Saoubi, R. (2008). Hardness-based flow stress for numerical simulation of hard machining AISI H13 tool steel. *Journal of Materials Processing Technology*, 199(1-3), 64–73.

Vashista, M. & Paul, S. (2012). Correlation between full width at half maximum (FWHM) of XRD peak with residual stress on ground surfaces. *Philosophical Magazine*, 92(33), 4194–4204.

Velásquez, J. P., Bolle, B., Chevrier, P., Geandier, G. & Tidu, A. (2007). Metallurgical study on chips obtained by high speed machining of a Ti–6 wt.% Al–4 wt.% V alloy. *Materials Science and Engineering: A*, 452, 469–474.

Velásquez, J. P., Tidu, A., Bolle, B., Chevrier, P. & Fundenberger, J.-J. (2010). Sub-surface and surface analysis of high speed machined Ti–6Al–4V alloy. *Materials Science and Engineering: A*, 527(10-11), 2572–2578.

Wan, M., Ye, X.-Y., Wen, D.-Y. & Zhang, W. (2019). Modeling of machining-induced residual stresses. *Journal of materials science*, 54, 1–35.

Wan, Z., Zhu, Y., Liu, H. & Tang, Y. (2012). Microstructure evolution of adiabatic shear bands and mechanisms of saw-tooth chip formation in machining Ti6Al4V. *Materials Science and Engineering: A*, 531, 155–163.

Wang, B. & Liu, Z. (2014). Investigations on the chip formation mechanism and shear localization sensitivity of high-speed machining Ti6Al4V. *The International Journal of Advanced Manufacturing Technology*, 75, 1065–1076.

Wang, B. & Liu, Z. (2015). Shear localization sensitivity analysis for Johnson–Cook constitutive parameters on serrated chips in high speed machining of Ti6Al4V. *Simulation Modelling Practice and Theory*, 55, 63–76.

Wang, B., Liu, Z., Su, G., Song, Q. & Ai, X. (2015). Investigations of critical cutting speed and ductile-to-brittle transition mechanism for workpiece material in ultra-high speed machining. *International Journal of Mechanical Sciences*, 104, 44–59.

Wang, B., Xiao, X., Astakhov, V. P. & Liu, Z. (2019). The effects of stress triaxiality and strain rate on the fracture strain of Ti6Al4V. *Engineering Fracture Mechanics*, 219, 106627.

Wang, B., Liu, Z., Cai, Y., Luo, X., Ma, H., Song, Q. & Xiong, Z. (2021). Advancements in material removal mechanism and surface integrity of high speed metal cutting: A review. *International Journal of Machine Tools and Manufacture*, 166, 103744.

Wang, C., Ding, F., Tang, D., Zheng, L., Li, S. & Xie, Y. (2016a). Modeling and simulation of the high-speed milling of hardened steel SKD11 (62 HRC) based on SHPB technology. *International Journal of Machine Tools and Manufacture*, 108, 13–26.

Wang, F., Liu, Z., Guo, Y., Zhao, J. & Liu, Z. (2017a). Efficient multiscale modeling and validation of residual stress field in cutting. *Journal of Manufacturing Science and Engineering*, 139(9), 091004.

Wang, L., Li, R., Liu, E. & Zhang, H. (2022). Experimental research on chip morphology of Ti-5553 cutting under high-pressure cooling. *Integrated Ferroelectrics*, 229(1), 62–77.

Wang, Q. & Liu, Z. (2018). Microhardness prediction based on a microstructure-sensitive flow stress model during high speed machining Ti-6Al-4V. *Journal of Manufacturing Science and Engineering*, 140(9), 091003.

Wang, Q., Liu, Z., Wang, B., Song, Q. & Wan, Y. (2016b). Evolutions of grain size and micro-hardness during chip formation and machined surface generation for Ti-6Al-4V in high-speed machining. *The International Journal of Advanced Manufacturing Technology*, 82, 1725–1736.

Wang, Q., Liu, Z., Yang, D. & Mohsan, A. U. H. (2017b). Metallurgical-based prediction of stress-temperature induced rapid heating and cooling phase transformations for high speed machining Ti-6Al-4V alloy. *Materials & Design*, 119, 208–218.

Wang, Q., Niu, C., Liu, Z., Wang, Y., Cheng, Y. & Cui, Y. (2023a). The hardening effect of deformation twinning based on visco-plastic self consistent model and a multi-scale grain refinement prediction model during machining of titanium alloy. *Journal of Materials Research and Technology*, 26, 1922–1937.

Wang, Z.-Y., Ren, J.-X., Zhou, J.-H. & Cai, J. (2023b). Correlation analysis of microstructure evolution on microhardness and residual stress for cutting Ti-6Al-4V titanium alloy. *Proceedings of the Institution of Mechanical Engineers, Part B: Journal of Engineering Manufacture*, 237(6-7), 885–898.

Wang, Z., Zhou, J., Ren, J. & Shu, A. (2023c). Hybrid prediction model for residual stress profile induced by multi-axis milling Ti-6Al-4 V titanium alloy combined finite element with experiment. *The International Journal of Advanced Manufacturing Technology*, 126(9), 4495–4511.

Waqar, S., Guo, K. & Sun, J. (2022). Evolution of residual stress behavior in selective laser melting (SLM) of 316L stainless steel through preheating and in-situ re-scanning techniques. *Optics & Laser Technology*, 149, 107806.

Wyen, C.-F., Jaeger, D. & Wegener, K. (2013). Influence of cutting edge radius on surface integrity and burr formation in milling titanium. *The International Journal of Advanced Manufacturing Technology*, 67, 589–599.

Xiao, Y.-W., Lin, Y., Jiang, Y.-Q., Zhang, X.-Y., Pang, G.-D., Wang, D. & Zhou, K.-C. (2020). A dislocation density-based model and processing maps of Ti-55511 alloy with bimodal microstructures during hot compression in α+ β region. *Materials Science and Engineering: A*, 790, 139692.

Xiong, X., Hu, S., Hu, K. & Zeng, S. (2016). Texture and magnetic property evolution of non-oriented Fe–Si steel due to mechanical cutting. *Journal of Magnetism and Magnetic Materials*, 401, 982–990.

Xu, B., Zhang, J., Liu, H., Xu, X. & Zhao, W. (2021). Serrated chip formation induced periodic distribution of morphological and physical characteristics in machined surface during high-speed machining of Ti6Al4V. *Journal of Manufacturing Science and Engineering*, 143(10), 101006.

Xu, X., Zhang, J., Outeiro, J., Xu, B. & Zhao, W. (2020). Multiscale simulation of grain refinement induced by dynamic recrystallization of Ti6Al4V alloy during high speed machining. *Journal of Materials Processing Technology*, 286, 116834.

Xu, X., Outeiro, J., Zhang, J., Li, X. & Zhao, W. (2024). A framework to efficiently simulate the cyclic variation of the residual stresses induced by chip formation in machining of Ti-6Al-4 V alloy. *CIRP Journal of Manufacturing Science and Technology*, 51, 57–72.

Xu, Y., Yue, C., Chen, Z., Li, M., Wang, L. & Liu, X. (2023). Finite element simulation of residual stress in milling of aluminum alloy with different passes. *The International Journal of Advanced Manufacturing Technology*, 127(9), 4199–4210.

Yameogo, D., Haddag, B., Makich, H. & Nouari, M. (2019). A physical behavior model including dynamic recrystallization and damage mechanisms for cutting process simulation of the titanium alloy Ti-6Al-4V. *The International Journal of Advanced Manufacturing Technology*, 100, 333–347.

Yan, Y., Chibowski, E. & Szcześ, A. (2017). Surface properties of Ti-6Al-4V alloy part I: Surface roughness and apparent surface free energy. *Materials Science and Engineering: C*, 70, 207–215.

Yanagimoto, J. & Liu, J. (1999). Incremental formulation for the prediction of microstructural change in multi-pass hot forming. *ISIJ international*, 39(2), 171–175.

Yang, D., Liu, Z., Ren, X. & Zhuang, P. (2016). Hybrid modeling with finite element and statistical methods for residual stress prediction in peripheral milling of titanium alloy Ti-6Al-4V. *International Journal of Mechanical Sciences*, 108, 29–38.

Ye, G., Chen, Y., Xue, S. & Dai, L. (2014). Critical cutting speed for onset of serrated chip flow in high speed machining. *International Journal of Machine Tools and Manufacture*, 86, 18–33.

Zaghbani, I., Songmene, V. & Khettabi, R. (2009). Fine and ultrafine particle characterization and modeling in high-speed milling of 6061-T6 aluminum alloy. *Journal of materials engineering and performance*, 18, 38–48.

Zannoun, H. & Schoop, J. (2023). Analysis of burr formation in finish machining of nickel-based superalloy with worn tools using micro-scale in-situ techniques. *International Journal of Machine Tools and Manufacture*, 189, 104030.

Zhang, F.-y., Duan, C.-z., Wang, M.-j. & Sun, W. (2018). White and dark layer formation mechanism in hard cutting of AISI52100 steel. *Journal of Manufacturing Processes*, 32, 878–887.

Zhang, J., He, B. & Zhang, B. (2023). Failure mode change and material damage with varied machining speeds: a review. *International Journal of Extreme Manufacturing*, 5(2), 022003.

Zhang, X., Shivpuri, R. & Srivastava, A. (2014). Role of phase transformation in chip segmentation during high speed machining of dual phase titanium alloys. *Journal of Materials Processing Technology*, 214(12), 3048–3066.

Zhang, X., Wu, S. & Liu, C. R. (2011). The periodical fluctuation of residual stress in hard turned surface and its relationship with chip formation. *International Manufacturing Science and Engineering Conference*, 44304, 205–213.

Zhang, Y. & Bai, Q. (2023). Microstructure effects on surface integrity in slot micro-milling multiphase titanium alloy Ti6Al4V. *Journal of Materials Research and Technology*, 25, 6684–6701.

Zhao, G., Zhao, B., Ding, W., Xin, L., Nian, Z., Peng, J., He, N. & Xu, J. (2024). Nontraditional energy-assisted mechanical machining of difficult-to-cut materials and components in aerospace community: a comparative analysis. *International Journal of Extreme Manufacturing*, 6(2), 022007.

Zhao, J., Liu, Z., Wang, B., Song, Q., Cai, Y., Khan, A. M., Wan, Y. & Ren, X. (2023). A comprehensive review of generating, monitoring, evaluating, and controlling particle emissions during machining process. *Journal of Manufacturing Systems*, 70, 395–416.

Zhou, R. (2024). Modeling and simulation of residual stress in metal cutting process: A review. *Advances in Mechanical Engineering*, 16(12), 16878132241307714.

Zlatin, N. & Field, M. (1973). Procedures and precautions in machining titanium alloys. In *Titanium science and technology* (pp. 489–504). Springer.